THE EFFECT OF ULTRASOUND ON THE DRUG DELIVERY OF RGD-

TARGETED LIPOSOMES

by

Mohamad Mahmoud

A Thesis presented to the Faculty of the
American University of Sharjah
College of Engineering
In Partial Fulfillment
of the Requirements
for the Degree of

Master of Science in
Chemical Engineering

Sharjah, United Arab Emirates

May 2018

Approval Signatures

We, the undersigned, approve the Masters Thesis of Mohamad Mahmoud

Thesis Title: The Effect of Ultrasound on the Drug Delivery of RGD-Targeted Liposomes.

Signature   **Date of Signature**
                                                                 (29/04/2018)

_____   _____
Dr. Ghaleb Husseini
Professor, Department of Chemical Engineering
Thesis Advisor

_____   _____
Dr. Paul Nancarrow
Associate Professor, Department of Chemical Engineering
Thesis Committee Member

_____   _____
Dr. Gerassimos Barlas
Professor, Department of Computer Science and Engineering
Thesis Committee Member

_____   _____
Dr. Naif Darwish
Head, Department of Chemical Engineering

_____   _____
Dr. Ghaleb Husseini
Associate Dean for Graduate Affairs and Research
College of Engineering

_____   _____
Dr. Richard T. Schoephoerster
Dean, College of Engineering

_____   _____
Dr. Mohamed El-Tarhuni
Vice Provost for Graduate Studies

Acknowledgements

My deepest gratitude goes to Dr. Ghaleb Husseini, who is a dear friend before being my thesis advisor and professor. I have known Dr. Ghaleb since he was my academic advisor in 2009. His positive energy and guidance never failed to keep me motivated in times of doubt or frustration. He always suggested a solution for every challenge that I have encountered during my research. Your insight, profound discussions, broad experience, and continuous support have nonetheless contributed extensively towards the success of this thesis. You are an example of an excellent leader, Dr. Ghaleb. I wouldn't have done it without you. I would also like to thank Dr. Rute Vitor for her outstanding mentorship in the lab. Dr. Rute was always patient, very friendly, and never hesitated to stay overtime to teach me all the lab skills I needed to proceed. Furthermore, Dr. Mohammed Al Sayah always shared his expertise and provided wise comments whenever I had organic chemistry doubts. Dr. Nahid Awad, you have been a motherly figure for everyone in the lab before being our research supervisor. I will never forget how you always motivated me to attain my highest potential, and how you prioritized my research over yours. Mr. Vinod Paul, our friendly, helpful, and resilient research assistant has always offered help and maintained a comfortable, enjoyable and positive environment in the lab, alongside Dr. Nahid. I would like to thank our excellent Chemical Engineering faculty at the AUS for being supporting and inspiring. I would like to thank Dr. Naif Darwish for being a remarkable department head and for giving me this fantastic opportunity. I extend my thanks to Dr. Hussein Ahmed for being a supportive fatherly figure and my undergraduate senior design advisor. Dr. Amani Al-Othman is a great and supportive professor whom I have worked with and taught alongside for several semesters. I would like to thank my thesis committee, Dr. Paul Nancarrow, and Dr. Gerassimos Barlas for their time and their insightful output towards this thesis. I would also like to sincerely thank AUS for giving me this opportunity.

I would also like to acknowledge colleagues, friends, and family who supported me throughout this journey. Ms. Najla Mohammed is one of the hardworking pioneers in the Biomed lab whose thesis is a prestigious model in the field. Ms. Mihad Ibrahim is an enthusiastic character and a colleague who always offered a helping hand. Ms. Amal Ahmed is an intelligent, hardworking colleague whom I enjoyed her company while working in the lab. My eldest sister, Hiba, who has been my mentor in life since childhood. My loving father for supporting me and funding my education. And of course, I would like to dedicate this thesis to my mother for being the most supportive, caring, and loving person I have in my life.

Dedication

To my loving and caring mother…

Abstract

Approaches used to treat cancer, with the most prominent being chemotherapy, have detrimental effects on patients' health. Doxorubicin, a chemotherapeutic agent, alters normal cellular functions and can cause many fatal side effects, such as cell loss and congestive heart failure. Smart Drug Delivery Systems (DDS), such as liposomes, constitute a novel approach which can deliver a cytotoxic agent to the tumor without affecting healthy cells. A moiety, such as an RGD motif, can be conjugated to the liposome's surface. This modification increases the efficacy of such liposomes by actively targeting specific receptors which are overexpressed on the surface of cancer cells. Two types of carriers were developed in this study, RGD-positive, and their control counterparts, RGD-negative (NH_2 liposomes). The liposomes possessed radii of 88.26 ± 5.55 nm and 79.52 ± 4.81 nm, respectively, which classify them as Large Uni-lamellar Vesicles (LUVs). A 20-kHz ultrasound probe at three power densities, 7.46, 9.85, and 17.31 mW/cm^2, equivalent to mechanical index (MI) values of 0.11, 0.12, and 0.16, respectively, was used to trigger the liposomes into releasing their encapsulated fluorescent model-drug, calcein. Both types of liposomes were stable and showed a higher release rate as the power density increased. Nine drug release kinetics models were utilized to model the online release profiles, where the Korsmeyer-Peppas and the Weibull models presented the best fits, predicting diffusion and dissolution-driven drug release, respectively. Statistical analysis showed that the release rate constants were significantly affected by changes in power densities and the type of carrier. The calculated average release rate constants were $K_{KP} = 5.7291$ ($s^{-1.0789}$) and $K_W = 5.3734$ for NH_2 liposomes, and $K_{KP} = 9.3574$ ($s^{-0.9441}$) and $K_W = 6.2857$ for RGD liposomes. This thesis presents the preparation of the smart DDS (liposomes), evaluates its stability and storage, and analyzes its drug release and sensitivity to ultrasound. The overall goal is to design a drug delivery system capable of reducing the side effects of conventional chemotherapy and hence improving the quality of life of cancer patients worldwide.

Keywords: *Drug Delivery, Cancer, Liposomes, RGD, Active Targeting, Ultrasound, Triggered Release.*

Table of Contents

8

List of Figures

List of Tables

List of Abbreviations

BCA   Bicinchoninic Acid

CFR   Cumulative Fraction Released

DDS   Drug Delivery Systems

DLS   Dynamic Light Scattering

DOX   Doxorubicin

DPPC   1,2-DiPalmitoyl-*sn*-glycerol-3-PhosphoCholine

DSPE-PEG-NH_2 1,2-Distearoyl-*Sn*-glycero-3-PhosphoEthanolamine-N-[amino(Polyethylene Glycol)-2000]

EPR   Enhanced Permeability and Retention effect

KP   Korsmeyer-Peppas

LFUS   Low Frequency Ultrasound

LD   Liquid-Disordered

LO   Liquid-Ordered

LUV   Large Uni-lamellar Vesicles

MDR   Multi Drug Resistance

MLV   Multi-Lamellar Vesicles

MI   Mechanical Index

NH_2 Amine group

PBS   Phosphate-Buffered Saline

PEG   Poly-Ethylene Glycol

REV   Reverse phase evaporation

RGD   Arginine-Glycine-Aspartic acid

SO   Solid-Ordered

SUV	Small Uni-lamellar Vesicles
ULV	Uni-Lamellar Vesicles
US	Ultrasound

Chapter 1: Introduction and Literature Review

Cancer is an abnormal and uncontrollable growth of cells which develop into tumors. Treatments are implemented depending on the development stage of cancer. In its early stages, surgery and radiation are often used to eradicate local tumors. However, these methods are ineffective for late-stage cancers, especially when metastasis has occurred. In such stages of advanced cancers, chemotherapy is the primary choice of treatment. Such method utilizes lethal drugs, injected into the bloodstream of the patient, which affect healthy and malignant cells alike. In addition to that, chemotherapy comes with a long list of undesirable and severe side effects, affecting the patient's health. Doxorubicin, a widely used chemotherapeutic drug, has severe side effects on the human body, including cardiotoxicity. Smart drug delivery systems can be utilized to reduce the chemotherapeutic side effects while enhancing the efficacy of the treatment. These smart systems take advantage of irregularities possessed by cancerous cells, such as aberrant angiogenesis and receptor over-expression.

This study has established a smart drug delivery system comprised of calcein-encapsulated, stealthy liposomes which are sono-sensitive for triggered release, with RGD moieties attached to its surface to enable active targeting. Liposomes are spherical, phospholipid nanovesicles with an aqueous medium enclosed in their core, allowing them to carry drugs or other substances into tissues. Liposomes are very safe since they are nontoxic, biocompatible, and biodegradable. The small size of these nanovesicles allows for passive targeting, where they selectively diffuse into such growths due to their various peculiarities. One such peculiarity is irregular angiogenesis, where leaky and defective capillaries rapidly spawn around the growth. Furthermore, stealthy liposomes incorporate polyethylene glycol ligands on their surface to prevent them from being opsonized or detected by the reticuloendothelial system. RGD moieties on the surface of these liposomes enable them to actively target specific cancerous cells overexpressing RGD sequences, such as brain, bone, and liver cancer.

Once these smart liposomes have passively and actively targeted malignant growths, they are triggered with ultrasound to release their encapsulated drug contents. Ultrasound waves are safe, noninvasive, and nonradiative since it has been used to image the fetal development in pregnant women and various medical applications.

Ultrasound triggers drug release from liposomes due to cavitation. Cavitation is a mechanical effect caused by nucleated gas bubbles which oscillate and may eventually erupt. These mechanical effects, which are occurring inside the liposome, act on shearing and destroying the phospholipid's bilayer. These disturbances make the liposomes more permeable, allowing for the diffusion of its encapsulated drug. Modeling the kinetics of the drug release from these liposomes, as well as optimizing the parameters of the applied ultrasound is essential for effectively implementing controlled release.

These concepts are introduced and discussed in the following literature review section.

1.1.   Introduction to Cancer

Cancer is the general term used for an abnormal, uncontrollable growth of cells. Cancer leads to the development of neoplasms, which are new growths that can be divided into benign and malignant, although the distinction is unclear in some instances [12]. Malignant tumors will invade surrounding structures and metastasize (spread to distant sites), whereas a benign tumor will not [12]. Also, malignant tumors tend to show more rapid growth than benign neoplasms and are partly composed of cells showing frequent mitotic activity; progressive growth without self-limitation [12]. Malignant neoplasms are divided into two main types: sarcomas and carcinomas. Sarcomas arise from cells of mesenchymal origin (such as bone, muscle, and connective tissue), while carcinomas arise from epithelial cells and tissues (such as skin, mucosal membranes, and glandular tissues) [12].

Cells in different tissues in the body have distinct characteristics. Cells specialized in conducting the functions of a particular tissue or organ (differentiated cells) do not divide, while less well-differentiated stem cells within these tissues or organs can proliferate to replace senescent, well-differentiated cells [13]. When a healthy, proliferating stem cell differentiates, it loses its ability to divide, but in cancer, dividing cells seem to lose the capacity to differentiate [13]. These cells also acquire the ability to invade through basement membranes and metastasize to all areas of the body [13].

Factors involved in the development of cancer are thought to be genetic and environmental. It is hypothesized that cancer develops due to the influence of one or

both mentioned factors. The emergence of cancer appears to involve the accumulation of genetic damage in a target tissue [13]. Studying the developmental stages of cancer is difficult. Thus, research has focused on the identification, isolation, and characterization of oncogenes [13]. It is observed that the development of cancer in first-degree relatives is higher in families with a strong history [13]. Environmental factors involved in the development of cancers can be chemical, physical, or biological carcinogenic agents [13]. At least three stages, which are initiation, promotion, and progression, occur in the natural history of cancer development from environmental factors [13]. Initiation occurs when environmental agents induce the activation of oncogenes, which are genes that have potential to cause cancer and are usually highly expressed in cancer cells [13, 14]. Promotion involves promoting agents, which are incapable of inducing cancer on their own, significantly enhancing the development of cancers with the presence of initiating agents [13]. Progression is characterized by the development of aneuploidy (the condition of having an abnormal chromosome number) and clonal variation in the tumor, ultimately resulting in metastasis [13]. Inducing agents could be chemical, physical, or biological. Chemical carcinogens are usually dietary or environmental, such as tobacco smoke. Physical carcinogens are mainly ionizing radiation, ultraviolet radiation, and foreign bodies, with the latter thought of as a biological carcinogen as well.

1.2. Cancer Treatments

The treatment of cancer can be classified into four major approaches: surgery, radiation therapy, chemotherapy, and biological therapy or gene therapy. A combination of two or more approaches is often used together to achieve synergistic effects. Surgery and radiation therapy are usually implemented locally to reduce the bulk of the tumor, increasing the efficacy of subsequent treatment by other modalities [13]. Chemotherapy involves the use of toxic agents that exert maximum antitumor effects when employed at the maximum tolerated dose [13]. However, the success of this approach is limited due to its inability to deliver adequate doses, leading to the development of resistance [13]. Chemotherapy becomes the favorable approach when cancer has metastasized and thus cannot be removed by surgery or treated with radiation therapy [15]. Consequently, using targeted drug delivery systems, controlled release, and combination chemotherapy have developed recently to increase the efficiency of

chemotherapeutic agents. Biological therapy uses an agent that is capable of altering the host-tumor relationship in favor of the host, such as boosting the host's defense or attack against the tumor, or inhibiting the growth, invasiveness, and the metastatic potential of the tumor [13].

1.2.1. Chemotherapy. Chemotherapy involves the administration of chemical substances for the treatment of disease, especially cancer, or for the prevention of aberrant growth of cells or tissues [15]. Chemotherapy kills aberrant cells by inhibiting cell division and inducing apoptosis (programmed cell death) [15]. However, due to the inherent nature of their action, chemotherapeutic drugs also damage actively growing healthy cells [15]. New types of anticancer agents include antibodies, hormones, and immunotherapies, which are often used in conjunction with conventional chemotherapy for a more targeted treatment [15].

Chemotherapeutic agents can be branched into six main classifications:

1. Folic acid antagonists.
2. Nucleic acid antagonists.
3. Antitumor antibiotics.
4. Monoclonal antibodies.
5. Tyrosine kinase inhibitors.
6. Hormonal agents.

The first type of chemotherapeutic agents, folic acid antagonists, was designed to inhibit a cancer cell's ability to produce folic acid, which is an essential chemical metabolite for the growth and division of cells [15, 16]. Aminopterin was the first used folic acid antagonist when it was reported that over half of children with acute leukemia could obtain temporary diminutions in abnormal growth by using aminopterin [15]. Nucleic acid antagonists are designed to have a toxic effect on the cell's DNA. The tumor growth is stopped with chemicals that antagonize the nucleic acids, which are necessary for cancer growth and division [15]. One of the first used nucleic acid antagonists, 6-mercaptopurine, was used for the treatment of lymphoblastic leukemia [15]. Antitumor antibiotics are designed to exhibit cytotoxicity on human cells, rather than bacteria and fungi, as in the case of antimicrobial antibiotics [15]. Antitumor antibiotics became recognized as potential chemotherapeutic agents in 1954 when actinomycin D was studied [15]. Nowadays, Doxorubicin, belonging to the antitumor

antibiotics branch, is one of the most widely used anticancer drugs for both solid tumors and blood or bone marrow tumors [15]. Monoclonal antibodies are a new class of drugs that target specific cell receptors overexpressed in almost all cancer cells [15]. Such antibodies are either used to directly inhibit the growth of tumor cells by binding to their receptors or to deliver a chemotherapeutic agent to a specific tumor cell type using a monoclonal antibody [13, 15]. Another class of anticancer agents that have been introduced in clinical practice involves small-molecule tyrosine kinase inhibitors [15]. Tyrosine kinase enzymes regulate several of the intracellular processes ordinarily responsible for cell proliferation that are otherwise dysregulated in cancers [15]. Imatinib is one of the most promising recent drugs since it is a tyrosine kinase inhibitor, explicitly targeting myelocytic leukemia cells, resulting in hematologic, cytogenetic, and sometimes complete molecular remissions [15]. Hormonal agents function by inhibiting cancer cells which overexpress hormone receptors on the cell's surface [15]. One of the most representative hormonal agents is tamoxifen, which is a selective estrogen receptor modulator that also has partial estrogen agonist activity [15].

Chemotherapy or immunotherapy is applied based on three main principles. It is used when cancer has spread to multiple sites and cannot be removed surgically or treated with radiation therapy [15]. The approach is called adjuvant therapy when it is used to destroy the undetectable residual tumor after all detectable tumors have been exterminated [15]. Lastly, neoadjuvant chemotherapy is used to shrink a tumor before surgery or radiation [15].

Cells can become resistant to chemotherapeutic drugs through several ways. A general mechanism, referred to as multi drug resistance (MDR), results from an acquired ability of the cells to pump these drugs out before they can cause irreversible damage [15]. Also, cancer cells can become resistant to chemotherapy by increasing the amount of intracellular drug target, or reducing the uptake of drugs, or decreasing the expression of a drug target. Additionally, tumors grow exponentially in their early phases, and then a deceleration in the growth rate occurs, which means an increase in the number of cells that are not dividing [15]. Such cells are less susceptible to killing by drugs, which act only on dividing cells, thus reducing the efficiency of the chemotherapeutic agent [15]. Due to the previously mentioned factors, a combination of anticancer therapies, multidrug chemotherapy, or drug delivery systems is used to

overcome the drug resistance of cancer cells as well as increase the efficacy of the chemotherapeutic agents.

1.2.2. Doxorubicin. Doxorubicin (DOX), commonly referred to as Adriamycin, is an anticancer drug used for the treatment of solid tumors [17]. The anticancer activity of DOX has been attributed to its ability to intercalate into DNA, and inhibit topoisomerase II, since it is an anthracycline [17]. DOX spontaneously binds to DNA, by a mechanism termed intercalation, where the planar drug molecule inserts between and binds in parallel to the base pairs of DNA non-covalently [17, 18]. The observed inhibition of DNA replication and RNA transcription after subjecting cancer cells to treatment is caused by intercalation [18]. Additionally, doxorubicin induces specific single and double-strand protein associated breaks in the DNA, where the protein associated with these breaks has shown to be topoisomerase II and the damage to be catalyzed by the enzyme itself [18]. The ability of DOX is not specific to cancer cells since some healthy cells may also become targets of DOX, thereby altering the standard cellular functions and eventual cell loss [17]. Moreover, the effectiveness of DOX remains restricted to two fronts: dose intensity due to acute bone marrow toxicity and dose frequency due to the development of drug resistance and cardiotoxicity [19]. Moreover, DOX is also known to be fluorescent but with broad excitation and emission ranges since its fluorescence depends on the environment's pH, and most importantly, the solvent's dielectric constant [20]. It has been claimed that DOX possesses an excitation range of 488 nm, and two emission peaks at 560 and 590 nm, in a medium of phosphate buffered saline [21]. DOX self-quenches when it binds to DNA and when present at high concentrations, such as being encapsulated inside nanoparticles [20]. Figure 1 below is an illustration of the molecular structure of DOX.
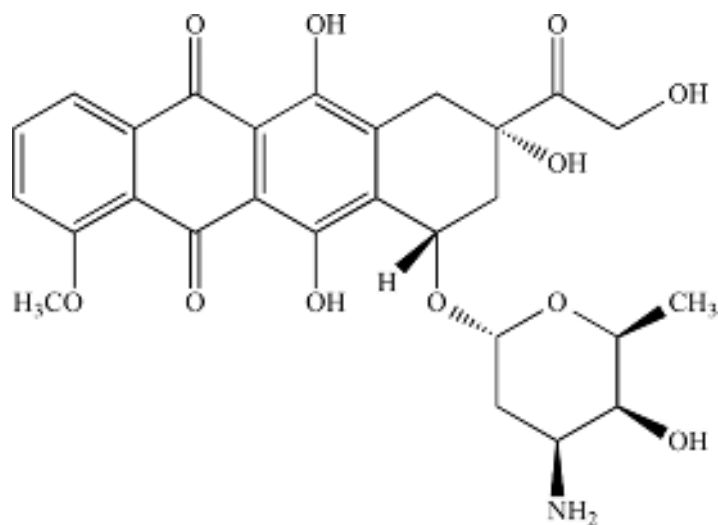
Figure 1: The molecular structure of Doxorubicin [5].

1.2.3. Calcein. Calcein, also referred to as fluorexon or fluorescein complex, is a fluorescent dye comprised of orange-colored crystals, with excitation and emission wavelengths of 495 and 515 nm, respectively [22, 23]. Calcein is commonly used as an indicator of lipid vesicle leakage and has self-quenching properties at a concentration higher than 70 mM [22, 23]. Due to the above-discussed properties, Calcein is a widely used fluorescent dye in drug delivery systems research, substituting the encapsulation of real drugs. Calcein does not possess chemotherapeutic properties and is used solely for fluorescence measurements. Spectrophotometers or fluorometers are utilized to study the release properties of calcein-encapsulated lipid vesicles by monitoring the fluorescence as a percentage with respect to time [24]. The utilization of calcein as a replacement to chemotherapeutic drugs is only applicable for fluorescent agents [24]. The light emission and excitation ranges for calcein are narrow and well-defined, unlike those of DOX. Additionally, calcein self-quenches at much lower concentrations than DOX does. Due to the discussed similarities and advantages, Calcein can be used as a model drug in fluorescence monitoring studies. Figure 2 below is an illustration of the molecular structure of Calcein.
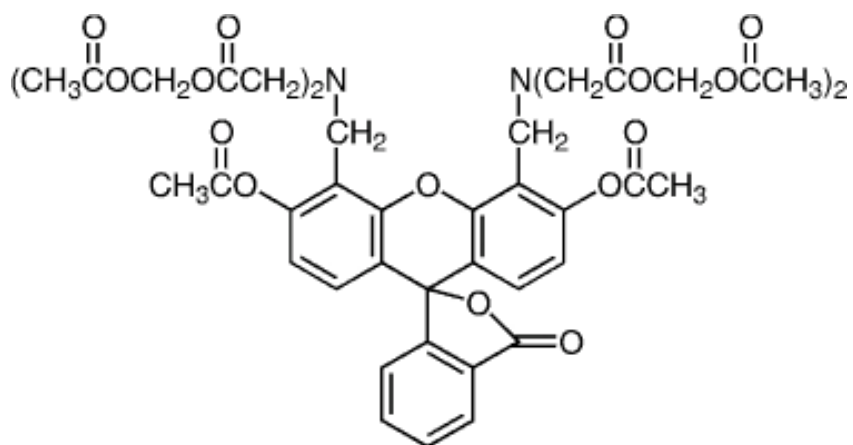
Figure 2: The molecular structure of Calcein [6].

1.3. Drug Delivery Systems (DDS)

Drug Delivery Systems (DDS) deliver controlled amounts of a therapeutic agent over a prolonged period or in a desirable temporal fashion, thereby maintaining required plasma or tissue drug levels [25]. Such systems can take a variety of forms such as mechanical pumps, polymer matrices, micro-particulates, and externally applied transdermal patches [25]. Controlled drug release is used to treat many diseases and has proven very effective in treating cancerous tumors.

Mechanical pumps are mature and low-risk DDS but have certain disadvantages. Mechanical pumps can deliver precisely controlled amounts of the anti-neoplastic agent to the targeted tumors. These pumps are integrated with biosensors, which continuously send measurements from a target tissue, enabling feedback control basis [25]. However, these devices are bulky, expensive, and require patients to visit their physicians regularly [25]. Additionally, the drugs are stored in a liquid reservoir before delivery, so only agents that are stable in solution at body temperature can be used [25].

Biocompatible polymers can be used as delivery vehicles to perform controlled-release while avoiding the disadvantages of pumps. Polymeric controlled release is classified into nondegradable polymers, biodegradable polymers, swellable polymers, and biopolymers [25]. Each application is tailored to suit a specific drug's rate, pattern, and duration of drug release. One type of nondegradable polymers is based on a semipermeable, hollow tube comprised of silicon or polyethylene-co-vinyl acetate,

which is filled with a liquid suspension of a drug that is released by diffusion through the walls [25]. Biodegradable polymers dissolve after implantation and hence are used to eliminate the need for surgically removing nonbiodegradable polymers at the end of the therapy. The most common biodegradable polymer is made up of polylactide-co-glycolide, which degrades in a controlled manner and does not form toxic byproducts [25].

Micelles are colloidal particles, often spherical, with the size in the nanometer range, into which many amphiphilic molecules self-assemble spontaneously [25]. When amphiphilic molecules are placed in an aqueous environment, the hydrophobic fragments form the core of a micelle, and the hydrophilic part forms the corona of the micelle [25]. The usage of micelles serves many advantages for poorly soluble therapeutic agents since the hydrophobic core can be used to store such agents [25]. This allows for increased bioavailability of the encapsulated therapeutic agent, protects it from harmful factors, and enhances its pharmacokinetics and biodistribution [25]. This DDS offers several advantages but is currently still at the preclinical development stage [25].

1.4. Liposomes

Liposomes, also known as artificial phospholipid vesicles or lipid vesicles, are aqueous compartments enclosed by lipid bilayer membranes [26]. Liposomes differ from micelles by the fact that liposomes are composed of two monolayer sheets of phospholipid molecules, instead of one, with their hydrophobic surfaces facing each other and their hydrophilic heads facing the aqueous medium [26]. Liposomes enclose a portion of the aqueous phase in which it was prepared in, essentially making it a cell membrane without its protein components [26]. The hydrophilic phospholipid heads that are found in nature, such as soybean and egg yolks, include phosphatidylcholine (PC), phosphatidylethanolamine (PE), phosphatidylinositol (PI), phosphatidylserine (PS), but are difficult to use in clinical applications due to their instabilities and contamination risks [27]. Therefore, synthetic phospholipid derivatives are favored, which include 1,2 dipalmitoyl-sn-glycerol-3-phosphoglycerol (DPPG), dipalmitoylphosphatidylcholine (DPPC), and hydrogenated soy phosphatidylcholine (HSPC) [27]. The structure of liposomes can be utilized by storing water-soluble drugs in the inner aqueous phase, and water-insoluble drugs in the liposomal membrane [25].

The incorporation of membrane-active sterols into the phospholipid bilayer can improve the permeability of the liposomes. The liposome's bilayer possesses a phase transition phase from Solid Ordered (SO) to Liquid Dis-ordered (LD) phase at a specific temperature, depending on the molecular structure of the phospholipid [28]. Moving from a SO to an LD state is what causes multi-layered liposomes to form when the raw materials are present in an aqueous solution in critical proportions [28]. An intermediate state, Liquid Ordered (LO), exists when a membrane-active sterol, such as cholesterol, is present in the bilayer [28]. Liposomes in an LO phase state are more permeable than liposomes in SO or LD phase states [28]. Moreover, incorporating cholesterol into the bilayer increases its stability by modulating the fluidity of the lipid bilayer, and thus preventing crystallization of the phospholipids acyl chains [29]. The addition of cholesterol in the presence of unsaturated fatty acids allows for better encapsulation of the drugs in the aqueous phase and increases the rigidity of the lipid bilayer due to the thick steroid rings that are present in cholesterol's structure [1]. Thus, incorporating cholesterol into the phospholipid bilayer is essential for enhancing the permeability, stability, and rigidity of the liposomes.

Liposomes are reported to be superior to other drug delivery systems but suffer from short circulation times, and low biodistribution [1, 25]. Liposomes are biologically inert and biocompatible, rarely produce toxic or antigenic reactions, protect the drugs enclosed within them from external factors, and can deliver their contents inside cells and even inside different cell compartments [25, 30]. Short circulation times of liposomes are attributed to several factors. Small liposomes of 5 nm or less can efficiently extravasate into tumor tissue but are rapidly filtered in the kidney, drastically decreasing their circulation time [1]. Increasing the size of liposomes enhances circulation time by slowing down kidney filtering, while still allowing for diffusion into tumor site, via pores and defects in angiogenic vessels [1, 30]. Liposomes are recognized and tagged by opsonins, which accelerates phagocytosis and hence causes short circulation times of liposomes [1]. A suggested remedy for this problem is coating the surface of the liposome with inert, biocompatible polymers, such as polyethylene glycol (PEG), insulating the surface of the liposome, hence slowing down opsonization [25]. The biodistribution of a liposome could be boosted by targeting; conjugating a moiety to the surface of the nanocarrier, and hence causing the liposome to develop a specific affinity towards an affected organ or tissue [25]. Furthermore, drugs or

chemotherapeutic agents can be incorporated into the aqueous core of the liposome to be delivered to a target tissue or organ. Encapsulated liposomes would circulate the body while retaining its sequestered content until triggered by an external stimulus [28]. Ultrasound is an example of an external stimulus where its non-invasive energy can disrupt the drug-encapsulated liposomes to accomplish precise drug delivery [28].
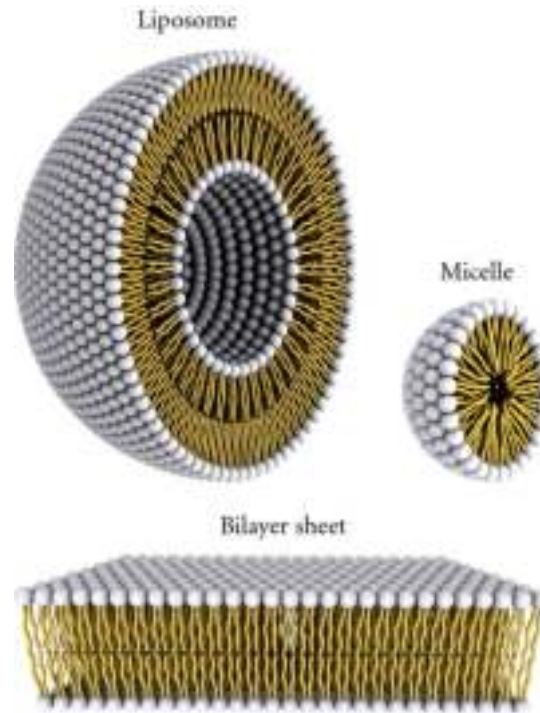
Figure 3: An illustration of a liposome's phospholipid bilayer and a micelle's single layer [7].

The classification of liposomes is based on size and number of bilayers present [27]. The three main classifications of liposomes are Uni-Lamellar Vesicles (ULVs, 25 nm - 1 μm), Multi-Lamellar Vesicles (MLVs, 0.1-15 μm), and Multi-Vesicular Vesicles (MVVs, 1.6-10.5 μm) [27]. ULV liposomes are also classified into two subcategories, which are Large Uni-Lamellar Vesicles (LUVs, 100 nm – 1 μm) and Small Uni-Lamellar Vesicles (SUVs, 25-50 nm) [27]. The size and number of bilayers affect the amount of drug encapsulation in liposomes and the circulation half-life in the body [31].

1.5.   Liposomes Preparation Methods

Due to the vital role which liposomes play in drug delivery, preparation and drug loading parameters are optimized according to the application of the liposome. According to Akbarzadeh *et al.* [31], drug loading into liposomes can be performed by passive or active methods. Passive methods involve the loading of the drug, through the aqueous or organic media, during the synthesis of a liposome. Active targeting occurs after the completion of liposomal synthesis by establishing a membrane potential, e.g., an ionic or a pH gradient. The most important variables considered in drug loading are trapping efficiency, drug retention, and drug-to-lipid ratio [32]. Trapping efficiency is defined as the amount of drug that has been trapped in the liposomes during the loading period, with respect to the initial drug amount [32]. Trapping efficiencies can be optimized to achieve over 90% of drug encapsulation. Drug retention could is the duration of time in which the liposome could retain the loaded drug, while being stored and *in vivo* [32]. Drug retention varies based on the application, for example, shelf life of at least a year is favored for storage purposes, but a half-life ranging from hours to days is desired for *in vivo* applications [32]. Varying compositions of different lipids and the inclusion of cholesterol could optimize drug-to-lipid ratios to achieve enhanced stability and retention *in vivo*.

The choice of liposome preparation methods depends on several factors [4]:

i.   The physicochemical properties of the liposomal ingredients and the material or drug to be encapsulated.

ii.   The type of the medium used to disperse the lipids.

iii.   The concentration and toxicity of the entrapped material.

iv.   The size, polydispersity, and shelf life of the liposomes.

v.   Batch-to-batch reproducibility.

The preparation methods are classified into three main categories, mechanical dispersion, solvent dispersion, and detergent removal [4]. Mechanical dispersion methods include lipid film hydration by handshaking and non-handshaking freeze drying, micro-emulsification, sonication, French cell pressurizing, membrane extrusion, dried reconstituted vesicles, and freeze-thawed liposomes. Solvent dispersion methods include ethanol injection, ether injection, double emulsion, reverse phase evaporation vesicles, and stable pluri-lamellar vesicles. Lastly, detergent removal

methods include detergent removal from mixed micelles by dialysis, column chromatography, and dilution.

1.5.1. Lipid film hydration method. One of the most common preparation methods for liposomes sequestering hydrophilic drugs is the lipid film hydration method. The lipids are first dissolved in one or more organic solvents, such as chloroform or chloroform/methanol, in a round bottom flask to obtain a clear, transparent, and homogenous mixture with a concentration of 10-20 mg lipids/ml of solvent [1, 3, 4]. Then, the organic solvent is evaporated under vacuum to form a lipid film, using a rotary evaporator, or by purging it using Argon or Nitrogen gas if the liquid volume is small (less than 1 ml) [1, 4]. The temperature at which the evaporation occurs should be above the phase transition temperature of the lipid/lipids to prevent crystallization [1, 4]. After that, the hydration step is performed by hydrating the lipid film with an aqueous solution containing the drug, in a rotary evaporator [1, 3, 4]. The hydration procedure must be performed in a hot bath above the transition temperature for about one hour, or more if the lipid film is not entirely dissolved [1, 3, 4]. At this stage, the product solution will become opaque, which is an indication that multi-lamellar large vesicles (MLVs) are forming [3].

Downsizing multi-lamellar large vesicles (MLVs) into small unilamellar vesicles (SUVs) can be performed using various techniques. Sonication is one of the most widely used mechanical techniques were a sonication probe is lowered into the solution, or the beaker containing the liposomes is lowered into a sonication bath [1, 3]. In both cases, the temperature of the solution must be carefully observed not to exceed the transition temperature. Otherwise, the lipids in the liposomes can de-esterify, distorting or destroying the liposomes [1, 3]. Centrifugation can be performed on the samples to remove any metal contamination caused by the tips of the sonication probes [1, 3, 4]. To avoid such contamination, sonication baths are preferred over sonication probes. As mentioned before, the sonication must be performed above the transition temperature, and for 10-15 minutes. At this stage, the solution will become less opaque and more translucent, indicating the formation of SUVs [1]. Because the freshly formed vesicles (<40 nm) are metastable, they tend to fuse with each other to form larger vesicles (60-80 nm) that are more stable [1, 3]. Extrusion is another method used to downsize MLVs, which involves forcing the liposome solution through an

orifice. This method possesses several advantages over the sonication method because it involves gentle handling of unstable materials [31]. For instance, it was noted that the proteins are not affected much in the sonication method, and the SUVs produced in this method tend to be larger than sonicated SUVs [31]. The drawback, however, is that a constant temperature is hard to attain and control volumes are much smaller than in sonication methods [31].

1.5.2. Reverse phase evaporation methods. The REV method introduced by Szoka and Papahadjopoulos in 1978 was a significant breakthrough since it was the first technique that allowed high encapsulation efficiency of an aqueous medium, at the time [1, 3]. In this method, prepared SUVs possess an aqueous volume-to-lipid ratio of up to 30 times more than those prepared by sonication, and up to four times than those obtained from lipid film hydration method [1, 3]. However, when proteins are required to be encapsulated in the liposomes, they tend to denature upon mixing with an organic medium, which poses a disadvantage for the REV method [1, 3].

The first step in the Reverse Evaporation Method (REV) commences by forming inverted micelles through sonication [1, 3]. As is the case with other methods of synthesis, a solution of lipids in an organic solvent, such as chloroform, is kept under vacuum in a rotary evaporator. The lipids are then re-dissolved in another organic solvent, e.g., diethyl ether, followed by an aqueous medium containing the hydrophilic drug, in a ratio of 3:1 (v/v) organic phase-to-aqueous medium. The solution is then sonicated for 2-5 minutes in a sonication bath until it becomes a one-phase solution. The sonication must occur at low temperatures to prevent the separation of dispersed micelles from the organic phase. After that, the diethyl ether is evaporated at room temperature in a rotary evaporator, keenly observing the formation of foam or bubbles. It is advised to reduce the pressure using a vacuum if such an undesirable change is observed. At this stage, the aqueous solution of inverted micelles becomes viscous, where some of the micelles will disintegrate to create another layer around the remaining inverted micelles, forming what is known as REV liposomes. If prepared successfully, these liposomes are mostly uni-lamellar with a heterogeneous size distribution of (100 nm – 1 μm).

1.6.   Liposome Modifications

Liposomes protect encapsulated drugs from degradation until the desired destination is reached but suffer from problems in biodistribution around the body and the lack of targeting to specific receptors [8]. Liposomes can passively target discontinuous endothelial tissues, such as the liver, spleen or bone marrow, due to the structure of capillaries that allow the liposomes to be trapped in these organs [8]. Liposomes can also target tumor tissue because of the presence of discontinuous epithelium. This accumulation of liposomes into the tumor site by passive targeting is referred to as the enhanced permeability effect (EPR). However, liposomes suffer from a significant disadvantage in which they get captured by phagocytes soon after intravenous admission [8]. Phagocytes cannot directly recognize liposomes without the help of opsonins. In fact, opsonins, such as immunoglobulins and fibronectin, are bound to the surface of the liposomes trigger the phagocytes into destroying and clearing these liposomes [8, 33]. In addition to that, opsonized liposomes experience instability as well as leakage of their contents into the bloodstream [8, 33].

1.6.1.   *PEG-ylated* liposomes. Liposomes coated with hydrophilic polymers, such as polyethylene glycol (PEG), are effectively isolated from opsonins, enhancing their circulation and bioavailability [8, 33]. Liposomes which underwent such treatment attract a water shell to their surface, providing a steric barrier against opsonins and the recognition by the mononuclear phagocyte system (MPS) [34]. Liposomes coated with PEG are referred to as *PEG-ylated or stealth liposomes*, as opposed to Conventional Liposomes (CL). The advantage of using PEG as a liposomal coating is very promising, in which the half-life of CLs was found to be approximately 6 hours, while that of stealth liposomes to be within 40 and 60 hours [33]. According to Immordino *et al*. [8], PEG is biocompatible, nontoxic, soluble in aqueous and organic media, has very low immunogenicity and antigenicity, and possesses good excretion kinetics [8]. An additional advantage discovered for *PEGylated* liposomes was the presence of PEG on the liposome's surface provided a strong repulsion between the bilayers which can overcome the Van der Waals forces, increasing the stability of the liposome and preventing aggregation [1, 8]. *PEGylated* or *stealth liposomes* can be prepared in various ways: by synthesizing a PEG-lipid conjugate and using it as a raw material for

the preparation of liposomes, by covalently attaching reactive groups to the surface of the liposomes, or by physical adsorption [8].

DSPC

DSPE-PEG

DSPE-PEG-Target moiety
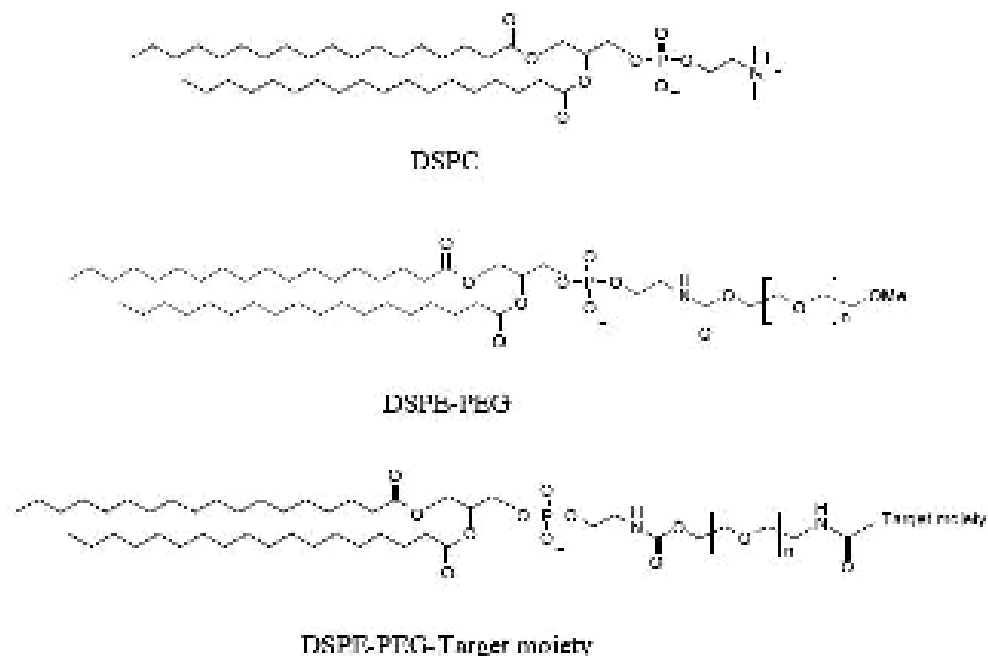
Figure 4: Chemical structures of distearoylphophatidylcholine (DSPC), distearoylphophatidylethanolamine (DSPE) after conjugation with poly-(ethylene glycol) (PEG) (DSPE-PEG) and DSPE-PEG-linked with a targeting moiety, e.g., RGD [8].

Despite all the advantages discussed earlier, conventional and stealth liposomes both suffer from a drawback when used in treatment. Wang *et al.* [34], claim that a second intravenous dose of *PEGylated* liposomes, injected a few days after the first dose, results in the loss of the long-circulating times aspect of these liposomes. The second dose accumulates in the liver as a result, despite the presence of PEG on the surface of liposomes. The author refers to this phenomenon as the Accelerated Blood Clearance (ABC) and hypothesizes a mechanism of this phenomenon [34]. Shortly after the first injection of the *PEGylated* liposomes, the spleen produces anti-PEG IgM in response, which selectively binds to the liposomes upon the second injection [34]. This initiates the opsonization of the liposomes, consequently enhancing their uptake of the Kupffer cells in the liver [34]. A correlation between the ABC phenomenon and the size of the liposomes, as well as the amount of initial dose, could be utilized to alleviate the effects of this effect. The initial amount of administered *PEGylated* liposomes was

found to be inversely proportional to the ABC phenomenon [35]. Additionally, upon the first injection of conventional liposomes of 110 nm into rats, the event occurred slightly [36]. When smaller liposomes (60 nm) were administered for the first time, the ABC phenomenon was accelerated [36].

1.7. Active Targeting

One of the most exploited properties of cancer cells is their overexpression of specific receptors, such as estrone, folate, fucose, and $\alpha_v\beta_3$ integrins, on their surface[8, 37]. These surface receptors allow for active targeting by conjugating moieties, to the surface of liposomes, that binds to specific receptors. Examples of such moieties are monoclonal antibodies, carbohydrates, fragments of proteins, and peptides [8]. Targeting is advantageous since the drug is delivered to a specific tumor or tissue, minimizing the side effects of the cytotoxicity in other tissues, such as fast-dividing cells. Some ligands have low individual affinities, which means a high concentration of such ligands could be conjugated to the surface of the liposome to increase the avidity [38]. However, the surface density of the ligands is an optimal parameter when it comes to the binding of the liposome to the desired target and the prolonged circulation times in the blood [39].

1.7.1. Integrins. Integrins, and specifically $\alpha_v\beta_3$, are critical targets in the development of anti-neoplastic therapies. Integrins are heterodimeric transmembrane receptor protein of animal cells that bind to components of the extracellular matrix on the outside of a cell and the cytoskeleton on the inside of the cell, functionally connecting the cell interior to its exterior [40]. Integrins facilitate interactions with extracellular molecules as well aids in cell adhesion functions [41]. What makes $\alpha_v\beta_3$ integrins a key focus in cancer research is their high expression on the surface of many cancer cells, such as gliomas and melanomas, as well as on the endothelial cells associated with tumors [37]. The expression of these integrins on tumor-associated endothelial cells makes them prominent targets since tumors require a steady blood supply for survival [37]. The binding of an adhesion molecule to a specific target, $\alpha_v\beta_3$ for instance, leads to changes within the cell, such as altering the cytoplasmic domain [9]. Given that this targeting molecule or moiety is attached to a liposome, it can actively target the $\alpha_v\beta_3$ integrins and consequently deliver the therapeutic agent that is contained in the liposome. Additionally, such binding of a targeting moiety to $\alpha_v\beta_3$

integrins can also suppress the angiogenesis of the targeted tumor cells, creating a somewhat synergistic effect with the chemotherapeutic agent.
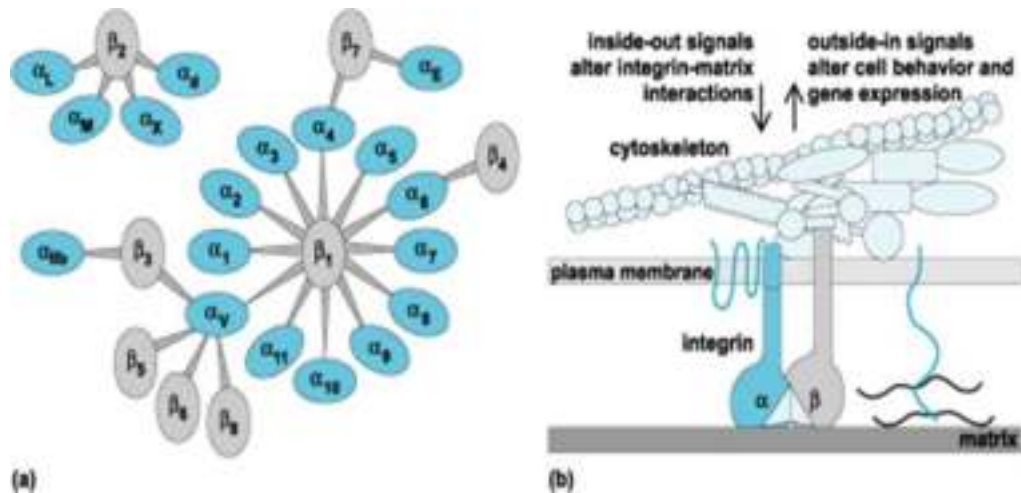
Figure 5: Integrin family. (*a*) Individual subunits are found in specific pairs (*b*) The integrins are membrane proteins—their extracellular domain interacts with components of the extracellular matrix, while their intracellular domain interacts with the components of the cytoskeleton and signaling systems [9].

1.7.2. **RGD peptides and sequences.** Arginine-Glycine-Aspartic acid (RGD) is a vital polypeptide that binds to integrins, including $\alpha_v\beta_3$, playing an essential role in cell adhesion systems [42-44]. Many animal cells grow healthy in a self-produced network, commonly referred to as the extracellular matrix [10]. The propagation of this network requires integrins as a mode of attachment for the extracellular matrix with the intracellular cytoskeleton [10]. In the absence of this connection, the cells undergo apoptosis [10]. One of the ways in which the development of such extracellular networks can be interrupted is the attachment of RGD or RGD containing peptides to $\alpha_v\beta_3$ [10]. Proteins containing the RGD sequence is a site recognized for cell attachment of adhesive extracellular matrix, blood, extracellular proteins, and over 20 known integrin types which act as receptors to facilitate binding to RGD [42]. Additionally, RGD peptides have been used in promoting cell attachment to a wide variety of biomaterials [43]. Natural ligands, such as vitronectin, fibronectin, and osteopontin, bind to the integrin by a conserved RGD tripeptide motif, located on a flexible loop which protrudes out of the protein [37]. RGD containing peptides are believed to be antagonists of $\alpha_v\beta_3$ integrins, possessing anti-angiogenic activity both *in*

vivo and *in vitro* [37]. In fact, scientists have developed a cyclic RGD (cRGDf[N(me)]V) which is currently pursued as an anti-angiogenic drug candidate, called Cilengitide™ [37].
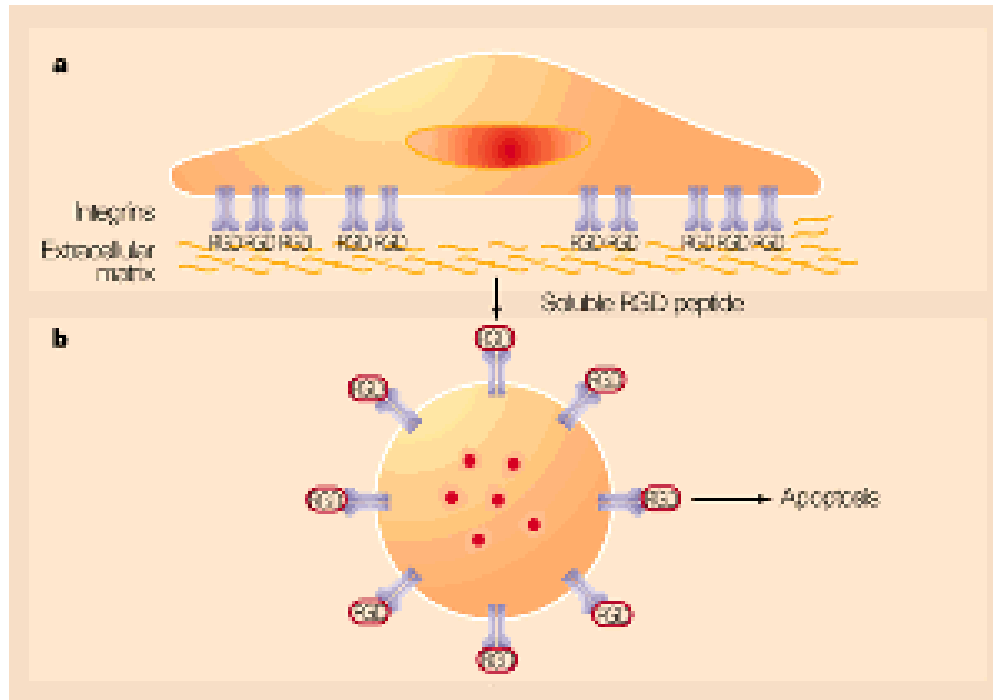
Figure 6: a. Cells attach, through integrins, to a substrate such as the extracellular matrix to survive. b. Addition of soluble RGD peptides blocks integrin signaling to the extracellular matrix, so the cell detaches, and the missing integrin signal causes apoptosis [10].

In vitro research of synthetic RGD sequences suffers from mild discrepancies compared to *in vivo* (animal studies) due to a myriad of complicated reasons [43]. A very critical factor which is not extensively studied by researchers is that RGD does not act in isolation. Whether dealing with *in vitro* or *in vivo* applications, cells regularly secrete integrin-binding proteins, which are also present in cell-culturing growth media, and body fluids and serum [43]. Such examples of integrin-binding proteins are fibronectin, vitronectin, and fibrinogen. Many biomaterials, including liposomes, will adsorb such proteins to some extent, exposing cells to synthetic RGD within a background of native integrin-binding proteins. This exposure has been proven to have a stronger integrin-signaling effect than the isolated, synthetic RGD would have [43]. Bellis attributes this behavior to the additional domains that are present in the integrin-

binding proteins, which work synergistically along with RGD to enhance the integrin-depending signaling [43]. Moreover, proteins adsorbed by the biomaterials can re-direct targeting in another direction. For instance, the sequence present in fibronectin has a synergistic effect with RGD in activating $\alpha_5\beta_1$, while those in vitronectin are usually aimed at $\alpha_v\beta_3$ integrins [43]. Furthermore, non-protein molecules present in the serum could be adsorbed by the biomaterials, modulating the strength and the specificity of the integrin-signaling [43]. Adsorbed growth factor receptors, known for regulating signaling networks related to adhesion, can affect the potency of RGD. Additionally, adsorbed albumin may competitively bind to the integrins to inhibit cell adhesion [43].

1.8.   Ultrasound

Ultrasound is an oscillating sound pressure wave having a frequency of 20 kHz or higher, which is above the audible range for humans [45]. Sound pressure waves travel in a medium through the oscillation of the matter particles in a medium. Therefore, such waves require a medium filled with matter to travel in, unlike electromagnetic waves [46]. US waves can be classified as low-intensity and high-intensity waves, with each having different applications. Low-intensity waves are mainly used for surveying information on the state of matter, such as flow studies and imaging [46]. High-intensity ultrasound is aimed at changing the properties or the state of the matter, such shattering kidney stones, and ablating tumor and fibroids [46]. Hence, the applications of low-intensity sound waves are usually non-destructive, while those of the high-intensity waves are usually associated with thermal and mechanical effects, such as inducing hyperthermia or cavitation [45].

1.8.1.   Ultrasound generation. In medical applications, both low-intensity and high-intensity US waves are usually generated using piezoelectric materials. Solids, such as crystals and ceramics, which can accumulate an electrical charge in response to mechanical stress are referred to as piezoelectric materials [47]. For instance, quartz crystals accumulate electrical charge on their surface after being exposed to mechanical tension. This very property is manipulated in a way where such materials could be polarized and then exposed to an electrical field, causing them to vibrate [47]. When the voltage applied is within the same direction material's poling, the material will experience elongation. On the other hand, when the direction of this voltage is reversed, the material will experience compression [47]. Consequently, US waves could be

generated by applying an alternating electrical field piezoelectric material. US waves usually require a pulse generator, an amplifier, a transducer, and a medium to travel through [45]. The pulse generator creates the electrical pulse that is applied on the transducer to generate the US waves. The amplifier is used mainly to amplify the magnitude of the electrical signal. The transducer, usually containing the piezoelectrical material, generates the US wave when subjected to the pulse [45]. What makes the application of US in drug delivery compelling is the ability to focus such waves at a local area, targeting liposomes and unhealthy cells only.

     1.8.2. Ultrasound triggering of liposomes. Controlling the amount of drug release, its location, and the period at which it is released, is referred to as triggered release in the science of drug delivery [48]. Liposomes encapsulating a drug could be triggered using various stimuli, such as pH, enzymes, temperature, and ultrasound [46, 48]. The liposomes can be synthesized to respond to a change in the pH, to benefit from the slight pH change around the tumor site, or to the presence of certain enzymes in the body. However, engineering liposomes that respond to a temperature change or US waves is more effective due to the ease and increased efficiency of triggering. US waves trigger liposomes through a localized thermal effect (by inducing hyperthermia), or a mechanical effect (cavitation of micro-bubbles) [46, 48]. When using US in drug delivery or treating cancer, the three main parameters of concern are the frequency, pulse duration, and intensity. High-frequency US waves are used due to its ability to induce thermal or mechanical effects. The intensity of the US usually varies on the application; low intensity triggers liposomes through mild cavitation and increasing porosity, while high intensity either triggers liposomes to release because of the temperature increase or directly kills the tumor through hyperthermia [46, 48].
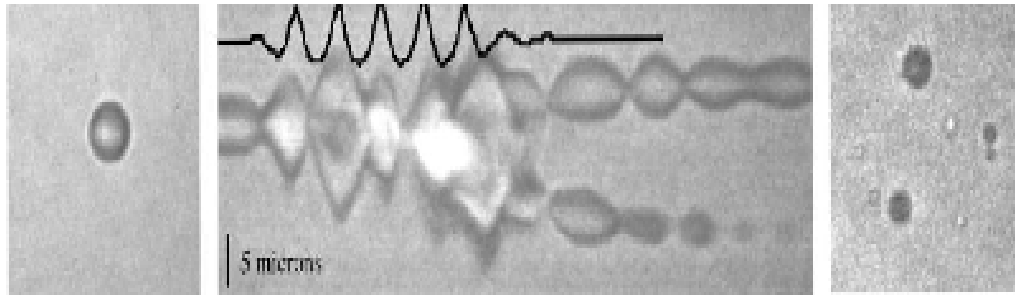
Figure 7: Optical images of a 2.5 µm-radius microbubble exposed to 5 cycles of 2.5 MHz ultrasound at 1.6 MPa pressure amplitude. The left panel shows the bubble before exposure. The central panel shows a streak photograph (an optical M-mode image of a line through the center of the bubble as a function of time) with the measured pressure superimposed at the top of the panel. The right panel shows bubble the fragments produced by the collapse of the cavitating bubble [11].

The presence or formation of microbubbles in liposomes is fundamental towards the success of ultrasound in triggering drug release. As discussed in section 1.4, liposomes encapsulate an aqueous medium in their core. The absence of a hydrophobic medium at the core eliminates the affinity of liposomes to store considerable amounts of dissolved gas that could nucleate micro-bubbles [28]. The interaction of ultrasound with liposomes necessitates the presence or the consequential formation of gas micro-bubbles either inside or in close proximity to the liposomes [28]. However, the dissolved gas in the aqueous medium at the liposome's core can form bubbles upon sonication [28, 30]. To improve the number of microbubbles, emulsions prepared from perfluorocarbon, for instance, could be incorporated into the liposome's core or attached to its surface [28, 49]. These existing or recently formed microbubbles contribute to cavitation effects, which are discussed below [30].

Mechanical effects induced by ultrasound in a medium are referred to as acoustic cavitation [28, 30, 50]. When a medium is exposed to ultrasound, the pressure in the liquid quickly oscillates, causing gas bubbles to form, explaining the acoustic cavitation phenomenon [30, 50, 51]. These gas bubbles form when the pressure recedes the vapor pressure of the medium or can be introduced externally, such as the presence of microbubbles in micro and nano-emulsion liposomes [46, 48]. *Stable cavitation* occurs when gas bubbles continuously inflate and dilate, at an equilibrium level without exploding, due to the pressure oscillation [30, 46, 50, 51]. Applying US waves with a frequency matching the natural resonance frequency of the bubbles yields the highest

amplitude of oscillation, which in turn applies considerable shear forces on the fluids nearby [30, 51, 52]. The previously discussed phenomenon is referred to as *collapse* or *transient cavitation*. When these bubbles oscillate with high amplitudes that exceed their equilibrium radii values, the bubbles vigorously expand and collapse abruptly [53]. This dynamic behavior generates an instantaneous local rise in temperature and pressure, up to 5000K and 1000 atm, followed by a rapid cooling rate, which classifies the entire event as adiabatic [30, 54, 55]. Such explosion of bubbles generates micro-jets of liquid traveling at a high velocity, pushing the nearby surfaces and thus enhancing mass transfer or aiding in porosity [30, 56]. *Collapse cavitation* depends on the type of the gas enclosed or forming the in the bubble, the size of the bubble, and the US density and frequency [46]. Low frequency, high power density US is favored in the generation of *Collapse cavitation*. *Stable cavitation* is more effective than *collapse cavitation* in drug release but suffers from side effects [11]. The shockwaves and the colossal shear stresses generated, as well as the free radicals that might form in the process, could have fatal effects on the surrounding healthy tissue [11, 30]. However, such side effects could be minimized by carefully optimizing the parameters of the ultrasound.
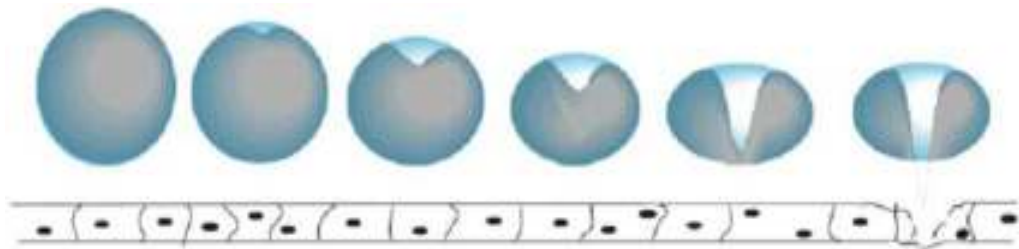
Figure 8: Illustration of an asymmetric collapse of a bubble near a surface, producing a jet of liquid toward the surface [11].

Chapter 2: Objectives

The objective of this thesis is to develop RGD-targeted liposomes that are sensitive to ultrasound and have applications in cancer drug delivery. The specific aims of this thesis are as follows:

1. The preparation of RGD liposomes with calcein as a model drug.
2. Characterizing the synthesized targeted liposomes using Dynamic Light Scattering (DLS).
3. Determining the lipid concentration of the liposomal suspension using a lipid quantification assay (Stewart assay).
4. Verifying the attachment of RGD to the liposomes using a protein quantification assay (BCA assay).
5. Evaluating the encapsulation efficiency of RGD liposomes using spectrofluorometry.
6. Measuring the release of the model drug at low-frequency (20-kHz) ultrasound and comparing the release profile of non-targeted vs. targeted liposomes.
7. Modeling the acoustic release of the drug using applicable mathematical kinetic models.

Chapter 3: Experimental Procedure

3.1.   Materials

The 1,2-dipalmitoyl-*sn*-glycerol-3-phosphocholine (DPPC) and 1,2-distearoyl-*sn*-glycero-3-phosphoethanolamine-N-[amino(polyethylene glycol)-2000] (DSPE-PEG$_{2000}$-NH$_2$) were obtained from Avanti Polar Lipids Inc. (Alabaster, AL, USA). Sephadex G-100, arginine-glycine-aspartic acid (Arg-Gly-Asp; RGD), calcein disodium salt (C$_{30}$H$_{24}$N$_2$Na$_2$O$_{13}$), 2,4,6 trichloro-1,3,5 triazine (NCCl)$_3$, and human transferrin were obtained from Sigma-Aldrich (St. Louis, MO, USA). Chloroform (CHCl$_3$), acetone (C$_3$H$_6$O), and the boric acid (H$_3$BO$_3$) used in the borate buffer were obtained from Panreac Quimica S.A. (Spain). Cholesterol was obtained from AlfaAesar (Ward Hill, MA, USA). Sodium chloride (NaCl) used in the PBS buffer was obtained from Merck Millipore (Burlington, MA, USA). Potassium chloride (KCl) used in the PBS buffer was obtained from (Unichem Laboratories Ltd., Mumbai, India). Monopotassium phosphate (KH$_2$PO$_4$) used in the PBS buffer was obtained from BDH Laboratory Supplies (Poole, England, UK). Disodium phosphate (Na$_2$HPO$_4$) and disodium tetraborate decahydrate Na$_2$[B$_4$O$_5$(OH)$_4$]·8H$_2$O used in the PBS and borate buffers, respectively, were obtained from VWR International (Radnor, PA, USA). The Avanti Mini Extruder extrusion kit was obtained from Avanti Polar Lipids Inc. (Alabaster, AL, USA). The 0.2 μm polycarbonate membranes and filter supports were obtained from Whatman PLC (Maidstone, England, UK).

3.2.   Methods

3.2.1. Preparation of DSPE-PEG$_{2000}$-NH$_2$ (control) liposomes encapsulating calcein [1-3]. In this protocol, DSPE-PEG$_{2000}$-NH$_2$, cholesterol, and 1,2-dipalmitoyl-*sn*-glycerol-3-phosphocholine (DPPC) were used in a mole ratio of 5:30:65, respectively. In a round bottom flask, 5.6 mg, 4.7 mg, and 19.2 mg of DSPE-PEG$_{2000}$-NH$_2$, cholesterol, and DPPC, respectively, were dissolved in 4 ml of chloroform. A bigger round bottom flask (250 ml), as opposed to a smaller one (50 ml or 100 ml), aids in the formation of a thin lipid film around the interior of the flask. The organic solvent (chloroform) was evaporated in a rotary evaporator at 50°C with vacuum for 15 min, where a dry, thin lipid film forms around the interior of the round bottom flask. The lipid film must be very dry since traces of chloroform have detrimental effects on the stability of the liposomes and is renowned for being toxic in

in vivo applications. The hydration solution was prepared using 66.7 mg of calcein dissolved in 2 ml of phosphate-buffered saline (PBS), and its pH was re-adjusted to 7.4. The hydration solution was added to the round bottom flask containing the lipid film and rotated in a rotary evaporator at 60°C without vacuum, for 45 min. After all the lipid film has dissolved, the round bottom flask was sonicated for 10-20 min in a sonication bath at 60°C. The liposomes were then extruded at 60°C using 0.2 μm polycarbonate filters for 30 times. The liposome solution was then purified in a column containing Sephadex G-100, which was previously soaked in PBS for 2-3 hrs. The supernatant contained a concentrated solution of DSPE-PEG$_{2000}$- NH$_2$ liposomes.

3.2.2. Preparation of DSPE-PEG$_{2000}$-NH$_2$ liposomes encapsulating calcein for RGD attachment [1-4].

NH$_2$ liposomes intended to undergo an attachment of RGD must be slightly modified. The steps for the synthesis of these liposomes are similar to those described in section 3.2.1. except for wetting the Sephadex G-100 in borate buffer (pH = 8.5), rather than PBS buffer. The resulting slightly basic medium is suitable for the RGD attachment protocol where HCl is released into the medium.

3.2.3. Preparation of calcein-free DSPE-PEG$_{2000}$-NH$_2$ (PBS) liposomes [1, 3, 4].

The steps for the synthesis of these liposomes are similar to those described in section 3.2.1. except for using 2 ml only of PBS as a hydration solution in the 45 min hydration step.

3.2.4. Synthesis of DSPE-PEG$_{2000}$-NH-N$_3$C$_3$Cl-RGD liposomes (RGD attachment protocol) [1, 2].

This reaction is composed of several steps, the first of which is the attachment of cyanuric chloride (N$_3$C$_3$Cl$_3$) to DSPE-PEG$_{2000}$-NH$_2$ liposomes. The chloride ions in cyanuric chloride are good leaving-groups, with each chloride ion leaving at a different temperature. The aim is to attach N$_3$C$_3$Cl$_3$ to the NH$_2$ present in the ligand on the surface of the liposomes. The first chloride atom leaves at 0°C, the second at room temperature, and the third at around 45°C. At high temperatures (45°C), all three chloride atoms leave, which is undesirable. The favored reaction was performed at 0°C where only one chloride atom leaves to avoid the possibility of dimerization of N$_3$C$_3$Cl$_3$. At 0°C, the leaving chloride atom reacts with one proton from the NH$_2$ group to form HCl. The vacant site on the NH group reacts with that on N$_3$C$_3$Cl$_3$ to form NH-N$_3$C$_3$Cl$_2$. First, 5 mg of N$_3$C$_3$Cl$_3$ were weighed and dissolved in 1 ml of acetone in a small glass vial to form a concentrated solution, which was then cooled in ice. Out of this concentrated solution, 1 μmol (36.88 μl) was added

to 0.5 ml of ice-cold de-ionized water. The liposome solution prepared in section 3.2.2. was cooled in ice while being stirred at very low speed to prevent co-aggulation or the breakdown of liposomes. The diluted $N_3C_3Cl_3$ solution was then added, drop by drop, to the ice-cold liposome solution. The mixture was left in ice while being stirred for 3 hr to ensure the reaction completion. At this point, DSPE-PEG-NH-$N_3C_3Cl_2$ liposomes were formed. After that, 5 mg of RGD were dissolved in 1 ml of borate buffer and were cooled in ice. Out of this concentrated RGD solution, 1 μmol (346.34 μl) was added to the liposome solution, drop by drop, while stirring. The mixture is left overnight at room temperature while stirring. At this point, DSPE-PEG-NH-N_3C_3Cl-RGD liposomes were formed. The liposomes were purified again by passing through a Sephadex G-100 column, which was previously wetted in PBS buffer for 2-3 hr, to change the medium's pH and to get rid of the byproducts and excess reagents.

3.3.   Characterizing Liposomes by Dynamic Light Scattering (DLS)

DLS works on the principles of Brownian motion and the Doppler shift effect to determine the size, the particle size distribution, and the quantity of particles in a suspended liquid [57, 58]. Particles in a suspension undergo random movement, defined as the Brownian motion [58]. When laser light is shined through the suspension, they pass through the light beam, which causes the light to scatter in all directions. The scattered light will experience a Doppler shift effect because the particles are moving. The speed at which the particles are moving dictates the magnitude of the Doppler shift. The fluctuations in the light intensity caused by this shift and the direction of the light scattered are measured by the photon counter in the machine to identify the size of the particles, and the relative number of particles of each size, also known as polydispersity analysis [58].

DynaPro NanoStar DLS instrument (Wyatt Technology Corp, California, USA) was used to determine the mean size of the liposomes [59]. The hydrodynamic radius (R_h) and polydispersity percentage (Pd%) were the parameters used to determine the average radius and particle size distribution of the liposomes. R_h is defined as the radius of a spherical particle evaluated using only its physical size and size-related behavior, such as its diffusion and viscosity [57]. R_h measurements for a particle by DLS or viscometry are not affected by density or molecular weight [57]. Pd% is defined as the standard deviation of the R_h distribution values from the mean R_h value, weighed by

their intensity fraction, divided by mean R_h, multiplied by 100 [60]. A low-value reading of Pd% confirms the uniformity of the particles' size in a suspension. The DLS measurements were performed on diluted liposomal samples (12 μl concentrated liposomal suspension in 1 ml of PBS) at room temperature.

3.4.   Liposome Concentration Quantification

Phospholipid quantification methods can be used to determine the concentration of liposomes in a suspension. The Stewart Assay is used to determine the concentration of the phospholipids present in a sample [61]. This assay relies on a colorimetric determination of the complex formed between a salt, which contains an ionic substance and a dye of the opposite charge, and a phospholipid [61]. Ammonium ferrothiocyanate forms a red colored complex with phospholipids, which allows for colorimetric measurements of phospholipids in the range 0.01-0.1 mg [61]. When a solution of chloroform containing phospholipids is mixed with ammonium ferrothiocyanate at room temperature, a colored complex is formed, which partitions in the chloroform phase [61]. The red ammonium ferrothiocyanate dye does not dissolve on its own in chloroform [61]. The presence of inorganic phosphate does not interfere with this assay, and therefore PBS buffer can be used as a medium for diluting the liposomes. Stewart assay gives different absorbance readings with the different phospholipid head groups [61]. Therefore, it requires the preparation of specific calibration curves for different phospholipid head groups.

The calibration curve for the Stewart assay was prepared according to Stewart, J. [61]. The ferrothiocyanate reagent was prepared by dissolving 2.7 g of ferric chloride hexahydrate and 3 g of ammonium thiocyanate with 100 ml of deionized water. A calibration curve prepared using a standard solution of DPPC is to be used as a reference for the liposomes. DSPE-PEG-NH_2 is only present in a small amount in the liposomes and can be safely neglected when preparing the calibration curve. A correction method for the presence of DSPE-PEG-NH_2 and all other species in the liposomal solution is implemented at a later stage. The correction is made by comparing the absorbance of RGD liposomes to that of NH_2 liposomes. The standard calibration solution was prepared by dissolving DPPC in chloroform, yielding a concentration of 0.1 mg/ml. Six samples, with a duplicate for each, were prepared by dissolving amounts of the standard calibration solution in chloroform, with a concentration range of 2.5 to 25 μg/ml. Then,

2 ml of the ferrothiocyanate reagent were added to each sample. After that, the samples were vortexed for 20 s, followed by centrifugation for 10 min at 1000 rpm and room temperature. At this stage, the supernatant of each sample is discarded, and the absorbance of the subnatant containing the colored complex is read in a spectrofluorometer at an absorbance wavelength of 485 nm. The absorbance of each sample is plotted against its DPPC concentration to yield a calibration curve.

The steps followed to determine the concentration of a liposomal suspension batch were performed according to Stewart, J. [61]. The protocol of preparing liposomes yields an aqueous suspension in PBS buffer. Any traces of water must be removed from a sample of liposomes before the Stewart assay can be performed. A 50 μl sample of liposomes in a round bottom flask is thoroughly dried in a rotary evaporator at 45 °C for 15 mins. The sample is then resuspended in 1 ml of chloroform and is sonicated at room temperature until the deposited lipid film has been dissolved (10-20 mins). At this stage, multiple dilute samples are prepared by adding a set amount of the liposome-chloroform sample into Eppendorfs, then completing the volume to a total of 2 ml using chloroform. Duplicate samples with three different concentrations, a total of six samples, are prepared for each batch of liposomes. Then, 2 ml of the ferrothiocyanate reagent were added to each sample. The samples were vortexed for 20 s, followed by centrifugation for 10 min at 1000 rpm and room temperature. At this stage, the supernatant of each sample is discarded, and the absorbance of the subnatant containing the colored complex is read in a spectrofluorometer at an absorbance wavelength of 485 nm. The absorbance values are then compared with the calibration curve to determine the exact concentration of lipids (μg/ml) in each sample. The lipid concentration in each sample is then converted to the concentration of the liposomal batch.

3.5.   Quantification of the Attached RGD

Protein quantification methods can be used to verify the attachment and determine the amount of RGD attached to a batch of liposomes. Bicinchoninic Acid (BCA) assay is a protein quantification method used to confirm the presence of proteins or peptides in a sample [62]. This assay can be used to verify the attachment of the RGD peptide to the surface of the liposomes since liposomes batches are purified from any un-attached RGD at the end of an attachment protocol. The BCA assay relies on

the formation of a Cu^{2+}-protein complex under alkaline conditions followed by the reduction of Cu^{2+} to Cu^{1+} [62]. The amount of reduction is proportional to the protein present [62]. Following the reduction, two molecules of BCA, which is a weak acid composed of two carboxylated quinoline rings, chelate with a single Cu^+ ion [62]. The Cu^+ chelate forms a purple-blue water-soluble complex under alkaline conditions and strongly absorbs light at 562 nm [62]. The change in color can be used as a basis to monitor the reduction alkaline Cu^{2+} by proteins [62].

A calibration curve for the BCA assay is performed according to the manufacturer's instructions [62]. The first reagent, QA, contains sodium carbonate, sodium tartrate, and sodium bicarbonate in a 0.2 M sodium hydroxide solution at a pH of 11.25 [62]. QB contains a 4% (w/v) bicinchoninic acid solution at a pH of 8.5 [62]. QC contains a 4% (w/v) copper(II) sulphate pentahydrate solution [62]. To prepare the working reagent, 25 parts each of reagents QA and QB were mixed 1 part of reagent QC (Copper (II) sulfate) until a uniform light green color was observed. A calibration curve must be prepared for pure RGD before conducting the assay on RGD liposomes. The QuantiPro BCA kit gives a linear response for protein concentrations of 0.5 to 30 µg/ml [62]. A standard calibration solution was prepared by dissolving pure RGD in PBS buffer to yield a concentration of 50 µg/ml. Six samples, with a duplicate for each, were prepared by dissolving amounts of the standard calibration solution in PBS. The samples were prepared with a concentration range of 0.5 to 30 µg/ml to span the entire linear absorbance range, which is recommended by the manufacturer. One ml of the working reagent is added to each of the RGD samples, followed by incubation of the samples at 60 °C for 1 hr. At this stage, the formation of the complex is evident by the development of a purple-blue color in the samples. The samples are then cooled to room temperature, and the absorbance of each sample is read in a spectrofluorometer at an absorbance wavelength of 562 nm. The absorbance of each sample is plotted against its RGD concentration to yield a calibration curve. Furthermore, the previously discussed steps for creating a calibration curve were repeated for human transferrin for comparison. The amounts are listed in section 4.3.2.

The steps followed in verifying and determining the amount of RGD attached to the liposomes are performed according to the manufacturer's instructions of the BCA assay [62]. To negate the possibility of other present species interfering with the results

of this assay, both RGD liposomes and NH2 liposomes were used in this assay with the latter used as a point of reference or a control group. For each batch of liposomes, three samples, with a duplicate for each, were prepared by dissolving specific amounts of the liposomal suspension in PBS. The liposome samples were prepared with a wide concentration range to ensure hitting the linear absorbance range, which is recommended by the manufacturer. One ml of the working reagent is added to each of the liposome samples, followed by incubation of the samples at 60 °C for 1 hr. At this stage, the formation of the complex is evident by the development of a purple-blue color in the samples. The samples are then cooled to room temperature, and the absorbance of each sample is read using a spectrofluorometer at an absorbance wavelength of 562 nm. The absorbance of each sample is compared to the calibration curve to obtain a hypothetical protein concentration. To obtain a real RGD concentration, the hypothetical protein concentration of the NH2 liposomal samples were subtracted from those of the RGD liposomal samples. The resultant real RGD concentration is a better indication of the amount of RGD present in the sample since the effects of all other species present in the liposomal solution are negated.

3.6.   Low-Frequency Ultrasound (LFUS) Online Release Experiments

A 20-kHz LFUS probe was used to trigger the release of calcein from RGD-targeted and non-targeted liposomes. The change in fluorescence in the sample, which caused by the release of calcein to the external medium, was monitored using a PTI QuantaMaster 300 Phosphorescence Spectrometer (Horiba LTD., Kyoto, Japan) [63]. Calcein is a fluorescent dye with an excitation and emission wavelengths of 495 nm and 515 nm, respectively. Upon exposure to ultrasound, the liposomes release its encapsulated calcein to the surrounding medium due to the presence of a concentration gradient. As the concentration of calcein in the external medium increases, the fluorescence increases. This change in fluorescence over time is monitored using the spectrometer.

The online release studies require the preparation of a dilute liposomal suspension. To prepare the sample, 75 µl of the concentrated liposomal suspension was diluted with 3 ml of PBS buffer (pH 7.4) in a cuvette. The cuvette was then placed into the spectrofluorometric chamber, where the 20-kHz LFUS probe (model VC 130 PB, Sonics & Materials Inc., Connecticut, USA) was inserted 2 mm into the cuvette through

the spectrofluorometer's opening [64]. The baseline was generated by recording the initial intensity (I_0) for 50 seconds, in the absence of ultrasound. The sonication operated for a total of 7.67 minutes in a pulsed mode of 20/10 seconds of on/off cycles, respectively [65, 66]. The effect of three different ultrasonic power settings, 20%, 25%, and 30%, was examined, which correspond to power density values of 7.46, 9.85, and 17.31 $\frac{mW}{cm^2}$ [65, 66]. A brief description of measuring and calculating the power density values is presented in section 4.4.

Chapter 4: Results and Discussion

4.1. Dynamic Light Scattering Measurements

The liposomes were sized by measuring their hydrodynamic radii (R_h) and polydispersity percentages, using Dynamic Light Sizing (DLS), which is discussed in section 3.3. NH_2 liposomes possessed R_h and Pd% values of 79.52 nm and 11.23%, while the RGD liposomes possessed R_h and Pd% values of 88.26 nm and 19.20%, respectively. The sizes of these liposomes classify them as Uni-Lamellar Vesicles (ULVs), according to section 1.4. The values reported show a significant difference in size between the NH_2 and RGD liposomes. This is not attributed to attachment of RGD to NH_2 liposomes since the molecular weight of RGD is 346.34 $\frac{g}{mol}$, which does not characterize it as a big peptide. The difference in size could be attributed to the dimerization of C_3Cl_3N or RGD, which are both present at the end of the PEG ligands, forming liposomal aggregates. The difference in size could be also caused by disturbances to the liposomes' size during the overnight attachment reaction of RGD to $NH-PEG-C_3Cl_3N_2$, which is the ligand emanating from the liposomes' surfaces. The DLS measurements are demonstrated in Table 1 below.

Table 1: DLS measurements.

Type	Radius (nm)	% Polydispersity
NH$_2$	79.52 ± 4.81	11.23 ± 1.78
RGD	88.26 ± 5.55	19.20 ± 4.70

A single-factor ANOVA analysis performed on the DLS measurements is presented in Table 2. Comparing NH_2 liposomes to RGD liposomes, the F-value is higher than the critical F-value and p-value is lower than the standard α-value ($\alpha = 0.05$). Thus, there is a significant difference in size between liposome-types that cannot be neglected, as explained earlier.

Table 2: Single-factor ANOVA analysis of DLS measurements.

Source of Variation	SS	Df	MS	F	P-value	F crit
Between Groups	266.85	1	266.85	7.05	0.02	4.75
Within Groups	454.00	12	37.83			
Total	720.85	13				

4.2. Liposome Concentration Quantification

The Stewart assay is used for the quantification of the DPPC concentration in liposomes samples, according to methods described in section 3.4.

4.2.1. Calibration curve preparation. Before performing the Stewart assay, a calibration curve must be prepared. As discussed in section 3.4, the samples used for the calibration curve preparation are listed in Table 3.

Table 3: Samples used in the calibration curve preparation for the Stewart assay.

DPPC Conc. (mg/ml)	DPPC Std. Cal. Soln. (ml)	Chloroform (ml)	Ferrothiocyanate Rgnt. (ml)
Blank	0.0	2.0	2.0
0.0025	0.1	1.9	2.0
0.0050	0.2	1.8	2.0
0.0100	0.4	1.6	2.0
0.0150	0.6	1.4	2.0
0.0200	0.8	1.2	2.0
0.0250	1.0	1.0	2.0

Upon completion of the Stewart assay protocol explained in section 3.4, the absorbance values of the faintly red-colored subnatant of the samples are measured at an absorbance wavelength of 485 nm. A plot of the absorbance values versus their corresponding DPPC concentrations is illustrated in figure 9 below.
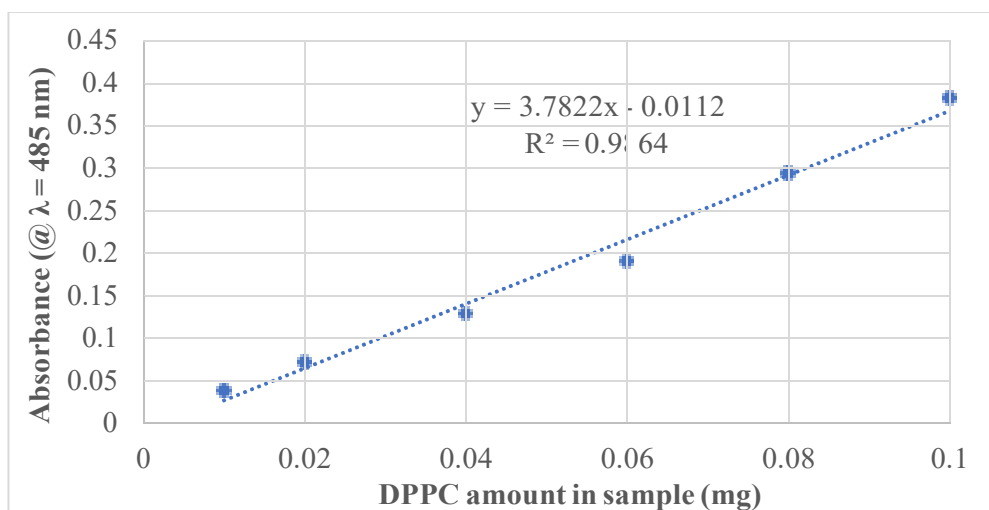
Figure 9: DPPC calibration curve for the Stewart assay.

4.2.2. Viability evaluation of the Stewart assay. The concentration of a batch of liposomes is determined by quantifying the phospholipids present in the batches. However, a batch of liposomes contains species, such as calcein, DSPE-PEG-NH2, and RGD, which may affect the viability of this assay by interfering with the absorbance values read by the spectrofluorometer. To correct for this interference, two types of aqueous media were encapsulated in the liposomes. One of the liposome batches was prepared using a calcein-free PBS medium (PBS liposomes), while the other was prepared using a PBS medium incorporating calcein (calcein liposomes). Additionally, each of the previously prepared liposome batches was split into two batches, keeping one of them as a control (NH2 liposomes) while conjugating RGD to the other (RGD liposomes). The Stewart assay is performed on the resultant four batches, as explained in section 3.4, and their results were compared to examine the effects of any of the previously mentioned species on the viability of this assay. The preparation of the samples used in performing the Stewart assay is listed in Table 4.

Table 4: Preparation of liposome samples used in the viability study for the Stewart assay.

Sample	Liposomes in Chloroform (μl)	Chloroform (μl)	Ferrothiocyanate Rgnt. (μl)
Calcein NH₂ liposomes	75	1925	2000
Calcein NH₂ liposomes	125	1875	2000
Calcein NH₂ liposomes	200	1800	2000
PBS NH₂ liposomes	75	1925	2000
PBS NH₂ liposomes	125	1875	2000
PBS NH₂ liposomes	200	1800	2000
Calcein RGD liposomes	75	1925	2000
Calcein RGD liposomes	125	1875	2000
Calcein RGD liposomes	200	1800	2000
PBS RGD liposomes	75	1925	2000
PBS RGD liposomes	125	1875	2000
PBS RGD liposomes	200	1800	2000
Blank	0	2000	2000

As described in section 3.4, three duplicate samples with different liposome concentrations for each batch of liposomes were prepared. The protocol for the Stewart assay is performed, and the absorbance value for each sample was measured. The absorbance value for each sample was compared to the calibration curve, and an apparent DPPC concentration was obtained. The absorbance readings for the samples including calcein-free NH2 liposomes are taken as a basis, and hence an actual reading.

The presence of other species in the remaining samples, which influence the absorbance of light, is what makes the measured DPPC concentration apparent, rather than real or actual. The DPPC concentration values obtained by comparing the absorbance values with the calibration curve are listed in Table 5 below.

Table 5: Apparent DPPC concentrations of liposome samples obtained from the calibration curve.

Batch	Apparent DPPC Conc. (mg/ml)
Calcein NH$_2$ Liposomes	16.45
Calcein RGD Liposomes	5.1
PBS NH$_2$ Liposomes	6.05
PBS RGD Liposomes	1.35

The presence of the RGD moiety on liposomes had no significant effect on the viability of the Stewart assay. The concentration difference between NH$_2$ and RGD liposomes arises from the nature of the liposomes batch preparation protocol itself. During the preparation of RGD liposomes, two passes through a Sephadex G-100 column are required to remove excess reactants and to change the medium buffer. On the other hand, a single passage during the preparation of NH$_2$ liposomes is required. Therefore, the additional passage encountered by the RGD liposomes is the main reason for the dilution of the RGD liposomes.

The effect of calcein on the absorbance readings was studied. To reduce the effect of RGD liposomes dilution, two liposome types (NH$_2$ and RGD) were used in the comparison between calcein-free and calcein-encapsulated liposomes. Values in Table 5 show that the apparent concentration of calcein-encapsulated NH$_2$ liposomes was higher than that of calcein-free NH$_2$ liposomes by an exaggeration factor 2.72. Also, from Table 5, the apparent concentration of calcein-encapsulated RGD liposomes was higher that of calcein-free RGD liposomes by an exaggeration factor 3.78. Therefore, an average calcein exaggeration factor of 3.25 was taken for both types of

liposomes. This factor proves that calcein has a considerable effect on the viability of this essay. However, a simple remedy to neglect the effect of this phenomenon is to ensure consistency in the encapsulated media of the liposomes. In this thesis, only calcein-encapsulated NH_2 and RGD liposomes were used throughout the research, which safely allows for neglecting the calcein exaggeration effect.

4.2.3. Liposomal phospholipid quantification. Methods of obtaining the liposomal concentration through phospholipid quantification (Stewart assay), described in section 3.4., were regularly performed on random batches of liposomes. The results were consistent in all the batches tested. The calculated DPPC concentration of batches of NH_2 and RGD liposomes was found to be 15-20 $\frac{mg}{ml}$ and 5-7 $\frac{mg}{ml}$, respectively. An average concentration factor of 2.8 to 3.0 between both liposome types was always observed after every repetition of the Stewart assay. The reason for the dilution of RGD liposomes is explained in section 4.2.2.

4.3. Quantification of the Attached RGD

The BCA assay is a protein quantification method used to verify the attachment and determine the amount of RGD conjugated to a batch of liposomes. The methods used in this protocol are described in section 3.5.

4.3.1. Calibration curve preparation. Before performing the BCA assay, a calibration curve must be prepared. As discussed in section 3.5, the samples used for the calibration curve preparation are listed in Table 6.

Table 6: Samples used in the RGD calibration curve preparation for the BCA assay.

Smpl. Name	Buffer (μl)	RGD Std. Soln. [50μg/ml] (μl)	Protein Conc. (μg/ml)	BCA Rgnt. (μl)
Blank	1000	0	0.0	1000
RGD (1)	990	10	0.5	1000
RGD (2)	900	100	5.0	1000
RGD (3)	800	200	10.0	1000
RGD (4)	600	400	20.0	1000
RGD (5)	400	600	30.0	1000

Upon completion of the chelation reaction to form a complex, as explained in section 3.5, the absorbance values for each sample are measured at an absorbance wavelength

of 562 nm. A plot of the absorbance values versus their corresponding RGD concentrations is illustrated in figure 10 below.
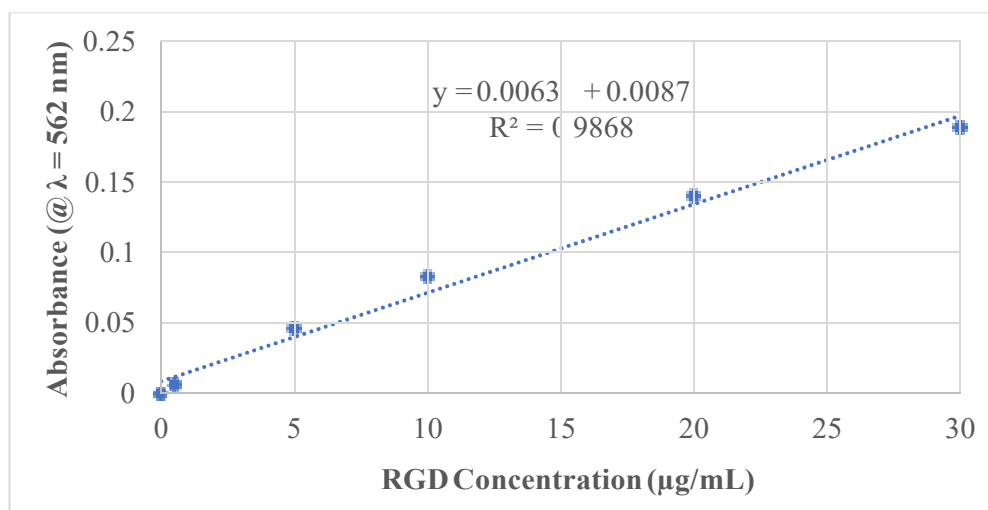

Figure 10: RGD calibration curve for the BCA assay.

4.3.2. RGD sensitivity to the BCA assay. A protein with pre-known moderate sensitivity, albumin, was used for comparison to evaluate the sensitivity of RGD. The calibration curve protocol, described in sections 3.5 and 4.3.1, was performed for albumin and its results were compared with those of RGD. The samples used for the calibration curve preparation for albumin are listed in Table 7.

Table 7: Samples used in the transferrin calibration curve preparation for the BCA assay.

Sample name	Buffer (μl)	Transferrin std. soln. [50μg/ml] (μl)	Protein (μg/ml)	BCA reagent (μl)
Blank	1000	0	0.0	1000
Transferrin (1)	990	10	0.5	1000
Transferrin (2)	900	100	5.0	1000
Transferrin (3)	800	200	10.0	1000
Transferrin (4)	600	400	20.0	1000
Transferrin (5)	400	600	30.0	1000

Upon completion of the chelation reaction to form a complex, as explained in section 3.5, the absorbance values for each sample are measured at an absorbance wavelength

of 562 nm. A plot of the absorbance values versus their corresponding RGD concentrations is illustrated in figure 11 below.
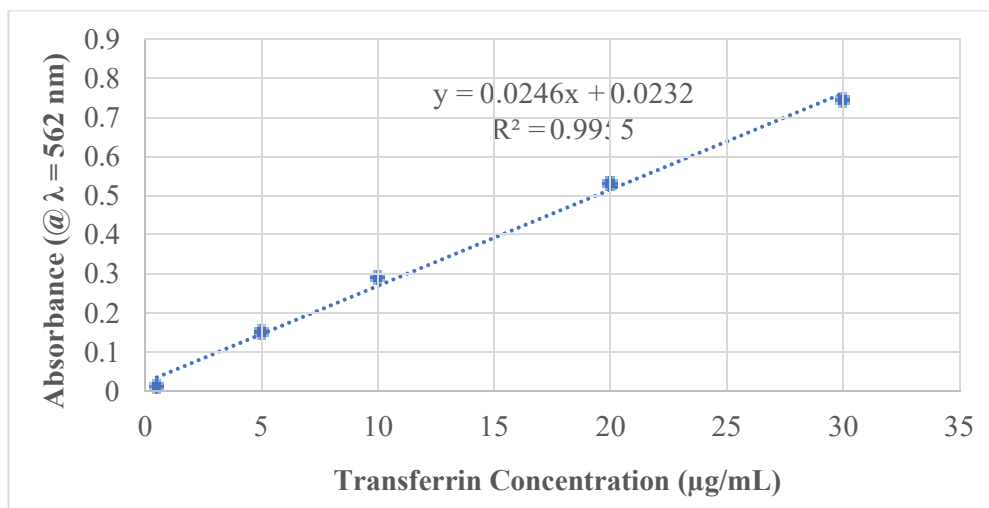

Figure 11: Transferrin calibration curve for the BCA assay.

It was noted that the sensitivity of transferrin to the BCA assay is higher than that of RGD. RGD is a considerably smaller molecule with much less NH_2 groups, due to its low molecular weight, compared to transferrin. Therefore, the reduction of Cu^{2+} to Cu^+ is lower in RGD, which is directly proportional to the intensity of the purple-blue color formed upon chelation. Figure 12 compares the color intensity of RGD and transferrin. This difference was also observed in the lower absorbance values of the RGD samples compared to those of transferrin. Therefore, RGD possesses a lower sensitivity or response towards this assay, compared to other larger proteins. However, the reduced sensitivity of RGD to this assay does not affect the viability of this report. RGD responded to the chelation reaction as expected, and the trend seen in its calibration curve was linear and directly proportional, as expected with any compatible protein according to the manufacturer [62].
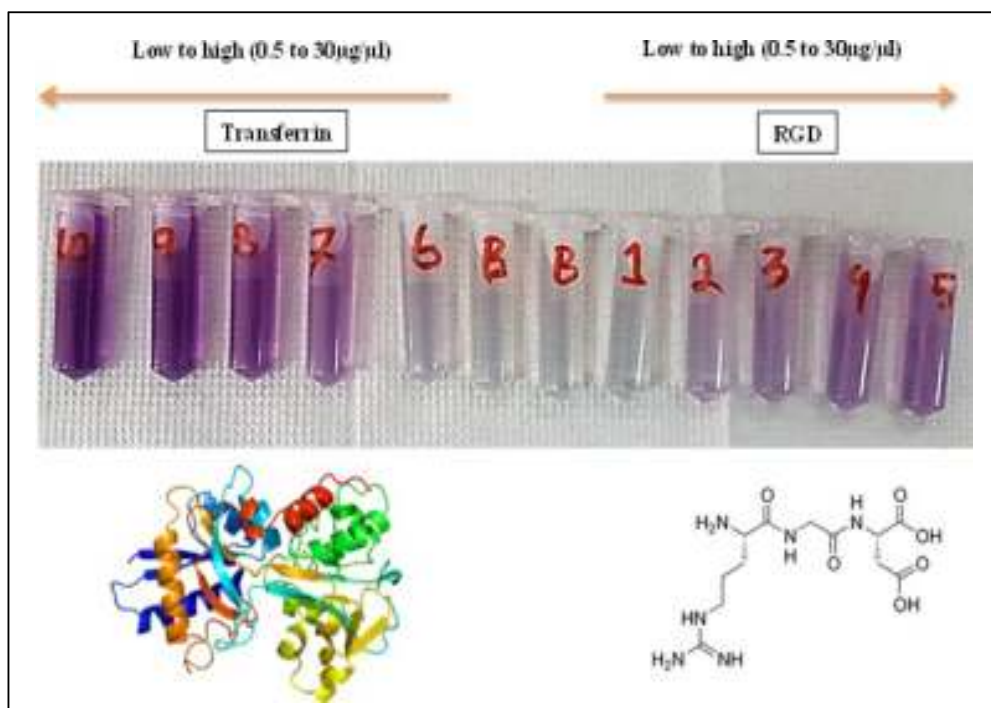
Figure 12: A comparison of color intensity between RGD and transferrin samples upon completion of the chelation reaction.

4.3.3. Other species affecting the viability of the BCA assay. The BCA assay was used to verify the attachment of RGD to the liposomes and quantify its amount with the help of a calibration curve. Methods used in this assay are explained in section 3.5. A variety of samples were prepared to determine the effect of each of the present species, which are lipids, cholesterol, calcein, and RGD, on the viability of this assay. Two standard solutions, one including calcein and the other excluding it, where prepared using the raw materials used to synthesize liposomes. These standard solutions are used as a reference to the liposomes samples. The standard solution was prepared using DPPC, DSPE-PEG-NH2, Cholesterol, and RGD, in the exact proportions used to prepare the liposomes. It is also important to note that the amount of RGD added was equivalent to that added during the protein attachment step. Two more batches of liposomes, NH2 and RGD liposomes, were also prepared. The sample preparations and their equivalent absorbance values are summarized in Table 8, and the actual samples upon completion of the chelation reaction can be seen in figure 13 below.

Table 8: Samples used in the BCA assay viability study.

Sample No.	Sample Name	Liposomes Used (μL)	Absorbance @562nm
B	Blank	0	0
1	Lipids + RGD	200	0.762
2	Lipids + RGD	400	1.269
3	Lipids + RGD	800	2.004
4	Calcein + Lipids + RGD	200	1.175
5	Calcein + Lipids + RGD	400	1.479
6	Calcein + Lipids + RGD	800	2.011
7	Calceinated NH_2 Liposomes	150	0.281
8	Calceinated NH_2 Liposomes	300	0.635
9	Calceinated NH_2 Liposomes	600	1.478
10	Calceinated RGD Liposomes	200	0.330
11	Calceinated RGD Liposomes	400	0.680
12	Calceinated RGD Liposomes	800	1.239
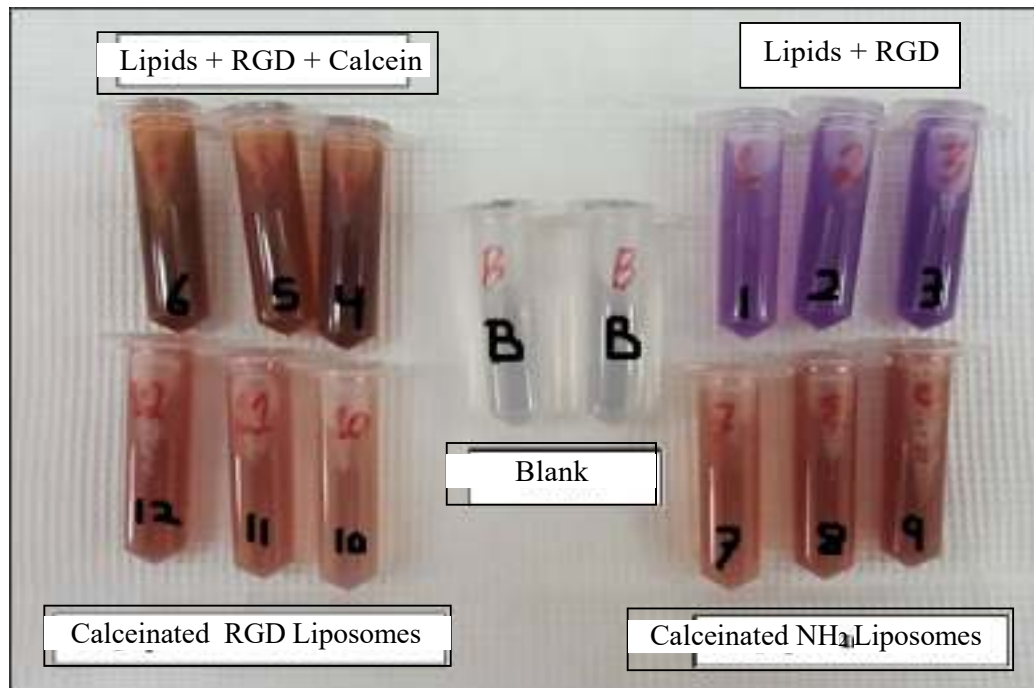
Figure 13: Samples used in the BCA viability study upon completion of the chelation reaction.

The absorbance values in Table 8 above, which represent the amount of apparent protein present in each sample, were read at an absorbance wavelength of 562 nm. The slope of the BCA calibration curve was used, along with the absorbance values, to calculate the apparent concentration of protein in each sample. The calculated values are listed in Table 9 below.

Table 9: Absorbance and apparent protein concentration values of samples used in the BCA assay viability study.

Smpl. No.	Lpd. Amt. in smpl. (mg)	Absorbance @562nm	Apparent Conc. of Prtn. (µg/mL)
B	0	0	-
1	2.95	0.762	119.57
2	5.90	1.269	200.05
3	11.80	2.004	316.71
4	2.95	1.175	185.13
5	5.90	1.479	233.38
6	11.80	2.011	317.83
7	1.05	0.281	43.22
8	2.10	0.635	99.41
9	4.20	1.478	233.22
10	0.36	0.330	51.00
11	0.72	0.680	106.56
12	1.44	1.239	195.29

Each batch of liposomes possessed a different liposome concentration (lipid concentration per milliliter; mg DPPC/mL), which does not openly allow for comparison. The liposome concentrations were determined earlier for each batch of liposomes through the Stewart assay, described in section 3.4. Therefore, the lipid concentrations and the apparent protein concentrations had to be re-scaled to allow for comparison. The most dilute batch of liposomes, which is the RGD-liposomes batch (samples 10 to 12), was used as a reference for re-scaling the other batches. The actual concentration of protein seen in the standard solutions is used as a reference. The discussed adjustments are demonstrated in Table 10.

Table 10: Re-scaled values for samples used in the BCA assay viability study.

Smpl. No.	Re-scaled Lpd. Amt. in Smpl. (mg)	Re-Scaled App. Conc. of Prtn. (μg/mL)
B	0	-
1	0.361	14.64
2	0.722	24.48
3	1.444	38.76
4	0.361	22.66
5	0.722	28.56
6	1.444	38.90
7	0.361	14.85
8	0.722	34.17
9	1.444	80.15
10	0.361	51.00
11	0.722	106.56
12	1.444	195.29

The trends observed in the data presented in Table 10 showed value exaggerations in samples containing calcein. The absorbance value for pure calcein was measured by preparing duplicate samples of calcein only dissolved in PBS. The absorbance profile across 450-650 nm, showing a unique calcein peak at 498 nm, are presented in figure 14.
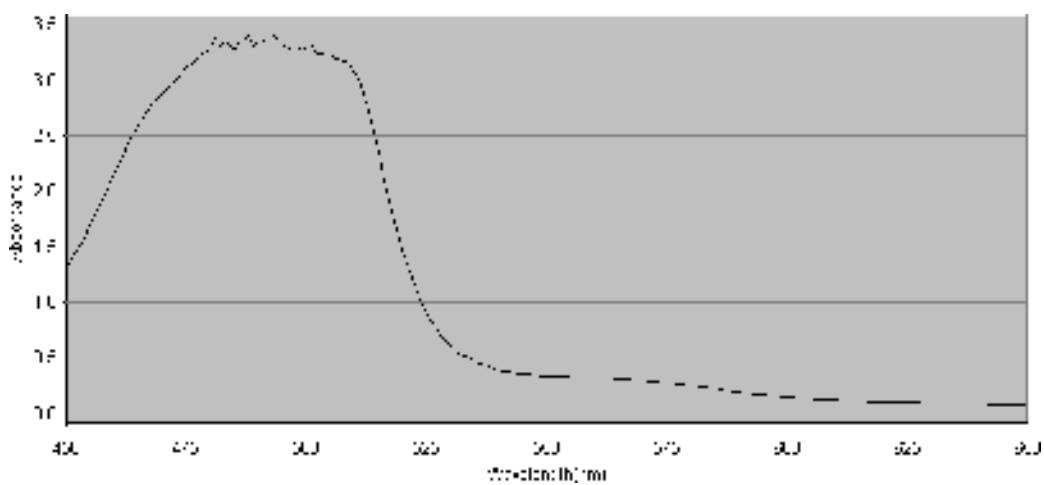
Figure 14: The absorbance values profile of the control calcein sample demonstrating a unique calcein peak at 498 nm.

Comparing raw material samples of calcein-free lipid + RGD with calcein-containing lipid + RGD (samples 1-3 and 4-6, respectively) in Table 10, a clear trend could be seen. At any equal concentration of both samples, the apparent protein concentration obtained from the absorbance reading for the calcein-containing sample was higher than that for the calcein-free sample. For example, the apparent protein concentration for sample 6 (calcein-containing) was higher than that for sample 3 (calcein-free). It is important to note that samples 1-3 include the same amount of RGD as samples 4-6. Hence, the only explanation for the higher apparent concentration value (higher absorbance reading) in the calcein-containing samples is the presence of calcein.

The calcein-exaggeration phenomenon has no negative impact on the validity of this essay. When comparing calcein-encapsulated samples of NH_2 liposomes and RGD liposomes, the latter possessed higher apparent protein concentration values (higher absorbance readings) than the former. For example, the apparent protein concentration for sample 12 (RGD liposomes) was higher than that for sample 9 (NH_2 liposomes). Both liposome samples encapsulated calcein in equal proportions during their preparation. Therefore, samples containing calcein behaved similarly to samples excluding calcein regarding higher absorbance readings for RGD. Although the presence of calcein in samples exaggerates absorbance readings, calcein does not impact the viability of this assay when it is present in both compared samples. The presence of calcein in NH_2 and RGD liposomes would exaggerate both of their absorbance readings, but the reading for the samples containing RGD would still be higher than their NH_2 counterparts. Figures 15 and 16 below demonstrate the visibility of the absorbance peak in samples of calcein-free and calcein-encapsulated RGD liposomes.
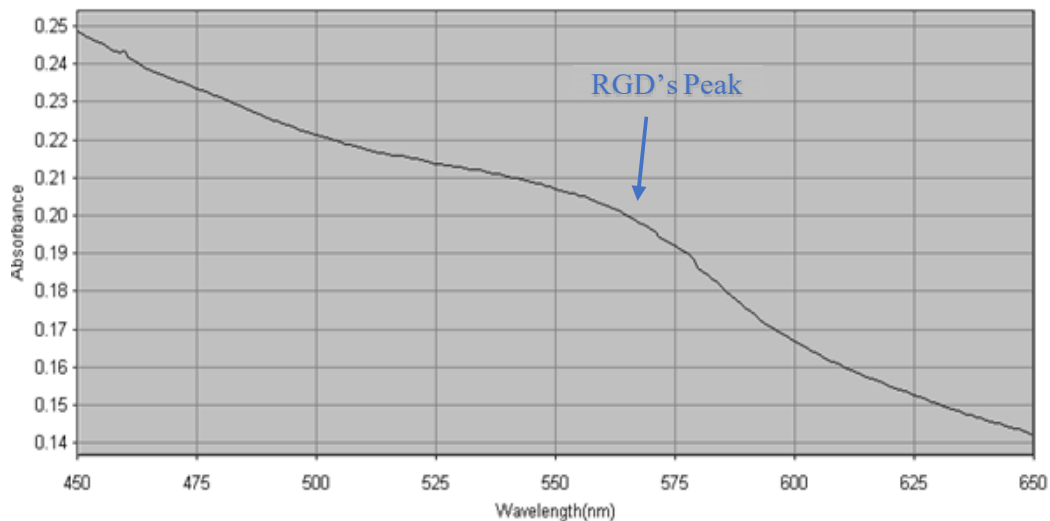
Figure 15: The absorbance values profile of the calcein-free RGD liposomes sample demonstrating an RGD peak at 562 nm.
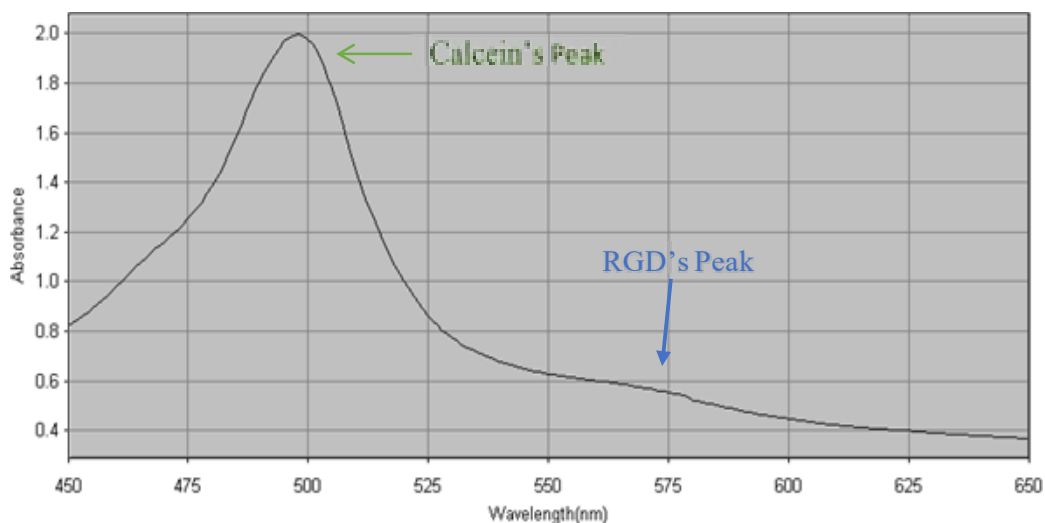
Figure 16: The absorbance values profile of the calcein-encapsulating RGD liposomes sample demonstrating two unique peaks peak at 498 and 562 nm.

4.3.4. Attachment confirmation and quantification of RGD. The BCA assay was used to verify the attachment of RGD to the liposomes and quantify its amount with the help of a calibration curve. Methods used in this assay are explained in section 3.5. Samples were prepared to compare between NH_2 liposomes (protein-free) and RGD liposomes (protein-attached). Sample preparations are listed in Table 11 below.

Table 11: Samples used in the BCA assay.

Smpl. No.	Smpl. Name	Liposomes Used (μL)	PBS Bffr. (μl)	BCA Wrkng. Rgnt. (μl)
B	Blank	0	0	1000
1	NH$_2$ Liposomes	200	800	1000
2	NH$_2$ Liposomes	400	600	1000
3	NH$_2$ Liposomes	800	200	1000
4	RGD Liposomes	250	750	1000
5	RGD Liposomes	500	500	1000
6	RGD Liposomes	1000	0	1000

The absorbance values, which represent the amount of apparent protein present in each sample, were read at an absorbance wavelength of 562 nm. The slope of the calibration curve of the BCA assay was used, along with the absorbance values, to calculate the apparent concentration of protein in each sample. The discussed calculated values are listed in Table 12.

Table 12: Apparent protein concentrations of samples used in the BCA assay.

Smpl. No.	Liposomes Batch	App. Conc. of Prtn. (μg/mL)
B	-	0
1	NH$_2$ Liposomes	27.73
2	NH$_2$ Liposomes	46.32
3	NH$_2$ Liposomes	75.30
4	RGD Liposomes	45.59
5	RGD Liposomes	85.37
6	RGD Liposomes	140.15

Each batch of liposomes possessed a different liposome concentration (lipid concentration per milliliter; mg DPPC/mL), which does not openly allow for

comparison. The liposome concentrations were determined earlier for each batch of

liposomes through the Stewart assay, described in section 3.4. Therefore, the lipid concentrations and the apparent protein concentrations were re-scaled to allow for comparison. These adjustments are demonstrated in Table 13.

Table 13: Re-scaled apparent protein concentrations of samples used in the BCA assay.

Smpl. No.	Liposomes Batch	Re-scaled Lpd. Amt. in Smpl. (mg)	Re-Scaled App. Conc. of Prtn. ($\mu g/mL$)
B	-	0	-
1	NH$_2$ Liposomes	0.27	11.27
2	NH$_2$ Liposomes	0.54	19.37
3	NH$_2$ Liposomes	1.08	30.69
4	RGD Liposomes	0.27	24.73
5	RGD Liposomes	0.54	45.36
6	RGD Liposomes	1.08	72.69

The trends observed in the data presented in Table 13 confirm the attachment of the RGD moiety to the liposomes. Comparing NH$_2$ and RGD liposomes (samples 1-3 and 4-6, respectively), a clear trend could be seen. At any equal concentration of liposomes between two samples, the apparent protein concentration obtained from the absorbance value for RGD liposomes was higher than that for NH$_2$ liposomes. For example, the apparent protein concentration for sample 6 (RGD liposomes) was higher than that for sample 3 (NH$_2$ liposomes).

Further preparations and analysis were made to re-confirm the attachment of RGD to liposomes while negating the exaggeration effect of calcein. The purpose of this addition is to ensure that the RGD present in the liposome samples is attached rather than freely present. Calcein-free RGD liposomes were compared with the calcein-free control solution comprised of all the raw materials used to prepare RGD liposomes. The lipid amounts and the absorbance values of these samples were re-scaled to allow for comparison, and are listed in Table 14.

Table 14: Re-scaled values for samples used in the BCA assay viability study.

Smpl. Name		Re-scaled Lpd. Amt. in Smpl. (mg)	Re-Scaled App. Conc. of Prtn. (µg/mL)
Calcein-Free Liposomes	RGD	0.271	117.98
Calcein-Free Liposomes	RGD	0.542	63.70
Calcein-Free Liposomes	RGD	1.083	30.68
Lipids + RGD		0.271	3047.28
Lipids + RGD		0.542	1302.57
Lipids + RGD		1.083	2179.24

The apparent protein concentration of the lipids+RGD samples was higher than those for RGD liposomes samples. It is expected to observe equal readings between both sample sets in Table 14 since the lipids+RGD control solution contained the exact proportions used in the preparation of liposomes. However, the control solution samples demonstrated higher apparent protein concentration values (higher absorbance readings). This observation confirms the removal of free RGD from the RGD liposomes during the Sephadex G-100 purification step after the RGD attachment protocol has succeeded. For more details on the RGD attachment protocol, refer to section 3.2.4. Another observation that re-confirms the attachment of RGD to the RGD liposomes is the fact that RGD liposomes possessed higher absorbance readings than NH_2 liposomes, as discussed previously. Otherwise, both liposome batches should demonstrate equivalent absorbance readings, i.e., equivalent apparent protein concentrations.

4.4. Power Density Measurements

As discussed before, frequency, power density, and pulse duration characterize ultrasound waves. The power density values of the LFUS sonicator probe are provided in percentages. To quantify these values, a hydrophone (Hydrophone Type 8103, Brüel & Kjær, Nærum, Denmark) was used to measure the voltage which is created by the

ultrasound waves, at each percentage rating [67]. Along with the hydrophone, an oscilloscope was integrated into the apparatus to convert the hydrophone signals into quantifiable voltage readings. MATLAB was used to process the voltage readings into average root mean square values, which were used to obtain the power density values for each percentage rating. The discussed calculations are presented in the equations below:

Average Root Mean Square Voltage: $\overline{V_{RMS}}$ (V)

Nominal Voltage Sensitivity of the Hydrophone [67]: $V_s = 29 *10^{-6}\left(\frac{V}{Pa}\right)$ (1)

Acoustic Pressure: $P = \dfrac{\overline{V_{RMS}}}{V_s}$ (Pa) (2)

Density of Water at 23°C [68]: $p = 997.538 \frac{kg}{m^2}$ (3)

Speed of Sound in Water at 23°C [69]: $c = 1488.997 \frac{m}{s}$ (4)

Acoustic Impedance in Water at 23°C: $z = p *c = 1.485 *10^6 \left(\frac{kg}{m^2s}\right)$ (5)

Acoustic Intensity of Ultrasound waves: $l = \dfrac{P^2}{z}\left(\frac{mW}{cm^2}\right)$ (6)

The values acquired from the equations listed above are summarized in Table 15 below. The percentage ratings of the three power density settings on the US machine, 20%, 25%, and 30%, after calculations, are 7.46, 9.85, and 17.31 $\frac{mW}{cm^2}$, respectively.

Table 15: Power densities for the ratings provided by the ultrasonic probe.

Rating	$\overline{V_{RMS}}$ (V)	P (Pa)	$I\left(\frac{-}{c^2}\right)$
20%	3.053*10⁻¹	10.527*10³	7.46
25%	3.507*10⁻¹	12.093*10³	9.85
30%	4.649*10⁻¹	16.031*10³	17.31

4.5. Mechanical Index Calculations

A parameter called the "Mechanical Index" (MI) is used to classify cavitation and determine the thresholds at which biological effects and tissue damage occur [50, 70, 71]. The Mechanical Index is defined as the ratio of the negative pressure in (MPa) to the square root of the frequency in (MHz), illustrated in equation (7) [50, 70, 71]:

$$I = \frac{P\ (MPa)}{\sqrt{f(MHz)}}$$ (7)

The probability and strength of collapse cavitation increases at lower US frequency and intensity [50, 70, 71]. As reported in literature, the threshold of collapse cavitation is expected to occur at around MI = 0.3, biological effects are observed at MI > 0.6, and tissue damage is expected to occur at MI > 1 [50, 70, 71]. The acoustic impedance in water (z) and the intensity of the low-frequency ultrasound (I) are acquired from equations (5) and (6), respectively, from section 4.4. The negative pressure, or the pressure amplitude (P^-) is calculated from equation (8) below [50, 70, 71].

$$P^- = \sqrt{2Iz} \ (Pa) \tag{8}$$

For the three power densities used in this study, 7.46, 9.85, and $17.31 \frac{mW}{cm^2}$, the calculated MI values are 0.11, 0.12, and 0.16, respectively. These values indicate the occurrence of stable cavitation and safely below the collapse cavitation threshold of 0.3. Consequently, higher power densities could be safely used in the future for low-frequency ultrasound studies. The calculated maximum power density for 20-kHz ultrasound which can be safely used to avoid collapse cavitation is $58.64 \frac{mW}{cm^2}$, which is equivalent to MI = 0.3.

4.6.   Low-Frequency Ultrasound (LFUS) Online Release Studies

The details and steps of LFUS release or online release experiments are explained in section 3.6. As discussed, the release was performed using pulsed (the 20 s on and 10 s off) 20-kHz ultrasound, at the three power densities mentioned above. The fluorescence of the dilute liposomal sample, which is prepared in a cuvette as discussed in section 3.6, is measured before sonication and is defined as the baseline intensity, I_0. This fluorescence value is the lowest amongst the others since the calcein is encapsulated in a self-quenched state inside the liposome. Upon sonication, the intensity gradually increases due to the release of calcein from the liposomes. This intensity is measured continuously with time (online) and is denoted as I_t. As discussed in section 3.6, pulsed sonication is applied for 7.67 minutes (6.67 sonication in total), where the intensity measured during this time is I_t. Once the intensity of the liposomes reaches a plateau, indicating a maximum amount of release, the liposomes are lysed using a detergent to release all their remaining content. Upon lysing the liposomes, the intensity demonstrates a slight sharp increase, followed by a plateau. The highest value of intensity recorded in the release experiment is denoted as I_∞. This experiment is

performed on three batches, with three replicates per batch, at each of the three power densities. Cumulative Fraction Released (CFR) is calculated using equation (9):

$$= \frac{-}{00^{-}}$$ (9)

4.6.1. LFUS online release studies with NH$_2$ liposomes. The online release from three batches of NH$_2$ liposomes was studied upon exposure to 20 kHz pulsed ultrasound at three different power densities, demonstrated in figure 17.
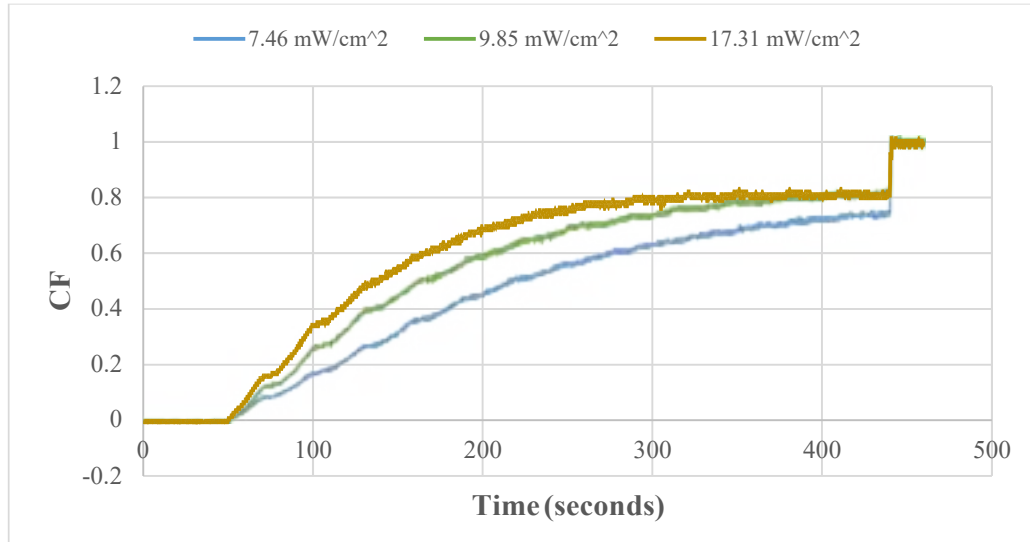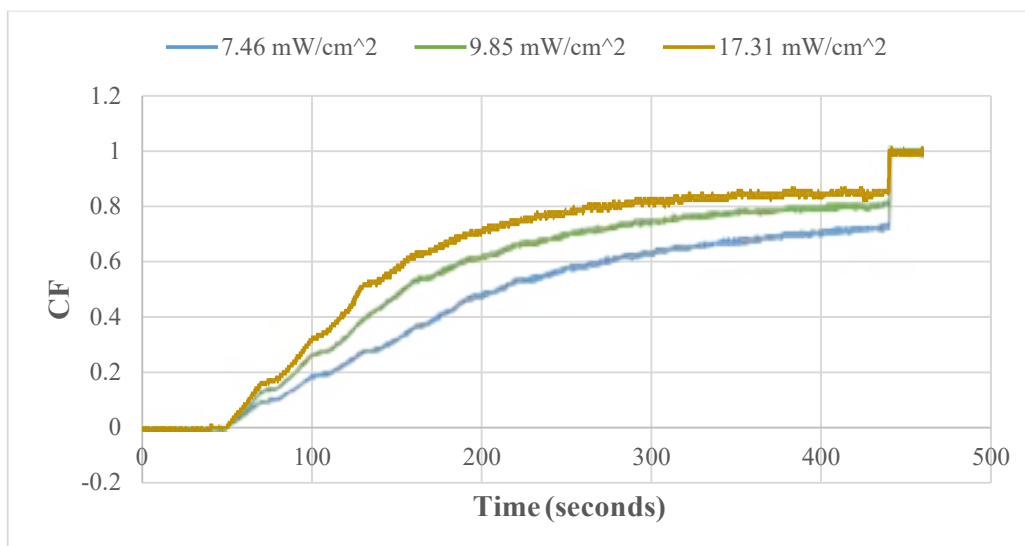

Figure 17: Online release profile for 3-batch averaged NH$_2$ liposomes.

Table 16: Statistics summary on the release profile of the 3-batch averaged NH$_2$ liposomes.

NH2 – All Batches and Power Densities	
Average Sum of Differences in CFR	0.0269
Average of Highest CFR	1.0029
Average Percentage Difference of CFR between Batches	2.68%

Figure 17 proves that the rate at which liposomes release their encapsulated contents increases as the power density increases. An increase in the power density subjects the liposomes to more collapse cavitation events, which is explained in section 1.8.2, enhancing the release percent from the liposomes. Table 16 shows that the

average percentage difference between the CFR of the batches at any time point and power density is 0.94%. Thus, the NH_2 batches used in the online release profile are reliable. An additional proof of enhanced release as the power density increases can be obtained via a comparison between the first and the second pulses at each power density, illustrated in figure 18.
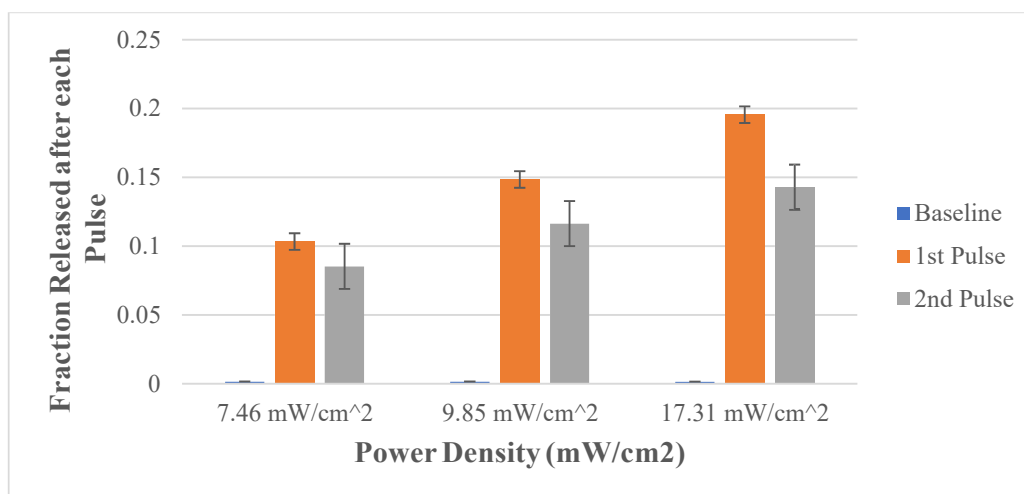
Figure 18: CFR measured at different pulses for NH_2 liposomes.

A comparison of the 1st pulse between each of the three power densities demonstrates a higher CFR per pulse value, equivalent to a higher release, as the power density is increased. Furthermore, it is observed that the release of the 1st pulse is always slightly higher than the release of the 2nd pulse, at any power density. This behavior occurs due to the initial high concentration gradient of calcein which decreases as calcein is released from the liposomes. This phenomenon is illustrated by the logarithmic behavior (slope gradually decreases as time increases) of the data presented in figure 17. This behavior is favorable since controlled release in tissues must commence with an initial rapid dose to reach the desired concentration, followed by short continuous doses to maintain the desired level constant.

4.6.2. LFUS online release studies with RGD liposomes. The online release from three batches of RGD liposomes was studied upon exposure to 20 kHz pulsed ultrasound at three different power densities, demonstrated in figure 19.

Figure 19: Online release profile for 3-batch averaged RGD liposomes.

Table 17: Statistics summary on the release profile of the 3-batch averaged RGD liposomes.

RGD – All Batches and Power Densities	
Average Sum of Differences between Batches	0.0559
Average of Highest Release	1.0000
Average Percentage Difference between Batches	5.59%

As observed with the NH$_2$ liposomes, Figure 19 demonstrates an increase in the release rate of RGD liposomes as the power density increases. Table 17 shows that the average percentage difference between the CFR of the batches at any time point and power density is 7.02%, which is considered acceptable. Thus, the RGD liposomes used in the online release profile are reliable. Furthermore, figure 20 illustrates a comparison between the first and the second pulses at each power density for RGD liposomes.
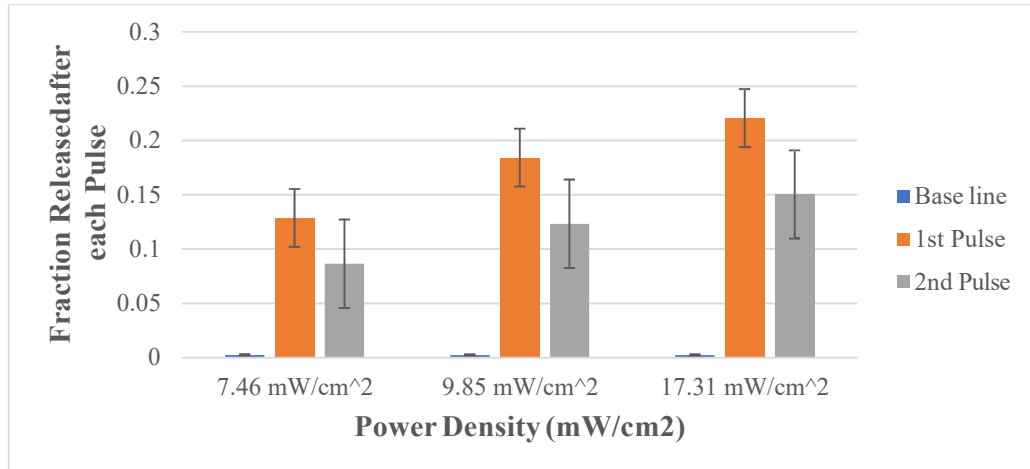
Figure 20: CFR measured at different pulses for RGD liposomes.

The behavior of RGD liposomes was consistent with that of NH_2 liposomes. In figure 20, a comparison of the 1st pulse between each of the three power densities demonstrates an increase in the release as the power density is increased. Also, it is observed that the release of the 1st pulse is always higher than the release of the 2nd pulse, at any power density.

4.6.3. LFUS for NH_2 versus RGD liposomes. Figures 21 and 22 below present a comparison between the release behavior after the 1st and 2nd pulses at different power densities, for both liposomes.
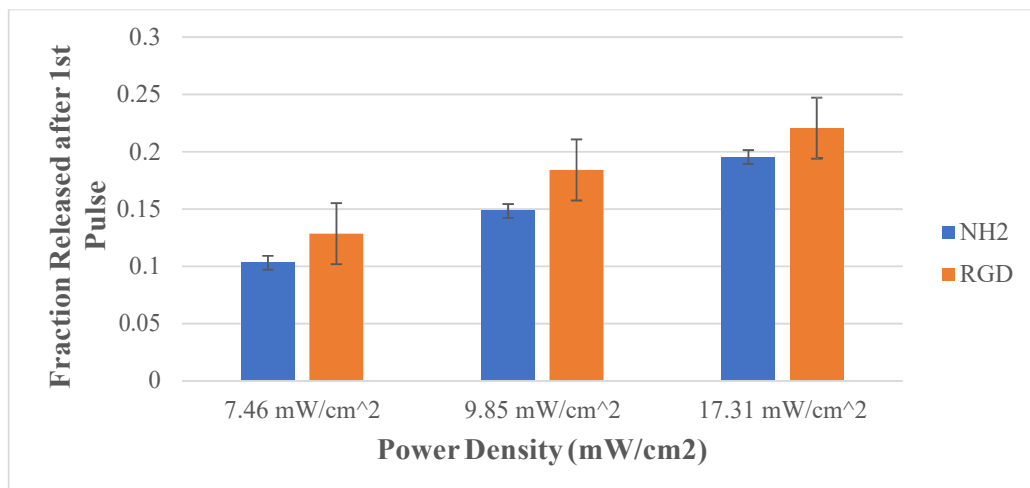
Figure 21: Fraction Released after the 1st pulse for both liposome types at different power densities.
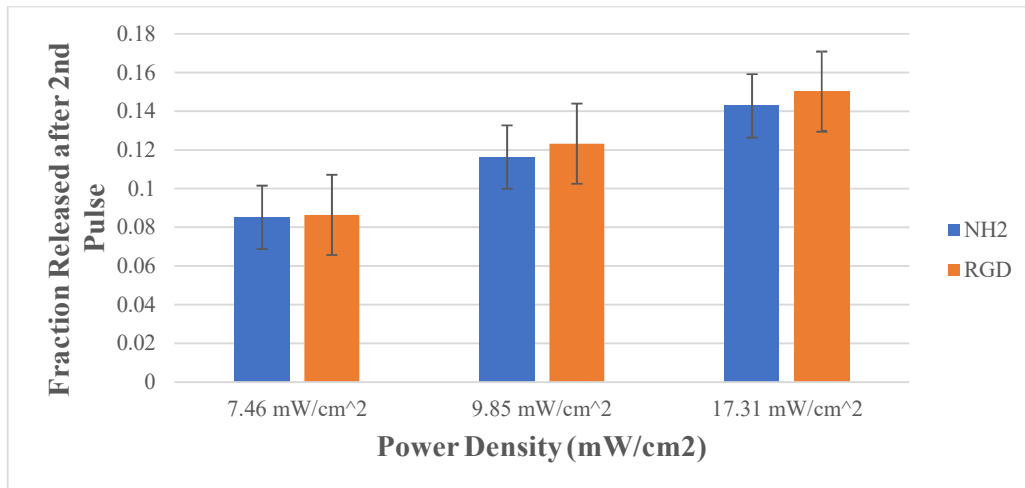
Figure 22: Fraction Released after the 2nd pulse for both liposome types at different power densities.

As observed in figures 21 and 22, RGD liposomes are more sono-sensitive or tend to respond better to ultrasound than NH$_2$ liposomes would. This desired property improves the efficacy of the encapsulated drug by allowing for enhanced controlled release at lower power densities. The difference between 1st and 2nd pulse for RGD liposomes was slightly higher than that for NH$_2$ liposomes. This finding does not hurt the performance of RGD liposomes. Comparing figures 17 and 19, the initial sharper increase in the slope of the release profile for RGD liposomes compared with that of NH$_2$ liposomes contributes positively towards reaching and maintaining the desired concentration in the tissue under treatment.
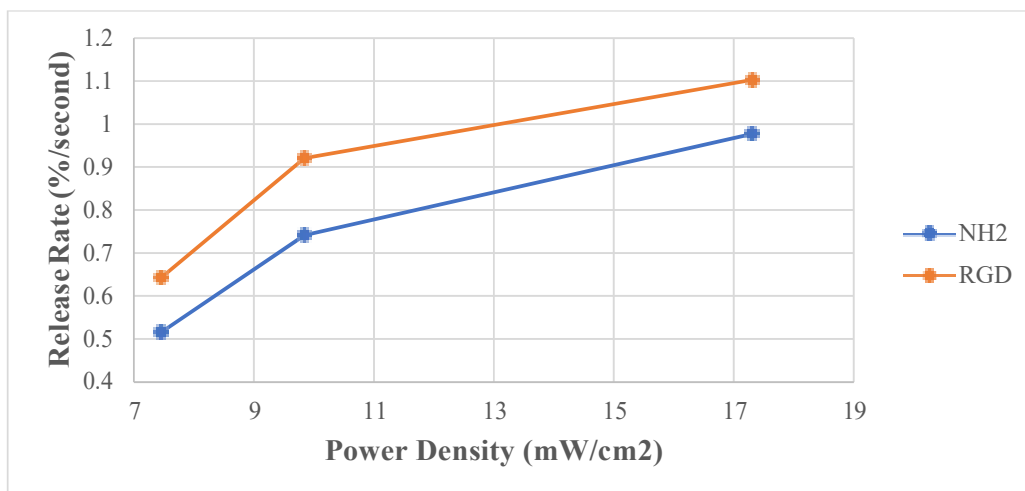
Figure 23: Release rate calculated at different power densities at the 1st pulse.
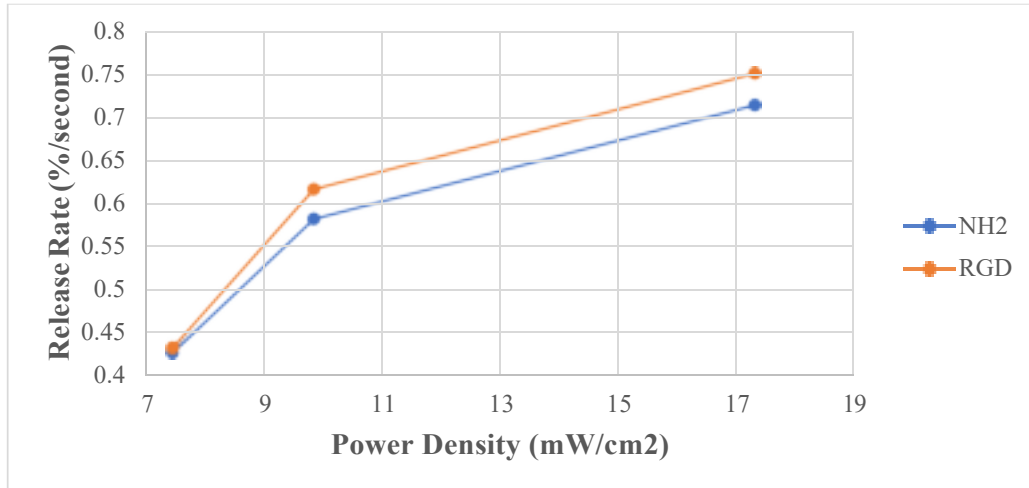
Figure 24: Release rate calculated at different power densities at the 2nd pulse.

A comparison between figures 23 and 24 further proves the previously observed property; RGD liposomes are more sono-sensitive than NH2 liposomes. The release rate per second given at any power density for RGD liposomes is always higher than that of NH2 liposomes. This observation is valid at both the 1st and 2nd pulses.
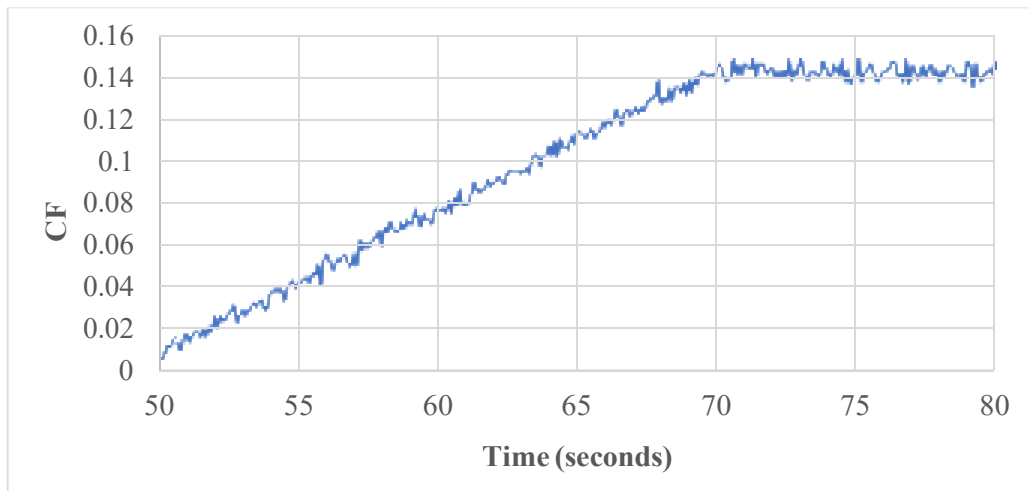
Figure 25: Release profile of RGD liposomes after the 1st pulse.

Figure 25 illustrates the release profile during the 1st pulse cycle (50-70s on and 70-80s). The release of the encapsulated calcein is triggered by the application of ultrasound (50-70s) in a linearly increasing manner. As soon as the ultrasound is switched off at 70 seconds, the release profile becomes horizontal which indicates a pause in the release. This proves that the liposomes immediately lose their tendency to

release their encapsulated content once the ultrasound is switched off. This observation suggests cavitation to be a player in the release mechanism. If thermal effects are to be suggested, some lag in the release profile is expected to be seen after ultrasound has been switched off, which is not the case. Figure 25 shows no lag at the point where ultrasound has been switched off (at 70 seconds), suggesting cavitation as the dominant release mechanism. Furthermore, the results in section 4.5 indicate the occurrence of stable cavitation since the MI values, 0.11, 0.12, and 0.16, for all three power densities used 7.46, 9.85, and 17.31 $\frac{mW}{cm^2}$, respectively, were below the collapse cavitation threshold of MI = 0.3.

4.7.   Release Kinetics Studies

The cumulative fraction of calcein released as a function of time is shown above in equation 7. This value can be used to find the best fitting model for release kinetics. The nine models investigated were:

4.7.1.   Zero-order model. This model assumes a drug dissolution rate from dosages that release the drug slowly and do not disaggregate, given by equation (10) [72]:

$$Q_t = Q_0 + K_0 t \tag{10}$$

Where Q_t = the amount of drug dissolved in time t

Q_0 = the initial amount of drug in the solution

k_0 = the zero-order release constant in units of concentration/time

A re-definition of the model to make it compatible with the variables of this study yields:

$$= k_0 t + constant \tag{11}$$

Where CFR = Cumulative Fraction Released

t = time in seconds

k_0 = the zero-order release constant

Therefore, a plot of the CFR versus time can be used to study the release kinetics and obtain k_0 from the slope [72].

4.7.2. First-order model. This model assumes drug dissolution in pharmaceutical dosages like those containing water-soluble drugs in porous matrices, or liposomes in this case [72]:

$$\frac{dC}{dt} = -k_1 \tag{12}$$

Where C = the drug concentration at time t

$\quad$ k_1 = the first-order release constant

After linearization and a re-definition of the model to make it compatible with the variables of this study yields:

$$log \quad = k_1 t + constant \tag{13}$$

According to equation (13), a plot of log(CFR) versus time would yield k_1 as the slope.

4.7.3. Higuchi model. Initially conceived for planar systems, it was the first mathematical model, which was proposed by Higuchi in 1961, derived to describe drug release from a matrix system [72-74]. The model was then extended to different geometrics and porous systems, and is based on the following hypothesis [72, 73]:

$\quad$ i. $\quad$ The initial drug concentration in the liposome is much higher than the drug solubility.

$\quad$ ii. $\quad$ Drug diffusion takes place in one dimension only.

$\quad$ iii. $\quad$ The drug particles are much smaller than the thickness of the system.

$\quad$ iv. $\quad$ Swelling and dissolution of the liposomes are negligible.

$\quad$ v. $\quad$ Drug diffusivity is constant.

$\quad$ vi. $\quad$ Perfect sink conditions are attained in the release environment.

According to the listed assumptions, the model can be expressed as [73]:

$$Q = A\sqrt{D(2 \quad _{lip} - \quad _s) \, _s t} \tag{14}$$

Where Q = the amount of drug released in time t per unit area A

$\quad$ C_{lip} = the initial drug concentration in the liposome

$\quad$ C_s = the drug solubility in liposome media

$\quad$ D = the diffusivity (diffusion coefficient) of the drug molecules in the liposome substance

The unknowns are grouped, and the model is re-written as:

$$= k_{HIi}\sqrt{t} + constant \tag{15}$$

Where k_{Hi} = Higuchi release constant

According to equation (15), a plot of CFR versus the square root of time would yield k_{Hi} as the slope.

4.7.4. Korsmeyer-Peppas model. This model was derived by Korsmeyer et al. in 1983 from a polymeric system equation to describe drug release [72, 74]. This model applies to release data from several formulations of microcapsules or microspheres [74]. This simple power-law model is described as:

$$\frac{M}{M_{00}} = k_{KP}t^n \tag{16}$$

Where $\frac{M}{M_{00}}$ = the fraction of drug release at time t

k_{KP} = the Korsmeyer-Peppas release constant

n = the release exponent

In this model, the value of n characterizes the mechanism of the drug release [72]. For $0.45 \leq n$, the mechanism follows Fickian diffusion. For $0.45 < n < 0.89$, the mechanism follows non-Fickian transport. For $n = 0.89$, the mechanism follows relaxational transport. For $n > 0.89$, the mechanism follows super transport. The portion of the release curve where $M_t/M_\infty < 0.6$ should be used when determining the value of the exponent n [72].

After linearization and a re-definition of the model to make it compatible with the variables of this study yields:

$$= k_{KP}t^n \tag{17}$$

$$log\quad = n\, log\, t + log\, k_{KP} \tag{18}$$

According to equation (18), a log-log plot of CFR versus time would yield k_{KP} from the y-intercept, and the value of n as the slope.

4.7.5. Hixson-Crowell model. This model was derived by Hixson and Crowell in 1931 upon the recognition that the natural area of the particles is

proportional to the cube root of its volume [72, 74]. This model describes the release from systems where the surface area and diameter of particles or tablets are changing [72]. The model is described as:

$$W_0^{1/3} - W_t^{1/3} = Kt \tag{19}$$

Where W_0 = the initial amount of drug in the liposome

W_t = the remaining amount of drug in the liposome at time t

κ = a constant incorporating the surface-volume relationship

After linearization and a re-definition of the model to make it compatible with the variables of this study, the model becomes:

$$[100(1 -)]^{1/3} = k_{HC}t + constant \tag{20}$$

Where k_{HC} = Hixson-Crowell release constant

According to equation (20), a plot of $[100(1 -)]^{1/3}$ versus time would yield k_{HC} as the slope.

    4.7.6. Baker-Lonsdale model. In 1974, Baker and Lonsdale derived this model from the Higuchi model, where they described the drug release from spherical matrices, such as microcapsules and microspheres, as [72, 74]:

$$\frac{3}{2}\left(1 - \left(1 - \frac{M}{M_{00}}\right)^{2/3}\right) - \frac{M}{M_{00}} = kt \tag{21}$$

Where $\frac{M}{M_{00}}$ = the fraction of drug released at time t

k = the release constant

A re-definition of the model to make it compatible with the variables of this study yields:

$$\frac{3}{2}[1 - (1 -)^{2/3}] - = k_{BL}t \tag{22}$$

Where k_{BL} = the Baker-Lonsdale release constant

According to equation (22), a plot of $\frac{3}{2}[1 - (1 -)^{2/3}]$ - versus time would yield k_{BL} as the slope.

4.7.7. Weibull model. This model has been derived for different dissolution and drug delivery processes of microcapsules and microspheres type matrices [72, 74]. This model is represented as:

$$M = M_0 [1 - e^{-(\frac{T}{a})^b}] \qquad (23)$$

Where M = the amount of drug dissolved as a function of time t

M_0 = the total amount of drug being released

T = the lag time resulting from the dissolution process

a = a scale parameter describing the time dependence

b = a parameter describing the shape of the dissolution curve progression

After linearization and a re-definition of the model to make it compatible with the variables of this study, the model becomes:

$$log(- ln(1 - M)) = log(t) - log k_W \qquad (24)$$

Where k_w [72, 74] = the Weibull release constant $= \frac{1}{a}$

According to the authors of both papers [72, 74], the rate constant (k) is proportional to the shape parameter (b). This justifies the appearance of k_W at the intercept rather than at the slope.

According to equation (24), a log-log plot of -ln(1-CFR) versus time would yield k_W from the intercept.

4.7.8. Hopfenberg model. Hopfenberg developed this model to describe the drug release from surface eroding polymers as long as the surface area remains constant during the degradation or release process [72, 74]. The model is described as:

$$\frac{M}{M_{00}} = 1 - [1 - \frac{k_t}{C_l a}]^n \qquad (25)$$

Where $\frac{M}{M_{00}}$ = the cumulative fraction of drug released at time t

k_0 = the zero order rate constant describing the surface erosion process

C_L = the initial drug loading throughout the system

81

a = the system's half thickness, such as the radius of a sphere or cylinder

n = a geometrical exponent, having values of 1, 2, and 3 for flat, cylindrical, and spherical geometries, respectively

After an algebraic re-arrangement, setting n = 3, and a re-definition of the model to make it compatible with the variables of this study, the model becomes:

$$1 - (1 - \quad)^{1/3} = k_{Hf}t \tag{26}$$

Where k_{Hf} = the Hopfenberg release constant

According to equation (26), a plot of $1 - (1 -)^{1/3}$ versus time would yield k_{Hf} as the slope.

4.7.9. Gompertz model. This model has been developed for drugs possessing good stability and intermediate release rate [72, 74]. A simple exponential model describes the dissolution profile, expressed by the equation:

$$X(t) = X_{max}\, exp(-ae^{(\beta log\, t)}) \tag{27}$$

Where X(t) = the fraction of drug dissolved at time t

X_{max} = the maximum dissolution fraction

α = a scale parameter equivalent to the undissolved drug proportion at t=1

β = a shape parameter equivalent to the dissolution rate per unit time

After linearization and a re-definition of the model to make it compatible with the variables of this study, the model becomes:

$$ln\, (-ln \quad) = k_G\, log\, t + ln\, a \tag{28}$$

Where k_G = the Gompertz release constant = β

According to equation (28), an ln-log plot of -ln(CFR) versus time would yield k_G as the slope.

4.7.10. Model accuracy for NH$_2$ liposomes. The Cumulative Fraction Released, or CFR, which is described in section 4.5, was used in the following plots to denote the concentration or amount released from the liposome. Each of these CFR plots represents one of the previously discussed models. The linearized form of each of

the previous models was plotted to determine the desired parameters. The applicability of each model is determined by the R^2 value, which is obtained from the linear trendline equation shown in each graph.
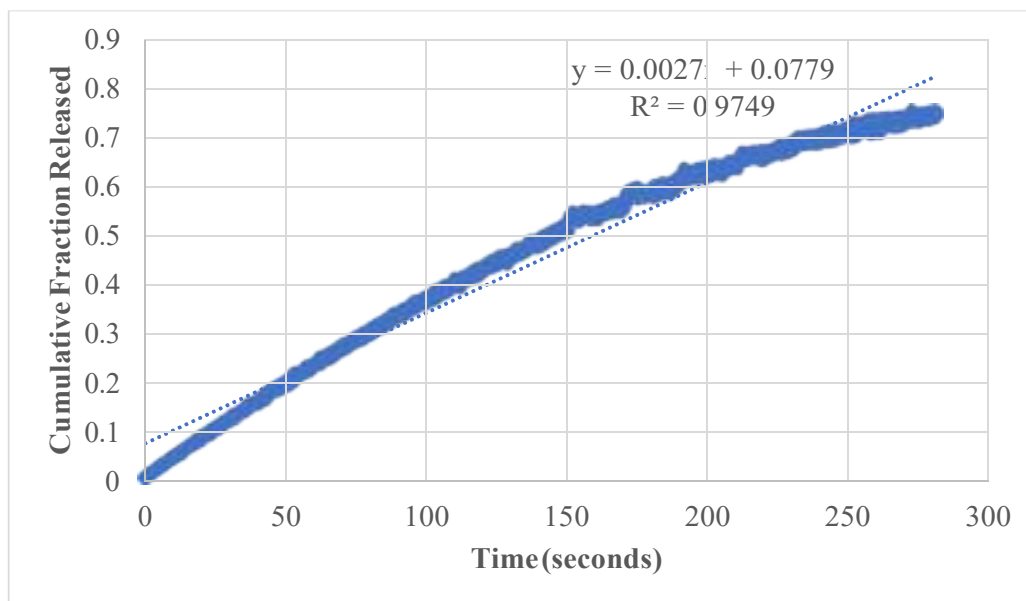
Figure 26: Zero-order plot for NH$_2$ liposomes, batch #1, at 7.46 $\left(\frac{mW}{cm^2}\right)$.
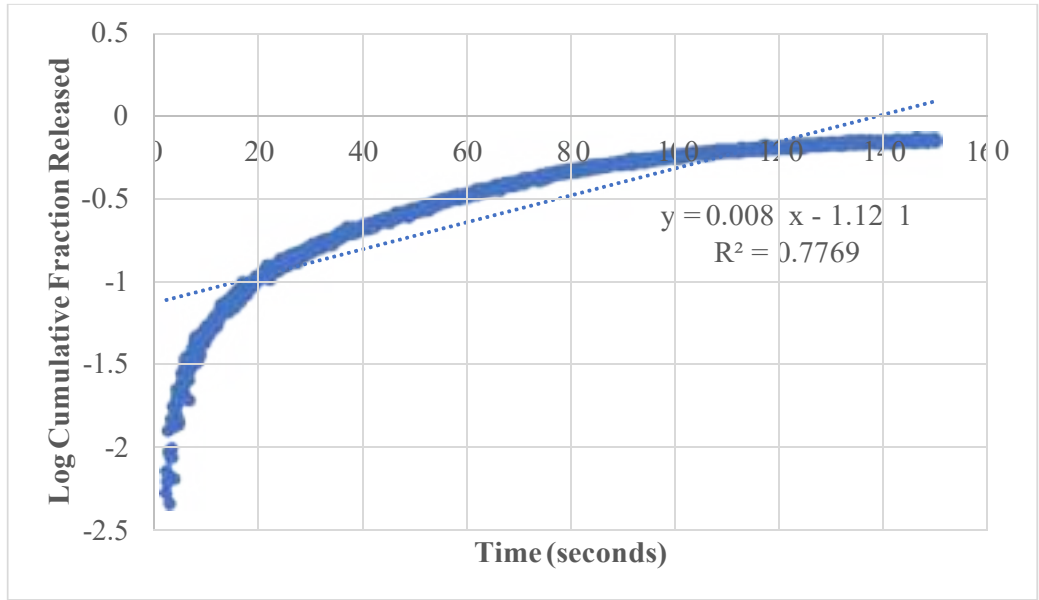
Figure 27: First-order plot for NH$_2$ liposomes, batch #1, at 7.46 $\left(\frac{mW}{cm^2}\right)$.
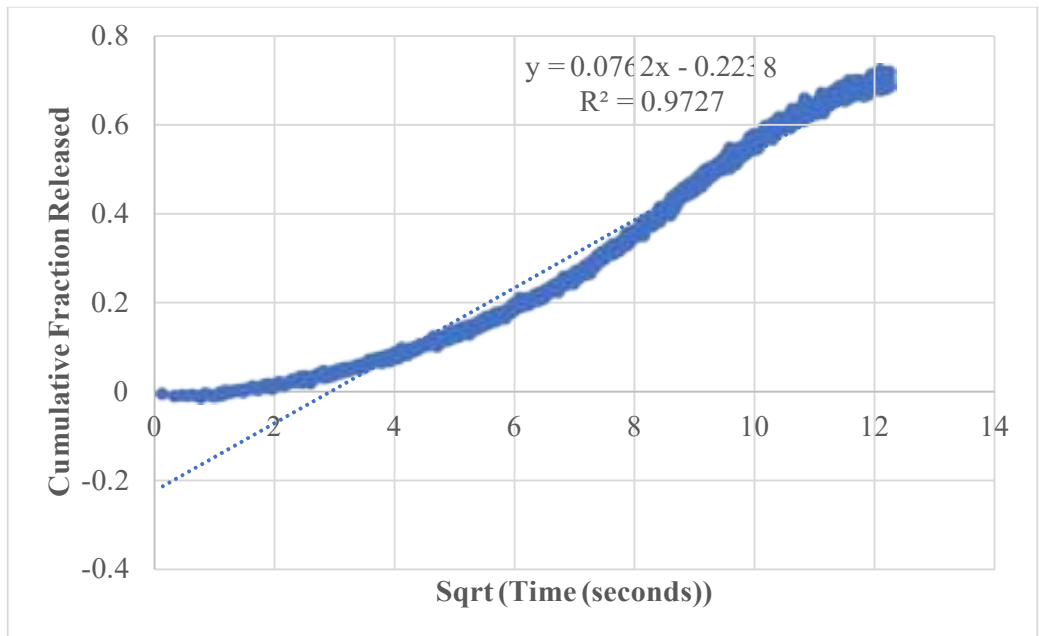
Figure 28: Higuchi model plot for NH$_2$ liposomes, batch #1, at 7.46 $\left(\frac{mW}{cm^2}\right)$.
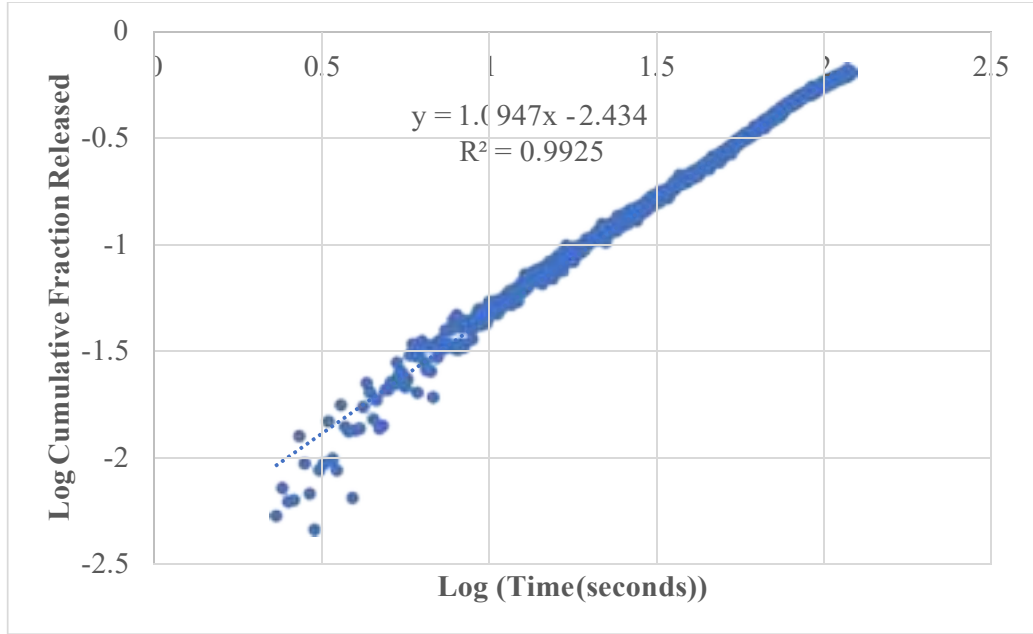
Figure 29: Korsmeyer-Peppas model plot for NH$_2$ liposomes, batch #1, at 7.46 $\left(\frac{mW}{cm^2}\right)$.
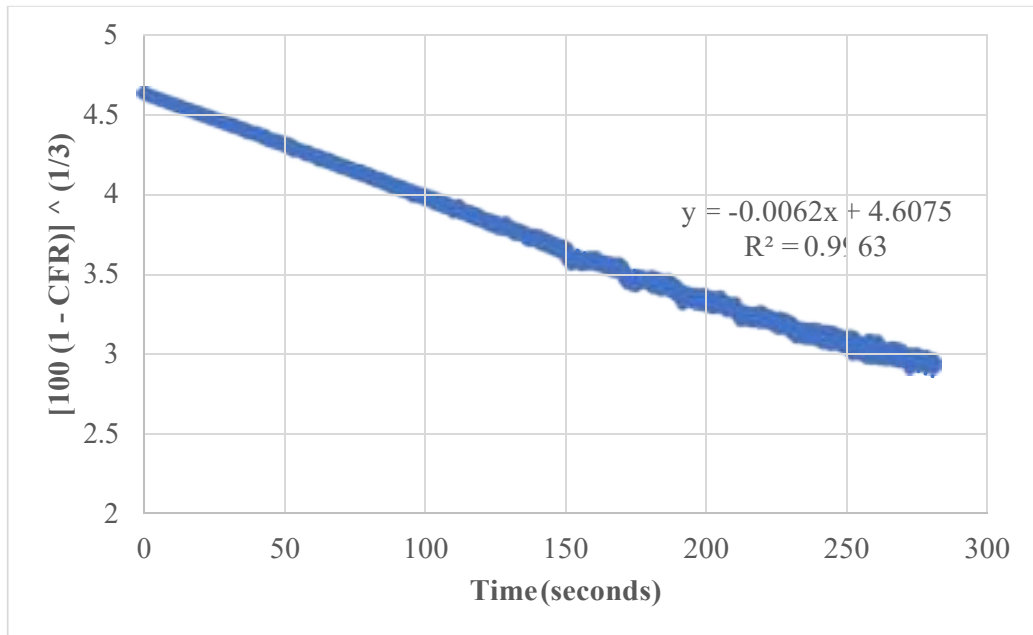
Figure 30: Hixson-Crowell model plot for NH$_2$ liposomes, batch #1, at 7.46 $\left(\frac{mW}{cm^2}\right)$.
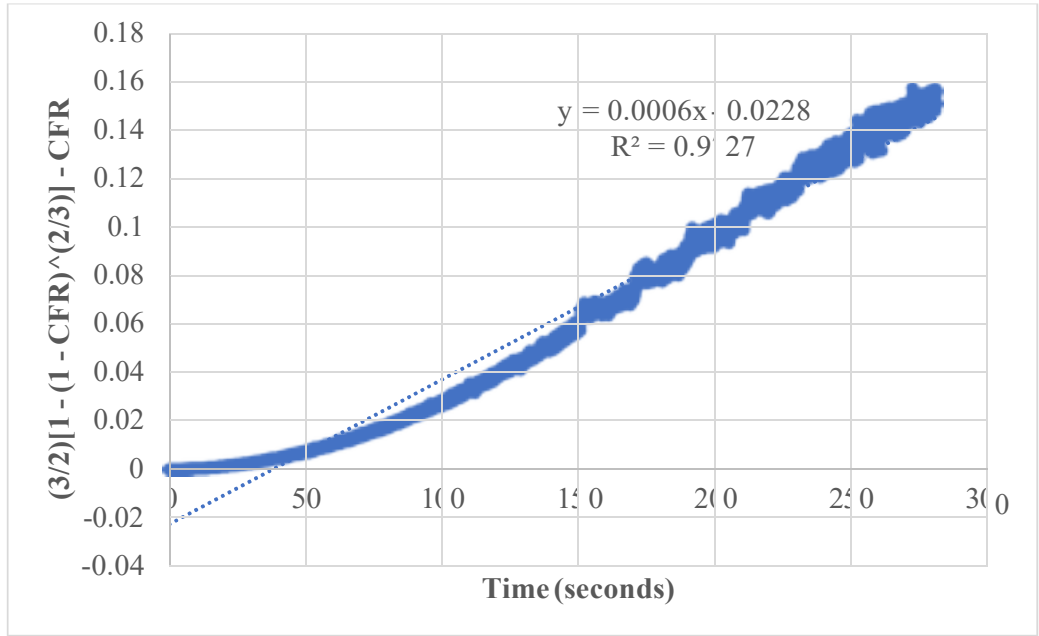
Figure 31: Baker-Lonsdale model plot for NH_2 liposomes, batch #1, at 7.46 $\left(\frac{mW}{cm^2}\right)$.
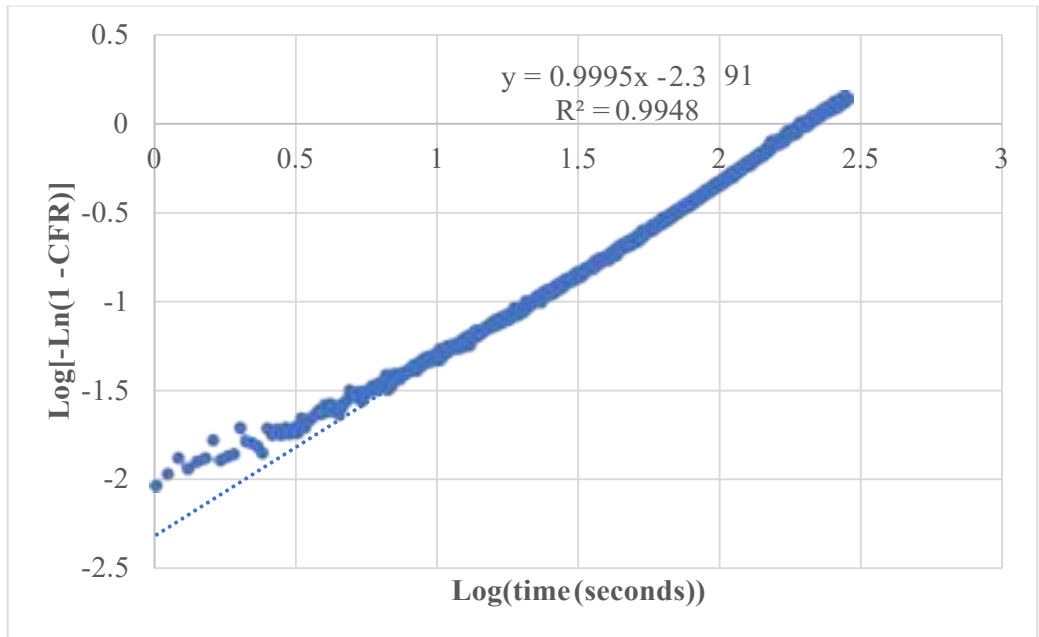
Figure 32: Weibull model plot for NH_2 liposomes, batch #1, at 7.46 $\left(\frac{mW}{cm^2}\right)$.
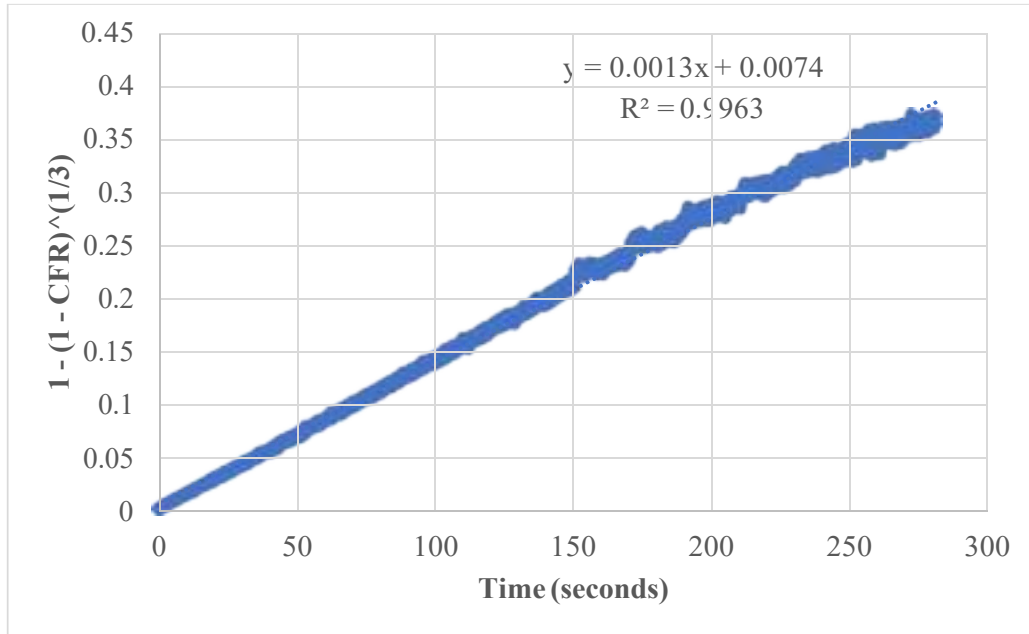
Figure 33: Hopfenberg model plot for NH$_2$ liposomes, batch #1, at 7.46 $\left(\frac{mW}{cm^2}\right)$.
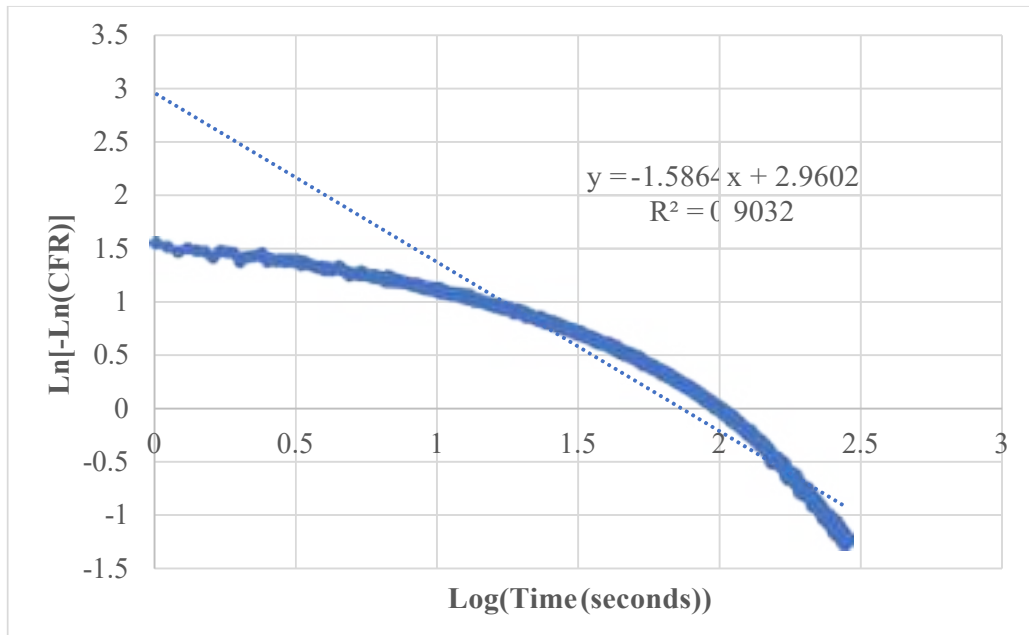
Figure 34 – Gompertz model plot for NH$_2$ liposomes, batch #1, at 7.46 $\left(\frac{mW}{cm^2}\right)$.

A comparison of the R^2 values for each model and parity plots are used to verify the best fitting models. The R^2 values for the first batch of NH$_2$ liposomes at

7.46 $\left(\frac{mW}{cm^2}\right)$ are presented in the plots above, with the rest included in the appendices. The summary of R^2 values for NH$_2$ liposomes presented in Tables 18 and 19 demonstrate excellent adherence of the data fits with the models of Korsmeyer-Peppas, Hixson-Crowell, Weibull, and Hopfenberg. However, the Korsmeyer-Peppas and Weibull models possessed the highest value of R^2 averages for NH$_2$ and RGD liposomes (0.9902 and 0.9917, respectively). This finding proves that both models provide the best fit to the data. In addition to that, parity plots comparing all models, except for the Baker-Lonsdale model, confirm the previous finding. The plots for all models were close to the plot for actual CFR, colored red, except for the first-order and Gompertz plot, due to their relatively lower R^2 values. The Baker-Lonsdale model was not included in the parity plots since the CFR derived from it cannot be estimated using mathematical methods. The parity plots for the kinetics models of a three-batch averaged CFR at each power density are presented below in figures 35, 36, and 37. Additional kinetics model plots for different batches of NH$_2$ liposomes at all three power densities are included in the appendices. Further analysis for both liposome types and their adherence to the models is discussed in section 4.6.11.

Table 18: R^2 values of different model fits for NH$_2$ liposomes.

R^2 values	NH$_2$ Batch	Zero Order	First Order	Higuchi	Korsmeyer-Peppas
7.46 $\left(\frac{-}{c^2}\right)$	#1	0.9749	0.7669	0.9727	0.9925
	#2	0.9799	0.7507	0.9865	0.9977
	#3	0.9844	0.7767	0.9727	0.9925
9.85 $\left(\frac{-}{c^2}\right)$	#1	0.9770	0.7461	0.9765	0.9763
	#2	0.9712	0.7075	0.9867	0.9868
	#3	0.9746	0.7462	0.9764	0.9777
17.31 $\left(\frac{-}{c^2}\right)$	#1	0.9709	0.7407	0.9765	0.9897
	#2	0.9765	0.7203	0.9849	0.9976
	#3	0.9627	0.7411	0.9764	0.9898

Table 19: R^2 values of different model fits for NH$_2$ liposomes, continued.

R^2 values	NH2 Batch	Hixson-Crowell	Baker-Lonsdale	Weibull	Hopfenberg	Gompertz
7.46 $\left(\frac{1}{c^2}\right)$	#1	0.9963	0.9727	0.9948	0.9963	0.9032
	#2	0.9965	0.9695	0.9955	0.9965	0.9215
	#3	0.9933	0.9498	0.9950	0.9933	0.9236
9.85 $\left(\frac{1}{c^2}\right)$	#1	0.9972	0.9568	0.9925	0.9972	0.8543
	#2	0.9932	0.9723	0.9951	0.9932	0.9410
	#3	0.9892	0.9629	0.9870	0.9892	0.9575
17.31 $\left(\frac{1}{c^2}\right)$	#1	0.9958	0.9645	0.9913	0.9958	0.8704
	#2	0.9957	0.9666	0.9976	0.9957	0.9265
	#3	0.9832	0.9678	0.9921	0.9832	0.9310
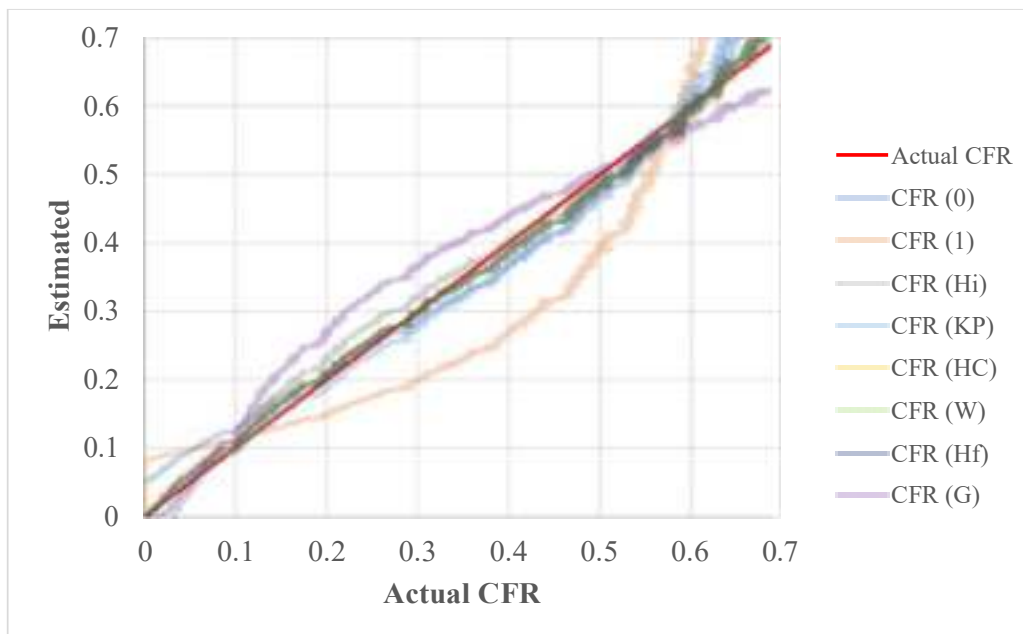
Figure 35 – Parity plot for 3-batch averaged NH$_2$ liposomes at 7.46 $\left(\frac{mW}{cm^2}\right)$.
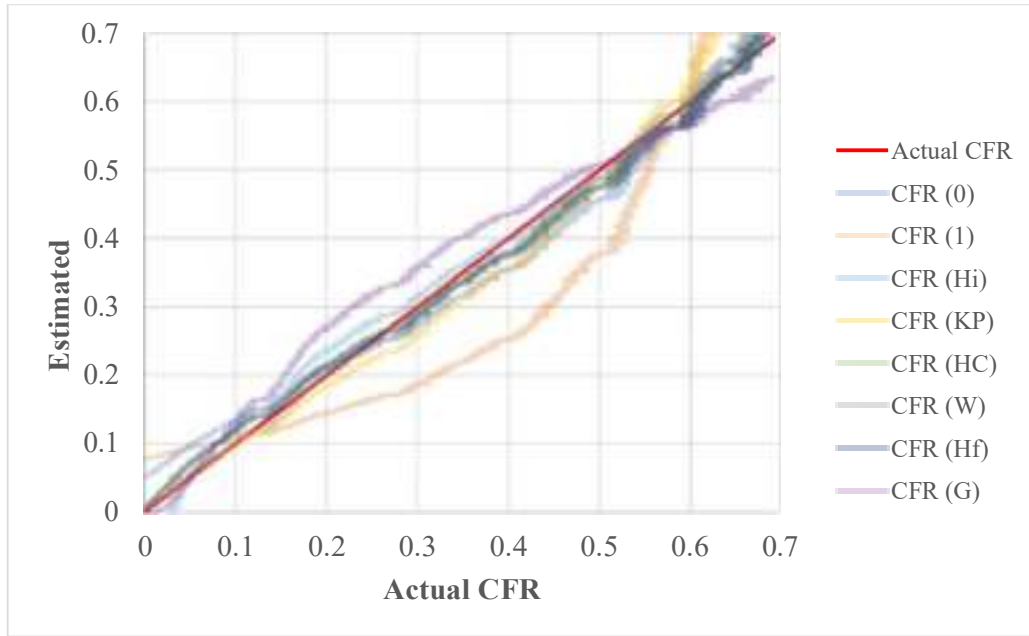
Figure 36 – Parity plot for 3-batch averaged NH_2 liposomes at 9.85 $\left(\frac{mW}{cm^2}\right)$.
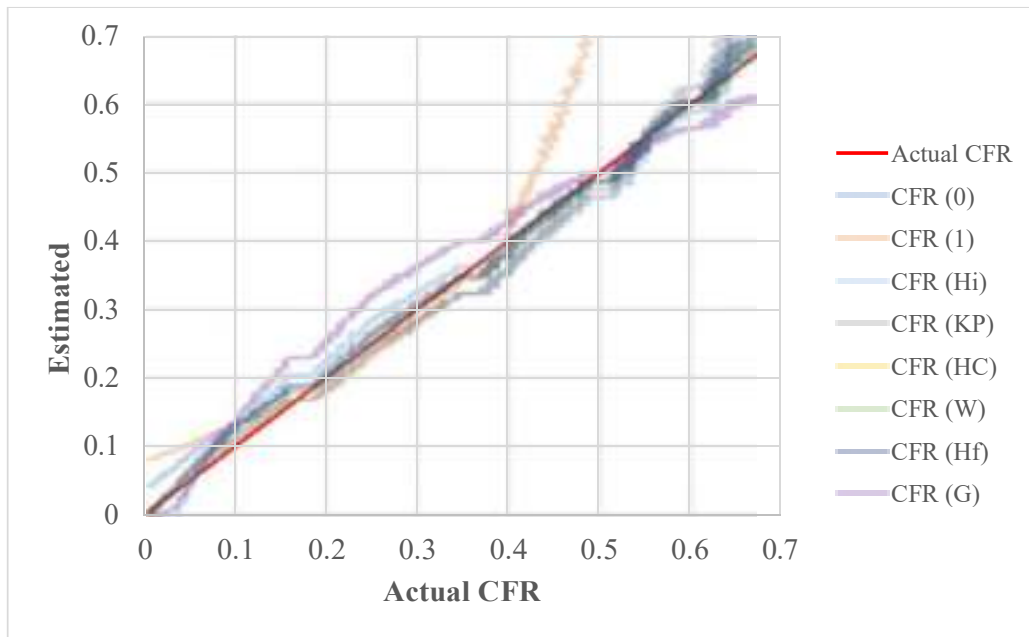
Figure 37 – Parity plot for 3-batch averaged NH_2 liposomes at 17.31 $\left(\frac{mW}{cm^2}\right)$.

4.7.11. Model accuracy for RGD liposomes. The analysis performed in section 4.6.10 for NH_2 liposomes is replicated in this section. kinetics model plots for all three batches of RGD liposomes at all three power densities are included in the

appendices. A summary of the R^2 values is presented in Tables 20 and 21 The behavior of RGD liposomes apparent after fitting the data is similar to that of NH_2 liposomes. The parity plots for all models were close to the plot for actual CFR, colored red, except for the first-order and Gompertz plots, due to their relatively lower R^2 values. The parity plots for the kinetics models of a three-batch averaged CFR at each power density are presented below in figures 38, 39, and 40. A comparison of the data fitting for both liposomes types concludes that the behavior of both can be accurately presented by the Korsmeyer-Peppas and Weibull models. Additionally, the average values of the power (n) for the Korsmeyer-Peppas model was n = 1.0789 for NH_2 liposomes and n = 0.9441 for RGD liposomes. The difference between both n-values is insignificant and can be safely averaged to n = 1.0115. Data adherence of both liposomes types to Korsmeyer-Peppas suggests diffusion-driven release, with n > 1 suggesting super transport. Diffusion-driven drug release from liposomes subjected to ultrasound is supported in the literature by Schroeder et al. [75]. Furthermore, data adherence of both liposome types to the Weibull model suggests dissolution-driven release. In summary, both liposome types adhere perfectly to two types of controlled-release mechanisms, diffusion and dissolution.
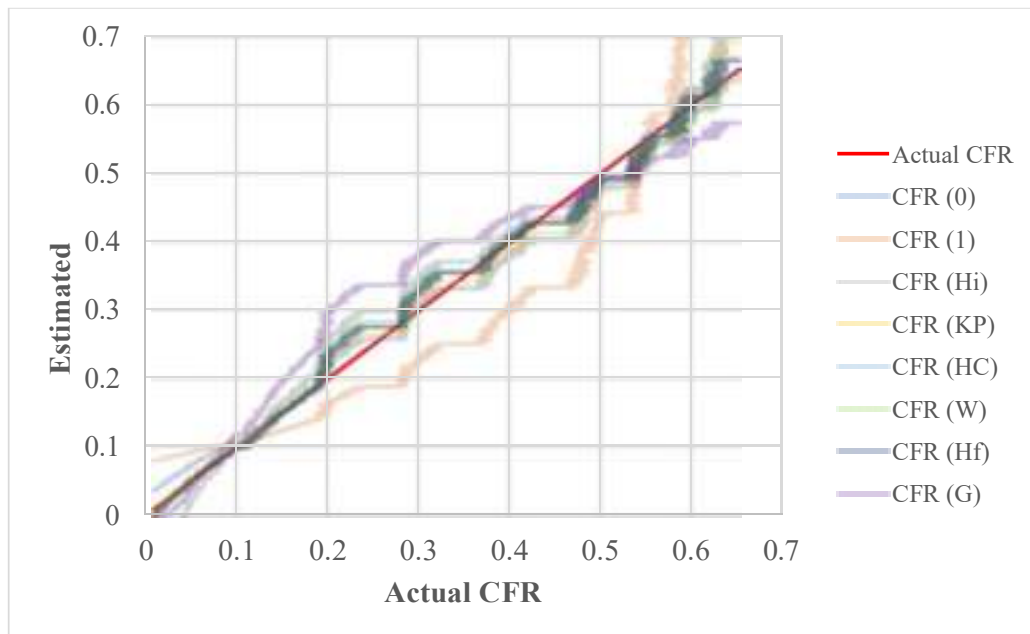
Figure 38 – Parity plot for 3-batch averaged RGD liposomes at 7.46 $\left(\frac{mW}{cm^2}\right)$.
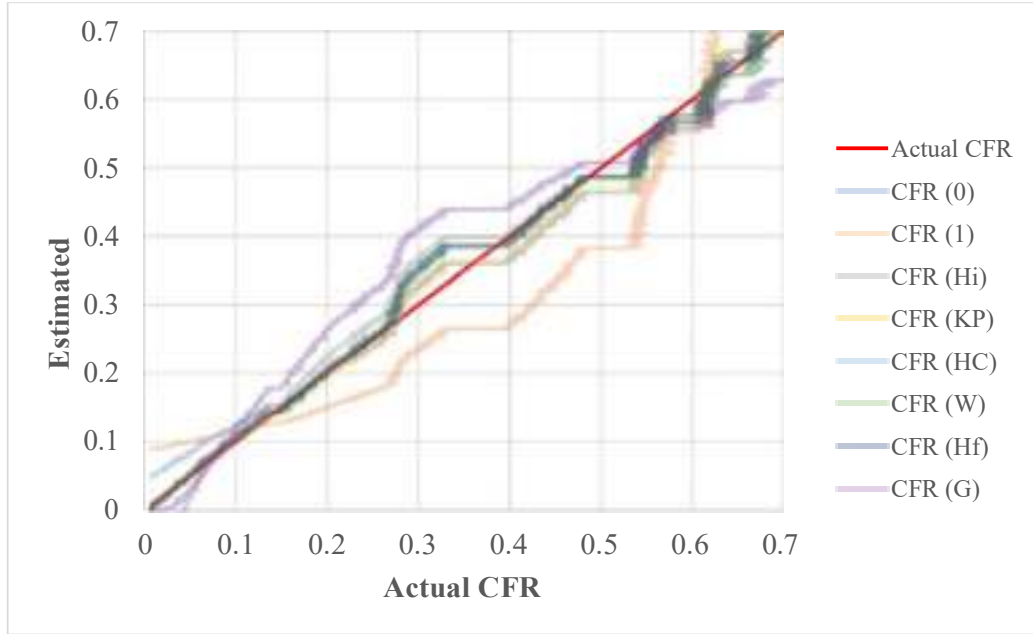
Figure 39 – Parity plot for 3-batch averaged RGD liposomes at 9.85 $\left(\frac{mW}{cm^2}\right)$.
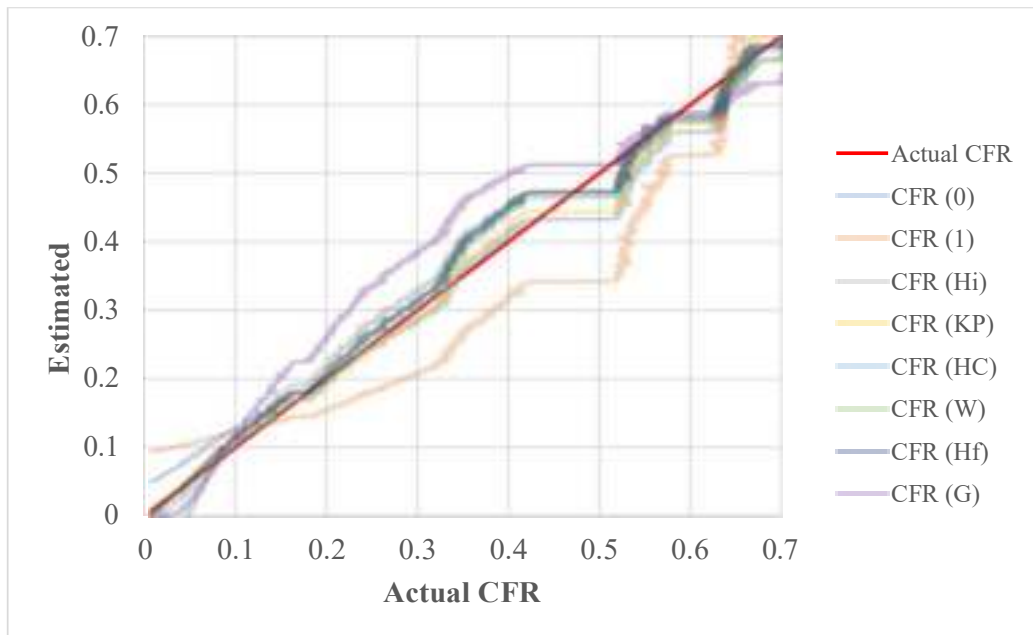
Figure 40 – Parity plot for 3-batch averaged RGD liposomes at 17.31 $\left(\frac{mW}{cm^2}\right)$.

Table 20: R^2 values of different model fits for RGD liposomes.

R^2 values	RGD Batch No.	Zero Order	First Order	Higuchi	Korsmeyer-Peppas
7.46 $\left(\dfrac{-}{c}\right)_2$	#1	0.9327	0.7824	0.9773	0.9946
	#2	0.9554	0.6748	0.9930	0.9954
	#3	0.9873	0.7941	0.9774	0.9943
9.85 $\left(\dfrac{-}{c}\right)_2$	#1	0.9060	0.7537	0.9824	0.9957
	#2	0.9542	0.6580	0.9928	0.9710
	#3	0.9744	0.7614	0.9823	0.9950
17.31 $\left(\dfrac{-}{c}\right)_2$	#1	0.8947	0.7982	0.9777	0.9963
	#2	0.9473	0.6350	0.9925	0.9852
	#3	0.9804	0.7902	0.9776	0.9952

Table 21: R^2 values of different model fits for RGD liposomes, continued.

R^2 values	RGD Batch No.	Hixson-Crowell	Baker-Lonsdale	Weibull	Hopfenberg	Gompertz
7.46 $\left(\dfrac{-}{c}\right)_2$	#1	0.9653	0.9862	0.9804	0.9653	0.9265
	#2	0.9892	0.9865	0.9987	0.9892	0.9416
	#3	0.9957	0.9537	0.9911	0.9957	0.9081
9.85 $\left(\dfrac{-}{c}\right)_2$	#1	0.9578	0.9911	0.9801	0.9578	0.9419
	#2	0.9950	0.9813	0.9922	0.995	0.9542
	#3	0.9912	0.9869	0.9958	0.9912	0.924
17.31 $\left(\dfrac{-}{c}\right)_2$	#1	0.9582	0.9913	0.9749	0.9582	0.9527
	#2	0.9909	0.9859	0.9968	0.9909	0.9533
	#3	0.9949	0.9562	0.9905	0.9949	0.9005

4.7.12. Calculation of K_{KP} values. According to the model equation developed by Korsmeyer-Peppas, which is discussed in section 4.6.4, a log-inverse of the generated slope value yields the release constant, K_{KP}. The same procedure can be used to obtain the release constant, K_W for the model equation developed by Weibull, which is discussed in section 4.6.7. The release constant values for this model are listed in Table 22.

Table 22: K-values (K_{KP}) for the Korsmeyer-Peppas model at different power densities.

Liposomes Batch	$K_{KP}*10^3\ (s^{-n})$		
	$7.46\ (\frac{W}{cm^2})$	$9.85\ (\frac{W}{cm^2})$	$17.31\ (\frac{W}{cm^2})$
NH2 #1	3.6810	3.7670	7.7911
NH2 #2	6.7593	5.5873	9.0636
NH2 #3	3.5670	3.5703	7.7750
Average	4.6691	4.3082	8.2099
Std. Dev.	1.3935E-03	8.5270E-04	5.691E-04
RGD #1	7.2144	8.7100	9.5040
RGD #2	9.6316	8.6776	14.625
RGD #3	7.2210	8.8145	9.8197
Average	8.0223	8.7340	11.316
Std. Dev.	1.0728E-03	5.3640E-05	2.2058E-03

Presented in Table 23 is a two-factor ANOVA analysis performed on the K_{KP} values which are presented in Table 22. Comparing NH_2 and RGD liposomes, the F-value is much higher than the critical F-value, and the p-value is much lower than alpha (standard α; α= 0.05). Thus, the K_{KP} values are affected by the type of the carrier. Comparing different power densities, the F-value is also higher than the critical F-value, and the p-value is also much lower than the standard alpha. Thus, changes in the power density have significant effects on K_{KP}. The cause behind these results is believed to be the attachment of RGD moieties to the liposomes. This moiety reduces the stability of the liposomes, hence significantly affects the release kinetics. This instability in the liposomes causes the release rate constants to increase as the power density increases. Although the prediction of the K_{KP}-values for the Korsmeyer-Peppas model is not very accurate, its applicability still holds due to the perfect fitting (high R^2-values) demonstrated earlier.

Table 23: Two-factor ANOVA analysis of K_{KP} values.

Source of Variation	SS	df	MS	F	P-value	F crit
Sample	5.93E-05	1	5.93E-05	23.32	0.0004	4.75
Columns	4.44E-05	2	2.22E-05	8.74	0.005	3.89
Interaction	1.48E-06	2	7.38E-07	0.29	0.7530	3.89
Within	3.05E-05	12	2.54E-06			
Total	13.57E-05	17				

4.7.13. **Calculation of K_W values.** According to the model equation developed by Weibull, which is discussed in section 4.6.7, a log-inverse of the generated slope value yields the release constant, K_{KP}. The release constant values for this model are listed in Table 24.

Table 24: K-values (K_W) for the Weibull model at different power densities.

	K_W*10^3		
Liposomes Batch	**7.46** $\left(\frac{W}{c^2}\right)$	**9.85** $\left(\frac{W}{c^2}\right)$	**17.31** $\left(\frac{W}{c^2}\right)$
NH2 #1	9.8197	4.0860	5.9007
NH2 #2	5.0455	4.5646	6.8046
NH2 #3	2.6038	2.9248	6.6115
Average	5.8230	3.8585	6.4389
Std. Dev.	2.6645E-03	6.2244E-04	3.5882E-04
RGD #1	3.2426	3.8788	2.9964
RGD #2	7.7037	7.3131	1.2511
RGD #3	5.3064	6.7375	6.8818
Average	5.4176	5.9765	7.4631
Std. Dev.	1.5241E-03	1.3984E-03	3.3653E-03

Presented in Table 25 is a two-factor ANOVA analysis performed on the K_W values, which are presented in Table 24. Comparing NH_2 and RGD liposomes, the F-value is much lower than the critical F-value, and the p-value is much higher than alpha (standard α; $\alpha= 0.05$). Thus, the K_{KP} values are not affected by the type of the carrier. Comparing different power densities, the F-value is also lower than the critical F-value, and the p-value is much higher than the standard alpha. Thus, changes in the power density do not affect K_{KP}. Conclusively, the Weibull model is significantly better than the Korsmeyer-Peppas model at predicting the K-values.

Table 25: Two-factor ANOVA analysis of K_W values.

Source of Variation	SS	df	MS	F	P-value	F crit
Sample	3.74E-06	1	3.74E-06	0.49	0.50	4.75
Columns	1.28E-05	2	6.4E-06	0.84	0.46	3.89
Interaction	4.80E-06	2	2.4E-06	0.32	0.74	3.89
Within	9.13E-05	12	7.61E-06			
Total	11.30E-05	17				

Chapter 5: Conclusion and Recommendations

Smart drug delivery systems (DDS) are a promising alternative towards limiting the side effects of conventional chemotherapy. Although chemotherapy is a widely used approach for treating cancer, it is limited by its undesired side effects. Not only can smart DDS limit chemotherapy's side effects, it can also achieve better pharmacokinetics and controlled drug-release at the tumor site. Smart DDS can effectively protect healthy cells by actively accumulating at the tumor sites only. Smart DDS must also be biocompatible, biodegradable, resist opsonization, and retain their encapsulated content until triggered at the desired time and location. The smart DDS was developed in this study to satisfy all the above. A model drug, calcein, was encapsulated in a smart DDS nanocarrier, which is the liposome. These nano-vehicles were surface-treated to make them stealthy and were modified with RGD sequences to allow targeting of specific RGD-motif overexpressing tumors.

This study on liposomes was comprehensive regarding synthesis, encapsulation, characterization, response to sonication, and kinetic modeling. NH_2 liposomes (control) were used to compare the effects of RGD surface modification on the properties and behavior of the liposomes (RGD liposomes). Dynamic Light Sizing revealed both liposomes types to be Uni-Lamellar Vesicles (ULVs) possessing a uniform size distribution, with RGD liposomes having slightly larger radii. The DLS measurements yielded 88.26 ± 5.55 nm and 79.52 ± 4.81 nm for NH_2 and RGD liposomes, respectively. The concentrations of the liposome batches were successfully calculated using a phospholipid-quantification method (Stewart Assay), yielding 15-20 $\frac{mg\ DPPC}{ml}$ and 5-7 $\frac{mg\ DPPC}{ml}$ for NH_2 and RGD liposomes respectively. A protein-quantification method (the BCA Assay) successfully verified the attachment of the RGD sequence to the surface of the liposomes. The drug release of the liposomes was examined by monitoring the increase in fluorescence upon sonication with a 20-kHz US-probe at three power densities, 7.46, 9.85, and 17.31 mW/cm^2. The power density of the ultrasound and the release rate of the encapsulated content were directly proportional. Acoustic cavitation was found to be the dominant phenomenon responsible for the release of the model drug from the liposomes, confirmed by the online release profile and mechanical index (MI) measurements. Modeling the release kinetics concluded that the release of calcein from both types of liposomes upon sonication follows both

Korsmeyer-Peppas and Weibull kinetics models. The suggested drug-release mechanisms upon sonication for both models are both diffusion and dissolution-driven. Statistical analysis showed that the release rate constants were significantly affected by changes in power densities and the type of carrier. The calculated average release rate constants were $K_{KP} = 5.7291$ $(s^{-1.0789})$ and $K_W = 5.3734$ for NH_2 liposomes, and $K_{KP} = 9.3574$ $(s^{-0.9441})$ and $K_W = 6.2857$ for RGD liposomes.

This comprehensive study opens doors to various opportunities for future enhancement and improvement. In this study, ultrasound's ability to release the encapsulated contents from targeted-liposomes in a controlled manner, as well as its synergistic effects with active-targeting, was successfully confirmed. Future work must examine the ease of attachment and compatibility of different types of RGD motifs (linear and cyclic) with the liposomes. Examining the targeting efficiency of these motifs with RGD-positive cell lines is currently under investigation. Studying the interaction between RGD and phospholipids could help in further improving the stability and the sono-sensitivity of the liposomes. Additionally, optimization of the ultrasound's parameters to induce release from liposomes is a highly prized topic. Ultrasound parameters to be optimized include the power density, frequency, the safety limits of exposure time and dose on the body, pulsed versus continuous operation, and temperature effects. Specifically, high-frequency ultrasound is of a profound interest since it widely used in medical applications. Statistical methods could also be introduced to improve existing kinetics models or to implement new, better-fitting models.

References

[1] N. Mohammad. "Acoustically activated release of estrone-targeted liposomes used for breast cancer treatment." M.S. Thesis, American University of Sharjah, United Arab Emirates, 2016.

[2] C. Momah, "RGD Project Report," ed. Ultrasound in Cancer Research Group, American University of Sharjah, United Arab Emirates, 2015, pp. 13.

[3] V. Torchilin and V. Weissig, *Liposomes; A Practical Approach*, 2nd ed. (no. 264). Oxford University Press, 2003, pp. 396.

[4] J. S. Dua, A. C. Rana, and A. K. Bhandari, "Liposome: Methods of Preparation and Applications," *Int. J. Pharm. Stud. Res.,* vol. 3, no. 2, pp. 14-20, 2012.

[5] S. Hardinger. "Illustrated Glossary of Organic Chemistry." Internet: http://www.chem.ucla.edu/~harding/IGOC/D/doxorubicin.html, 2017. [Feb. 11, 2018].

[6] "Calcein, AM, Cell-Permanent Dye," Internet: https://www.thermofisher.com/order/catalog/product/C3100MP, 2017, pp. 1-8. [Apr. 10, 2018].

[7] D. Bitounis, R. Fanciullino, A. Illiadis, and J. Ciccolini, "Optimizing Druggability through Liposomal Formulations: New Approaches to an Old Concept," vol. 2012, ed: International Scholarly Research Network Pharmaceutics, 2012, p. 11.

[8] M. L. Immordino, F. Dosio, and L. Cattel, "Stealth liposomes: review of the basic science, rationale, and clinical applications, existing and potential," *International Journal of Nanomedicine,* vol. 1, no. 3, pp. 297-315, 2006.

[9] M. W. Klymkowsky. "Cell adhesion." Internet: http://www.accessscience.com/content/cell-adhesion/117900, 2016. [Feb. 5, 2017].

[10] E. Ruoslahti and J. Reed, "Cell adhesion: New way to activate caspases," *Nature,* vol. 397, no. 6719, pp. 479-480, 1999.

[11] W. G. Pitt, G. A. Husseini, and B. J. Staples, "Ultrasonic Drug Delivery – A General Review," *Expert opinion on drug delivery,* vol. 1, no. 1, pp. 37-56, 2004.

[12] S. P. Hammar. "Cancer." Internet: http://www.accessscience.com/content/cancer/105800, 2016. [Feb. 6, 2017].

[13] D. L. Longo. "Oncology." Internet: http://www.accessscience.com/content/oncology/469000, 2016. [Feb. 6, 2017].

[14] M. Cole. "Oncogenes." Internet: http://www.accessscience.com/content/oncogenes/468950, 2014. [Feb. 6, 2017].

[15] C. P. Burns and D. A. Vaena, "Chemotherapy and other antineoplastic drug treatments." Internet: https://www.accessscience.com/content/chemotherapy-and-other-antineoplastic-drug-treatments/128900, 2016. [Feb. 6, 2017].

[16] H. W. Bruckner and P. J. O'Dwyer. (1987, Jan. 23-26)."Development of folates and folic acid antagonists in cancer chemotherapy." (5th edition). [On-line]. 87(2901). Available: https://catalogue.nla.gov.au/Record/1805958, [Feb. 6, 2017].

[17] R. Sultana *et al.*, "Doxorubicin-Induced Thymus Senescence," *Journal of Proteome Research,* vol. 9, no. 12, pp. 6232-6241,2010.

[18] J. Cummings, L. Anderson, N. Willmott, and J. F. Smyth, "The molecular pharmacology of doxorubicin in vivo," *European Journal of Cancer and Clinical Oncology,* vol. 27, no. 5, pp. 532-535,1991.

[19] J. Cummings, L. Anderson, N. Willmott, and J. F. Smyth, "The molecular pharmacology of doxorubicin in vivo," *Eur. J. Cancer,* vol. 27, no. 5, pp. 532, 1991.

[20] K. K. Karukstis, E. H. Z. Thompson, J. A. Whiles, and R. J. Rosenfeld, "Deciphering the fluorescence signature of daunomycin and doxorubicin," *Biophysical Chemistry,* vol. 73, no. 3, pp. 249-263,1998.

[21] P. Kawak, "Ultrasound Triggered Release of Estrone-Targeted Liposomes." M.S. Thesis, American University of Sharjah, United Arab Emirates, 2017.

[22] T. M. Allen and L. G. Cleland, "Serum-induced leakage of liposome contents," *Biochimica et Biophysica Acta (BBA) - Biomembranes,* vol. 597, no. 2, pp. 418-426, 1980.

[23] H. Patel, C. Tscheka, and H. Heerklotz, "Characterizing Vesicle Leakage By Fluorescence Lifetime Measurements," *Biophysical Journal,* vol. 98, no. 3, Supplement 1, pp. 80a, 2010.

[24] G. Chen, Z. Jiang, M. Yoshimoto, and Y. Wei, "Electric impedance method for evaluation of the release property of calcein-encapsulated liposomes," *Colloids and Surfaces B: Biointerfaces,* vol. 74, no. 1, pp. 32-36, 2009.

[25] W. M. Saltzman and V. P. Torchilin. "Drug delivery systems." Internet: http://www.accessscience.com/content/drug-delivery-systems/757275, 2014. [Jan. 24, 2017].

[26] R. C. MacDonald. "Liposomes." Internet: https://www.accessscience.com/content/liposomes/385650, 2014. [Jan. 24, 2017].

[27] N. Monteiro, A. Martins, R. L. Reis, and N. M. Neves, "Liposomes in tissue engineering and regenerative medicine," *Journal of the Royal Society, Interface,* vol. 11, no. 101, pp. 4-59, 2014.

[28] G. A. Husseini, W. G. Pitt, and A. M. Martins, "Ultrasonically triggered drug delivery: Breaking the barrier," *Colloids and Surfaces B: Biointerfaces,* vol. 123, pp. 364-386, 2014.

[29] A. Porfire, I. Tomuta, L. Tefas, S. E. Leucuta, and M. Achim, "Simultaneous quantification of l-α-phosphatidylcholine and cholesterol in liposomes using near infrared spectrometry and chemometry," *Journal of pharmaceutical and biomedical analysis,* vol. 63, pp. 87-94, 2012.

[30] K. W. Ferrara, "Driving delivery vehicles with ultrasound," *Advanced Drug Delivery Reviews,* vol. 60, no. 10, pp. 1097-1102, 2008.

[31] A. Akbarzadeh *et al.*, "Liposome: classification, preparation, and applications," *Nanoscale Research Letters,* vol. 8, no. 1, pp. 102-102, 2013.

[32] P. R. Cullis, L. D. Mayer, M. B. Bally, T. D. Madden, and M. J. Hope, "Generating and loading of liposomal systems for drug-delivery applications," *Advanced Drug Delivery Reviews,* vol. 3, no. 3, pp. 267-282, 1989.

[33] S. Stewart and K. Harrington, "The Biodistribution and Pharmacokinetics of Stealth Liposomes in Patients with Solid Tumors," *Oncology,* vol. 11, no. 10, pp. 33-37, 1997.

[34] X. Wang, T. Ishida, and H. Kiwada, "Anti-PEG IgM elicited by injection of liposomes is involved in the enhanced blood clearance of a subsequent dose of PEGylated liposomes," *Journal of Controlled Release,* vol. 119, no. 2, pp. 236-244, 2007.

[35] T. Ishida and H. Kiwada, "Accelerated blood clearance (ABC) phenomenon upon repeated injection of PEGylated liposomes," *International Journal of Pharmaceutics,* vol. 354, no. 1–2, pp. 56-62, 2008.

[36] X. Y. Wang, T. Ishida, M. Ichihara, and H. Kiwada, "Influence of the physicochemical properties of liposomes on the accelerated blood clearance phenomenon in rats," *Journal of Controlled Release,* vol. 104, no. 1, pp. 91-102, 2005.

[37] S. Cressman, Y. Sun, J. Maxwell, N. Fang, D. D. Y. Chen, and P. R. Cullis, "Binding and Uptake of RGD-Containing Ligands to Cellular alpha(v)beta(3) Integrins," *Int. J. Pept. Res. Ther.,* vol. 15, pp. 49-59, 2009.

[38] M. Willis and E. Forssen, "Ligand-targeted liposomes," *Adv. Drug Deliv. Rev.,* vol. 29, no. 3, pp. 249-271, 1998.

[39] V. P. Torchilin, *Multifunctional Pharmaceutical Nanocarriers*. New York: Springer Science & Business Media, 2008, pp. 1532-55.

[40] "Integrins," in *McGraw-Hill Dictionary of Scientific and Technical Terms*, 6th ed. New York: McGraw-Hill Education, 2003.

[41] M. W. Klymkowsky. "Cell adhesion." Internet: http://www.accessscience.com/content/cell-adhesion/117900, 2016. [Apr. 16, 2017].

[42] E. Ruoslahti, "RGD and other recognition sequences for integrins," *Annu. Rev. Cell Dev. Biol.,* vol. 12, pp. 697-715, 1996.

[43] S. L. Bellis, "Advantages of RGD peptides for directing cell association with biomaterials," *Biomaterials,* vol. 32, no. 18, pp. 4205-4210, 2011.

[44] A. Orlando Robert, "Arginine-glycine-aspartic acid binding leading to molecular stabilization between integrin alpha;subv/subbeta;sub3/sub and its ligand," (in eng), *Journal of Biological Chemistry,* vol. 266, no. 29, pp. 19543-19550, 1991.

[45] D. Ensminger and L. J. Bond, *Ultrasonics: Fundamentals, Technologies, and Applications*, 3rd ed. New York: CRC Press, 2011.

[46] A. Schroeder, J. Kost, and Y. Barenholz, "Ultrasound, liposomes, and drug delivery: principles for using ultrasound to control the release of drugs from liposomes," *Chemistry and Physics of Lipids,* vol. 162, no. 1–2, pp. 1-16, 2009.

[47] S. N. Sen, *Accoustics, Waves, and Oscillations*. New Delhi: New Age International, 1990.

[48] A. M. Moussa Hg Fau - Martins, G. A. Martins Am Fau - Husseini, and G. A. Husseini, "Review on triggered liposomal drug delivery with a focus on ultrasound," *Curr. Cancer Drug Targets,* vol. 2, 2015.

[49] J. R. Lattin, W. G. Pitt, D. M. Belnap, and G. A. Husseini, "Ultrasound-Induced Calcein Release From eLiposomes," *Ultrasound in Medicine & Biology,* vol. 38, no. 12, pp. 2163-2173, 2012.

[50] G. A. Husseini, M. A. Diaz de la Rosa, E. S. Richardson, D. A. Christensen, and W. G. Pitt, "The role of cavitation in acoustically activated drug delivery," *Journal of Controlled Release,* vol. 107, no. 2, pp. 253-261, 2005.

[51] H. G. Flynn, "Physics of Acoustic Cavitation," *J. Acoust. Soc. Am.,* vol. 31, no. 11, pp. 1582, 1964.

[52] M. Margulis, *Sonochemistry/Cavitation*. Amsterdam: Gordon and Breach Science, 1995, pp. 311.

[53] T. Leighton, *The Acoustic Bubble*. Academic Press, 1994, pp. 312.

[54] W. B. McNamara, Y. T. Didenko, and K. S. Suslick, "Sonoluminescence temperatures during multi-bubble cavitation," *Nature,* vol. 401, no. 6755, pp. 772-775, 1999.

[55] A. E. Catania, A. Ferrari, M. Manno, and E. Spessa, "A Comprehensive Thermodynamic Approach to Acoustic Cavitation Simulation in High-Pressure Injection Systems by a Conservative Homogeneous Two-Phase Barotropic Flow Model," *Journal of Engineering for Gas Turbines and Power,* vol. 128, no. 2, pp. 434-445, 2005.

[56] M. Keswani, S. Raghavan, and P. Deymier, "Characterization of transient cavitation in gas sparged solutions exposed to megasonic field using cyclic voltammetry," *Microelectronic Engineering,* vol. 102, pp. 91-97, 2013.

[57] R. Weeks, "Introduction to Dynamic Light Scattering and Phase Analysis Light Scattering," W. T. Corp., Ed., ed: Wyatt Technology Corp., 2014.

[58] "How Dynamic Light Scattering Works." Internet: http://www.lightintegra.com/how-dls-works/, 2017. [Mar. 20, 2018].

[59] "DynaPro NanoStar." Internet: https://www.wyatt.com/products/instruments/dynapro-nanostar-dynamic-light-scattering-detector.html, 2014. [Mar. 20, 2018].

[60] "Dynamic Light Scattering Data Interpretation," W. T. Corp., Ed., ed: Wyatt Technology Corp., 2014.

[61] J. C. M. Stewart, "Colorimetric determination of phospholipids with ammonium ferrothiocyanate," *Analytical Biochemistry,* vol. 104, no. 1, pp. 10-14, 1980.

[62] "Product Information: QuantiPro™ BCA Assay Kit," Internet: https://www.sigmaaldrich.com/content/dam/sigma-aldrich/docs/Sigma/Bulletin/qpbcabul.pdf, 2011. [June. 11, 2017].

[63] "PTI QuantaMaster 300." Internet: http://www.horiba.com/scientific/products/fluorescence-spectroscopy/steady-state/pti-quantamaster-family/pti-quantamaster-300/, 2018. [Mar. 20, 2018].

[64] "VCX 130 PB / VCX 130 FSJ: Ultrasonic Processors for Small Volume Applications." Internet: https://www.sonics.com/liquid-processing/products/vibra-cell-processors/vcx-130-pb-vcx-130-fsj/, 2018. [Mar. 20, 2018].

[65] S. Ahmed, "Dynamics of Chemotherapeutic Drug Release from Liposomes using Low-Frequency Ultrasound," M.S. Thesis, American University of Sharjah, United Arab Emirates, 2015.

[66] H. Moussa, "Liposomal Drug Release Using Ultrasound and Modeling Release Dynamics for Model Predictive Controller Design," M.S. Thesis, American University of Sharjah, United Arab Emirates, 2015.

[67] R. Bogtrykheri. "Product Data: Hydrophones - Types 8103, 8104, 8105, 8106," B. Kjær, Ed., ed, 2006.

[68] R. Walker. "Mass, Weight, Density or Specific Gravity of water at various temperatures C and thermal coefficient of expansion of water." Internet: https://www.simetric.co.uk/si_water.htm, 2005. [Mar. 3, 2018].

[69] "Water - Speed of Sound." Internet: http://www.engineeringtoolbox.com/sound-speed-water-d_598.html, 2015. [Mar. 3, 2018].

[70] S. B. Stringham *et al.*, "Over-Pressure Suppresses Ultrasonic-Induced Drug Uptake," *Ultrasound in Medicine & Biology,* vol. 35, no. 3, pp. 409-415, 2009.

[71] B. J. Staples, G. A. Roeder Bl Fau - Husseini, O. Husseini Ga Fau - Badamjav, G. B. Badamjav O Fau - Schaalje, W. G. Schaalje Gb Fau - Pitt, and W. G. Pitt, "Role of frequency and mechanical index in ultrasonic-enhanced chemotherapy in rats," *Cancer Chemother. Pharmacol.,* vol. 64, no. 3, pp. 593-600, Jan. 2009.

[72] S. Dash, L. Murthy Pn Fau - Nath, P. Nath L Fau - Chowdhury, and P. Chowdhury, "Kinetic modeling on drug release from controlled drug delivery systems," (in eng), *Acta Poloniae Pharmaceutica - Drug Research,* vol. 67, no. 3, pp. 217-223, 2010.

[73]   T. Higuchi, "Rate of Release of Medicaments from Ointment Bases Containing Drugs in Suspension," *Journal of Pharmaceutical Sciences,* vol. 50, no. 10, pp. 874-875, 1961.

[74]   K. H. Ramteke, P. A. Dighe, A. R. Kharat, and S. V. Patil, "Mathemtical Models for Drug Dissolution: A Review," *Sch. Acad. J. Pharm.,* vol. 3, no. 5, pp. 388-396, 2014.

[75]   A. Schroeder *et al.*, "Controlling Liposomal Drug Release with Low Frequency Ultrasound: Mechanism and Feasibility," *Langmuir,* vol. 23, no. 7, pp. 4019-4025, 2007.
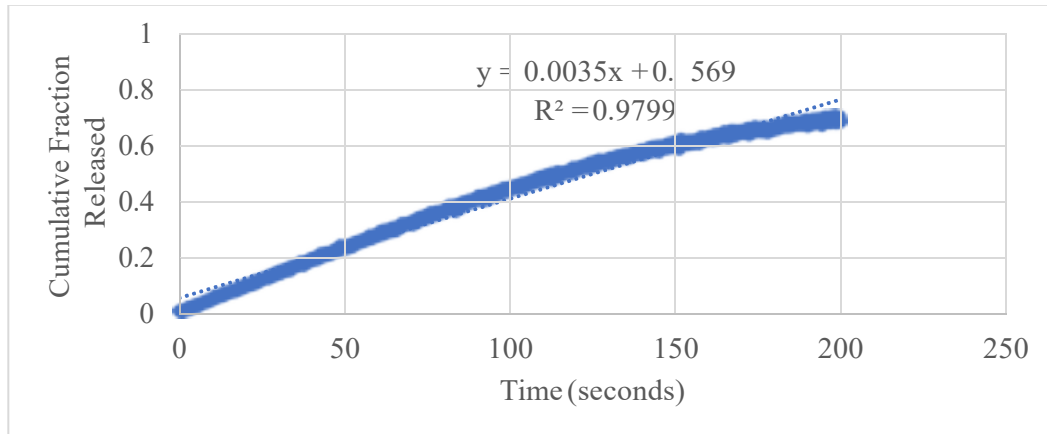
Figure 41: Zero-order model plot for NH₂ liposomes, batch #2, at 7.46 $(\frac{-}{c^2})$
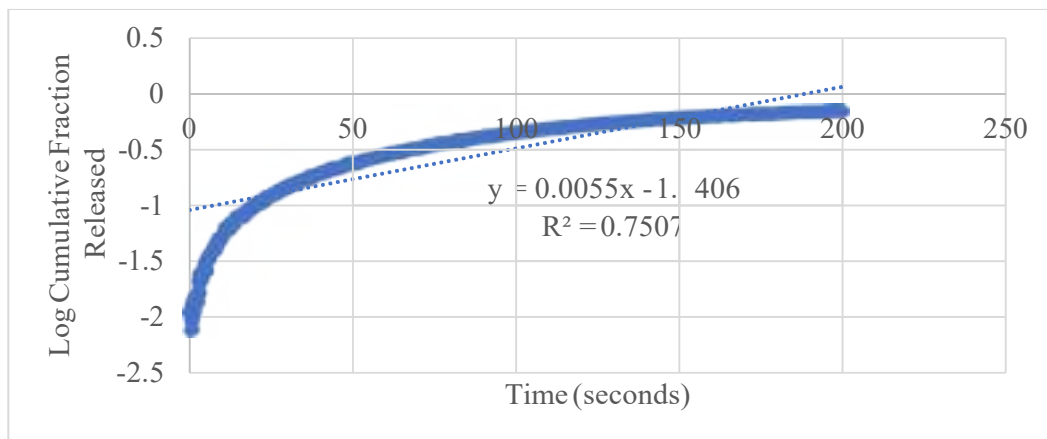
Figure 42: First-order model plot for NH₂ liposomes, batch #2, at 7.46 $(\frac{-}{c^2})$
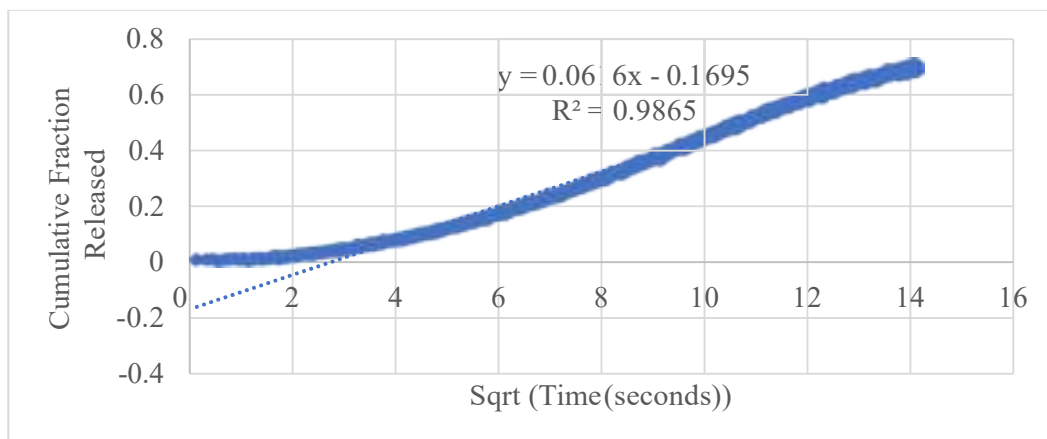
Figure 43: Higuchi model plot for NH₂ liposomes, batch #2, at 7.46 $(\frac{-}{c^2})$
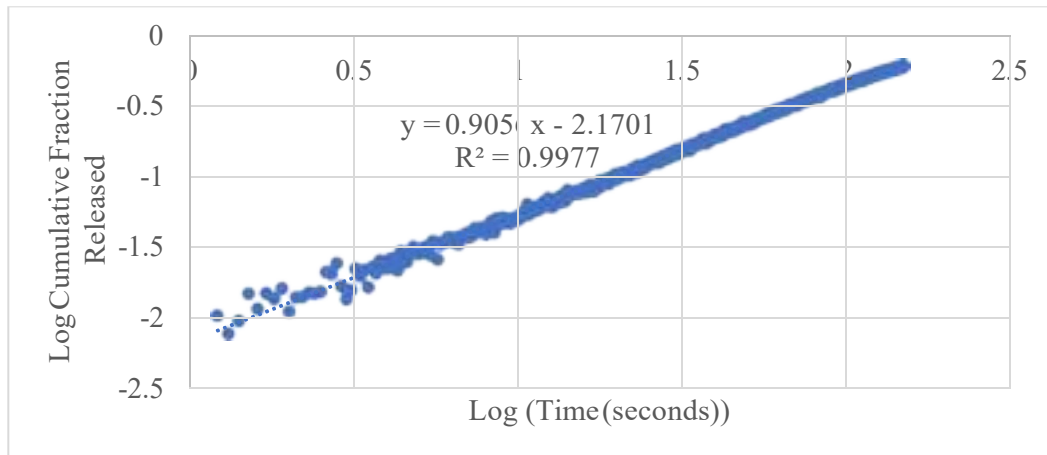
Figure 44: Korsmeyer-Peppas model plot for NH$_2$ liposomes, batch #2, at 7.46 $(\overline{c}^2)$
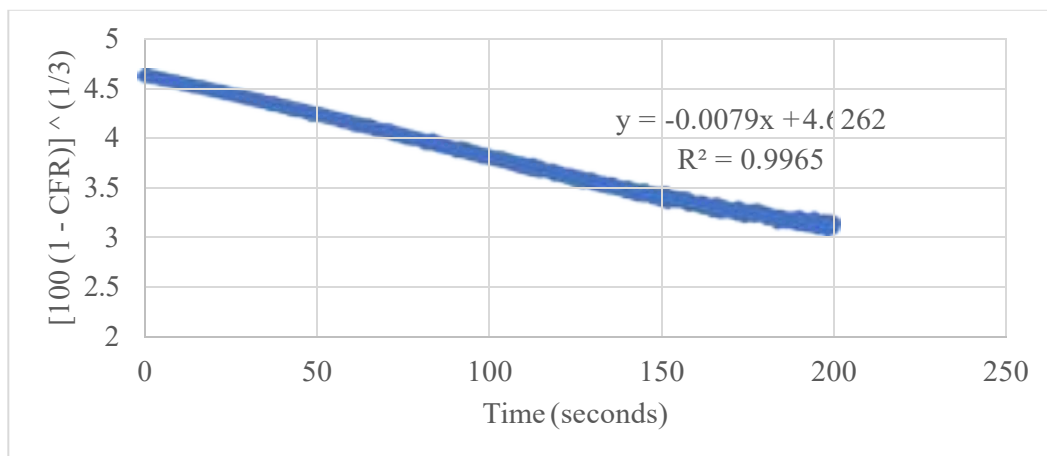
Figure 45: Hixson-Crowell model plot for NH$_2$ liposomes, batch #2, at 7.46 $(\frac{-}{c}^2)$
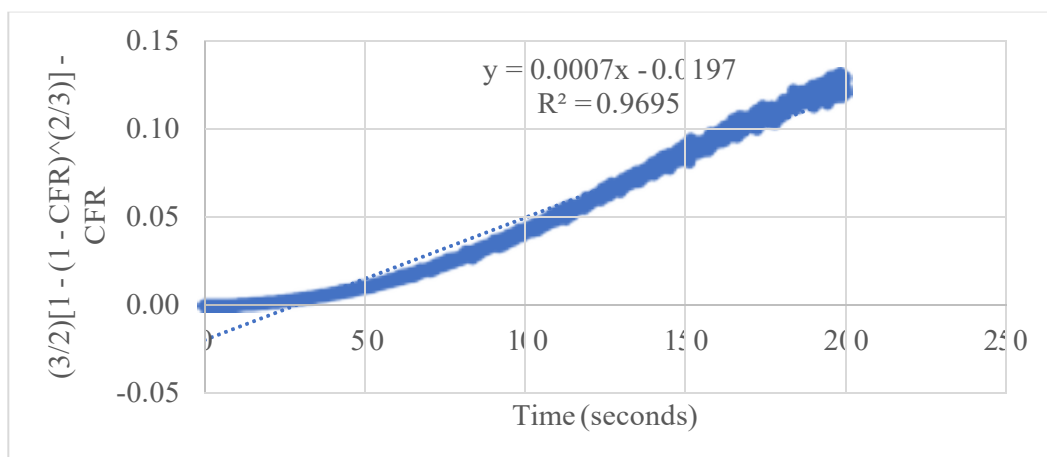
Figure 46: Baker-Lonsdale model plot for NH$_2$ liposomes, batch #2, at 7.46 $(\frac{}{c}^2)$
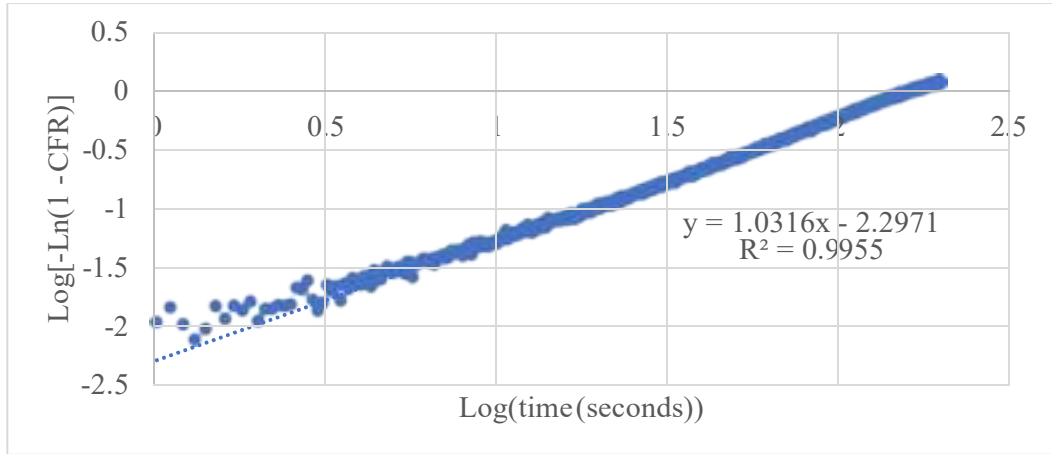
Figure 47: Weibull model plot for NH$_2$ liposomes, batch #2, at 7.46 $\left(\frac{-}{c^2}\right)$
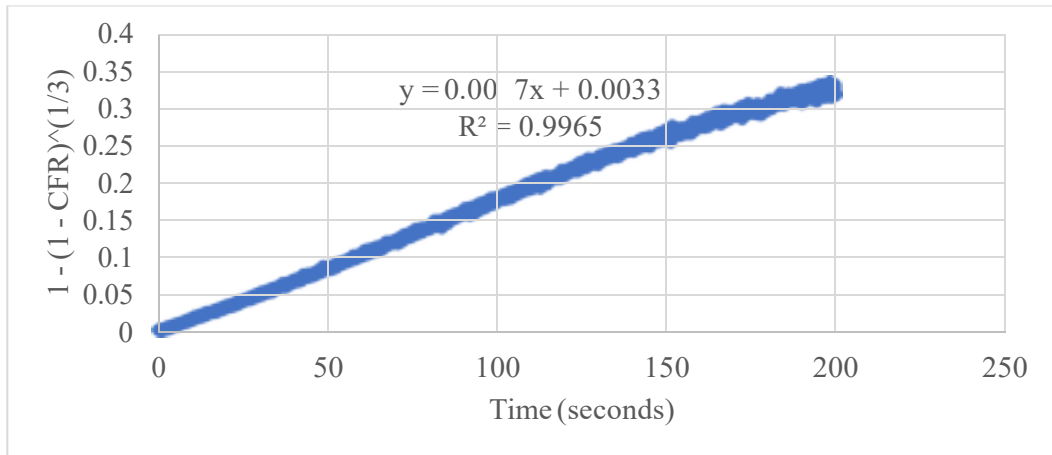
Figure 48: Hopfenberg model plot for NH$_2$ liposomes, batch #2, at 7.46 $\left(\frac{-}{c^2}\right)$
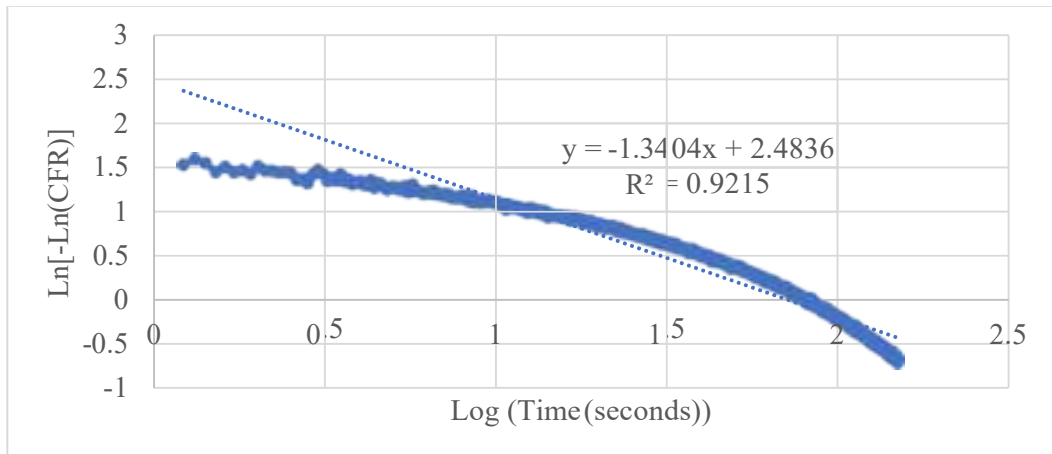
Figure 49: Gompertz model plot for NH$_2$ liposomes, batch #2, at 7.46 $\left(\frac{-}{c^2}\right)$

106

Appendix B: Plots of kinetics models fits for batch #3 of NH₂ liposomes at 7.46
$$\left(\frac{mW}{cm^2}\right)$$
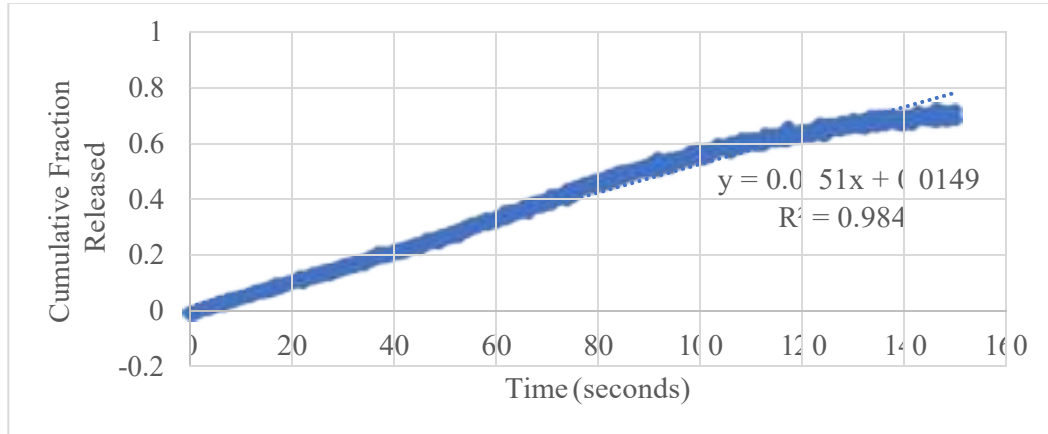
Figure 50: Zero-order model plot for NH₂ liposomes, batch #3, at 7.46 $\left(\frac{-}{c^2}\right)$
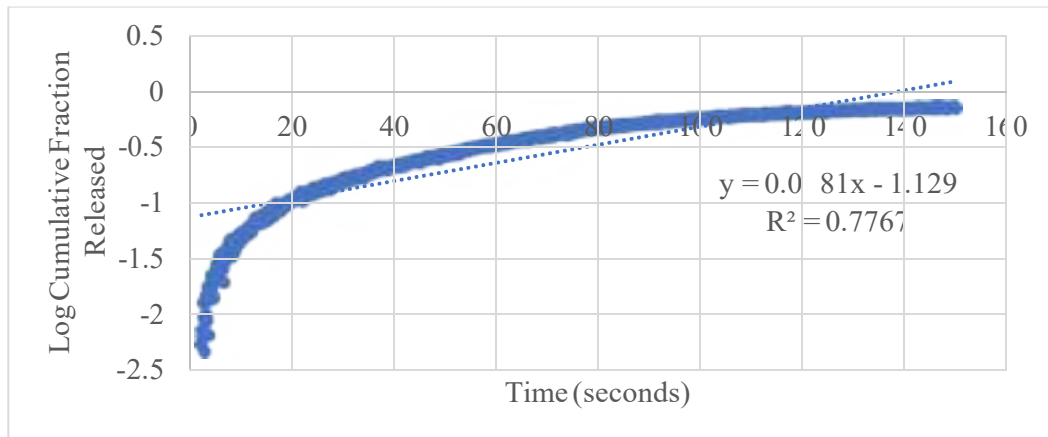
Figure 51: First-order model plot for NH₂ liposomes, batch #3, at 7.46 $\left(\frac{-}{c^2}\right)$
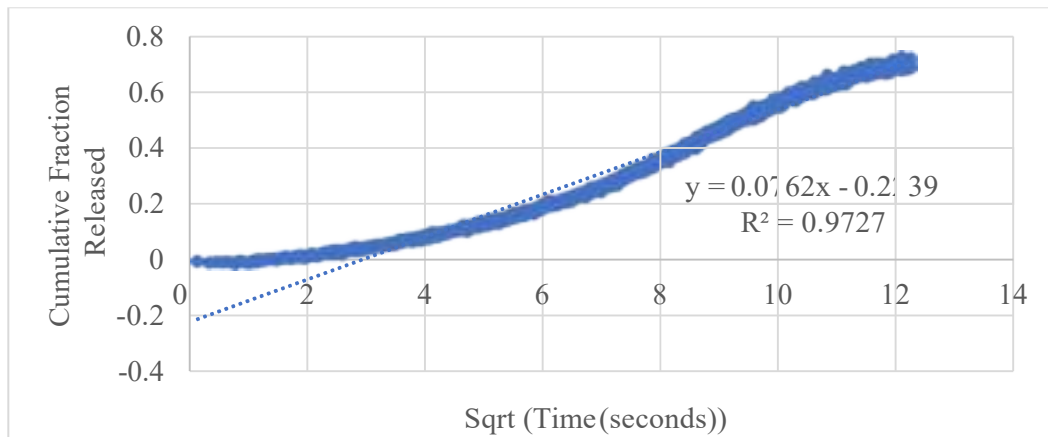
Figure 52: Higuchi model plot for NH₂ liposomes, batch #3, at 7.46 $\left(\frac{-}{c^2}\right)$
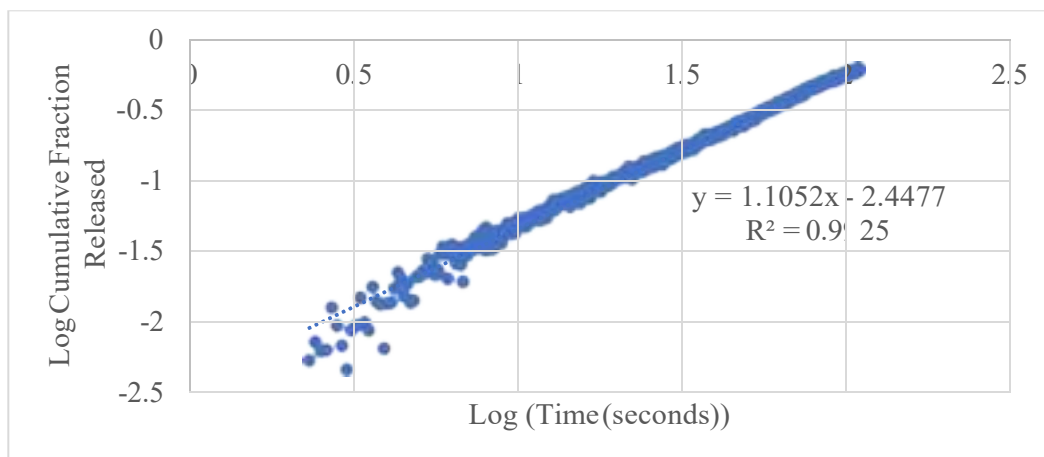
Figure 53: Korsmeyer-Peppas model plot for NH$_2$ liposomes, batch #3, at 7.46 $(\overline{c^2})$
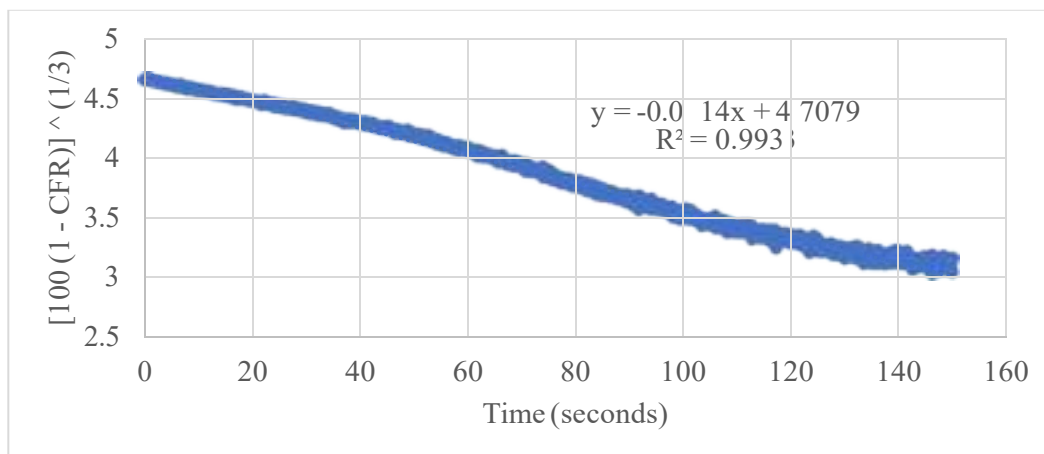
Figure 54: Hixson-Crowell model plot for NH$_2$ liposomes, batch #3, at 7.46 $(\frac{-}{c}^2)$
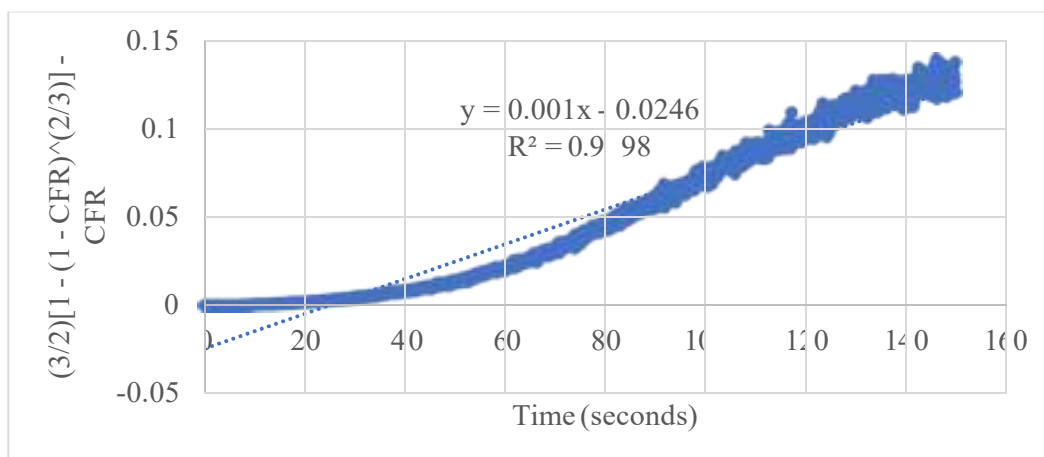
Figure 55: Baker-Lonsdale model plot for NH$_2$ liposomes, batch #3, at 7.46 $(\frac{}{c}^2)$

108
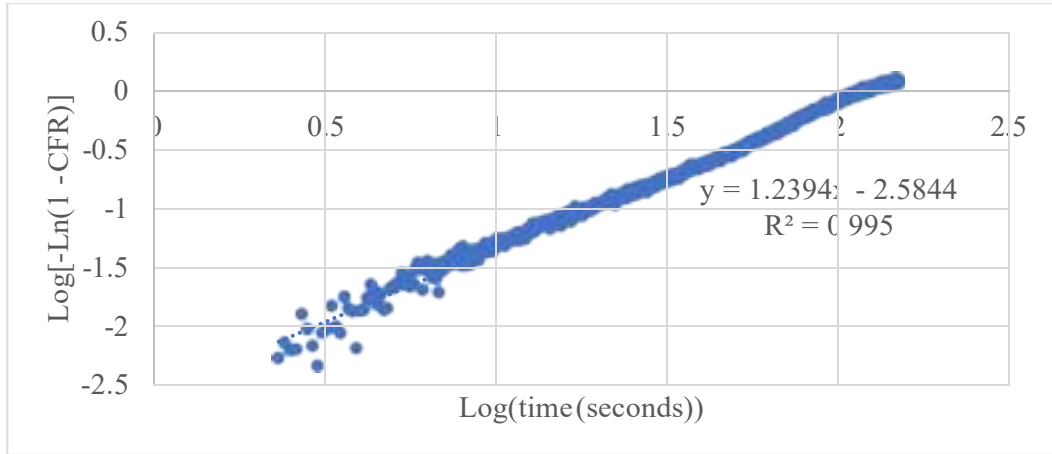
Figure 56: Weibull model plot for NH₂ liposomes, batch #3, at 7.46 $\left(\frac{-}{c^2}\right)$
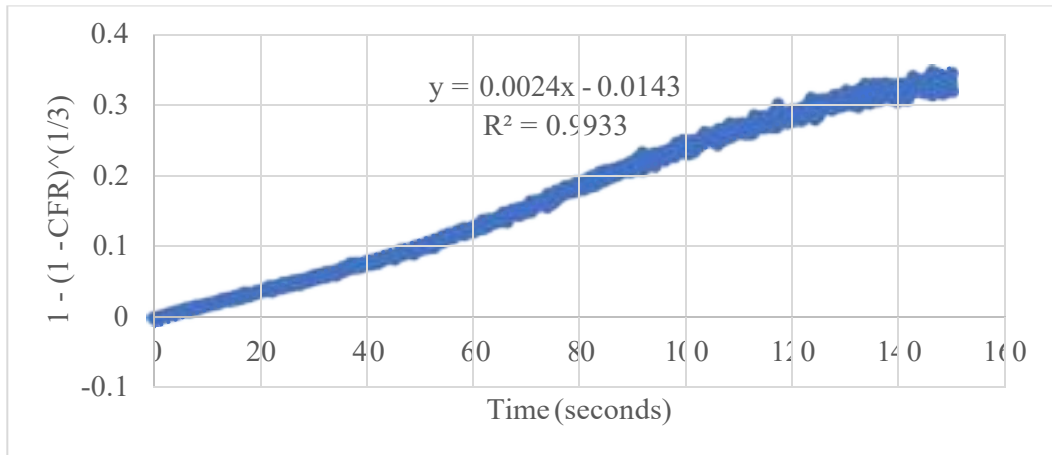
Figure 57: Hopfenberg model plot for NH₂ liposomes, batch #3, at 7.46 $\left(\frac{-}{c^2}\right)$
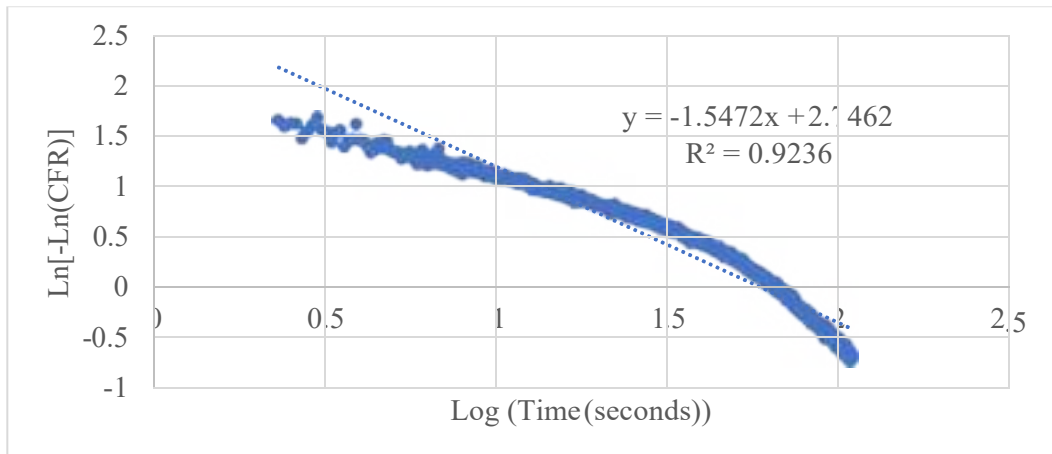

Figure 58: Gompertz model plot for NH₂ liposomes, batch #3, at 7.46 $\left(\frac{-}{c^2}\right)$

Appendix C: Plots of kinetics models fits for NH₂ liposomes, all batches, at 9.85

$$(\frac{mW}{cm^2})$$
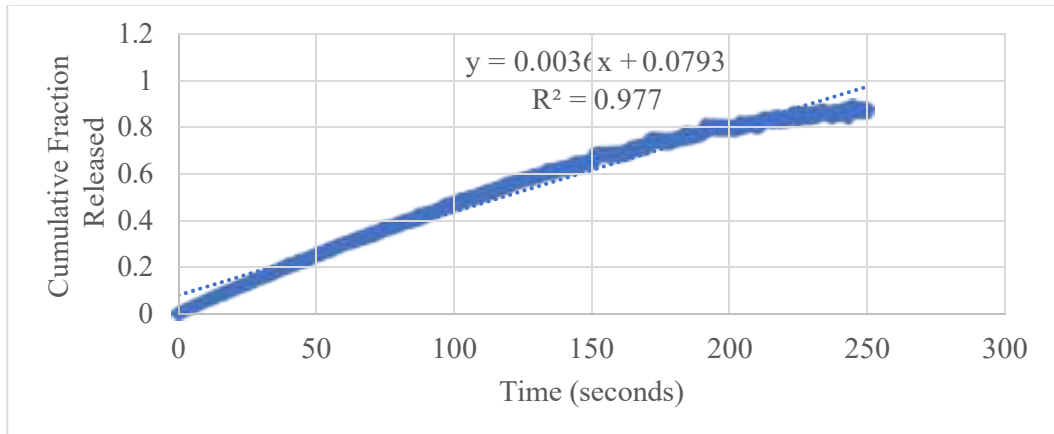
Figure 59: Zero-order model plot for NH₂ liposomes, batch #1, at 9.85 $(\frac{}{c^2})$
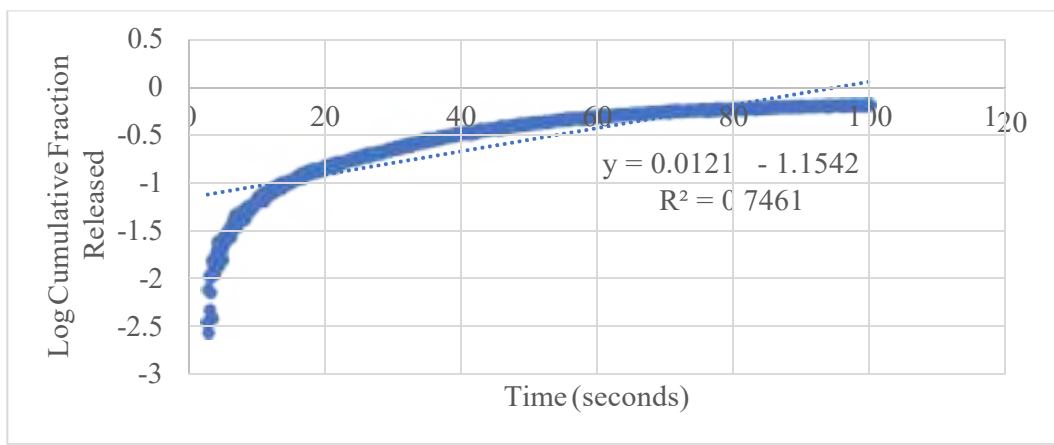
Figure 60: First-order model plot for NH₂ liposomes, batch #1, at 9.85 $(\frac{}{c^2})$
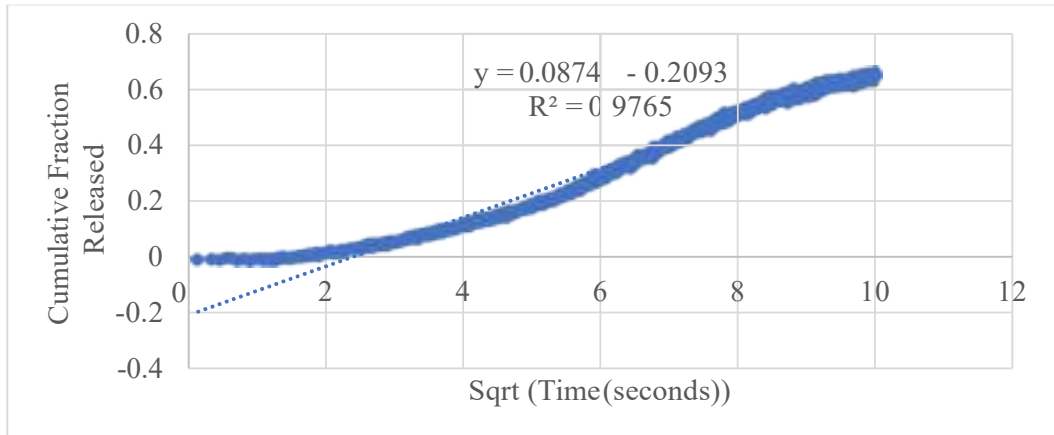
Figure 61: Higuchi model plot for NH₂ liposomes, batch #1, at 9.85 $(\frac{}{c^2})$
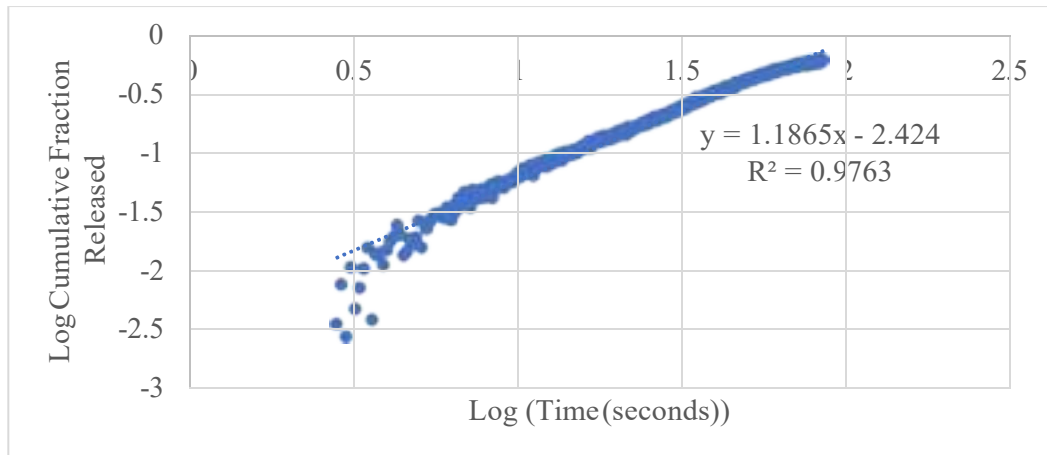
Figure 62: Korsmeyer-Peppas model plot for NH₂ liposomes, batch #1, at 9.85 $(\overline{c^2})$
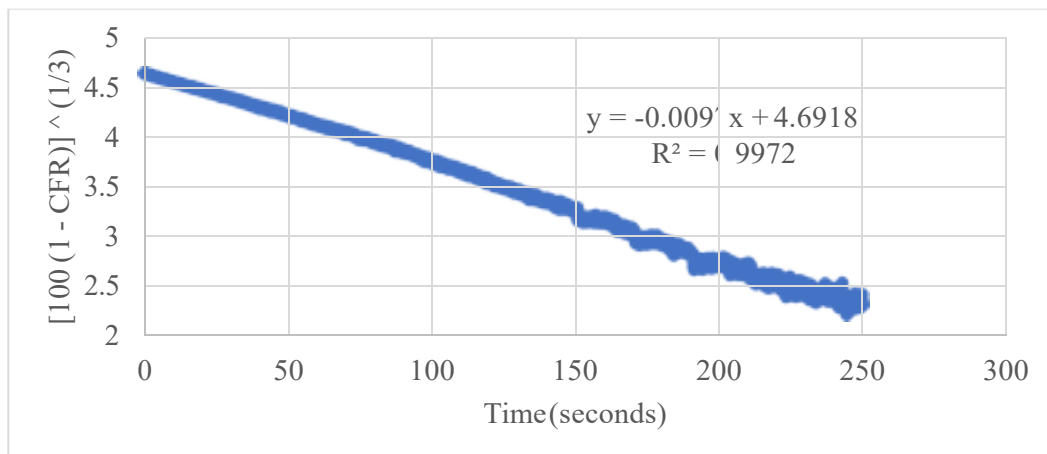
Figure 63: Hixson-Crowell model plot for NH₂ liposomes, batch #1, at 9.85 $(\frac{-}{c^2})$
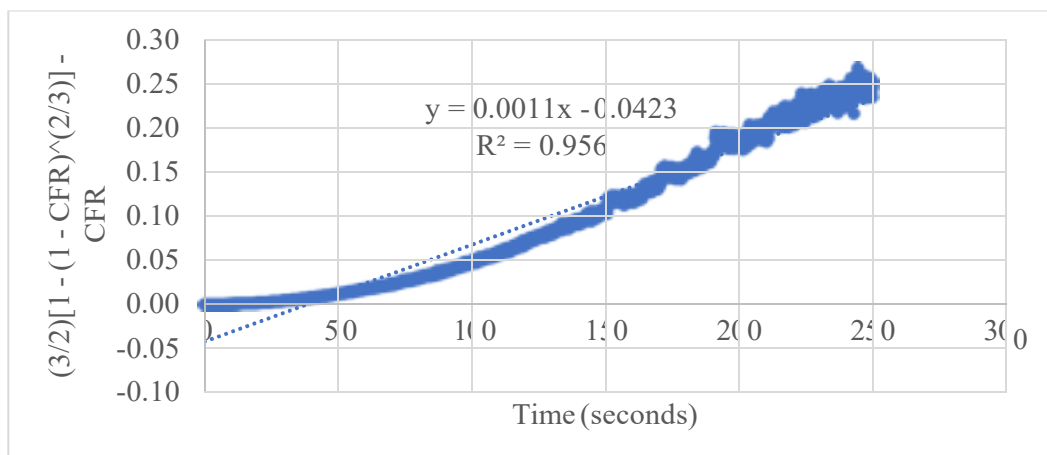
Figure 64: Baker-Lonsdale model plot for NH₂ liposomes, batch #1, at 9.85 $(\frac{()}{c^2})$

111
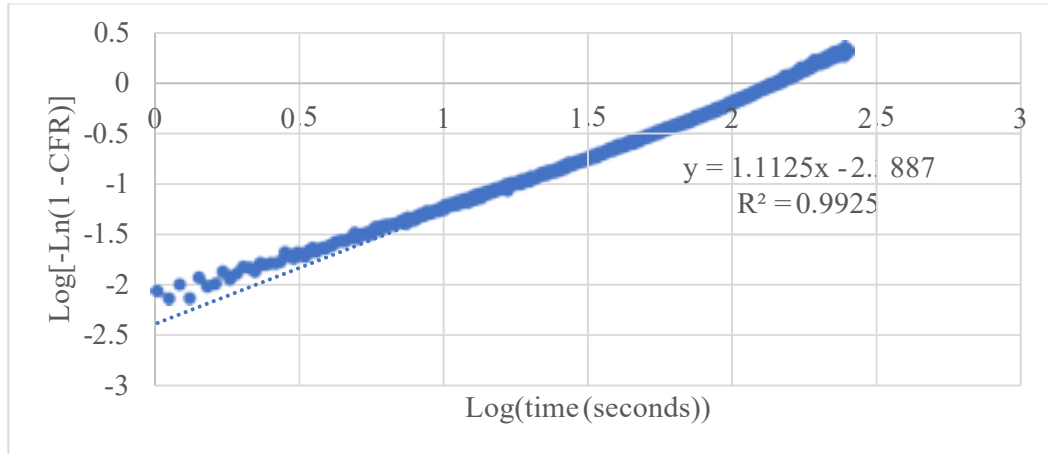
Figure 65: Weibull model plot for NH₂ liposomes, batch #1, at 9.85 $\left(\frac{-}{c^2}\right)$
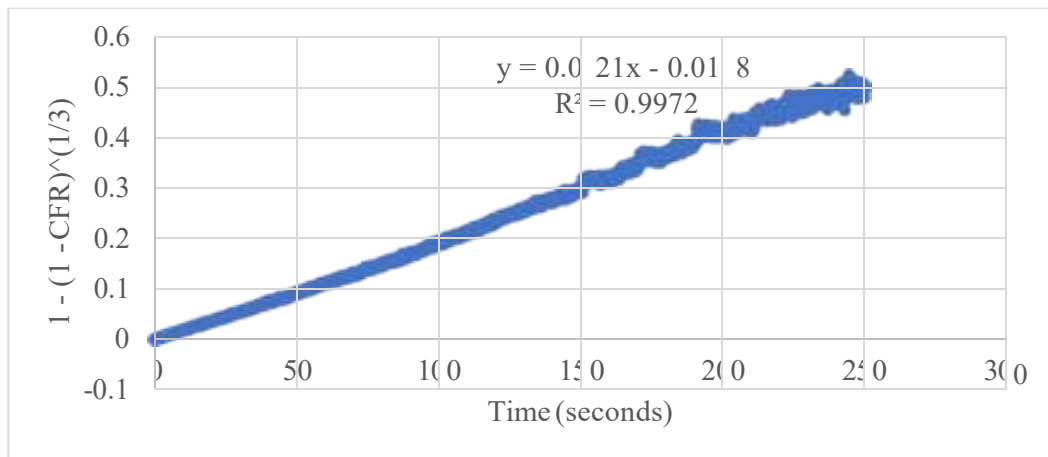
Figure 66: Hopfenberg model plot for NH₂ liposomes, batch #1, at 9.85 $\left(\frac{-}{c^2}\right)$
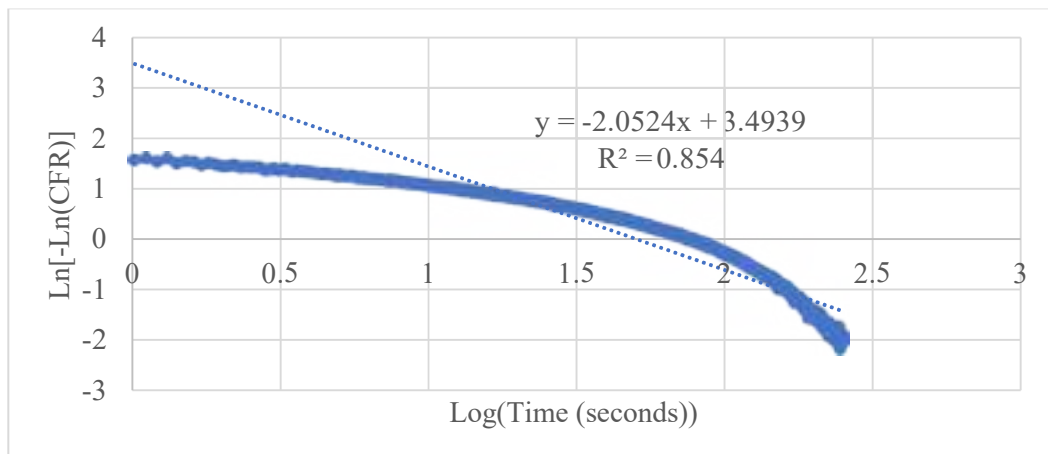
Figure 67: Gompertz model plot for NH₂ liposomes, batch #1, at 9.85 $\left(\frac{-}{c^2}\right)$
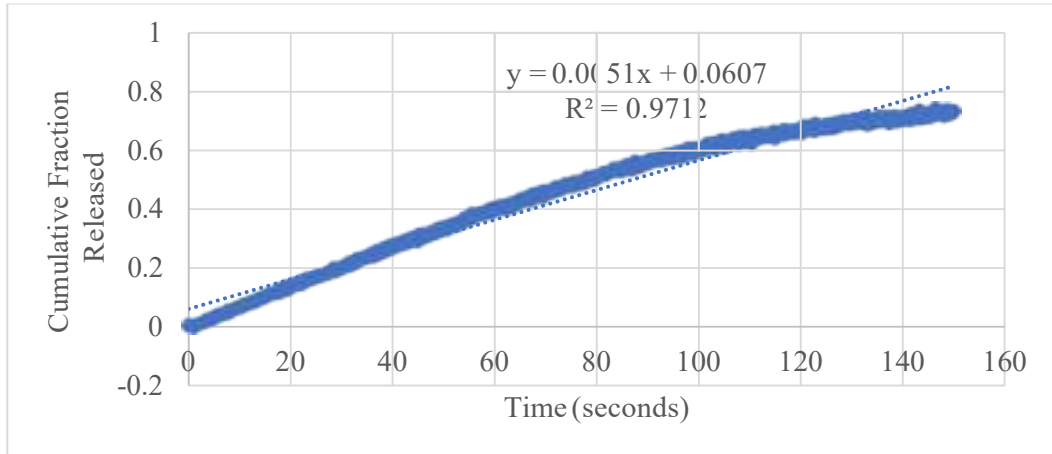
Figure 68: Zero-order model plot for NH$_2$ liposomes, batch #2, at 9.85 $\left(\dfrac{-}{c}\right)_2$
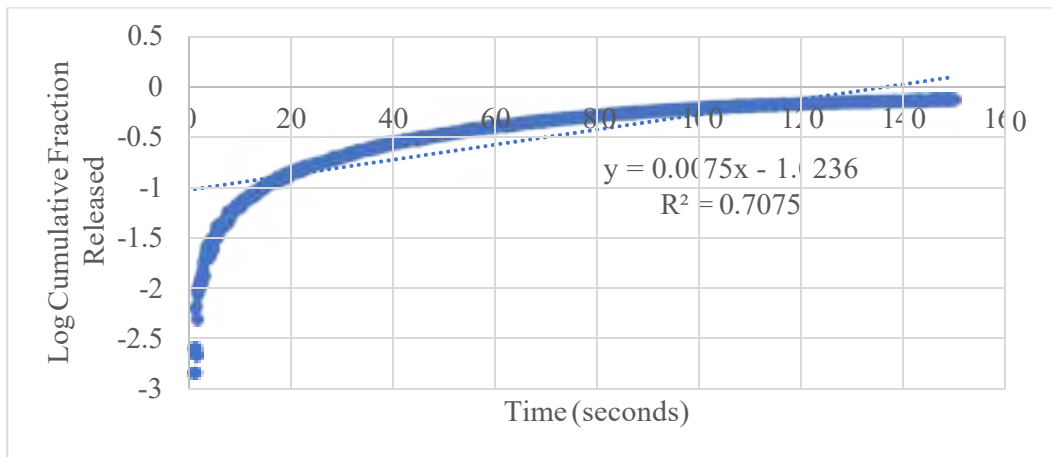
Figure 69: First-order model plot for NH$_2$ liposomes, batch #2, at 9.85 $\left(\dfrac{-}{c}\right)_2$
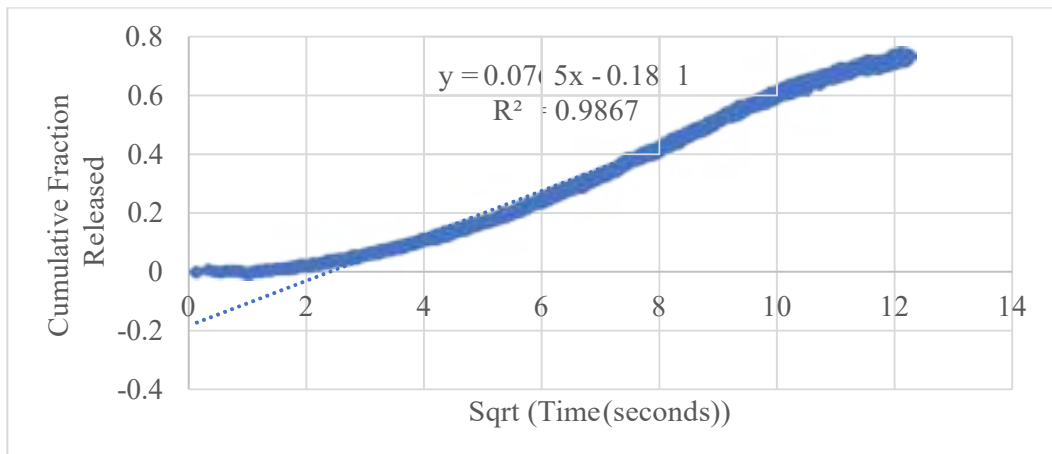
Figure 70: Higuchi model plot for NH$_2$ liposomes, batch #2, at 9.85 $\left(\dfrac{-}{c^2}\right)$

113
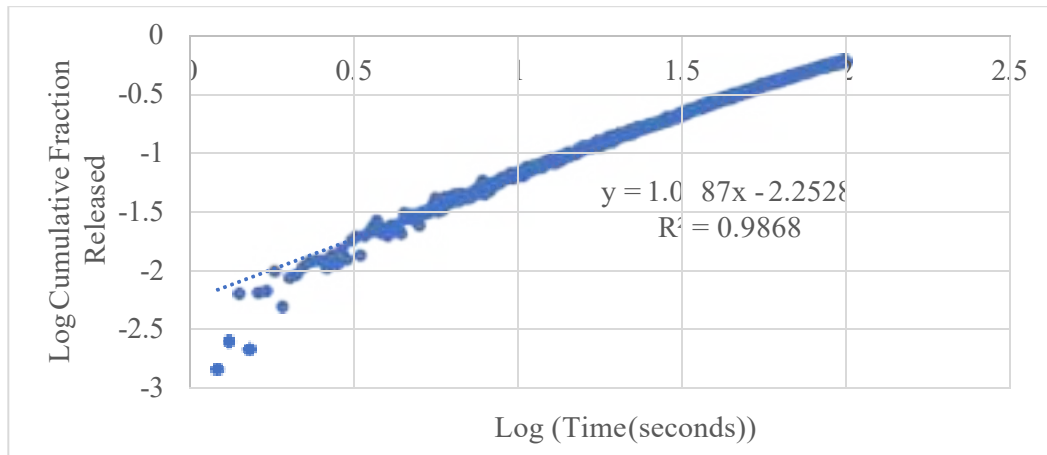
Figure 71: Korsmeyer-Peppas model plot for NH$_2$ liposomes, batch #2, at 9.85 $\left(\overline{c}^2\right)$
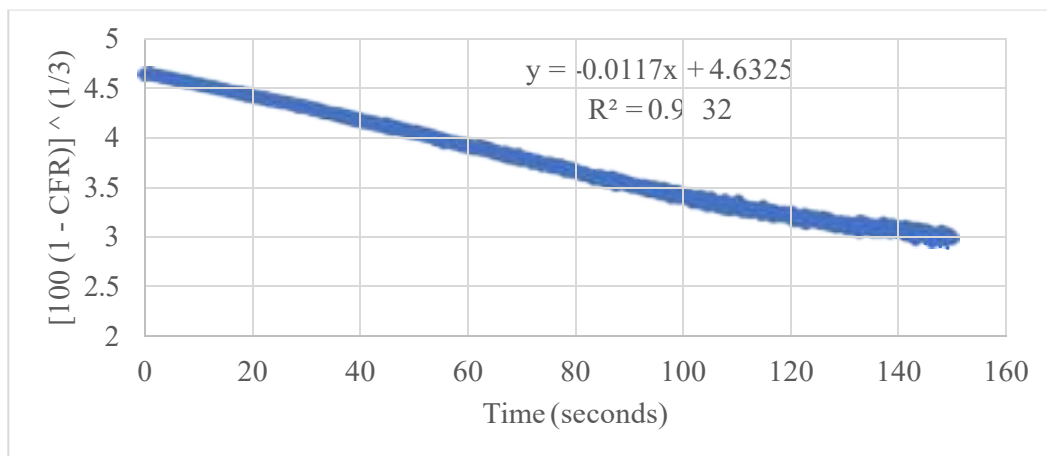
Figure 72: Hixson-Crowell model plot for NH$_2$ liposomes, batch #2, at 9.85 $\left(\dfrac{-}{c^2}\right)$
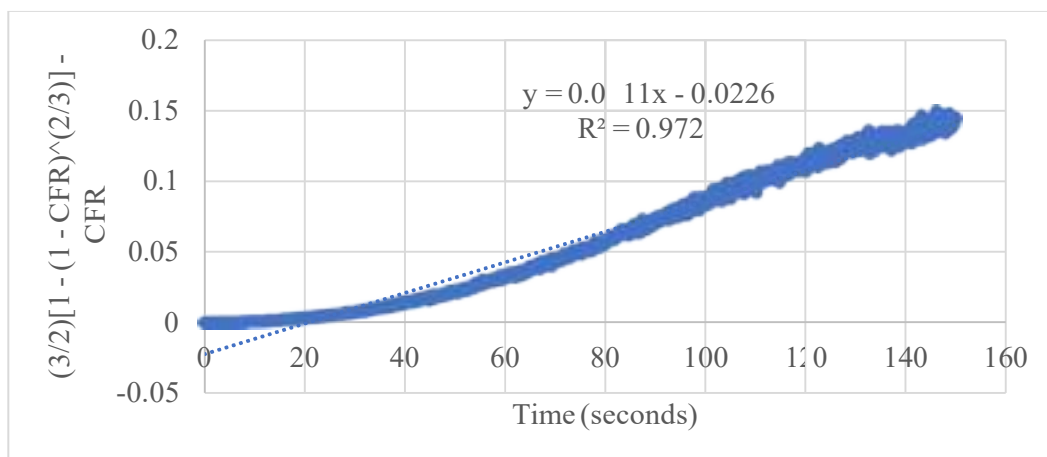
Figure 73: Baker-Lonsdale model plot for NH$_2$ liposomes, batch #2, at 9.85 $\left(\dfrac{-}{c^2}\right)$
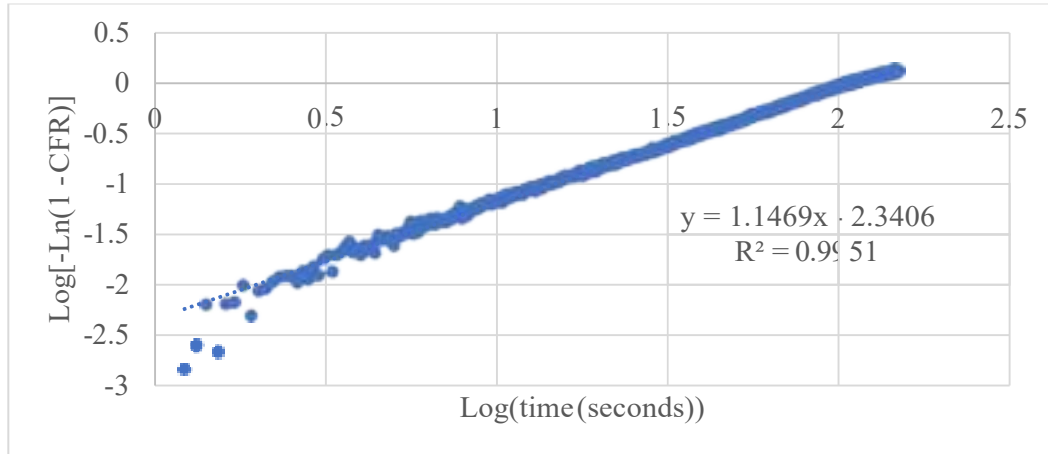
Figure 74: Weibull model plot for NH₂ liposomes, batch #2, at 9.85 $\left(\frac{-}{c^2}\right)$
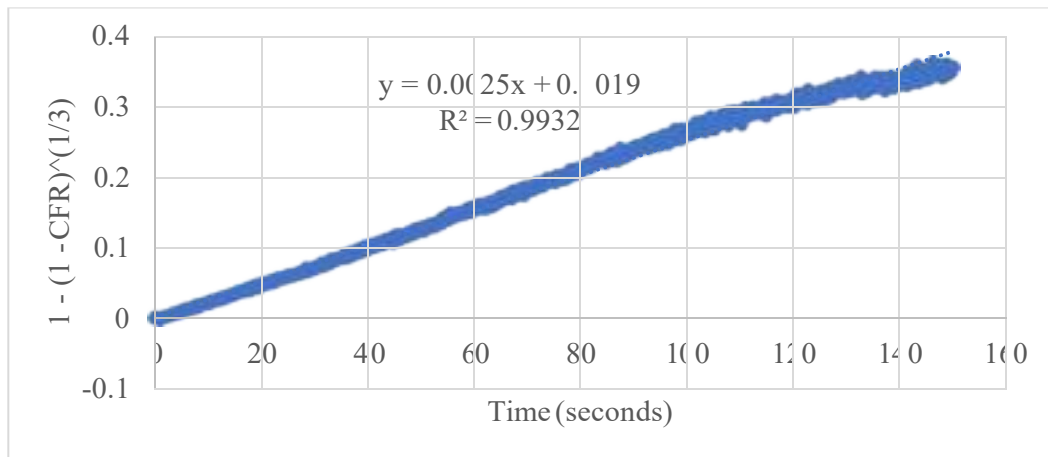
Figure 75: Hopfenberg model plot for NH₂ liposomes, batch #2, at 9.85 $\left(\frac{-}{c^2}\right)$
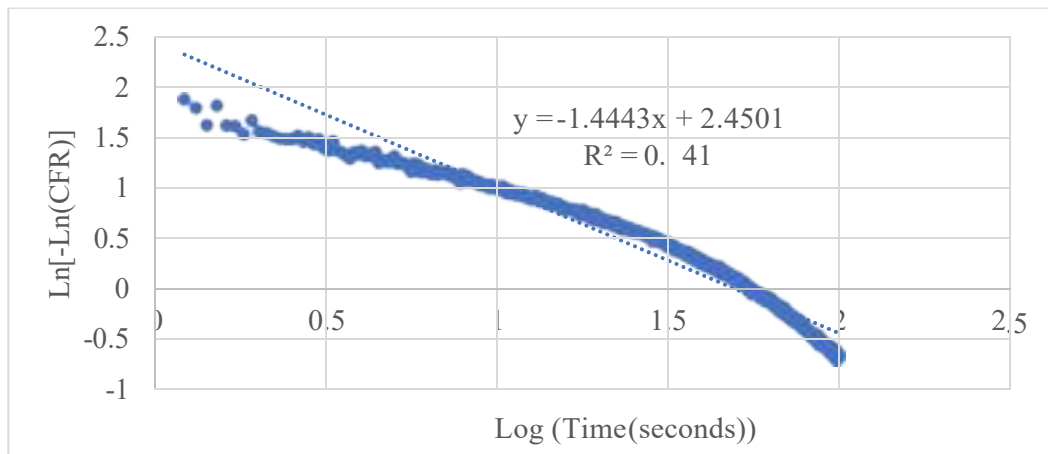
Figure 76: Gompertz model plot for NH₂ liposomes, batch #2, at 9.85 $\left(\frac{-}{c^2}\right)$
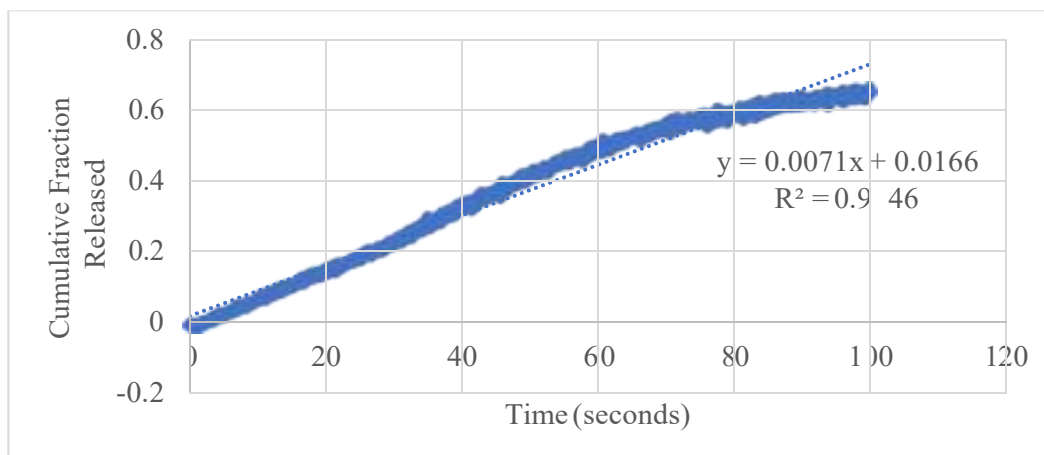
Figure 77: Zero-order model plot for NH$_2$ liposomes, batch #3, at 9.85 $\left(\frac{-}{c}\right)_2$
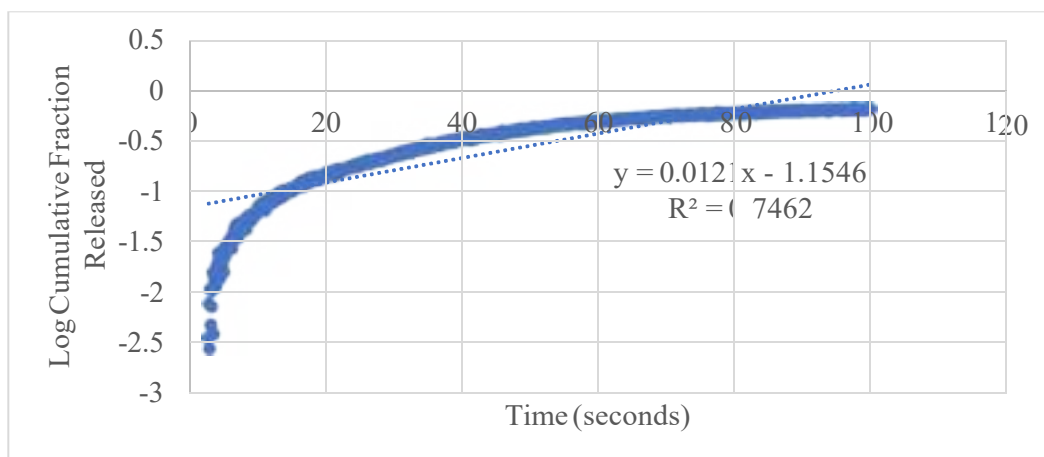
Figure 78: First-order model plot for NH$_2$ liposomes, batch #3, at 9.85 $\left(\frac{-}{c}\right)_2$
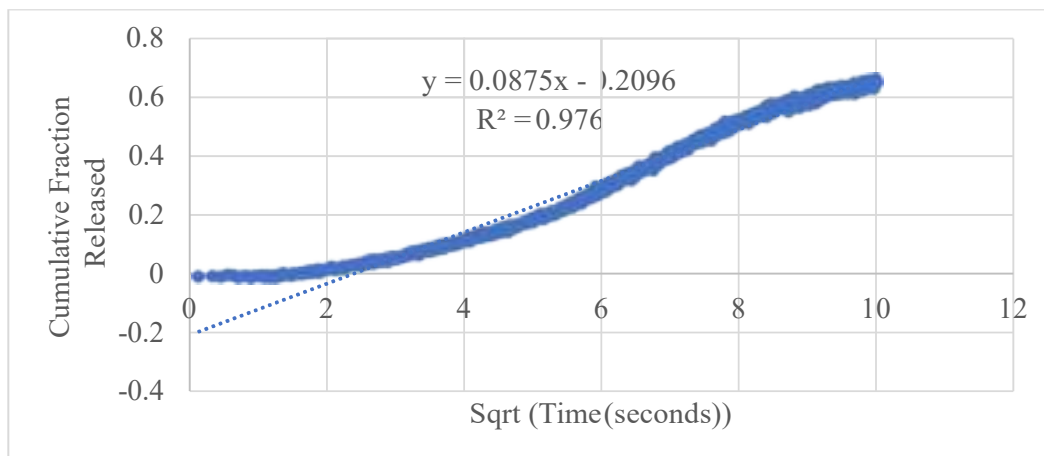
Figure 79: Higuchi model plot for NH$_2$ liposomes, batch #3, at 9.85 $\left(\frac{-}{c^2}\right)$
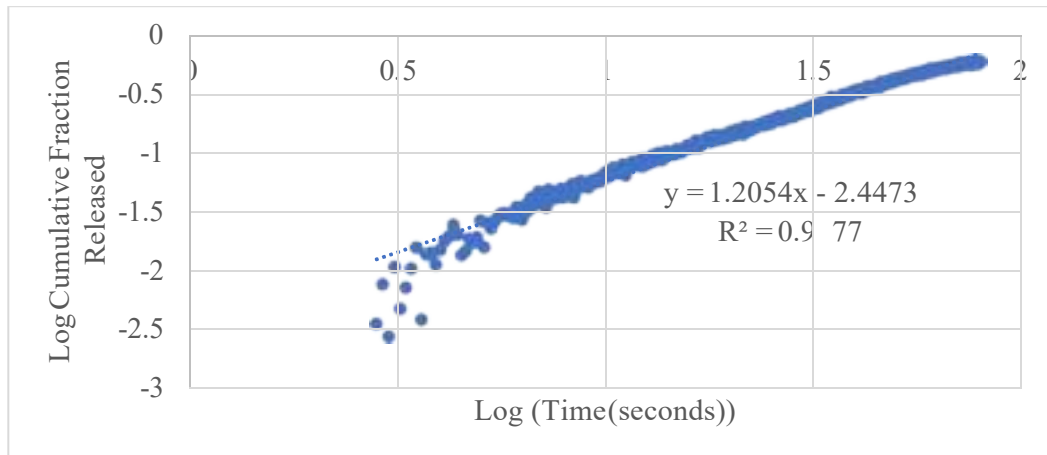
Figure 80: Korsmeyer-Peppas model plot for NH₂ liposomes, batch #3, at 9.85

$$\left(\frac{-}{c^2}\right)$$
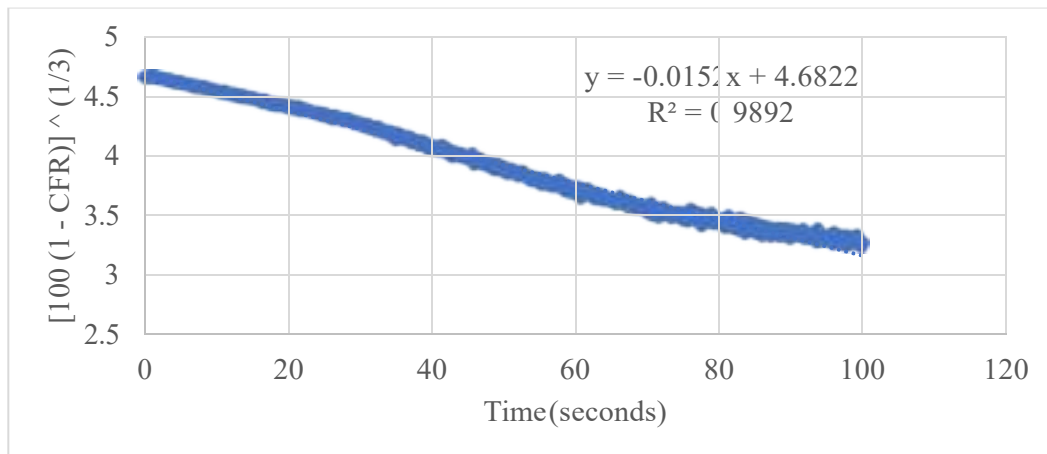
Figure 81: Hixson-Crowell model plot for NH₂ liposomes, batch #3, at 9.85 $\left(\frac{-}{c^2}\right)$
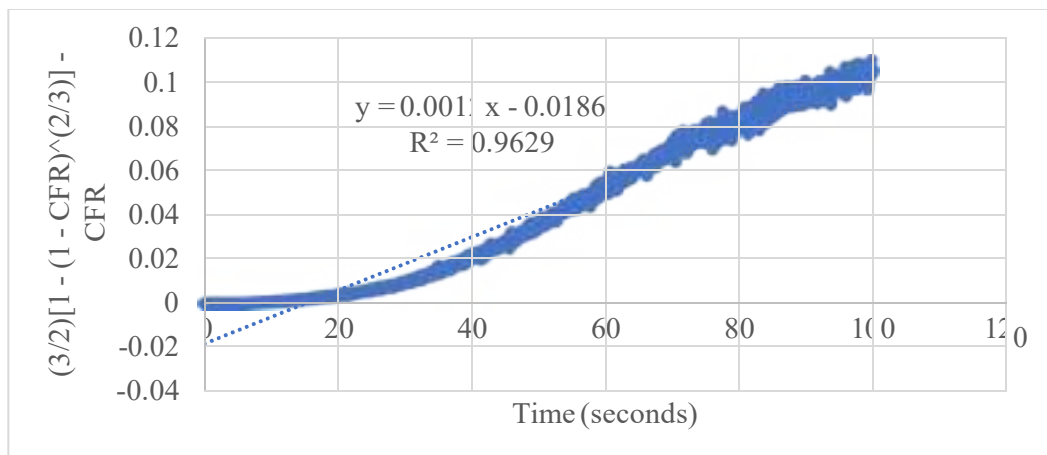
Figure 82: Baker-Lonsdale model plot for NH₂ liposomes, batch #3, at 9.85 $\left(\frac{()}{c^2}\right)$
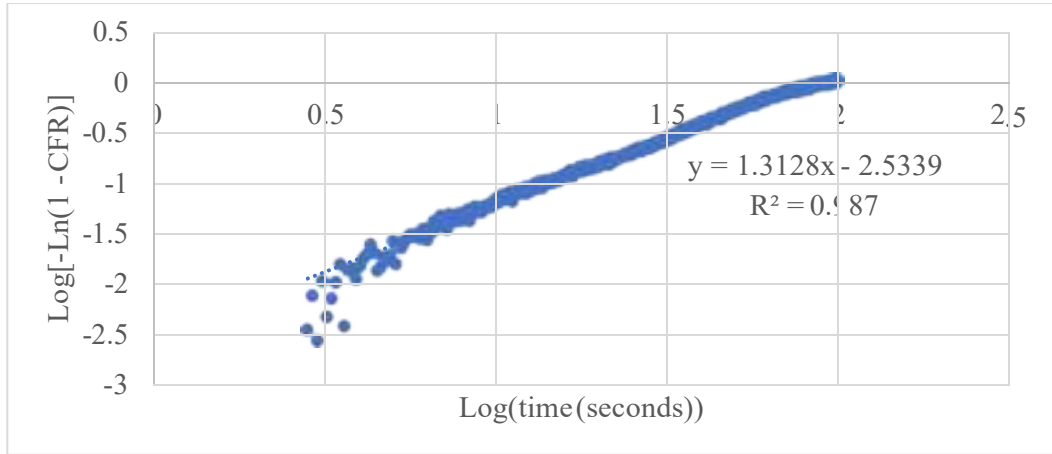
Figure 83: Weibull model plot for NH$_2$ liposomes, batch #3, at 9.85 $\left(\frac{-}{c}\right)^2$
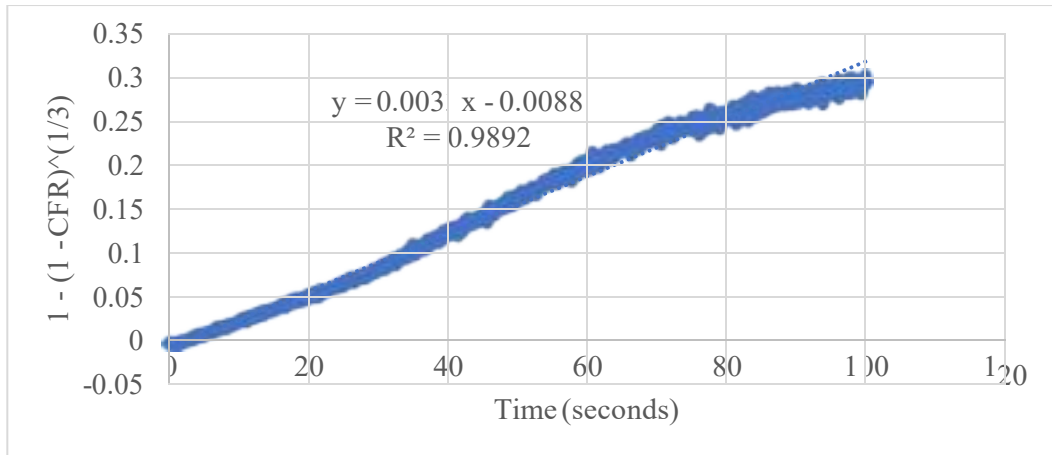
Figure 84: Hopfenberg model plot for NH$_2$ liposomes, batch #3, at 9.85 $\left(\frac{-}{c}\right)^2$
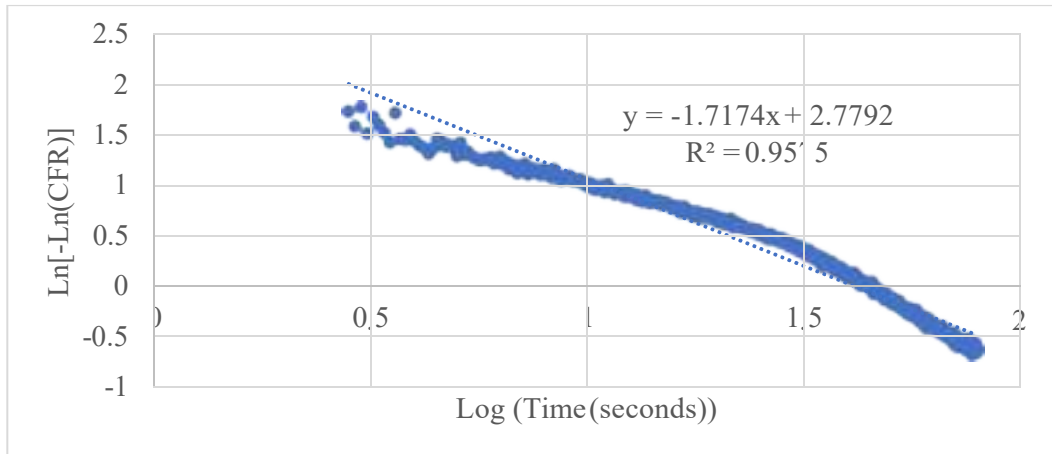
Figure 85: Gompertz model plot for NH$_2$ liposomes, batch #3, at 9.85 $\left(\frac{-}{c}\right)^2$

Appendix D: Plots of kinetics models fits for NH₂ liposomes, all batches, at 17.31

$$\left(\frac{mW}{cm^2}\right)$$
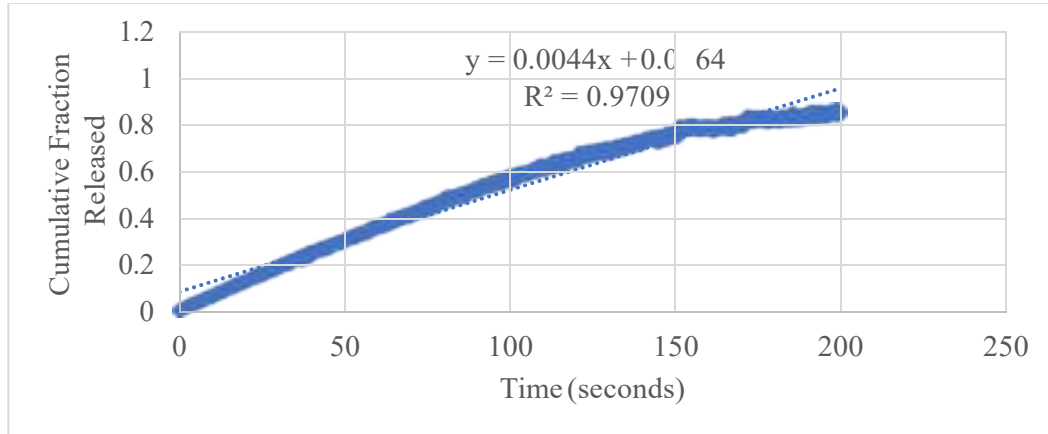
Figure 86: Zero-order model plot for NH₂ liposomes, batch #1, at 17.31 $\left(\frac{-}{c^2}\right)$
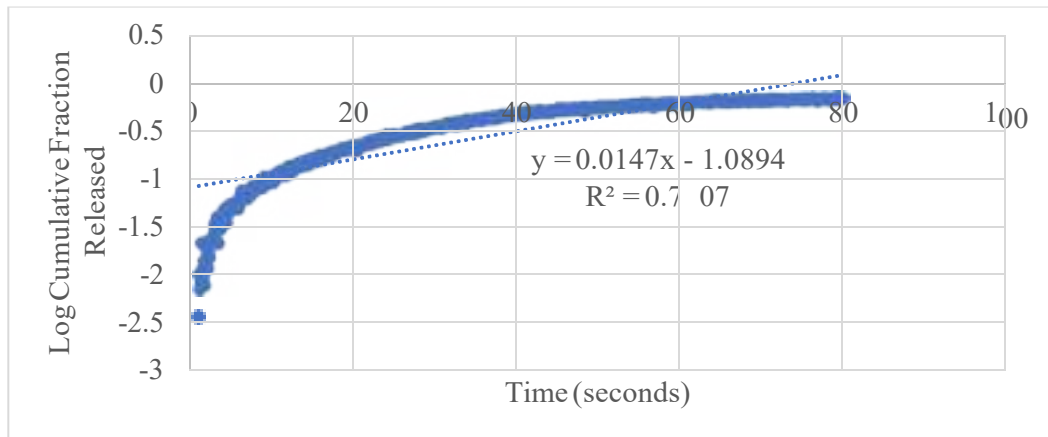
Figure 87: First-order model plot for NH₂ liposomes, batch #1, at 17.31 $\left(\frac{-}{c^2}\right)$
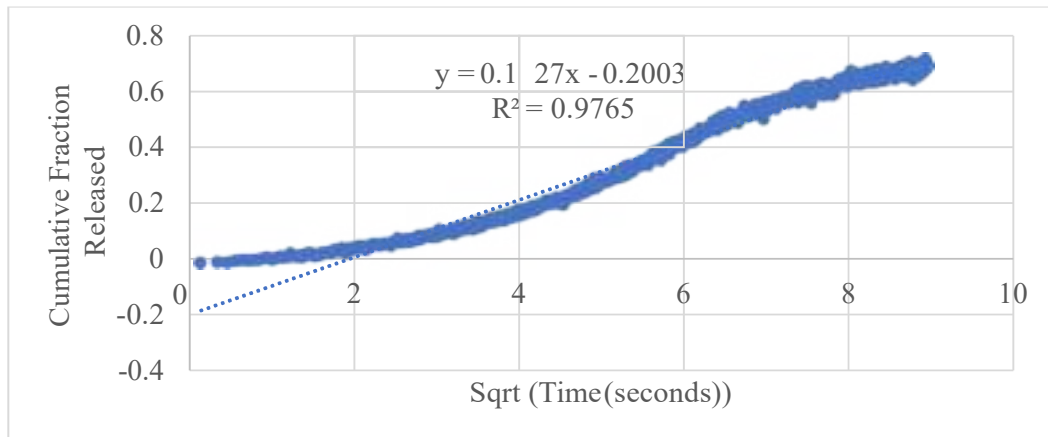
Figure 88: Higuchi model plot for NH₂ liposomes, batch #1, at 17.31 $\left(\frac{-}{c^2}\right)$
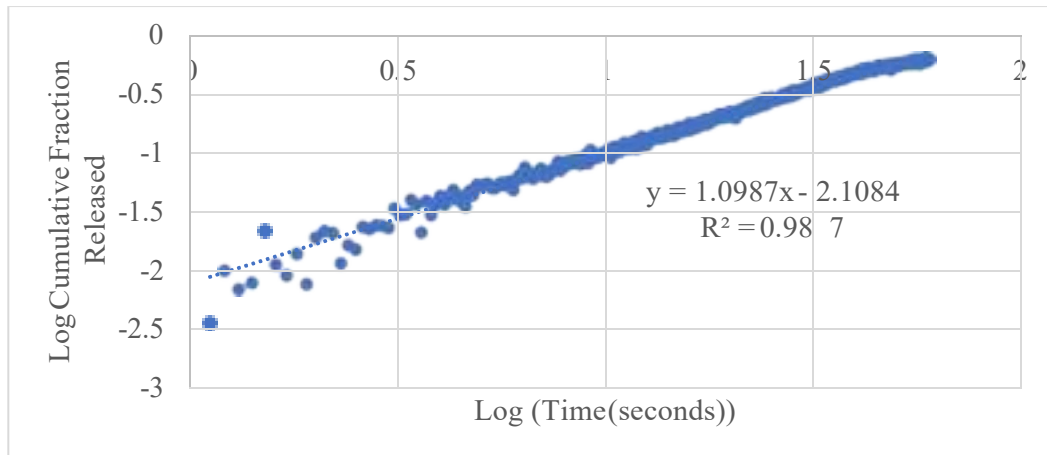
Figure 89: Korsmeyer-Peppas model plot for NH$_2$ liposomes, batch #1, at 17.31 $\left(\dfrac{}{c^2}\right)$

Chart 89 contains:
y = 1.0987x - 2.1084
R² = 0.98 7
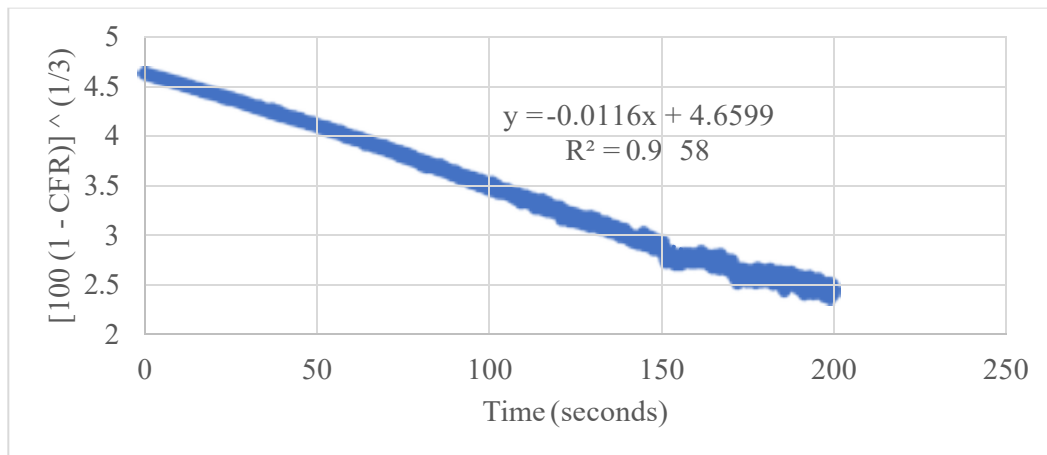
Figure 90: Hixson-Crowell model plot for NH$_2$ liposomes, batch #1, at 17.31 $\left(\dfrac{}{c^2}\right)$

Chart 90 contains:
y = -0.0116x + 4.6599
R² = 0.9 58
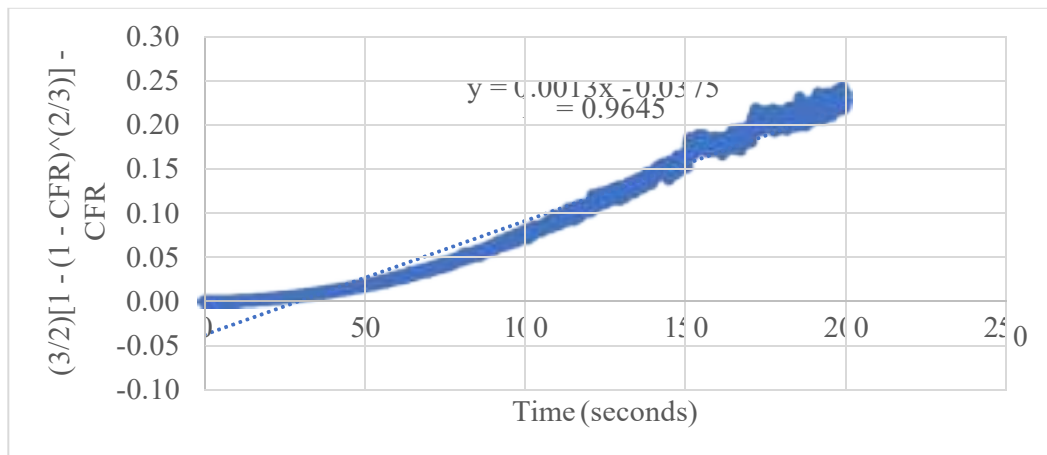
Figure 91: Baker-Lonsdale model plot for NH$_2$ liposomes, batch #1, at 17.31 $\left(\dfrac{}{c^2}\right)$

Chart 91 contains:
y = 0.0013x - 0.0375
= 0.9645
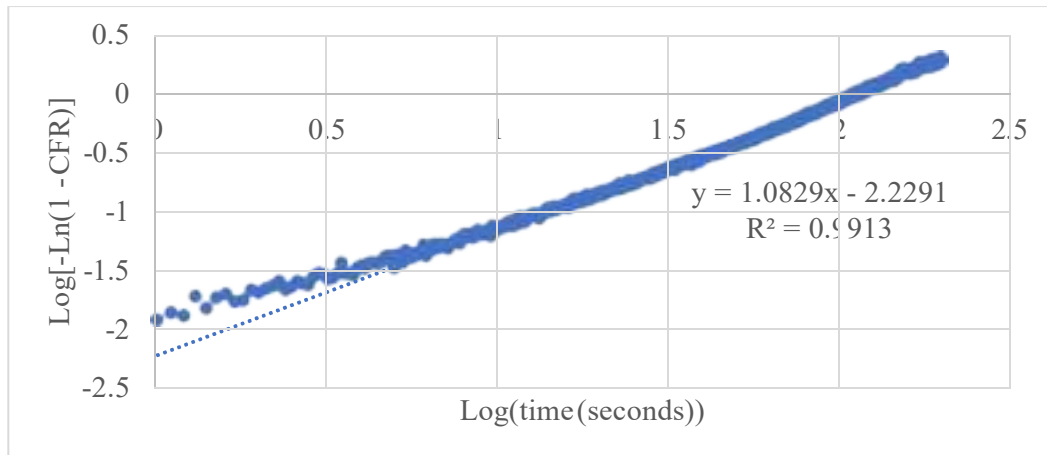
Figure 92: Weibull model plot for NH$_2$ liposomes, batch #1, at 17.31 $\left(\dfrac{-}{c^2}\right)$
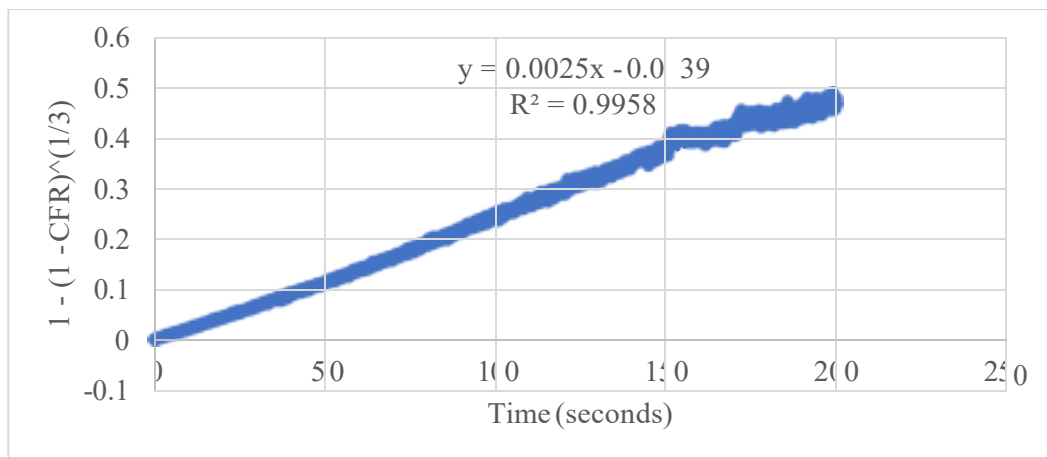
Figure 93: Hopfenberg model plot for NH$_2$ liposomes, batch #1, at 17.31 $\left(\dfrac{-}{c^2}\right)$
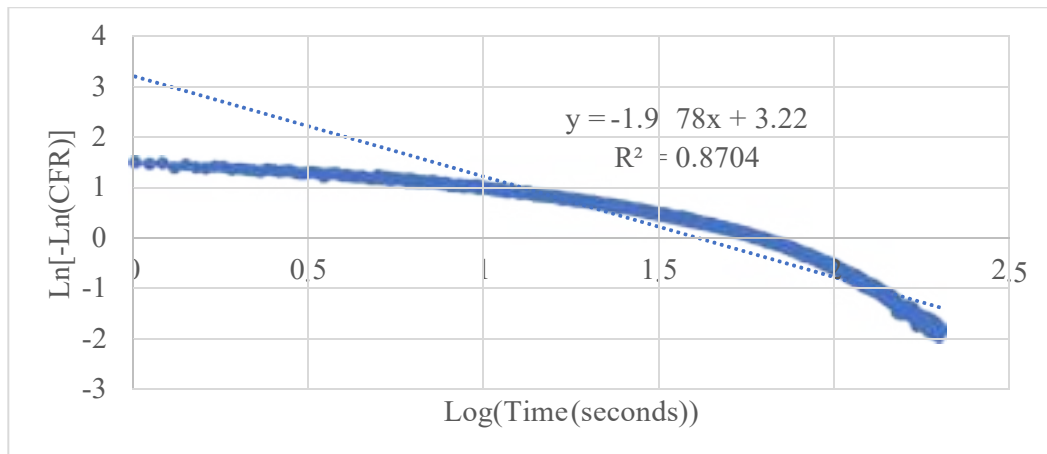
Figure 94: Gompertz model plot for NH$_2$ liposomes, batch #1, at 17.31 $\left(\dfrac{-}{c^2}\right)$
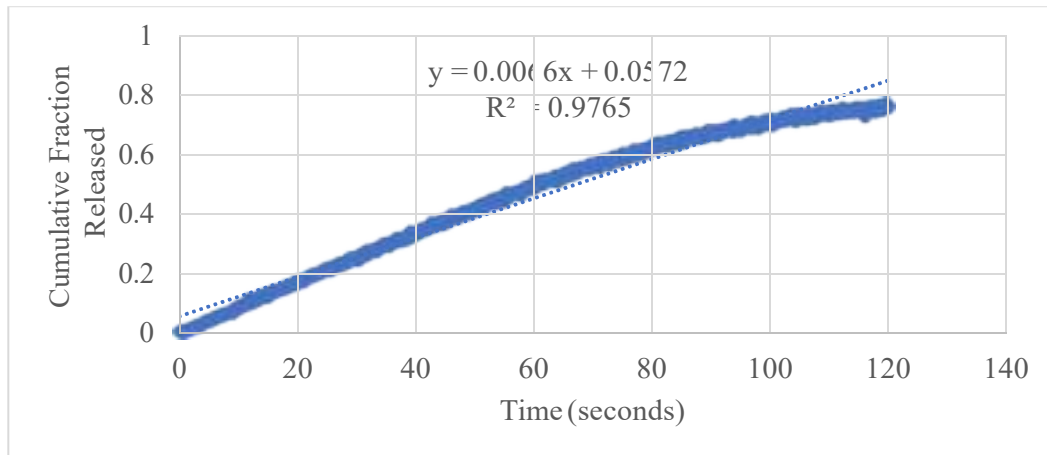
Figure 95: Zero-order model plot for NH₂ liposomes, batch #2, at 17.31 $\left(\frac{-}{c}\right)_2$
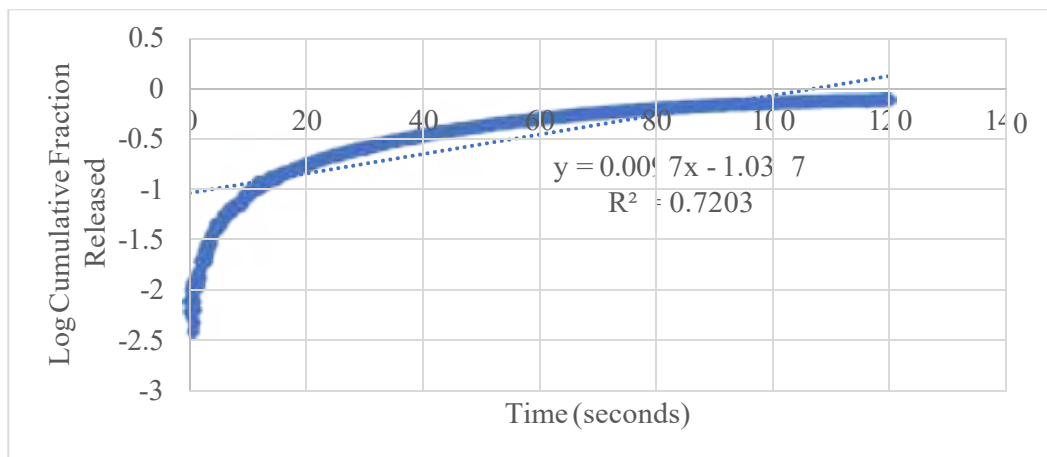
Figure 96: First-order model plot for NH₂ liposomes, batch #2, at 17.31 $\left(\frac{-}{c}\right)_2$
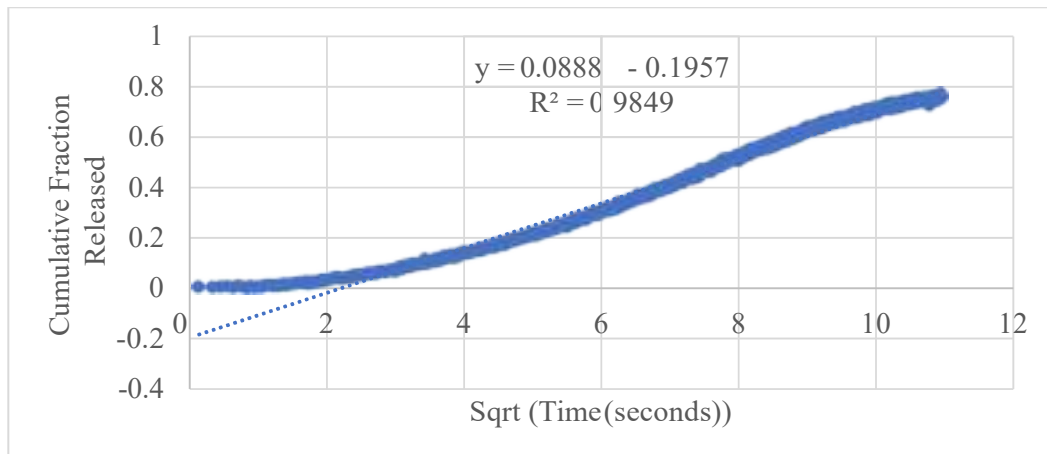
Figure 97: Higuchi plot for NH₂ liposomes, batch #2, at 17.31 $\left(\frac{-}{c^2}\right)$
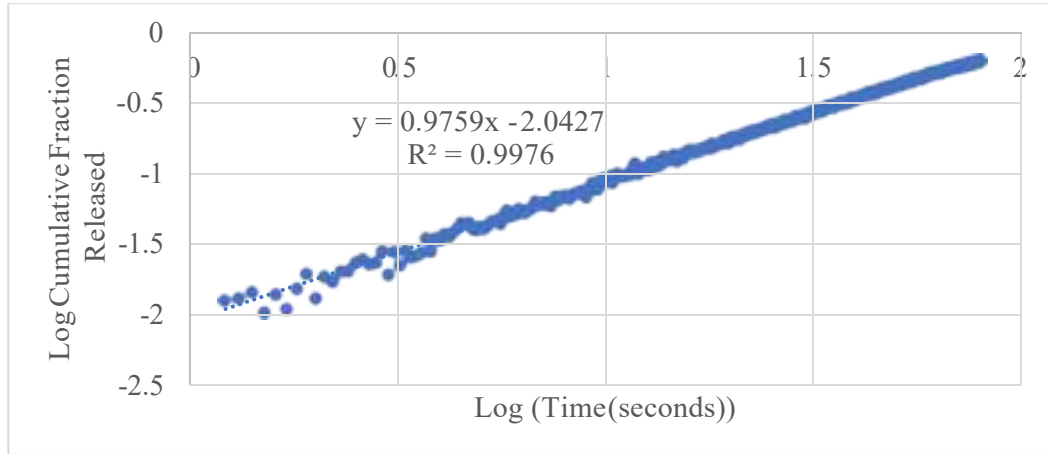
Figure 98: Korsmeyer-Peppas plot for NH₂ liposomes, batch #2, at 17.31 $\frac{(^-)}{c^2}$

The plot shows: $y = 0.9759x - 2.0427$, $R^2 = 0.9976$. Y-axis: Log Cumulative Fraction Released. X-axis: Log (Time(seconds)).
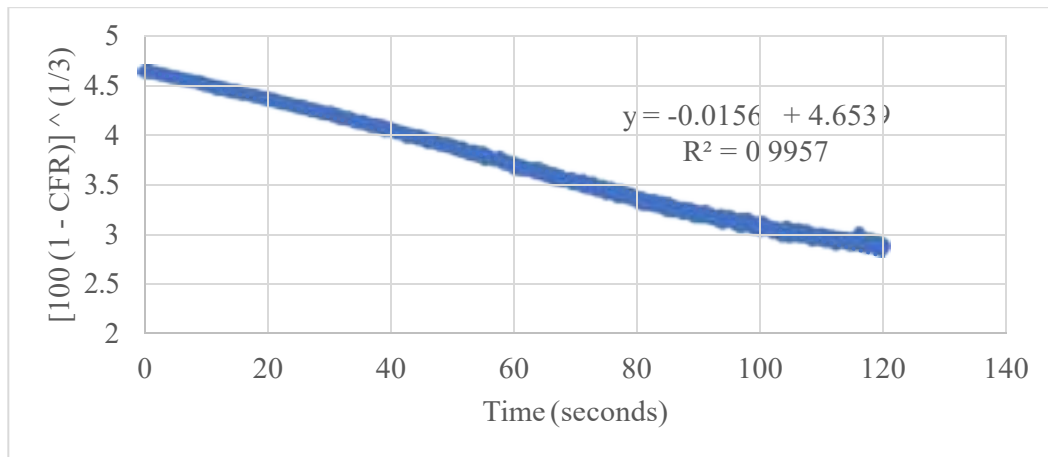
Figure 99: Hixson-Crowell plot for NH₂ liposomes, batch #2, at 17.31 $\frac{(^-)}{c^{\,2}}$

The plot shows: $y = -0.0156 + 4.653$, $R^2 = 0.9957$. Y-axis: $[100(1 - CFR)]^{\wedge}(1/3)$. X-axis: Time (seconds).
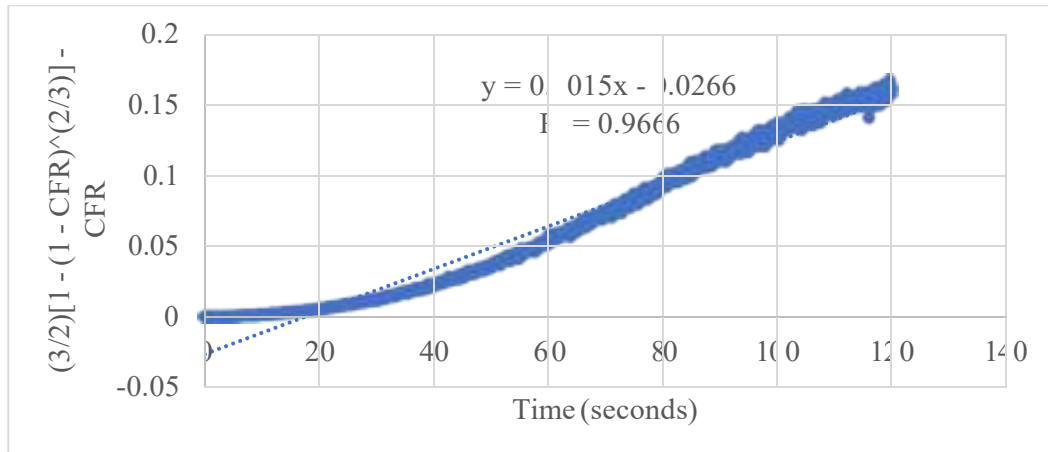
Figure 100: Baker-Lonsdale plot for NH₂ liposomes, batch #2, at 17.31 $\frac{()}{c^{\,2}}$

The plot shows: $y = 0.015x - 0.0266$, $R^2 = 0.9666$. Y-axis: $(3/2)[1 - (1 - CFR)^{\wedge}(2/3)] - CFR$. X-axis: Time (seconds).
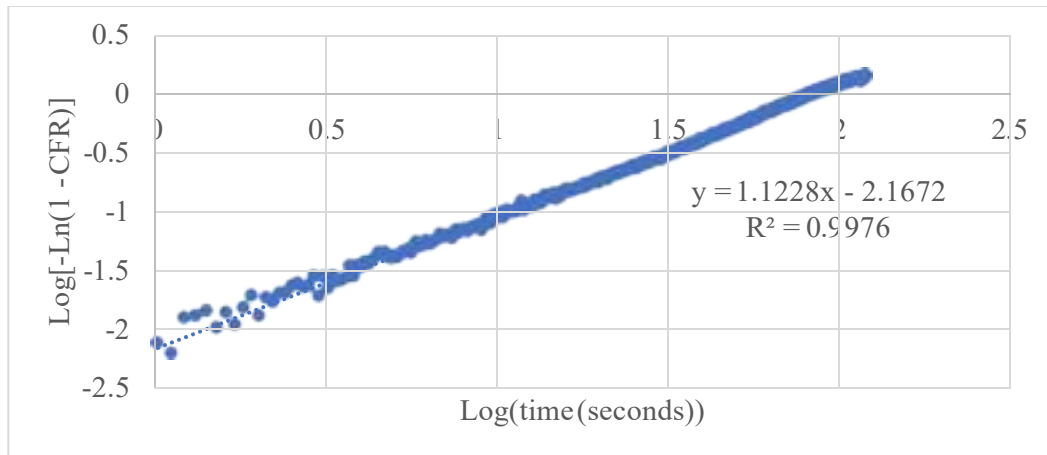
Figure 101: Weibull plot for NH₂ liposomes, batch #2, at 17.31 $\left(\frac{-}{c^2}\right)$
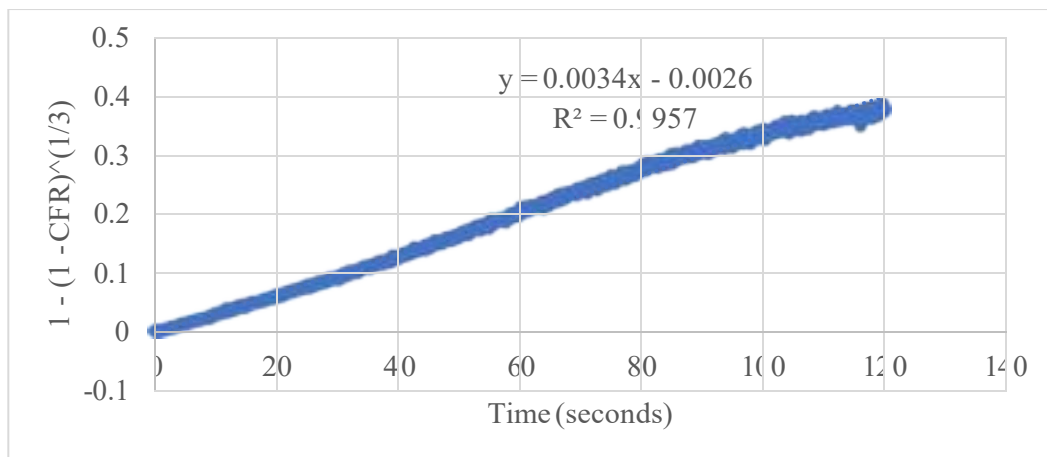
Figure 102: Hopfenberg plot for NH₂ liposomes, batch #2, at 17.31 $\left(\frac{-}{c^2}\right)$
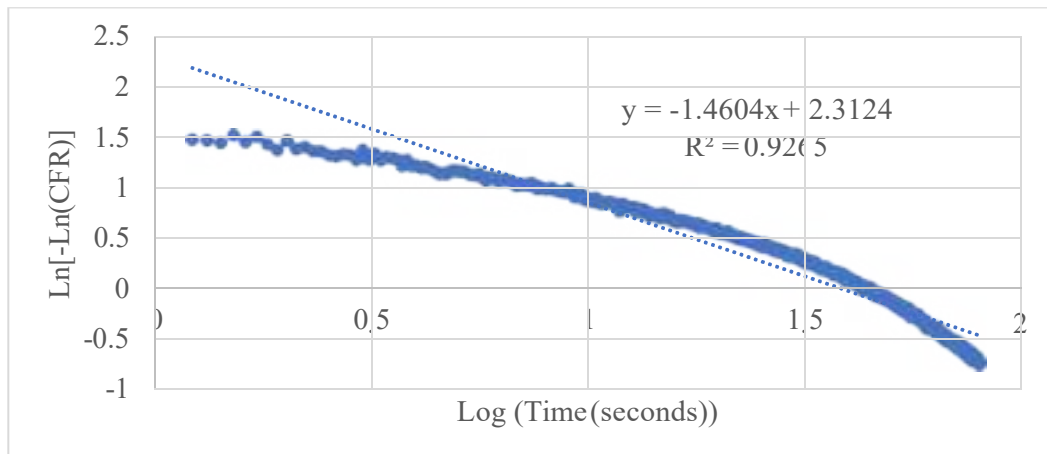
**Figure 103: Gompertz plot for NH₂ liposomes, batch #2, at 17.31 $\left(\frac{-}{c^2}\right)$**

124
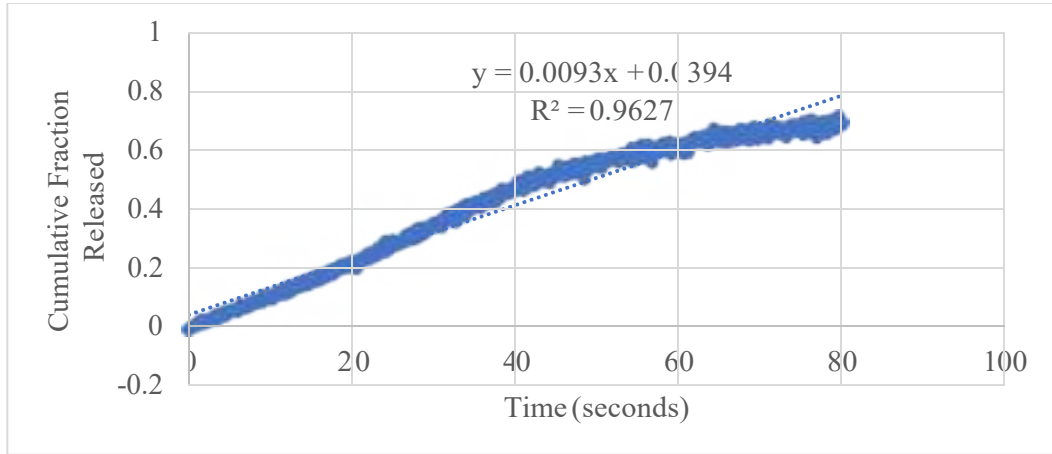
Figure 104: Zero-order plot for NH$_2$ liposomes, batch #3, at 17.31 $\left(\frac{-}{c^2}\right)$
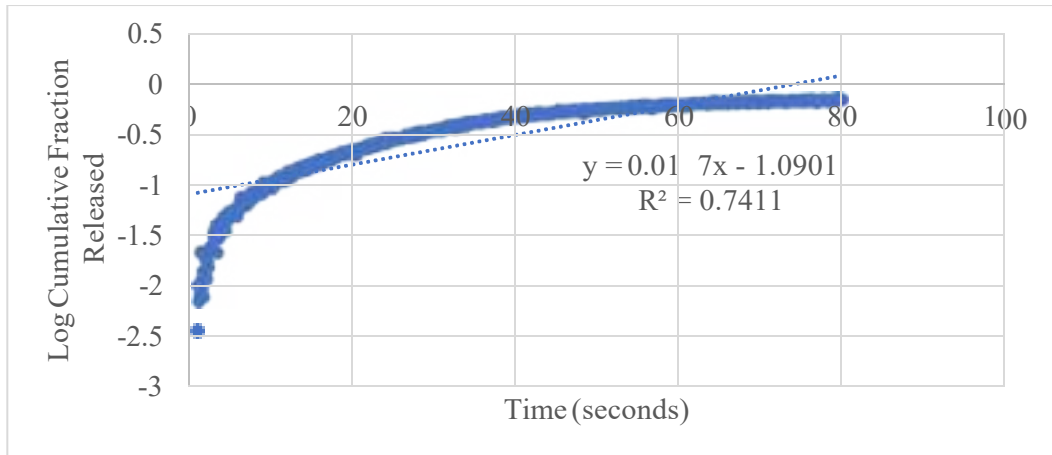
Figure 105: First-order plot for NH$_2$ liposomes, batch #3, at 17.31 $\left(\frac{-}{c^2}\right)$
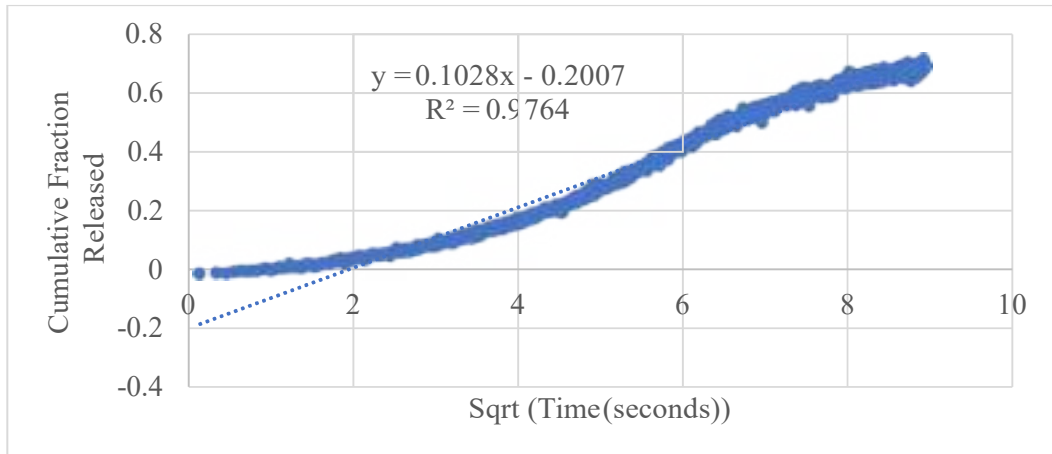
Figure 106: Higuchi plot for NH$_2$ liposomes, batch #3, at 17.31 $\left(\frac{-}{c^2}\right)$

125
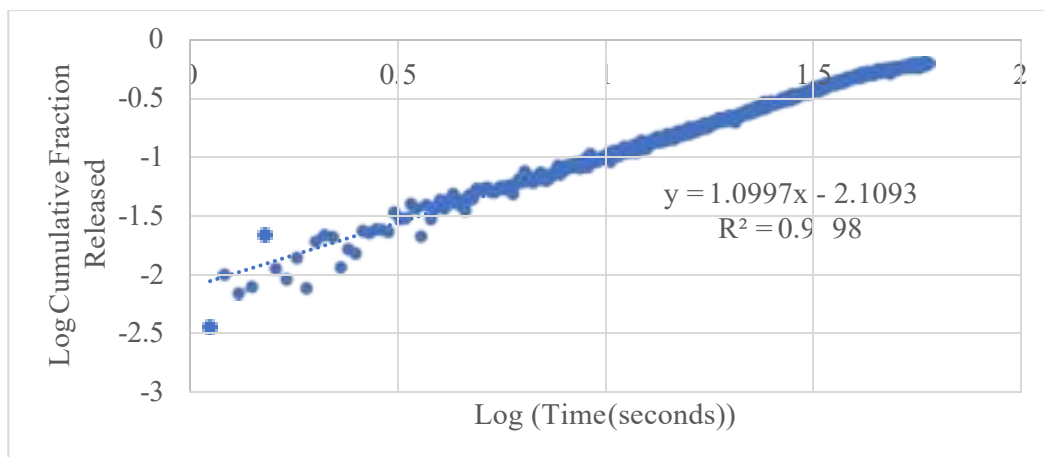
Figure 107: Korsmeyer-Peppas plot for NH₂ liposomes, batch #3, at 17.31 $\left(\dfrac{-}{c^2}\right)$
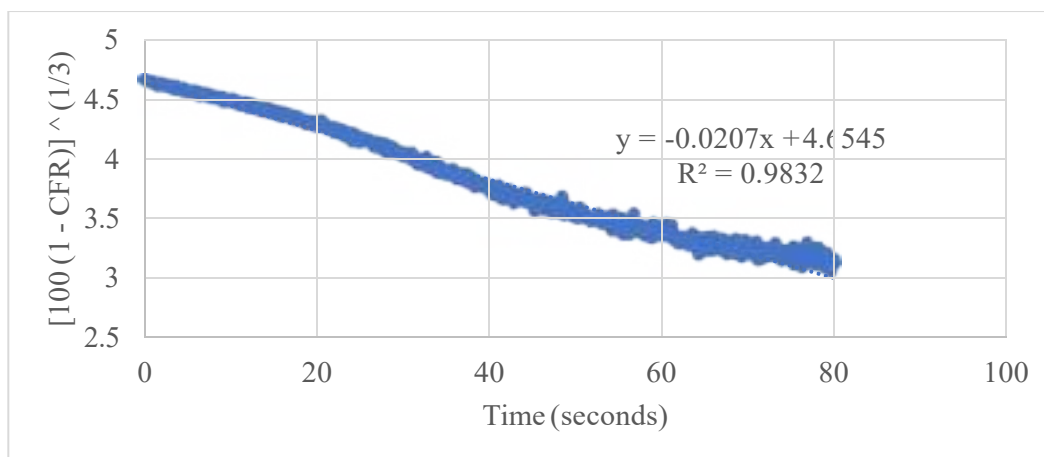
Figure 108: Hixson-Crowell plot for NH₂ liposomes, batch #3, at 17.31 $\left(\dfrac{-}{c^2}\right)$
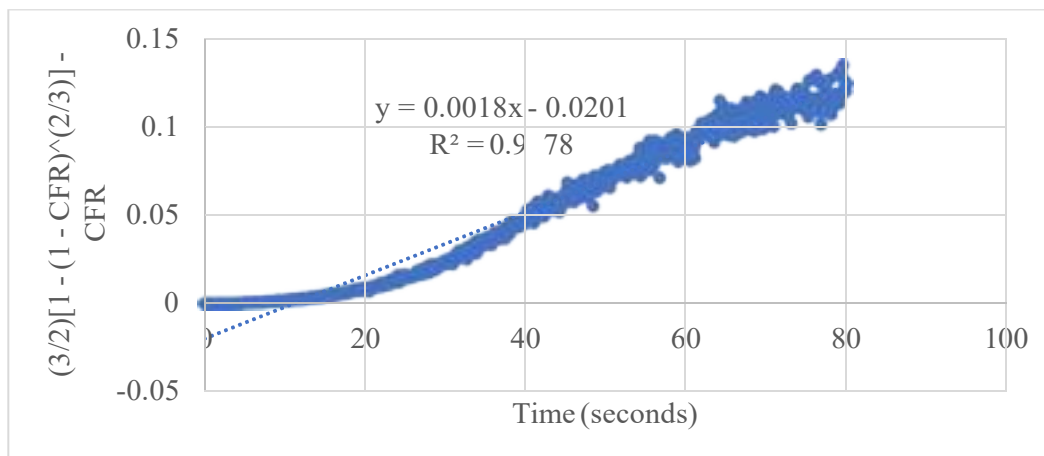
Figure 109: Baker-Lonsdale plot for NH₂ liposomes, batch #3, at 17.31 $\left(\dfrac{}{c^2}\right)$
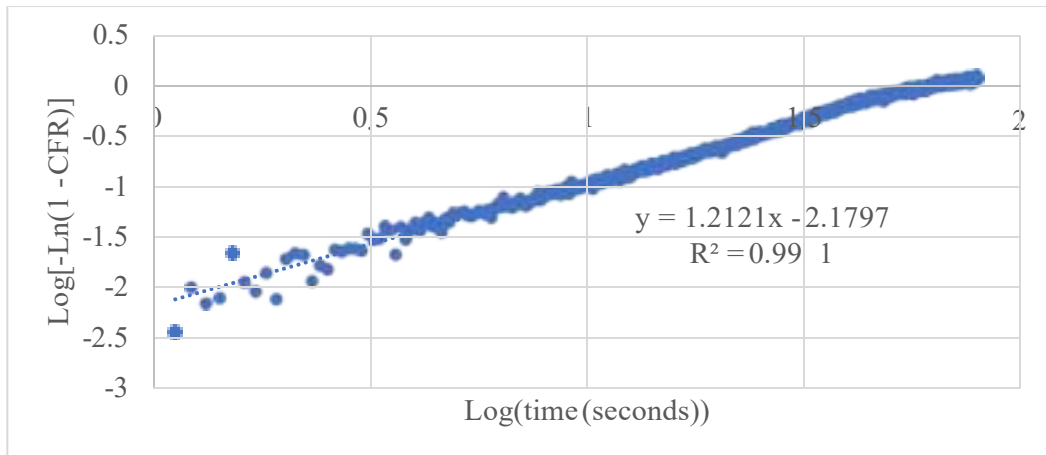
Figure 110: Weibull plot for NH$_2$ liposomes, batch #3, at 17.31 $\left(\frac{-}{c^2}\right)$
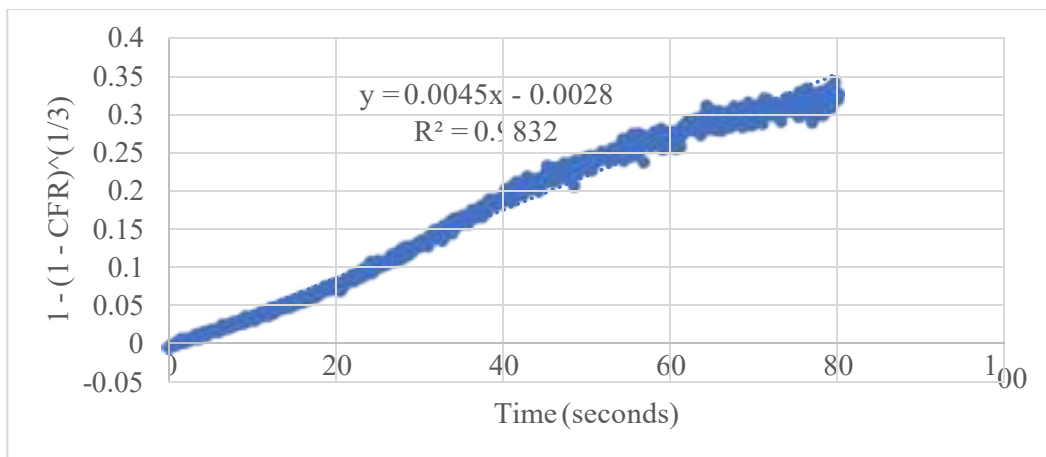
Figure 111: Hopfenberg plot for NH$_2$ liposomes, batch #3, at 17.31 $\left(\frac{-}{c^2}\right)$
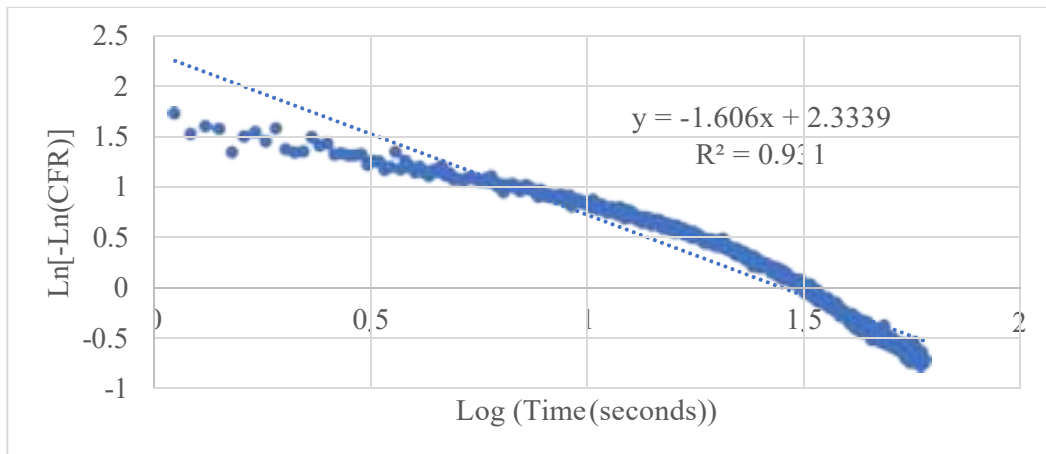
Figure 112: Gompertz plot for NH$_2$ liposomes, batch #3, at 17.31 $\left(\frac{-}{c^2}\right)$

Appendix E: Plots of kinetics models fits for RGD liposomes, all batches, at 7.46

$$\left(\frac{mW}{cm^2}\right)$$
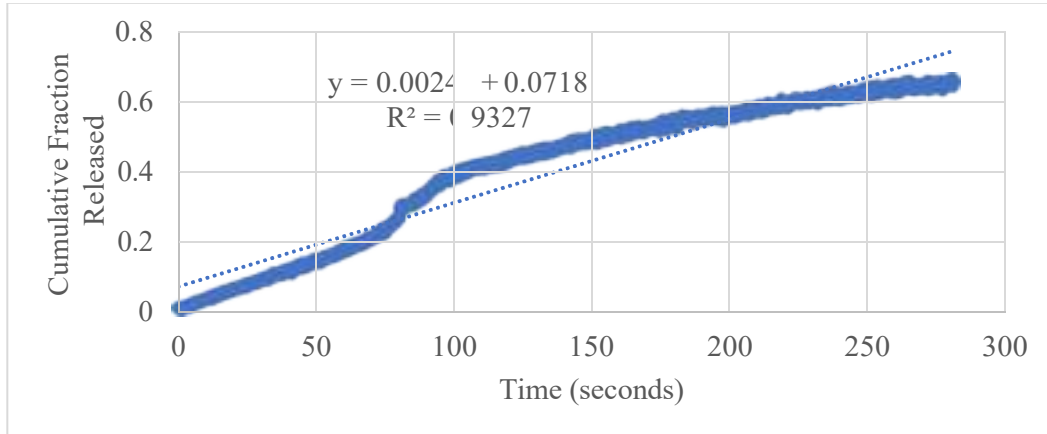
Figure 113: Zero-order plot for RGD liposomes, batch #1, at 7.46 $\left(\frac{-}{c^2}\right)$
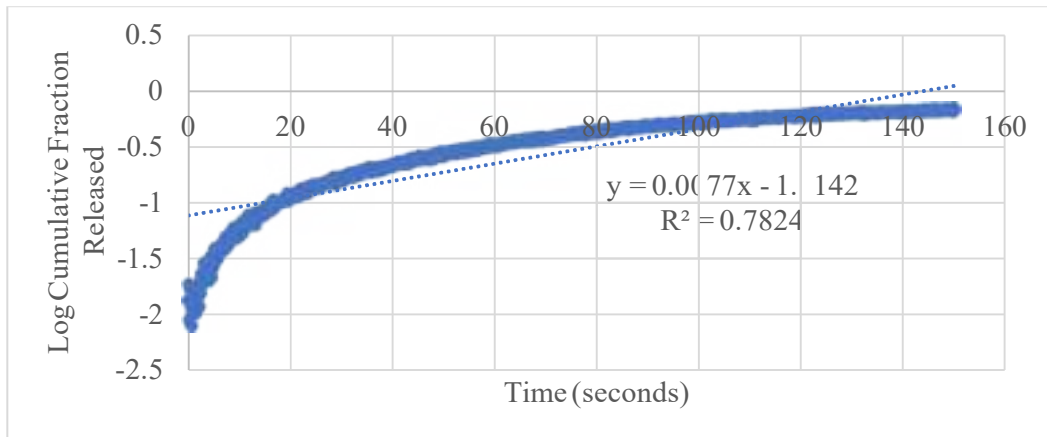
Figure 114: First-order plot for RGD liposomes, batch #1, at 7.46 $\left(\frac{-}{c^2}\right)$
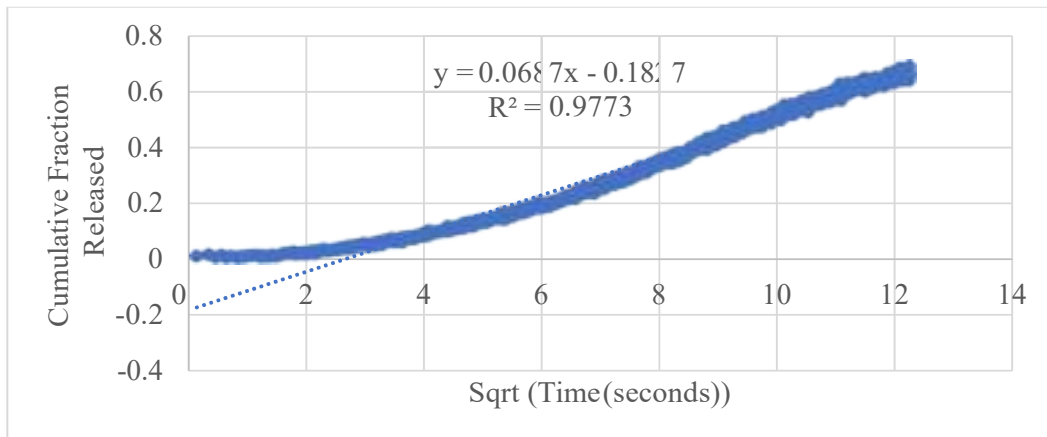
Figure 115: Higuchi plot for RGD liposomes, batch #1, at 7.46 $\left(\frac{-}{c^2}\right)$
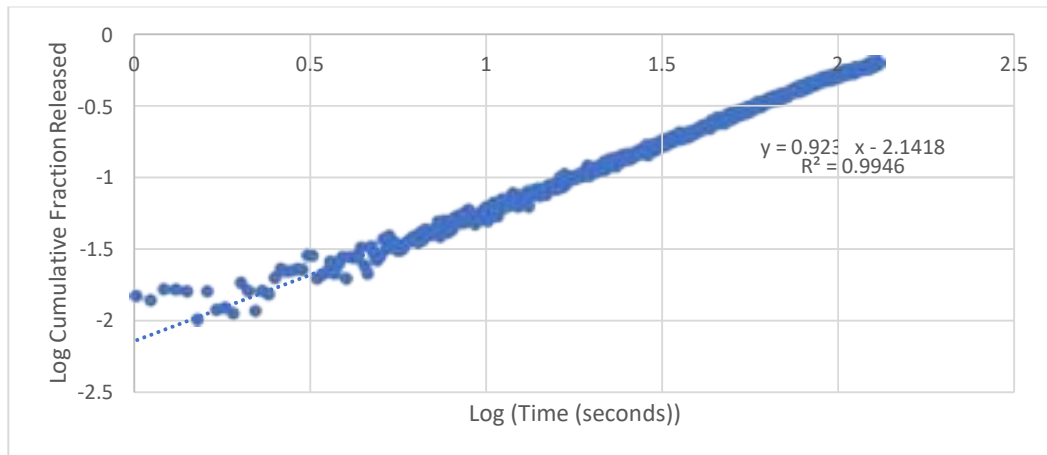
Figure 116: Korsmeyer-Peppas plot for RGD liposomes, batch #1, at 7.46 $\frac{(-)}{c^2}$
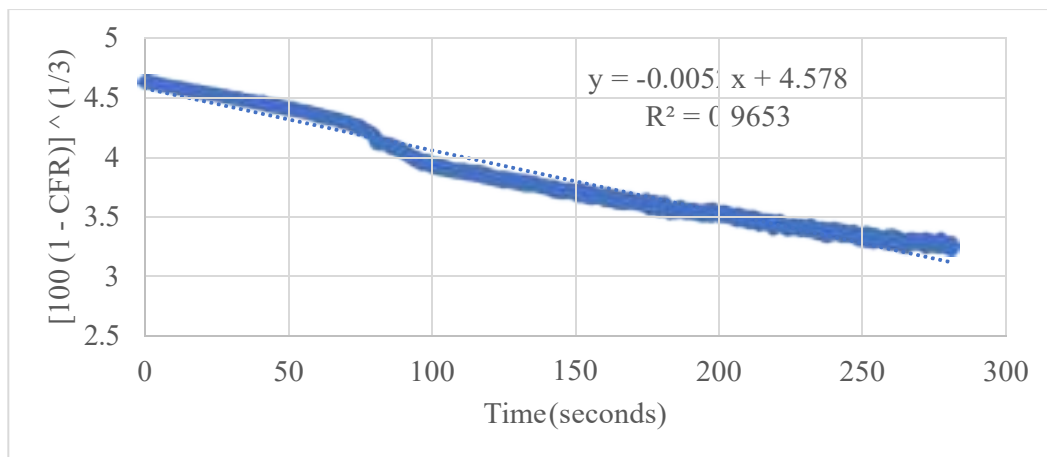
Figure 117: Hixson-Crowell plot for RGD liposomes, batch #1, at 7.46 $\frac{(-)}{c^2}$
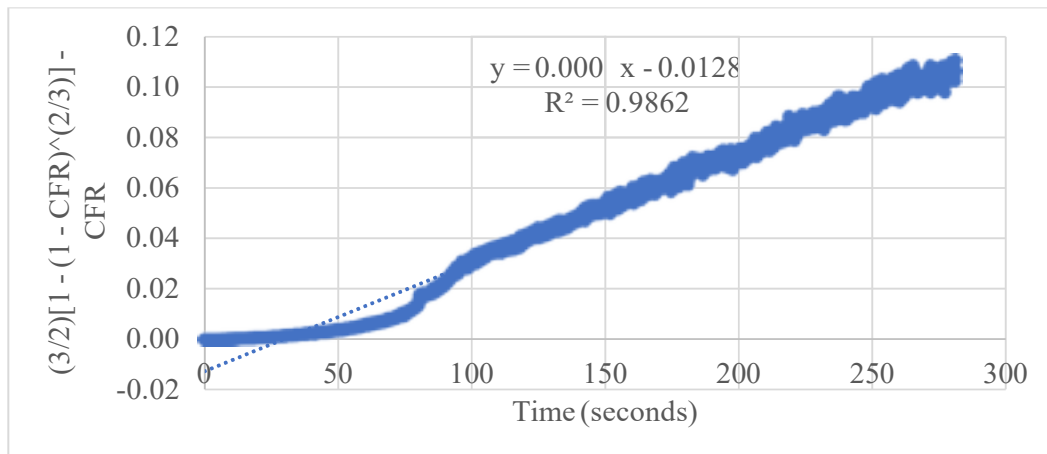
Figure 118: Baker-Lonsdale plot for RGD liposomes, batch #1, at 7.46 $\frac{(-)}{c^2}$
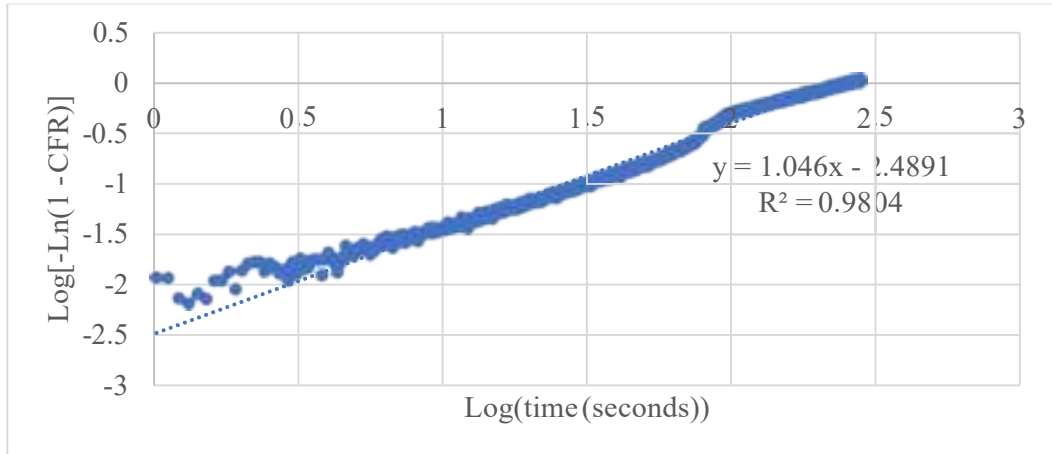
Figure 119: Weibull plot for RGD liposomes, batch #1, at 7.46 $\frac{(-)}{c^2}$
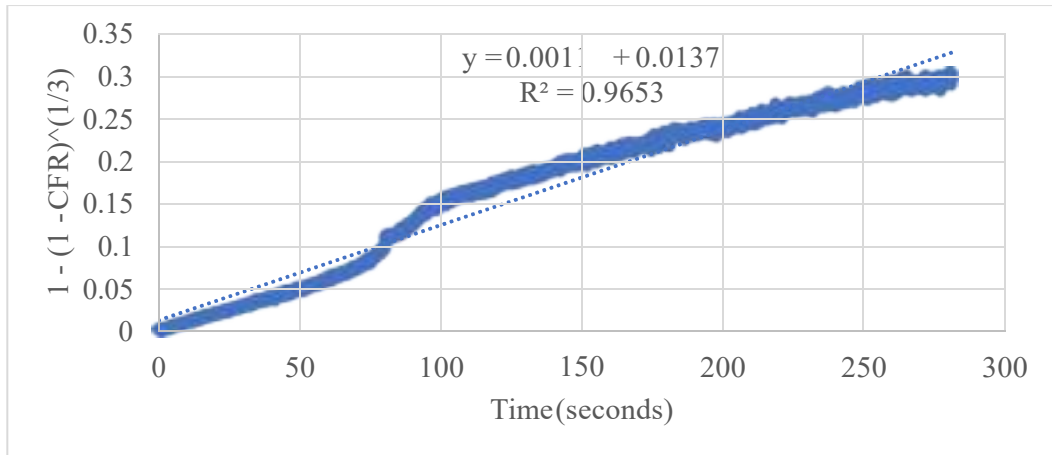
Figure 120: Hopfenberg plot for RGD liposomes, batch #1, at 7.46 $\frac{(-)}{c^2}$
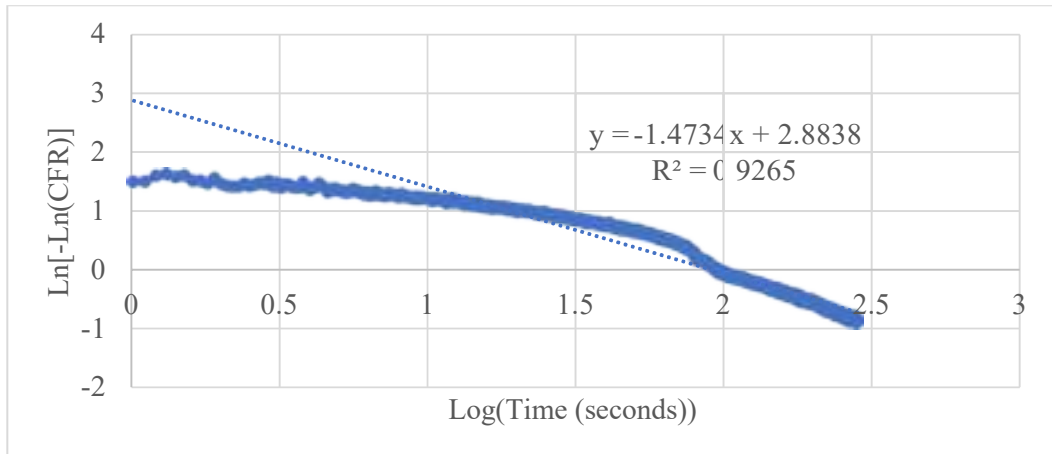
Figure 121: Gompertz plot for RGD liposomes, batch #1, at 7.46 $\frac{(-)}{c^2}$
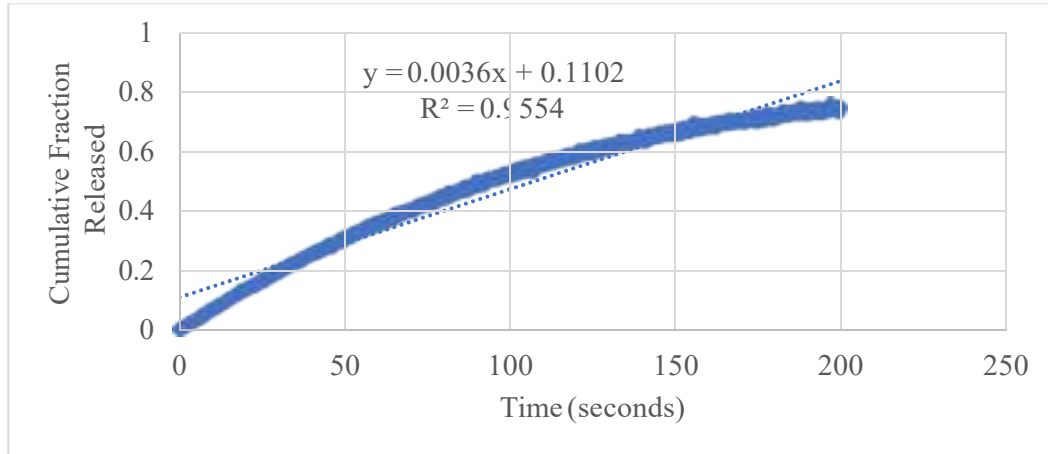
Figure 122: Zero-order plot for RGD liposomes, batch #2, at 7.46 $\left(\dfrac{-}{c^2}\right)$
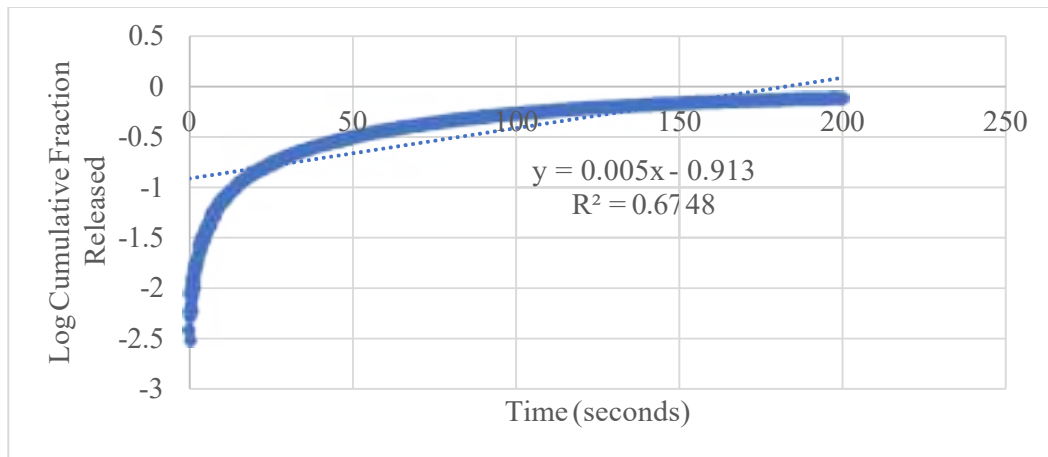
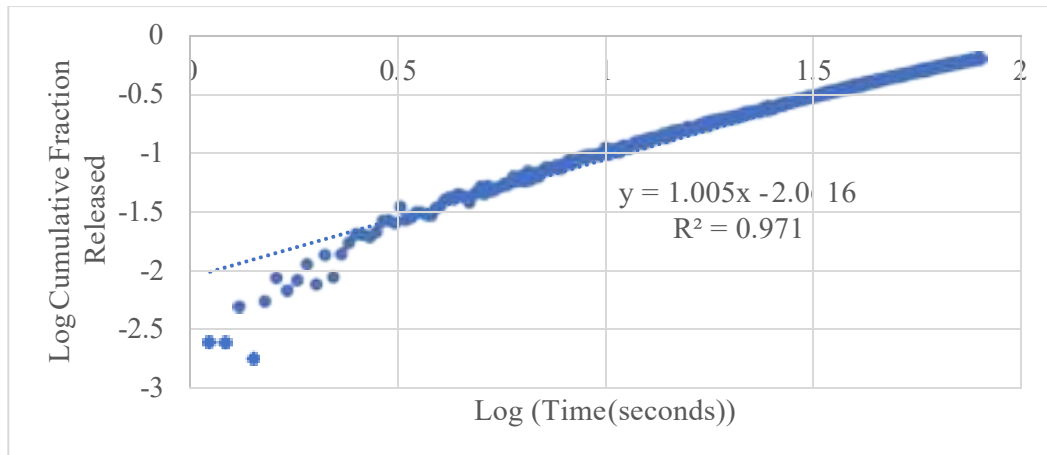**Figure 123: First-order plot for RGD liposomes, batch #2, at 7.46 $\left(\dfrac{-}{c^2}\right)$**
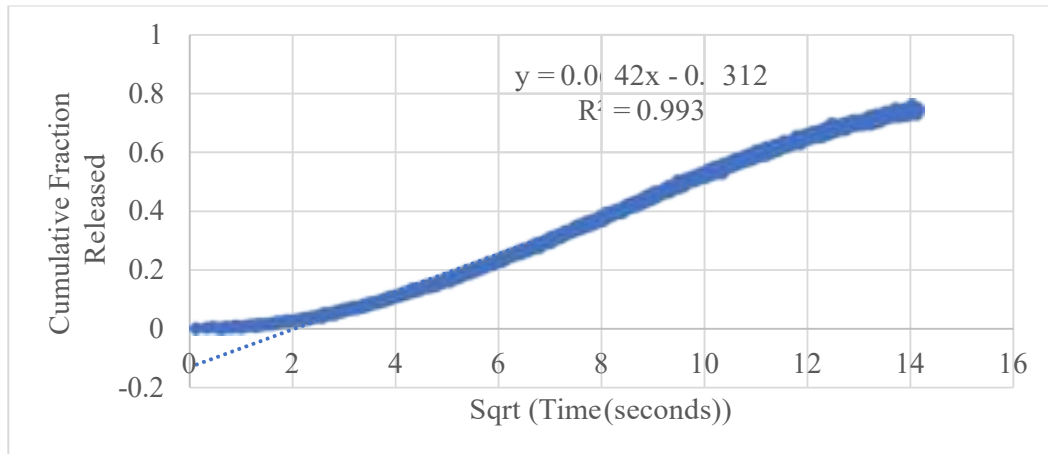
Figure 124: Higuchi plot for RGD liposomes, batch #2, at 7.46 $\left(\dfrac{-}{c^2}\right)$
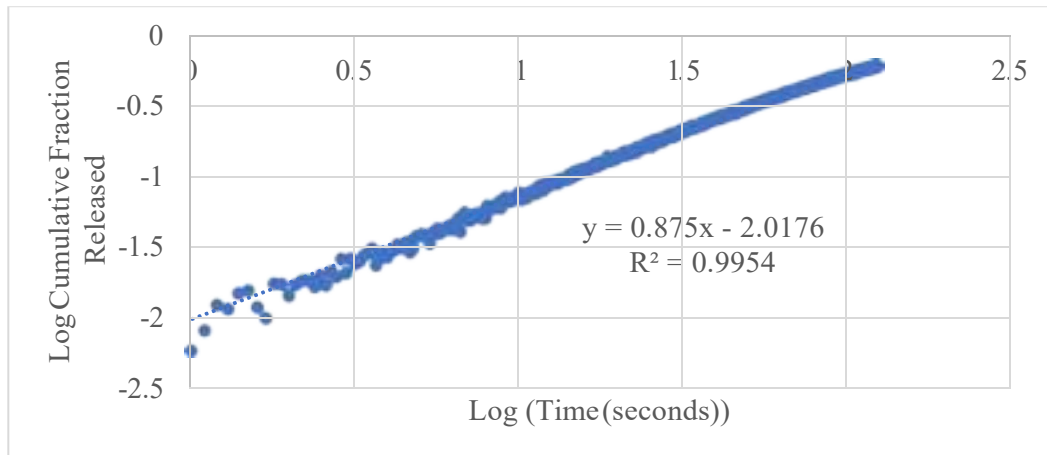
Figure 125: Korsmeyer-Peppas plot for RGD liposomes, batch #2, at 7.46 $\left(\frac{-}{c^2}\right)$
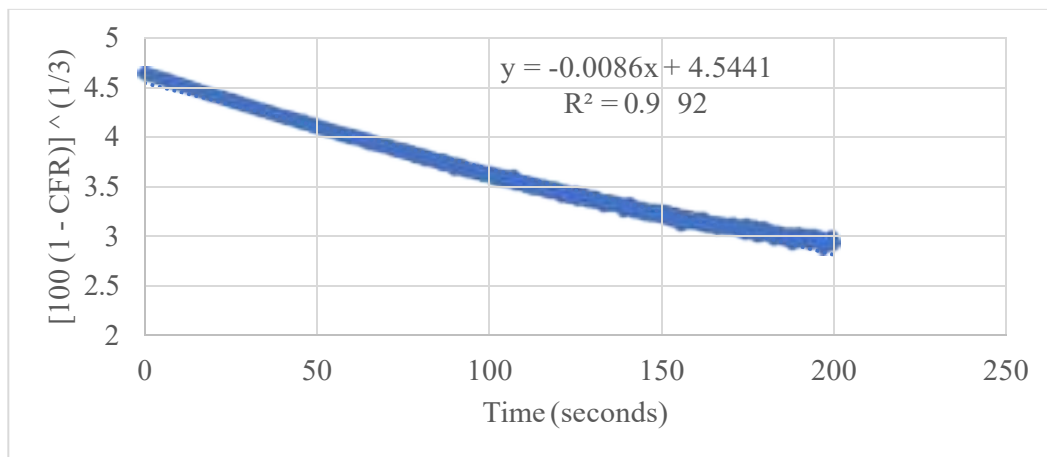
Figure 126: Hixson-Crowell plot for RGD liposomes, batch #2, at 7.46 $\left(\frac{-}{c^2}\right)$
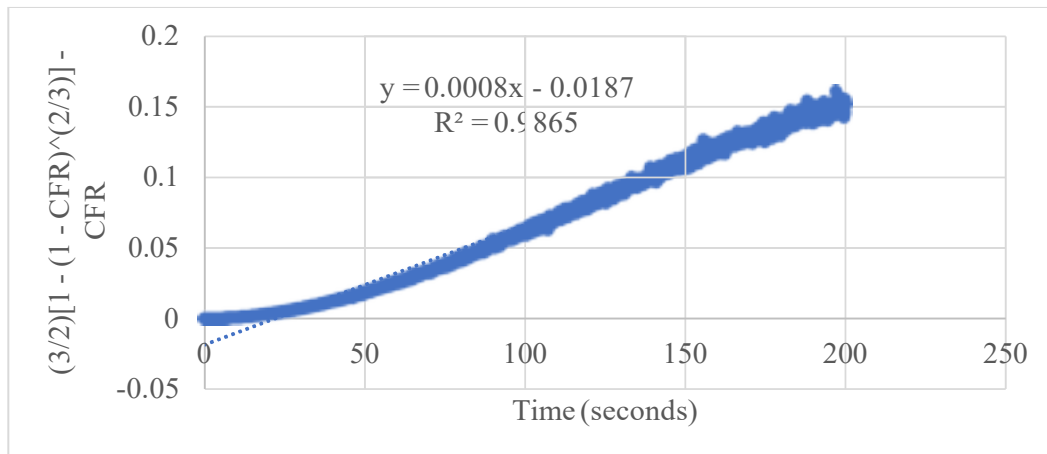
Figure 127: Baker-Lonsdale plot for RGD liposomes, batch #2, at 7.46 $\left(\frac{-}{c^2}\right)$

132
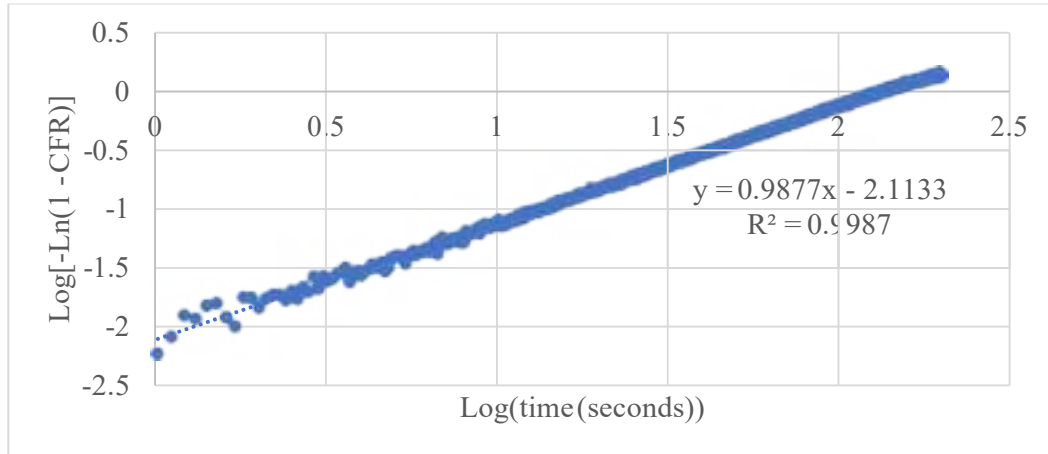
Figure 128: Weibull plot for RGD liposomes, batch #2, at 7.46 $\left(\frac{-}{c^2}\right)$
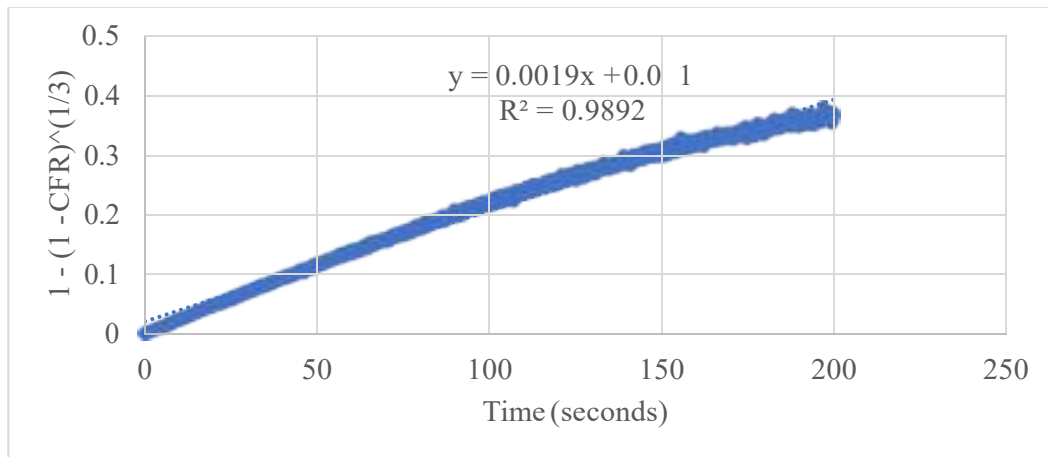
Figure 129: Hopfenberg plot for RGD liposomes, batch #2, at 7.46 $\left(\frac{-}{c^2}\right)$
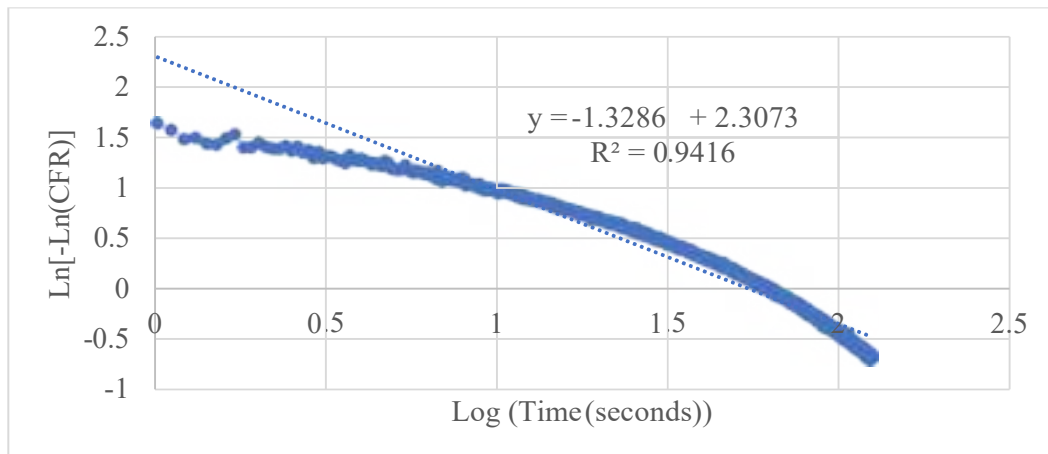
Figure 130: Gompertz plot for RGD liposomes, batch #2, at 7.46 $\left(\frac{-}{c^2}\right)$
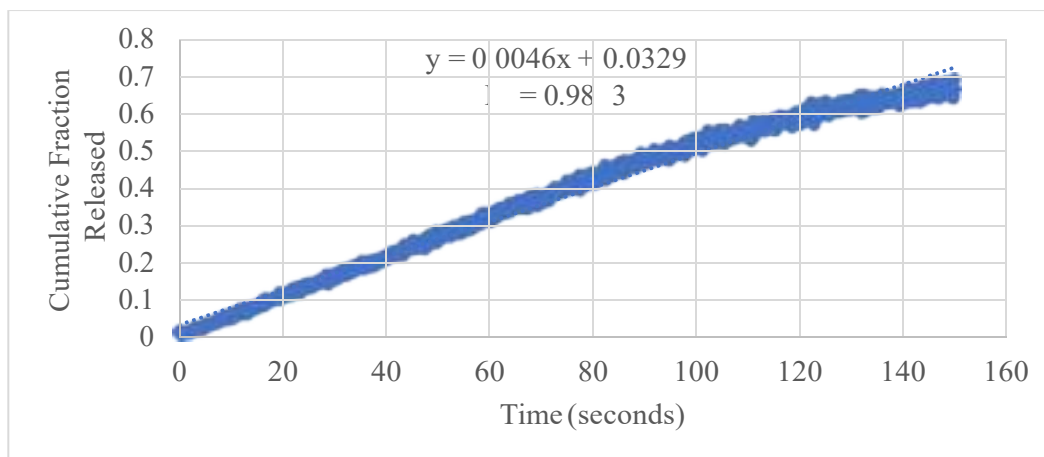
Figure 131: Zero-order plot for RGD liposomes, batch #3, at 7.46 $\left(\frac{()}{c^2}\right)$
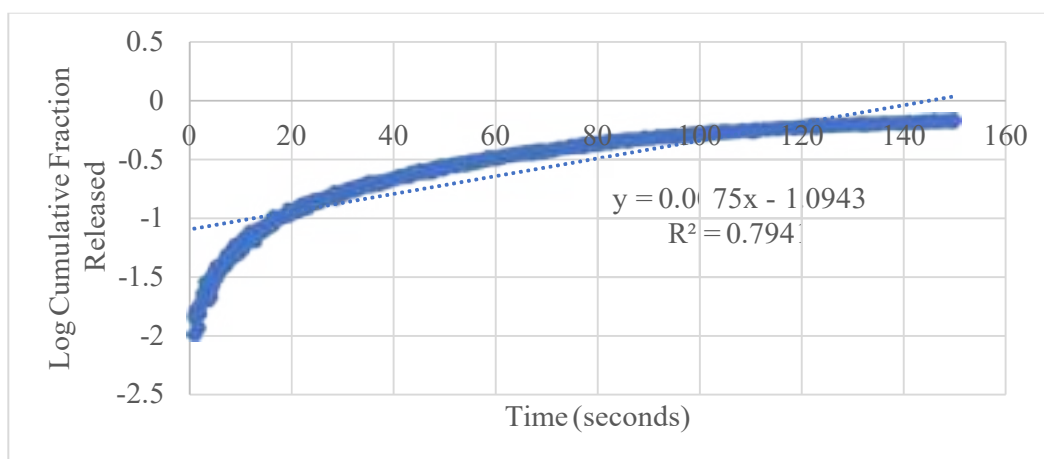
Figure 132: First-order plot for RGD liposomes, batch #3, at 7.46 $\left(\frac{()}{c^2}\right)$
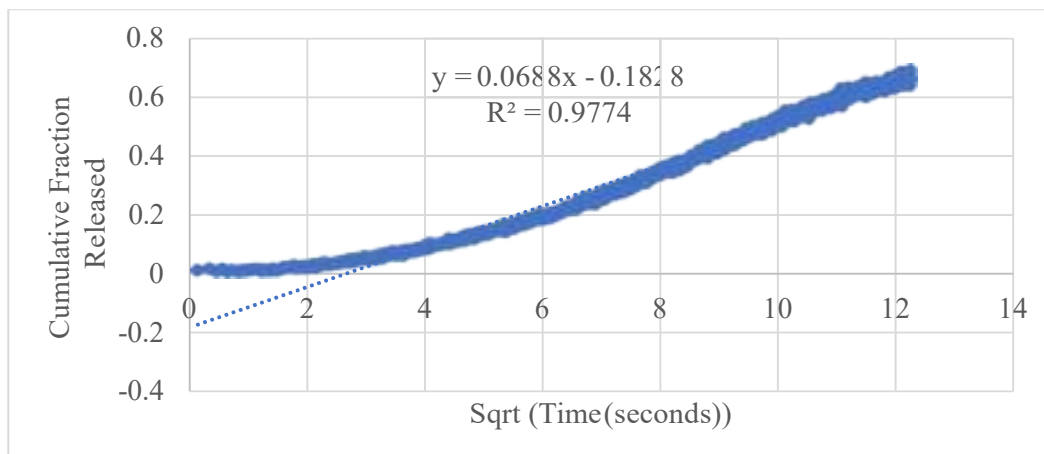
Figure 133: Higuchi plot for RGD liposomes, batch #3, at 7.46 $\left(\frac{()}{c^2}\right)$
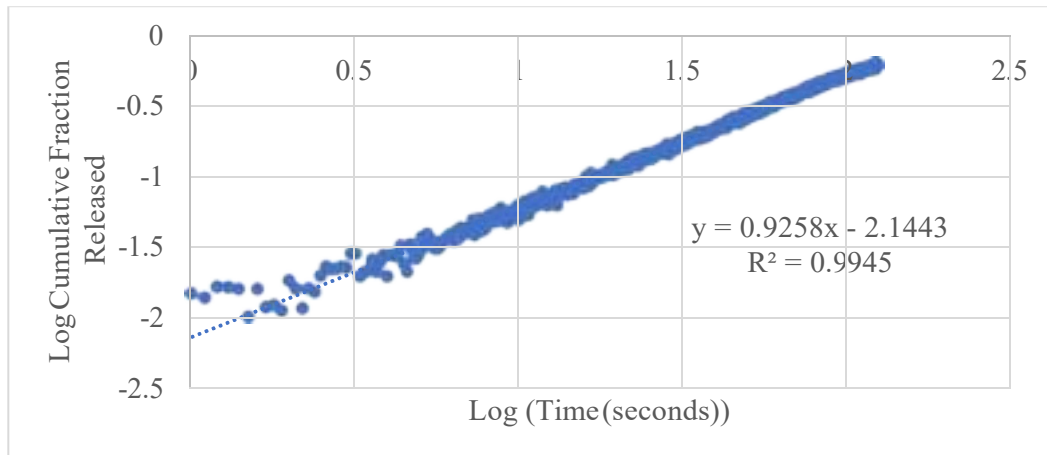
Figure 134: Korsmeyer-Peppas plot for RGD liposomes, batch #3, at 7.46 $\left(\frac{-}{c^2}\right)$
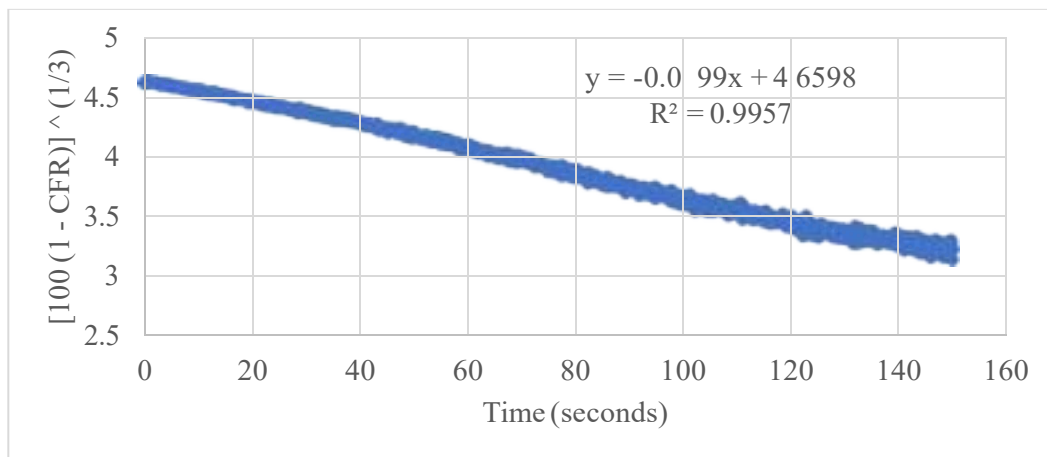
Figure 135: Hixson-Crowell plot for RGD liposomes, batch #3, at 7.46 $\left(\frac{-}{c^2}\right)$
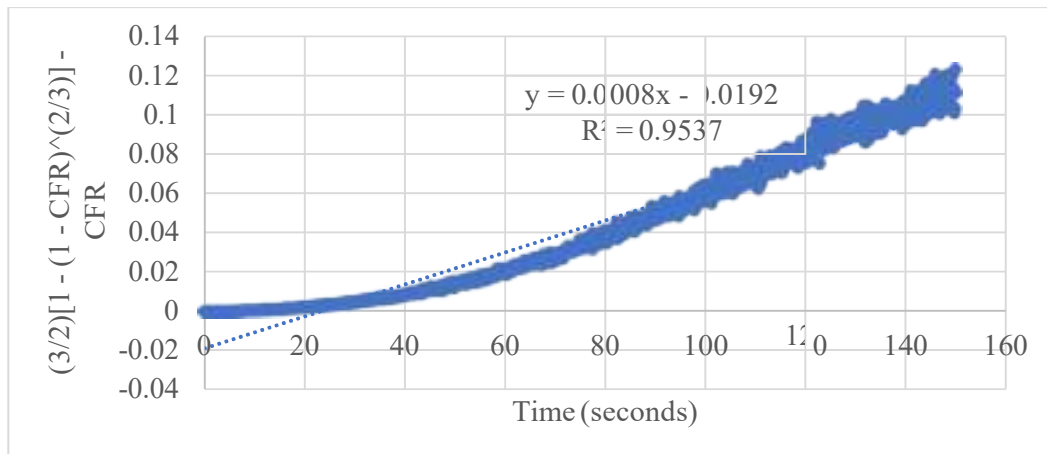
Figure 136: Baker-Lonsdale plot for RGD liposomes, batch #3, at 7.46 $\left(\frac{-}{c^2}\right)$
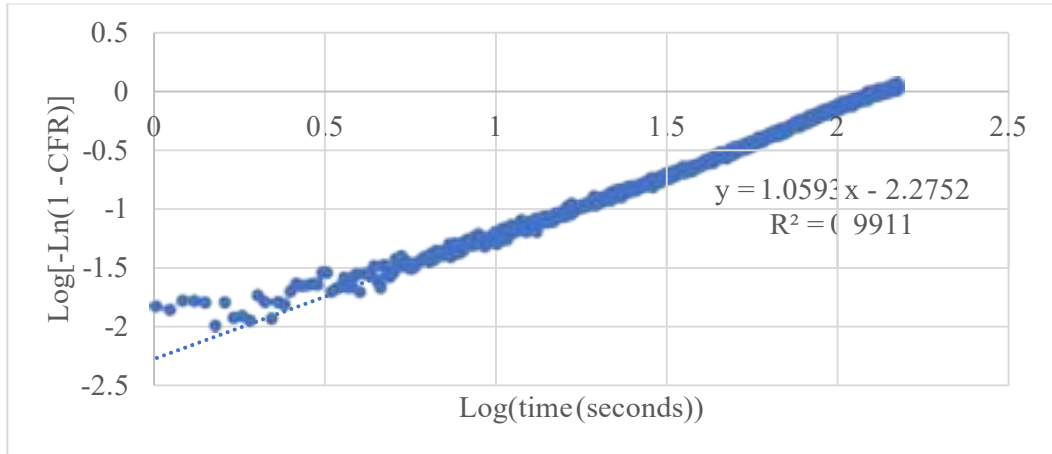
Figure 137: Weibull plot for RGD liposomes, batch #3, at 7.46 $\left(\frac{-}{c^2}\right)$

$$y = 1.0593x - 2.2752$$
$$R^2 = 0.9911$$
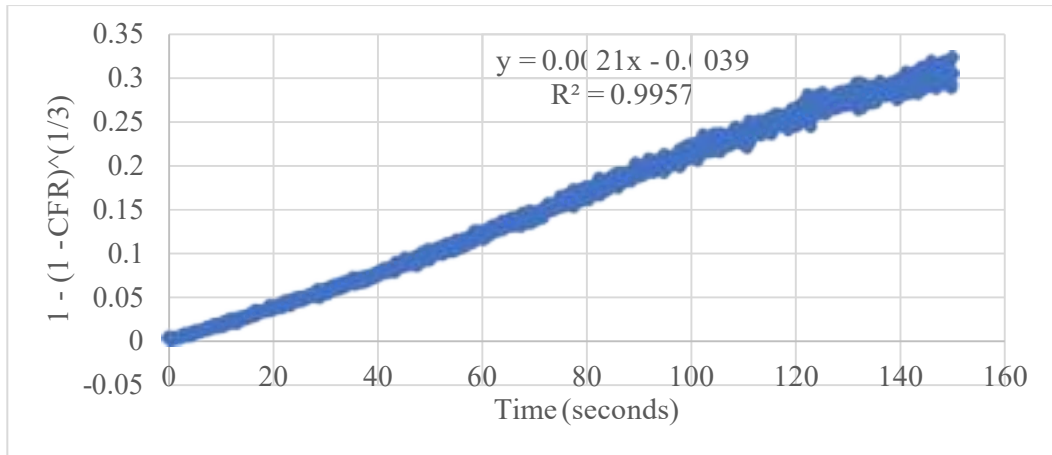
Figure 138: Hopfenberg plot for RGD liposomes, batch #3, at 7.46 $\left(\frac{-}{c^2}\right)$

$$y = 0.0021x - 0.0039$$
$$R^2 = 0.9957$$
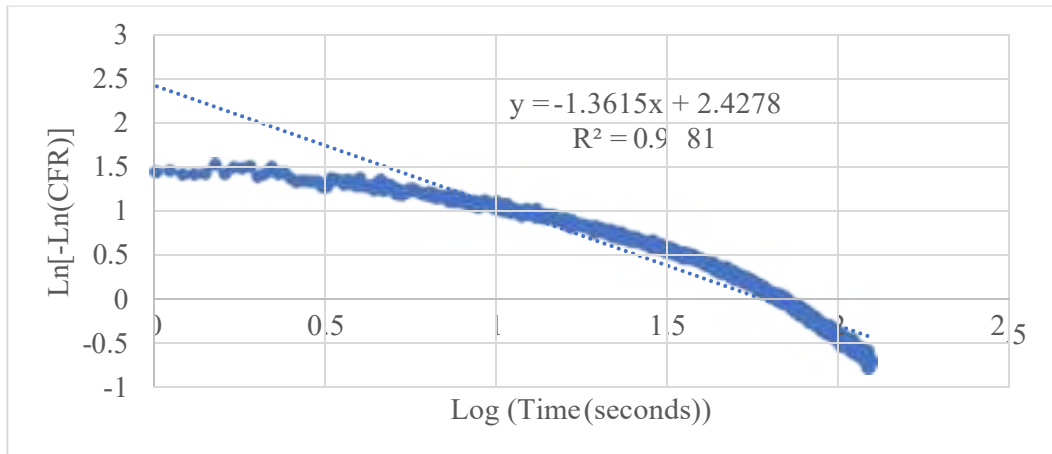
Figure 139: Gompertz plot for RGD liposomes, batch #3, at 7.46 $\left(\frac{-}{c^2}\right)$

$$y = -1.3615x + 2.4278$$
$$R^2 = 0.9981$$

Appendix F: Plots of kinetics models fits for RGD liposomes, all batches, at 9.85 $(\frac{mW}{cm^2})$
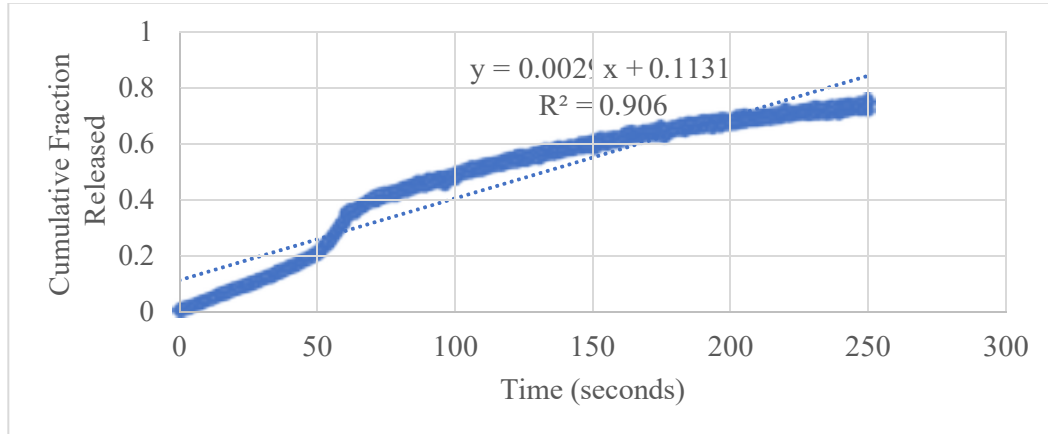
Figure 140: Zero-order plot for RGD liposomes, batch #1, at 9.85 $(\frac{-}{c^2})$
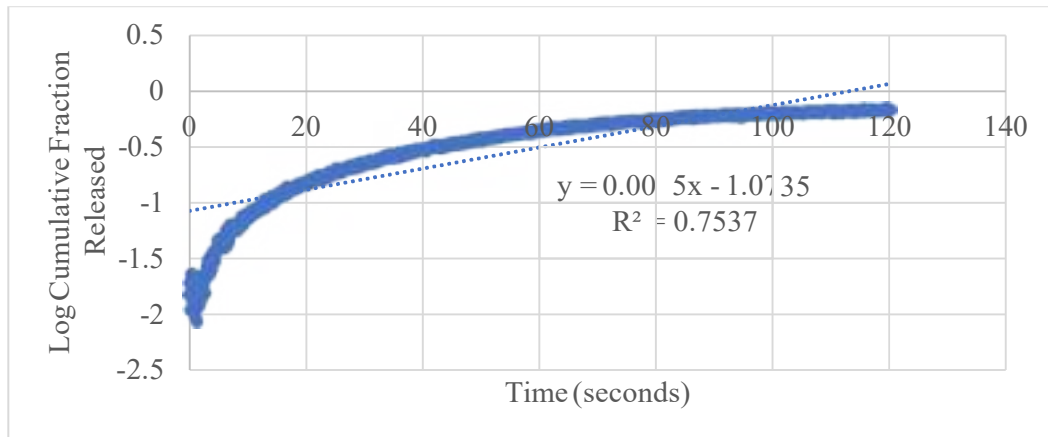
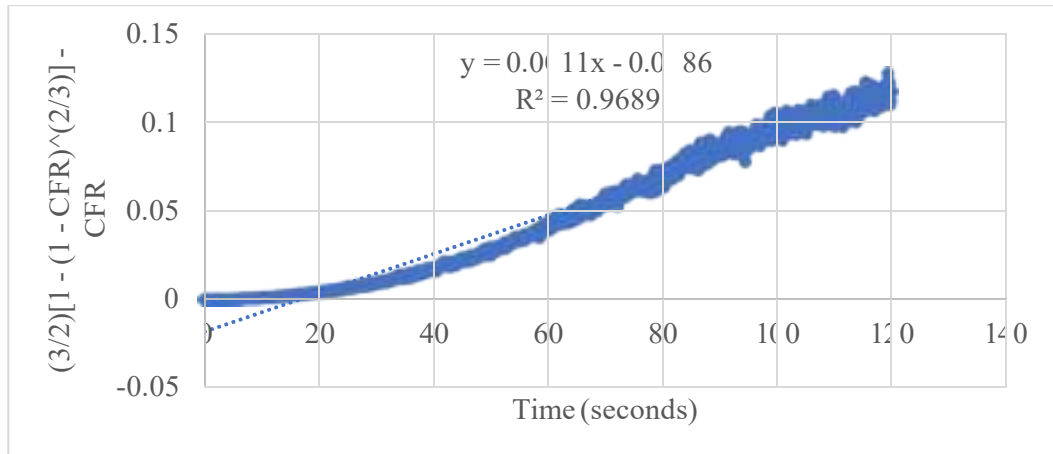**Figure 141: First-order plot for RGD liposomes, batch #1, at 9.85** $(\frac{-}{c^2})$
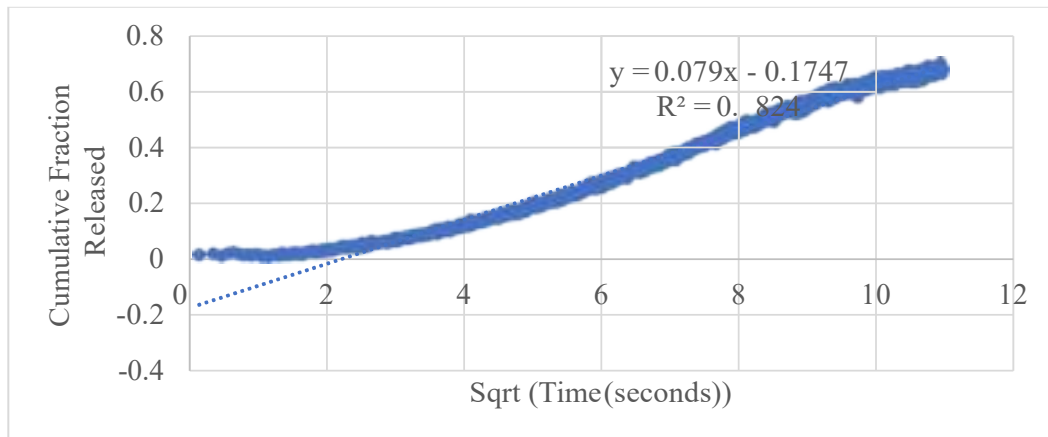
Figure 142: Higuchi plot for RGD liposomes, batch #1, at 9.85 $(\frac{-}{c^2})$

137
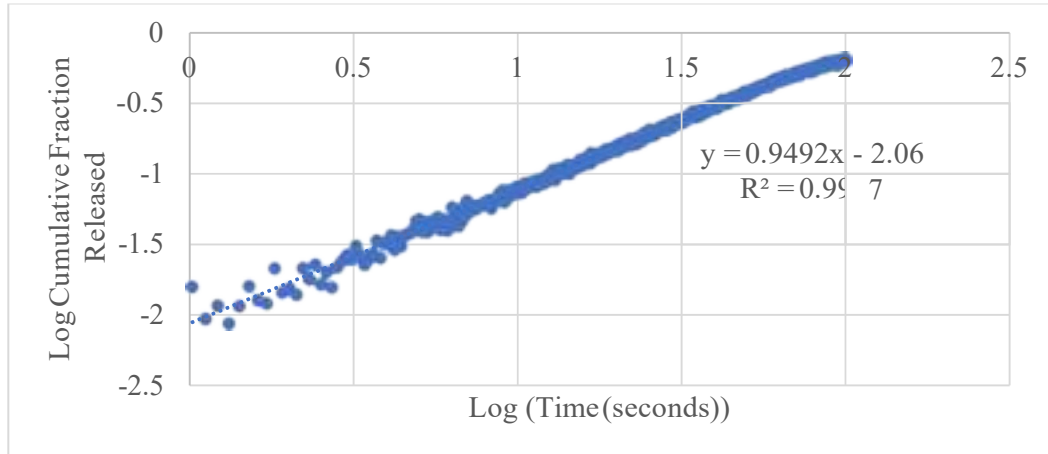
Figure 143: Korsmeyer-Peppas plot for RGD liposomes, batch #1, at 9.85 $\left(\frac{-}{c^2}\right)$
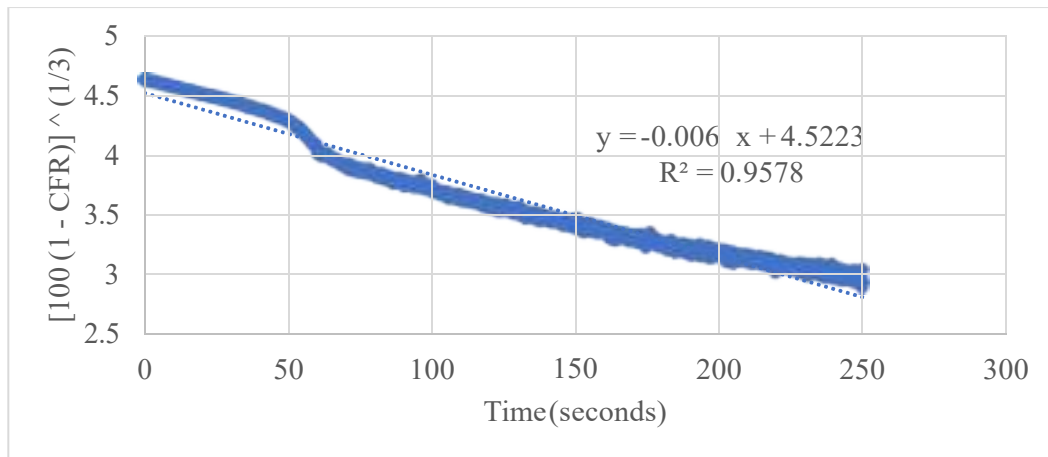
Figure 144: Hixson-Crowell plot for RGD liposomes, batch #1, at 9.85 $\left(\frac{-}{c^2}\right)$
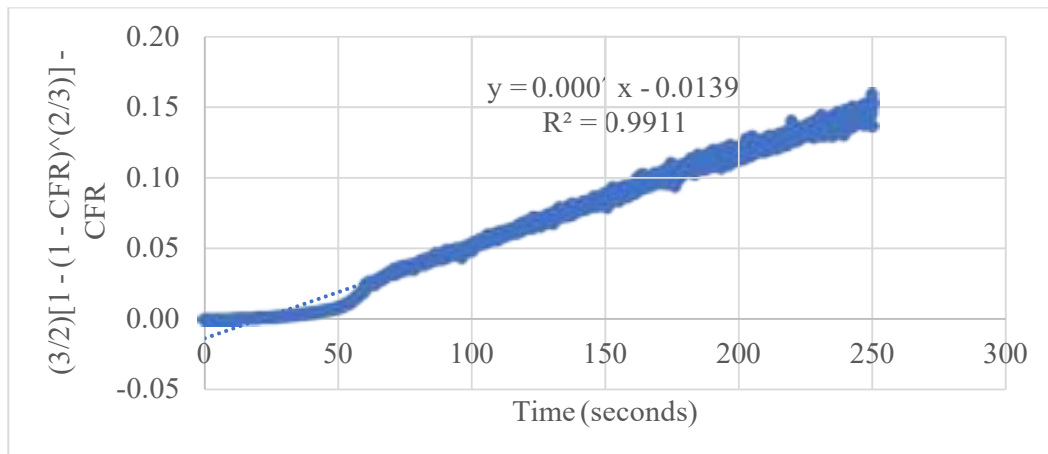
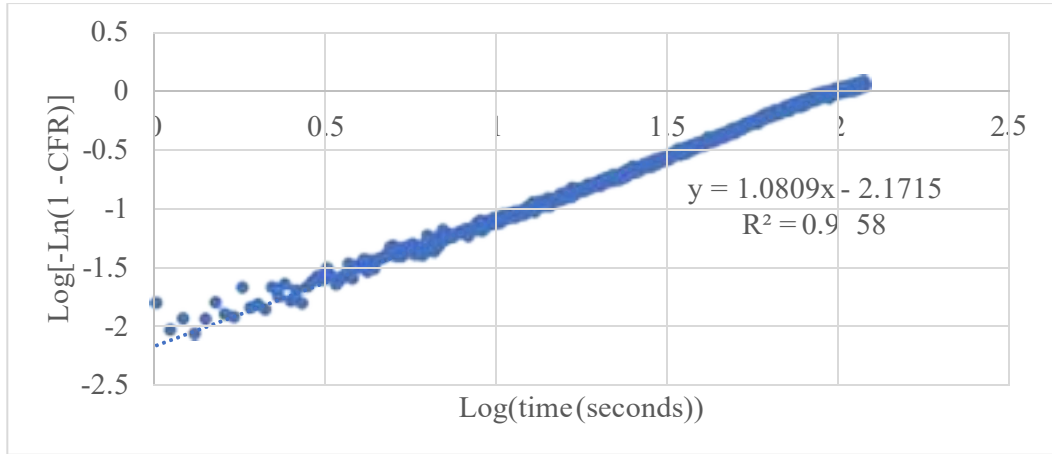**Figure 145: Baker-Lonsdale plot for RGD liposomes, batch #1, at 9.85 $\left(\frac{-}{c^2}\right)$**
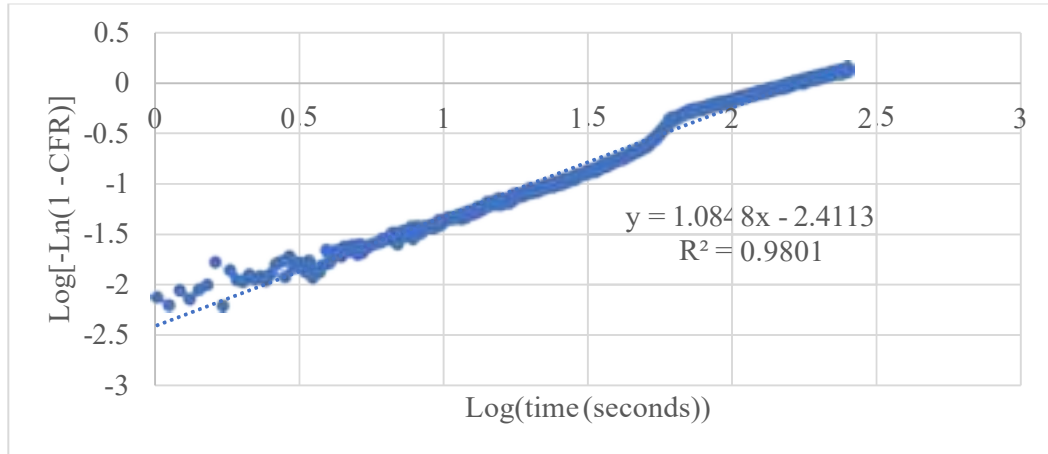
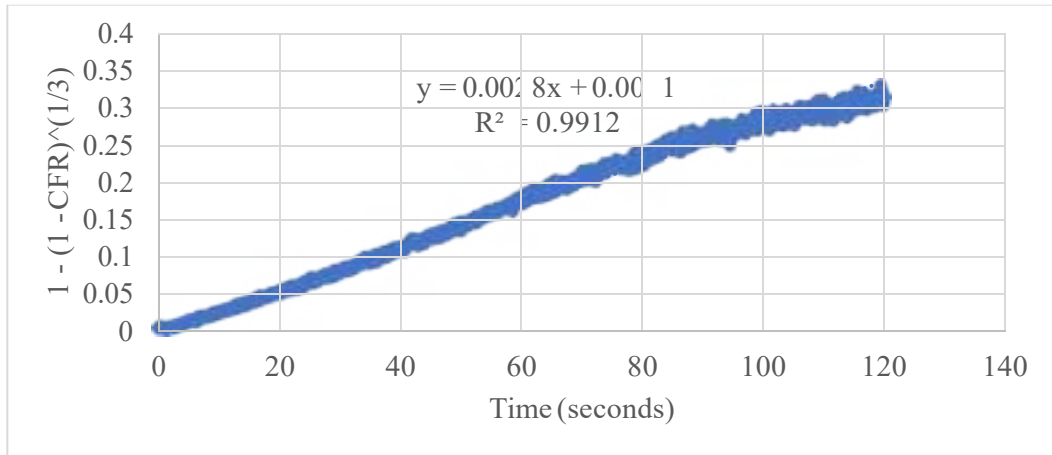**Figure 146: Weibull plot for RGD liposomes, batch #1, at 9.85 $\left(\frac{-}{c^2}\right)$**
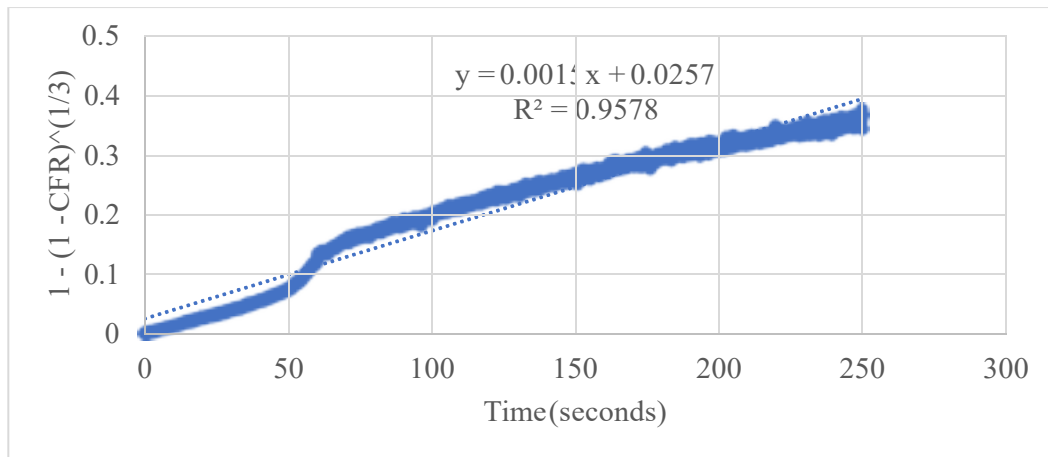
Figure 147: Hopfenberg plot for RGD liposomes, batch #1, at 9.85 $\left(\frac{-}{c^2}\right)$
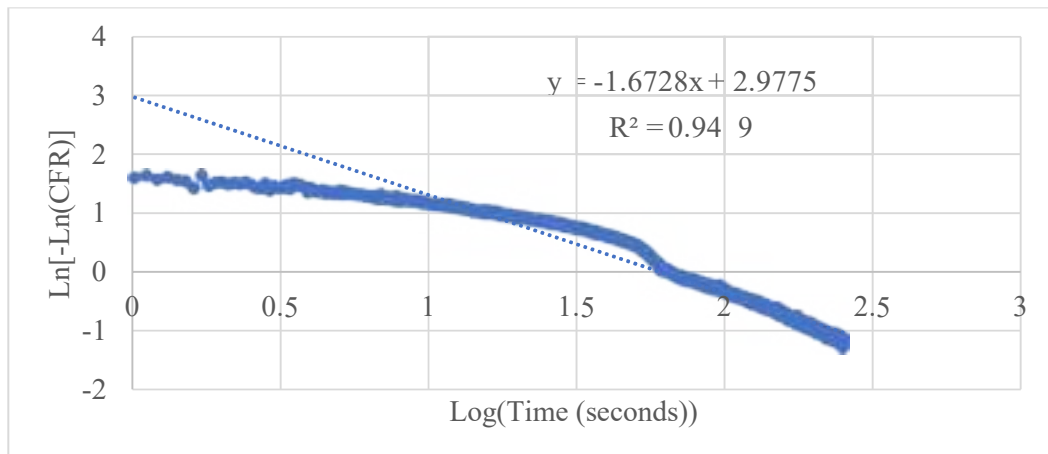
Figure 148: Gompertz plot for RGD liposomes, batch #1, at 9.85 $\left(\frac{-}{c^2}\right)$
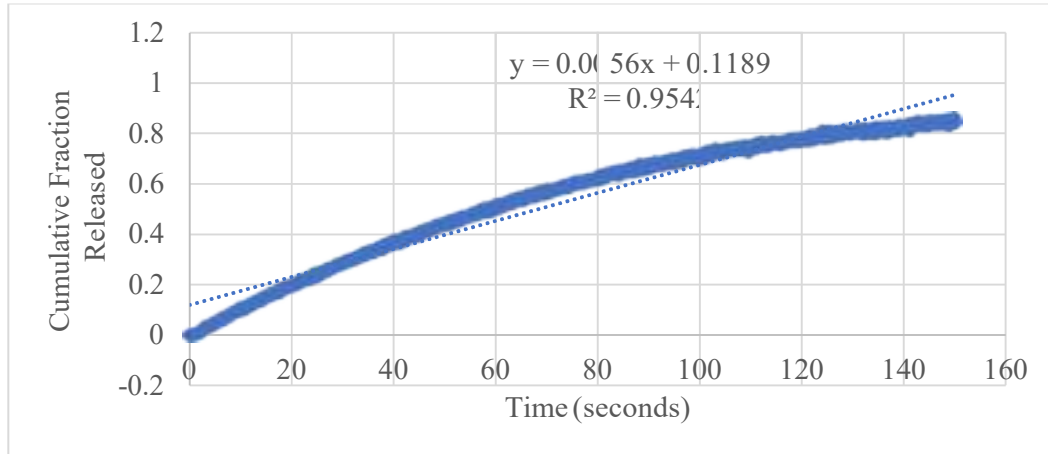
Figure 149: Zero-order plot for RGD liposomes, batch #2, at 9.85 $\left(\dfrac{-}{c^2}\right)$
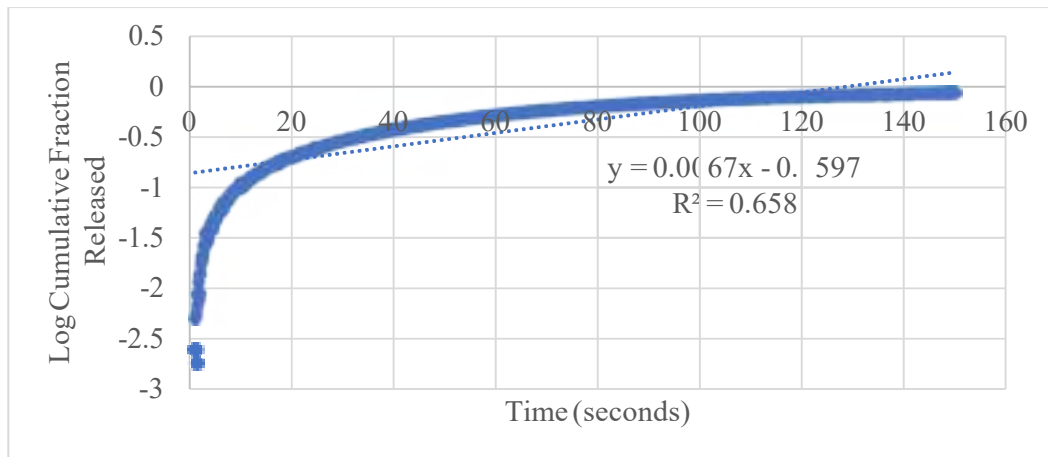
Figure 150: First-order plot for RGD liposomes, batch #2, at 9.85 $\left(\dfrac{-}{c^2}\right)$
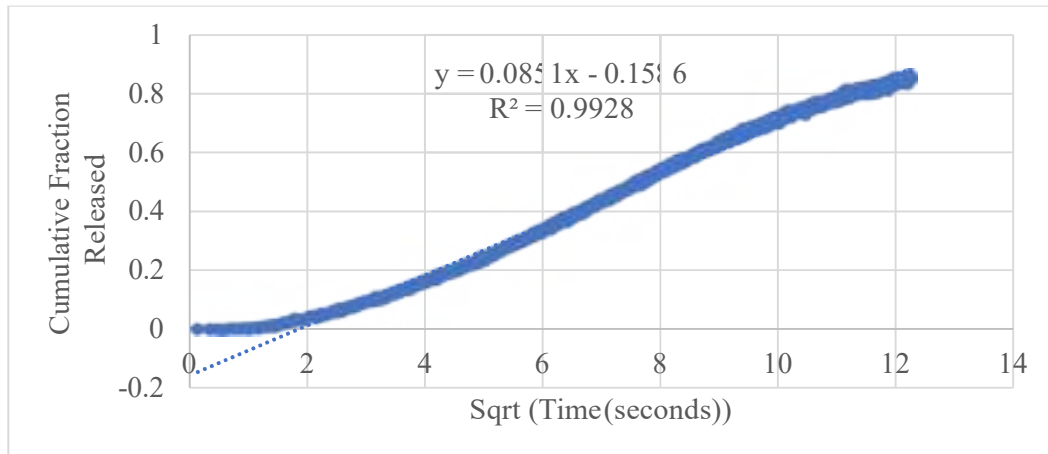
Figure 151: Higuchi plot for RGD liposomes, batch #2, at 9.85 $\left(\dfrac{-}{c^2}\right)$

Figure 152: Korsmeyer-Peppas plot for RGD liposomes, batch #2, at 9.85 $\left(\frac{-}{c^2}\right)$
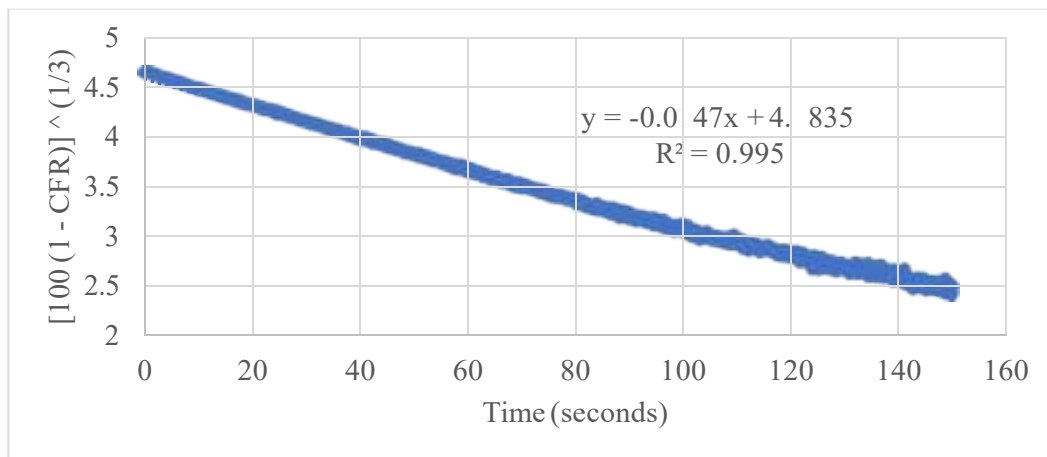
Figure 153: Hixson-Crowell plot for RGD liposomes, batch #2, at 9.85 $\left(\frac{-}{c^2}\right)$
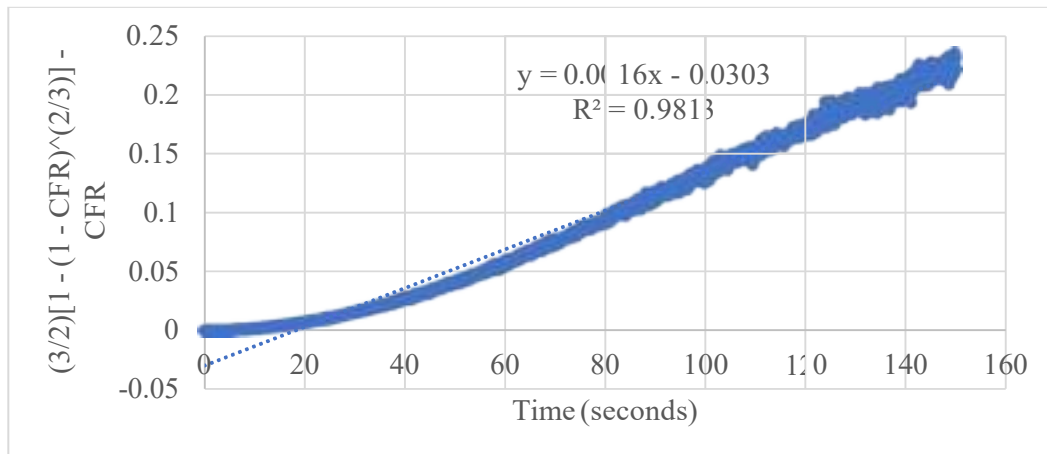
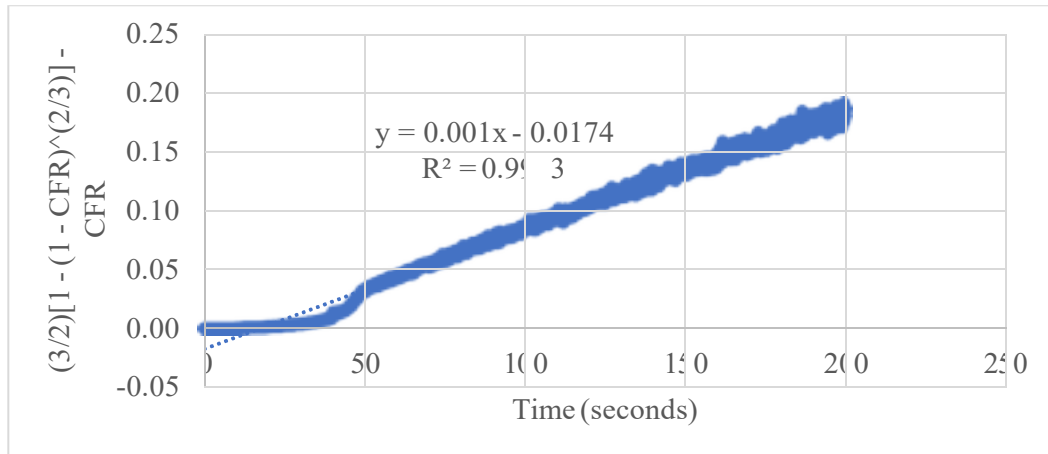**Figure 154: Baker-Lonsdale plot for RGD liposomes, batch #2, at 9.85 $\left(\frac{-}{c^2}\right)$**
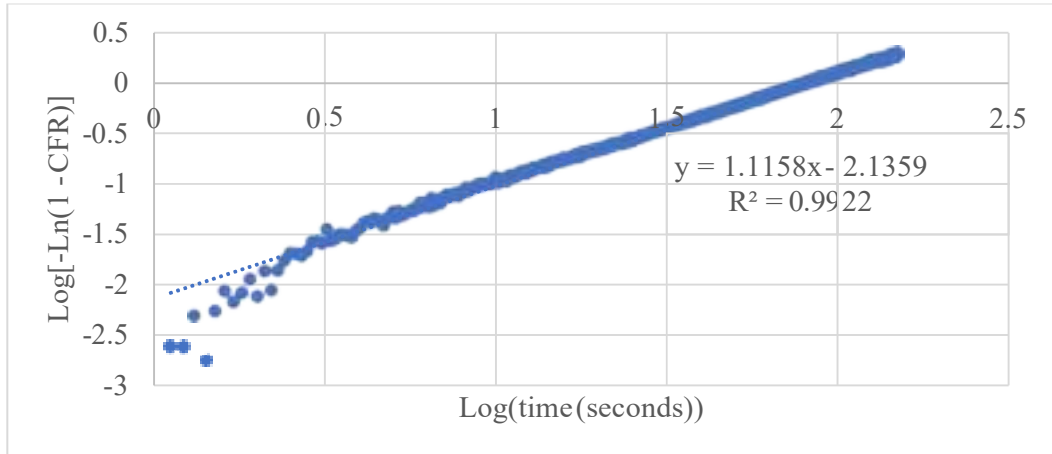
Figure 155: Weibull plot for RGD liposomes, batch #2, at 9.85 $\left(\frac{-}{c^2}\right)$
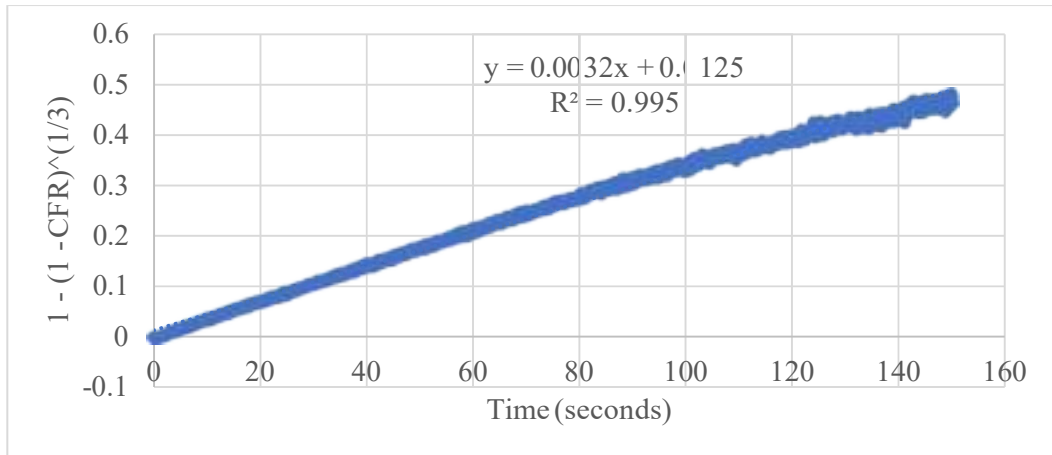
Figure 156: Hopfenberg plot for RGD liposomes, batch #2, at 9.85 $\left(\frac{-}{c}\right)_2$
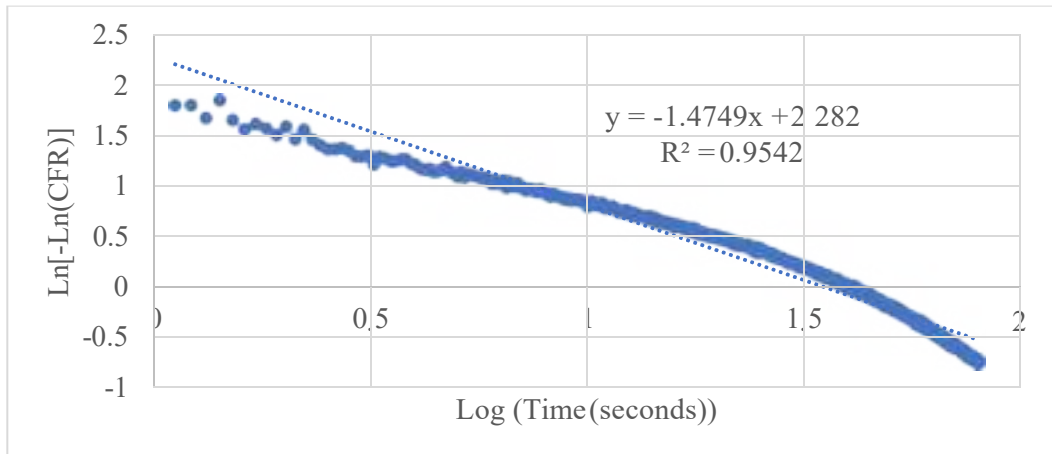
Figure 157: Gompertz plot for RGD liposomes, batch #2, at 9.85 $\left(\frac{-}{c}\right)_2$
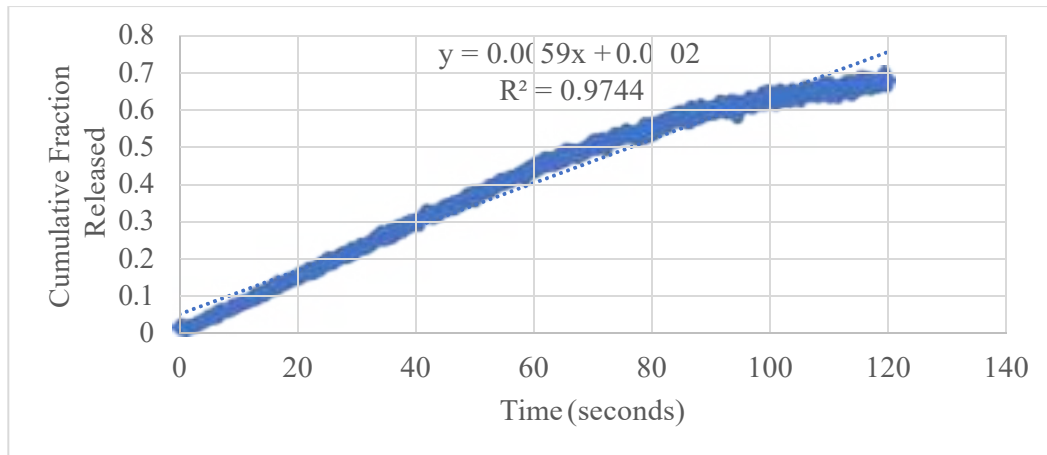
Figure 158: Zero-order plot for RGD liposomes, batch #3, at 9.85 $\left(\dfrac{-}{c^2}\right)$
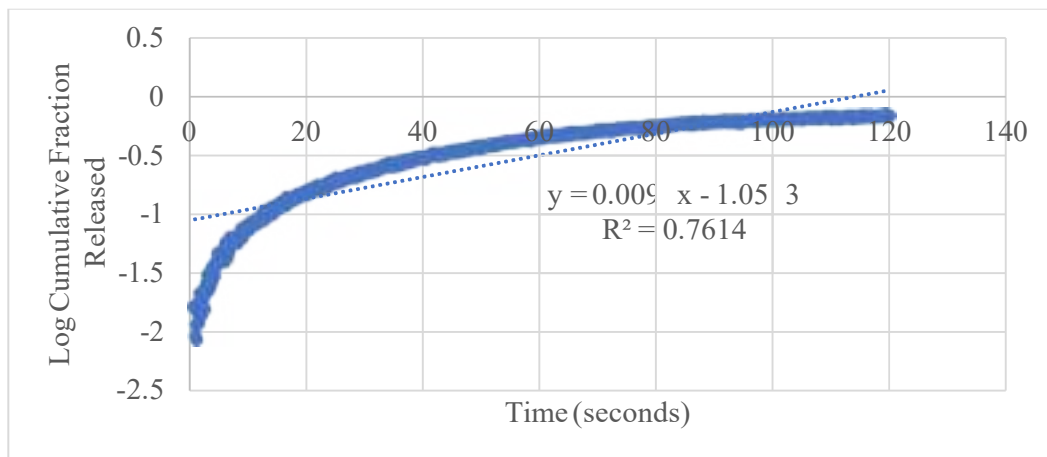
Figure 159: First-order plot for RGD liposomes, batch #3, at 9.85 $\left(\dfrac{-}{c^2}\right)$
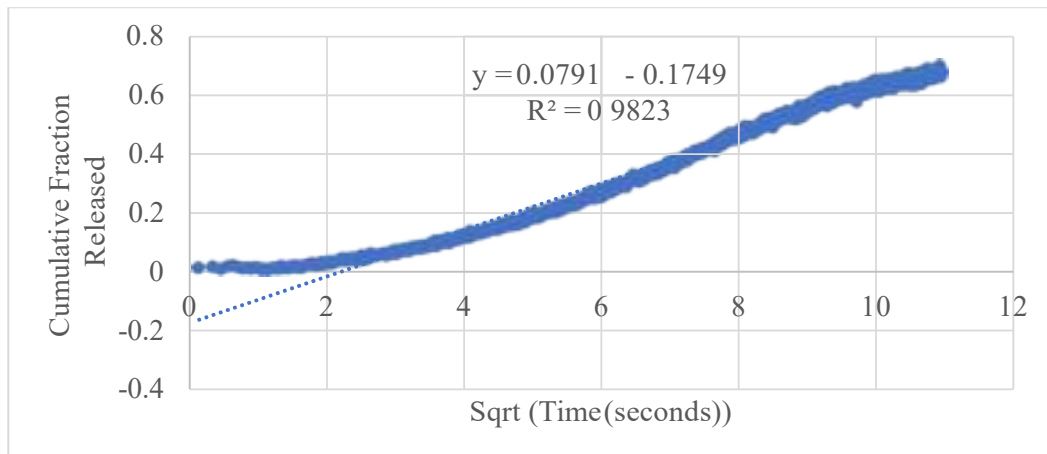
Figure 160: Higuchi plot for RGD liposomes, batch #3, at 9.85 $\left(\dfrac{-}{c^2}\right)$

143
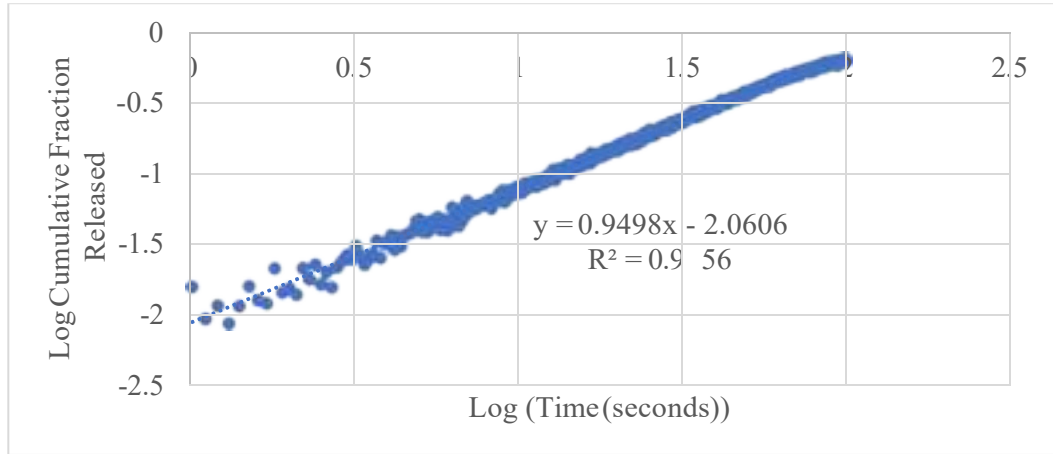
Figure 161: Korsmeyer-Peppas plot for RGD liposomes, batch #3, at 9.85 $\left(\frac{-}{c^2}\right)$
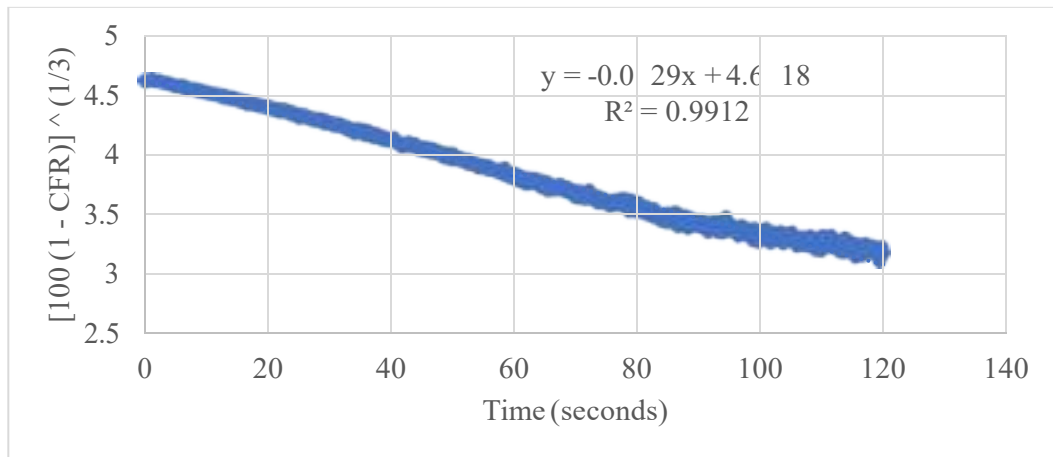
Figure 162: Hixson-Crowell plot for RGD liposomes, batch #3, at 9.85 $\left(\frac{-}{c}\right)_2$

Figure 163: Baker-Lonsdale plot for RGD liposomes, batch #3, at 9.85 $\left(\frac{-}{c}\right)_2$

Figure 164: Weibull plot for RGD liposomes, batch #3, at 9.85 $\frac{(-)}{C^2}$

Figure 165: Hopfenberg plot for RGD liposomes, batch #3, at 9.85 $\frac{(-)}{C^2}$
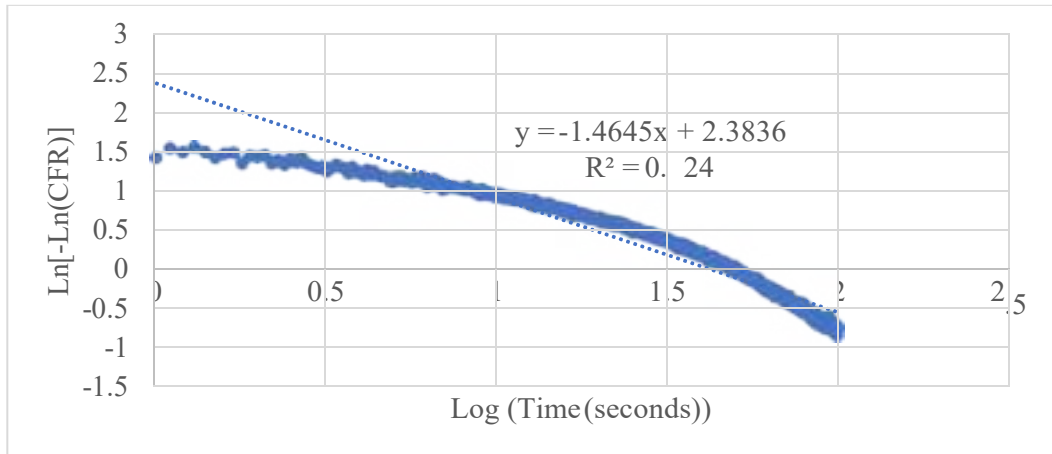
Figure 166: Gompertz plot for RGD liposomes, batch #3, at 9.85 $\frac{(-)}{C^2}$

145
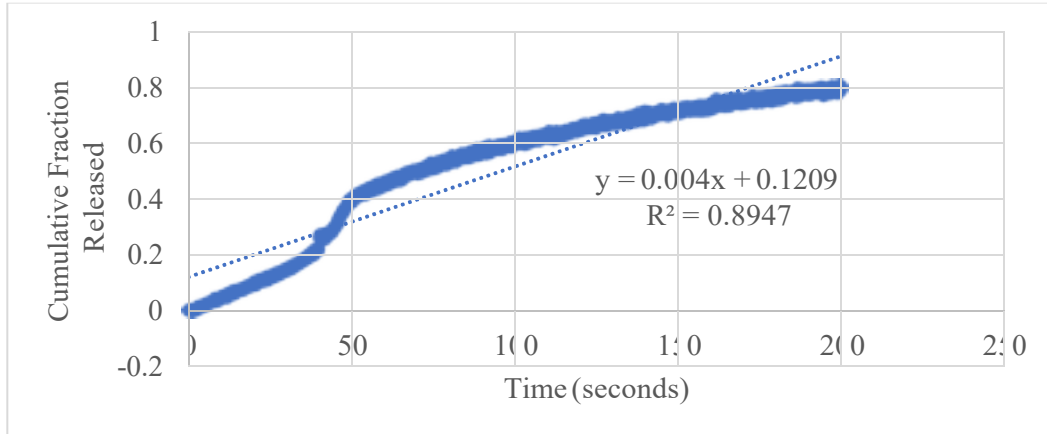
Figure 167: Zero-order plot for RGD liposomes, batch #1, at 17.31 $\left(\frac{-}{c^2}\right)$
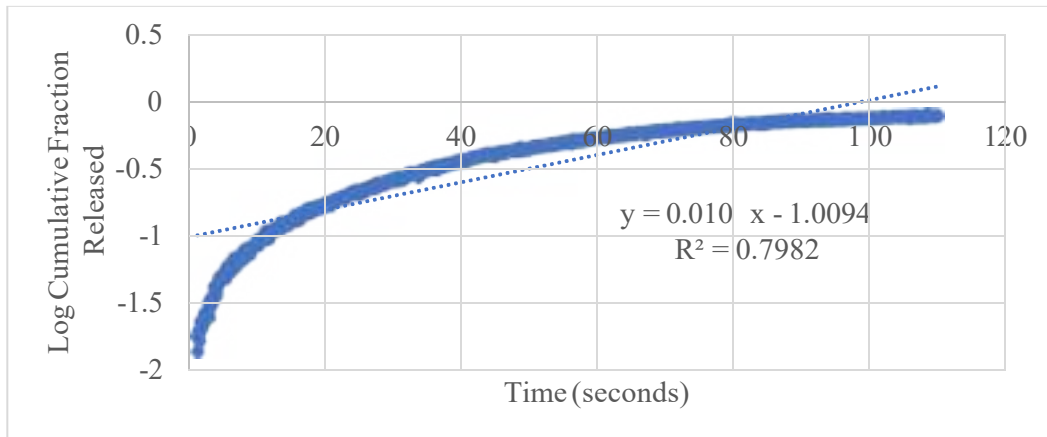
Figure 168: First-order plot for RGD liposomes, batch #1, at 17.31 $\left(\frac{-}{c^2}\right)$
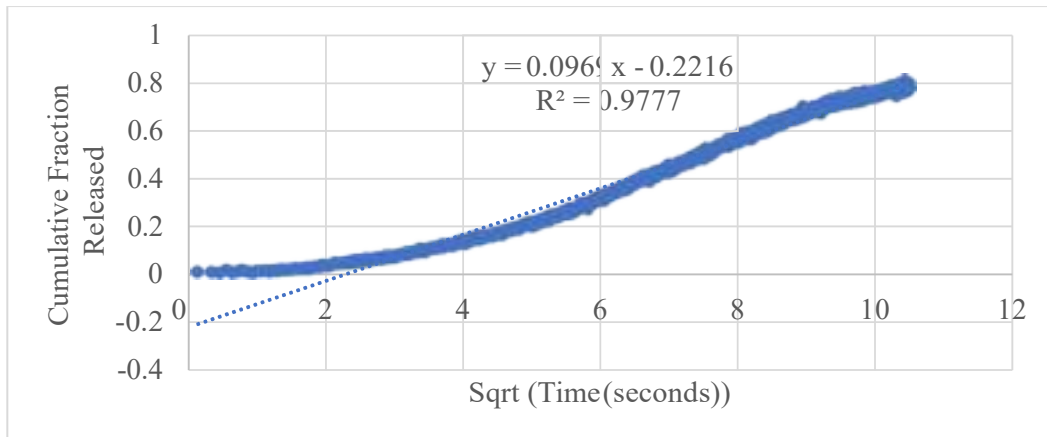
Figure 169: Higuchi plot for RGD liposomes, batch #1, at 17.31 $\left(\frac{-}{c^2}\right)$
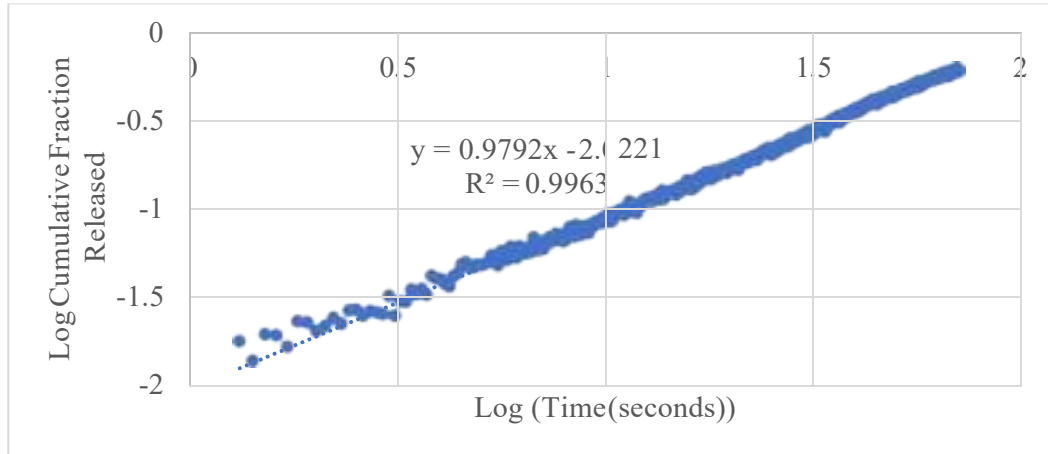
Figure 170: Korsmeyer-Peppas plot for RGD liposomes, batch #1, at 17.31 $\left(\dfrac{-}{c^2}\right)$

The equation shown on the plot: $y = 0.9792x - 2.0221$, $R^2 = 0.9963$
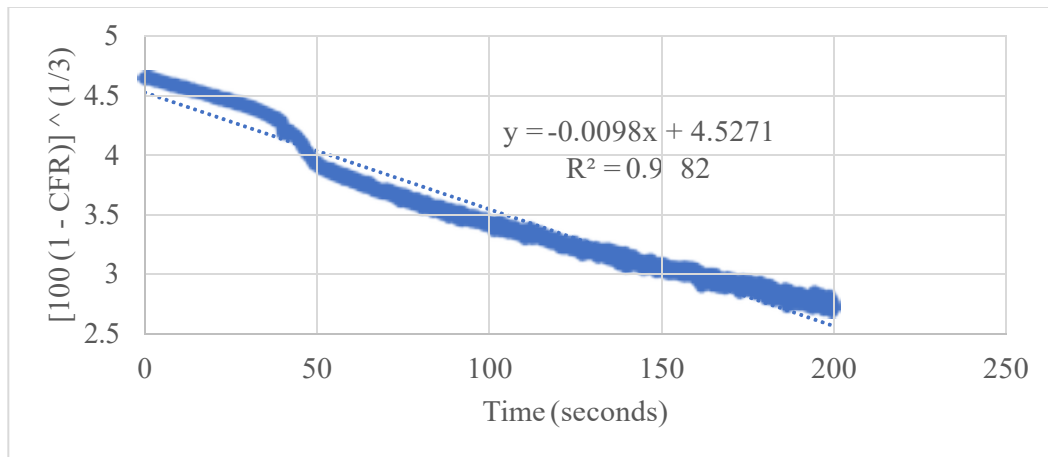
Figure 171: Hixson-Crowell plot for RGD liposomes, batch #1, at 17.31 $\left(\dfrac{-}{c^2}\right)$

The equation shown on the plot: $y = -0.0098x + 4.5271$, $R^2 = 0.9682$

Figure 172: Baker-Losndale plot for RGD liposomes, batch #1, at 17.31 $\left(\dfrac{-}{c^2}\right)$

The equation shown on the plot: $y = 0.001x - 0.0174$, $R^2 = 0.9963$
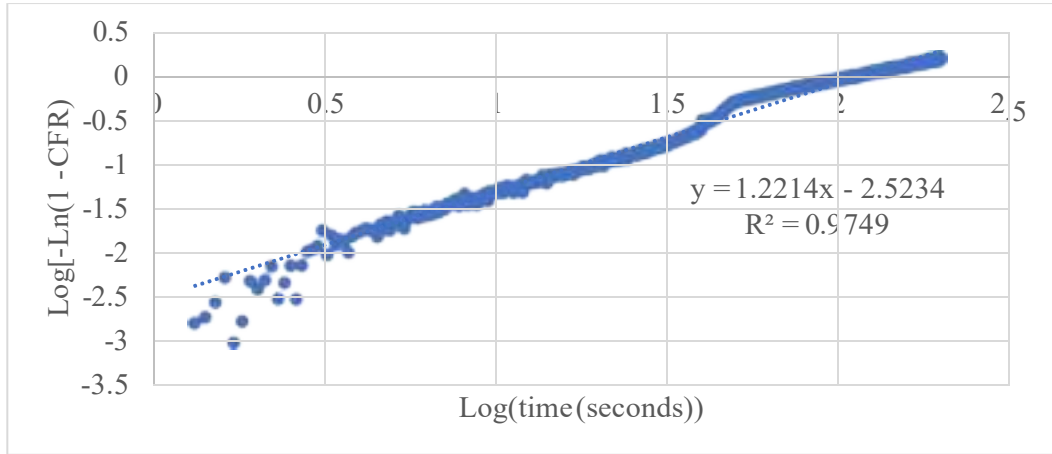
Figure 173: Weibull plot for RGD liposomes, batch #1, at 17.31 $\frac{(-)}{c^2}$
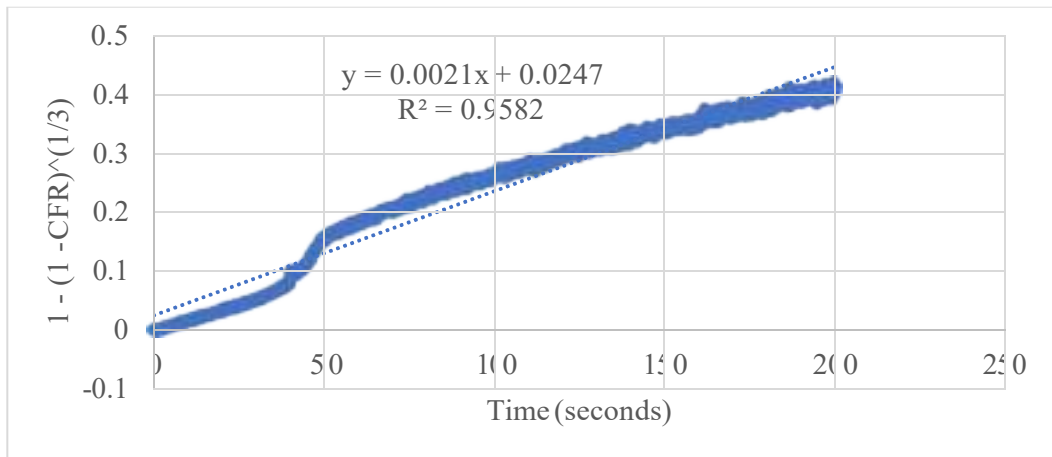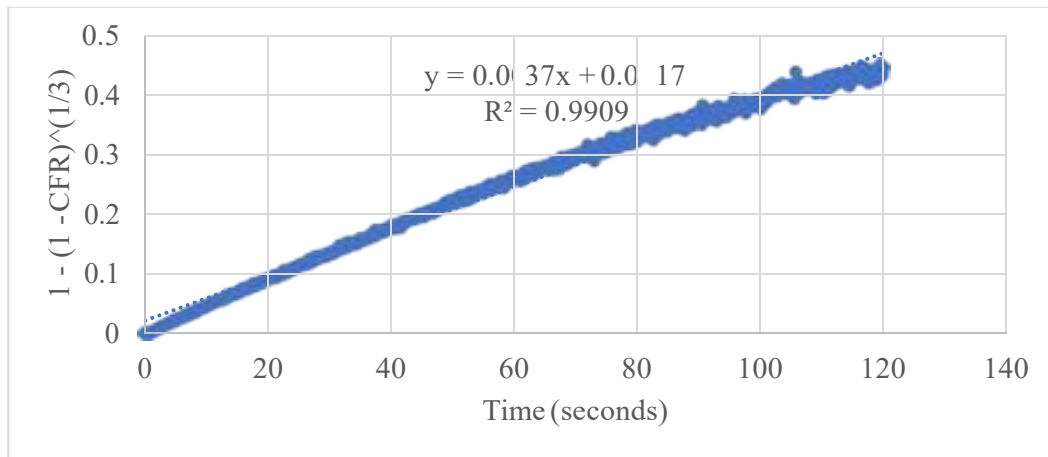

Figure 174: Hopfenberg plot for RGD liposomes, batch #1, at 17.31 $\frac{(-)}{c^2}$
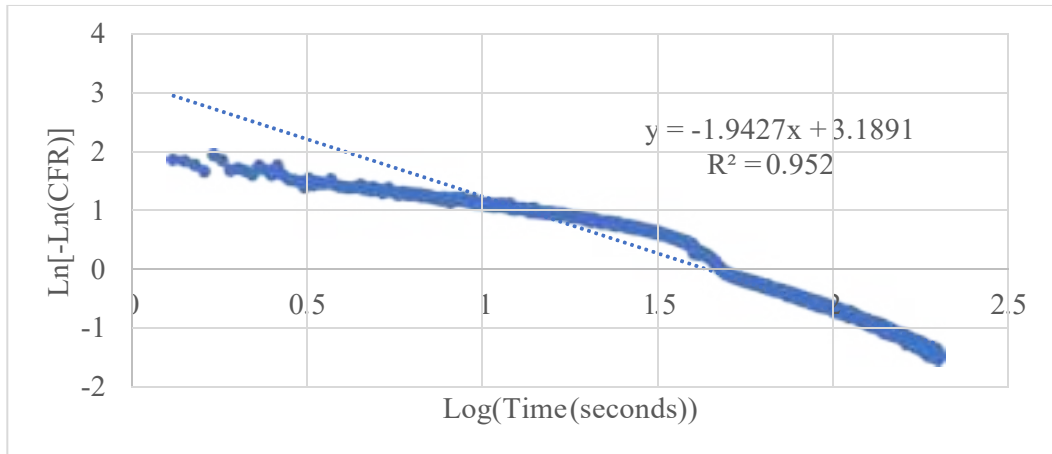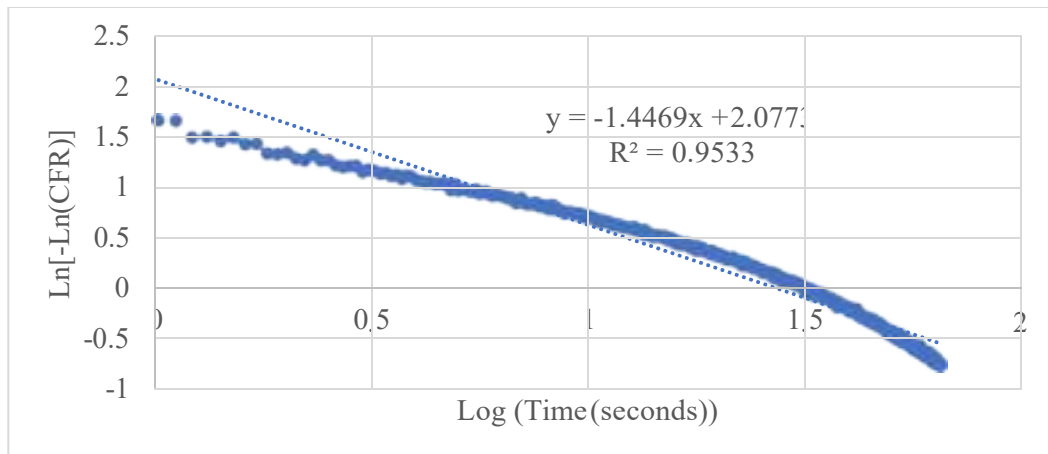

Figure 175: Gompertz plot for RGD liposomes, batch #1, at 17.31 $\frac{(-)}{c^2}$
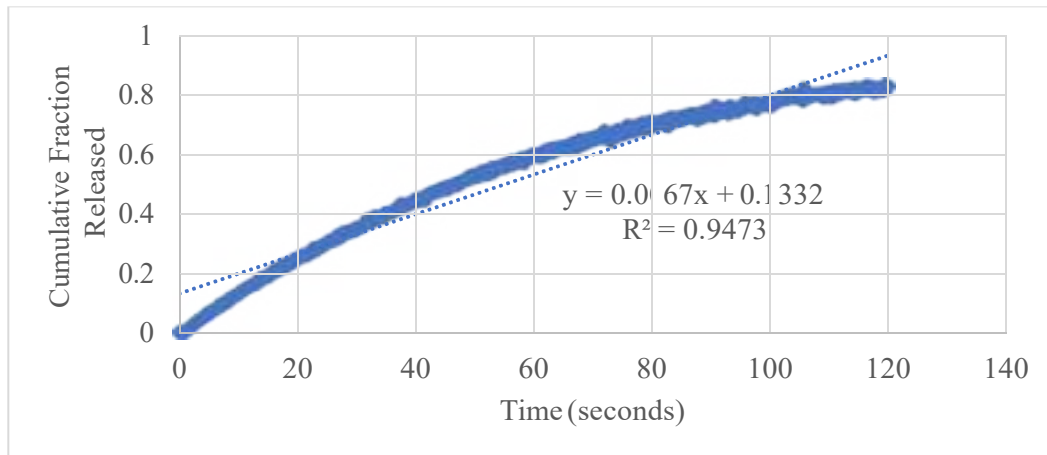
Figure 176: Zero-order plot for RGD liposomes, batch #2, at 17.31 $\left(\right)_{c^2}$

$$y = 0.0\,67x + 0.1\,332$$
$$R^2 = 0.9473$$
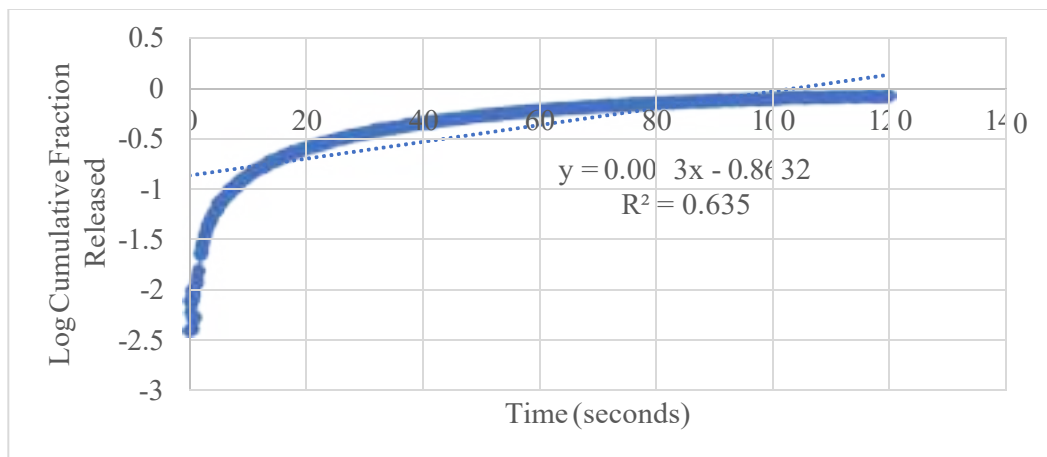
Figure 177: First-order plot for RGD liposomes, batch #2, at 17.31 $\left(\right)_{c^2}$

$$y = 0.00\,3x - 0.86\,32$$
$$R^2 = 0.635$$
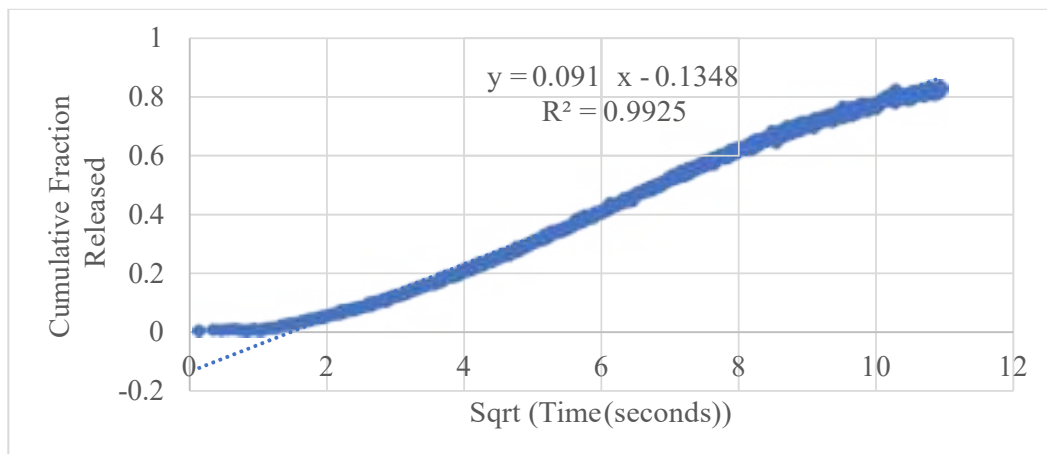
Figure 178: Higuchi plot for RGD liposomes, batch #2, at 17.31 $\left(\right)_{c^2}$

$$y = 0.091\,x - 0.1348$$
$$R^2 = 0.9925$$
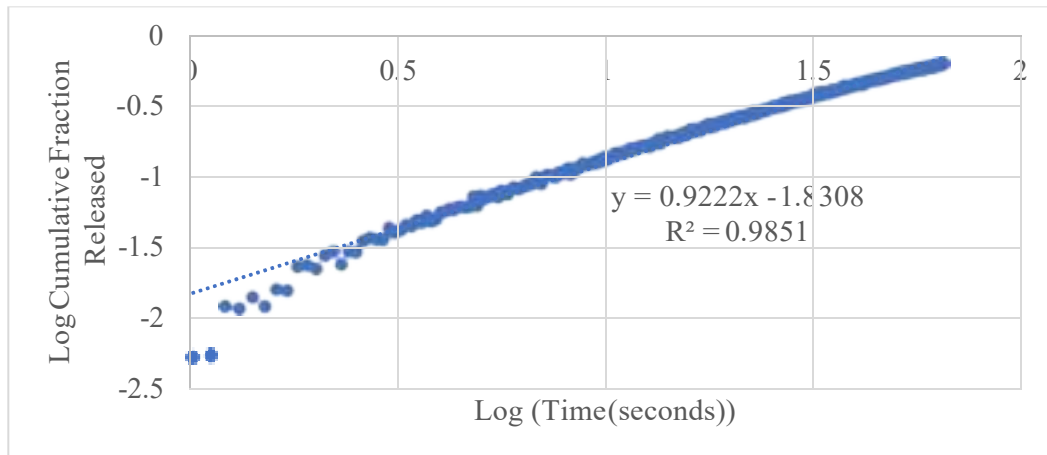
Figure 179: Korsmeyer-Peppas plot for RGD liposomes, batch #2, at 17.31 $\left(\dfrac{-}{c^2}\right)$
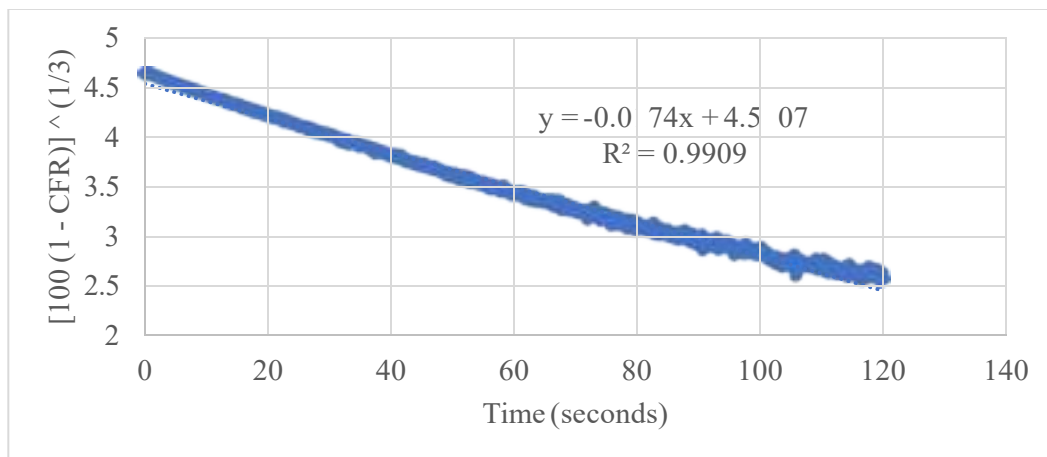
Figure 180: Hixson-Crowell plot for RGD liposomes, batch #2, at 17.31 $\left(\dfrac{-}{c^2}\right)$
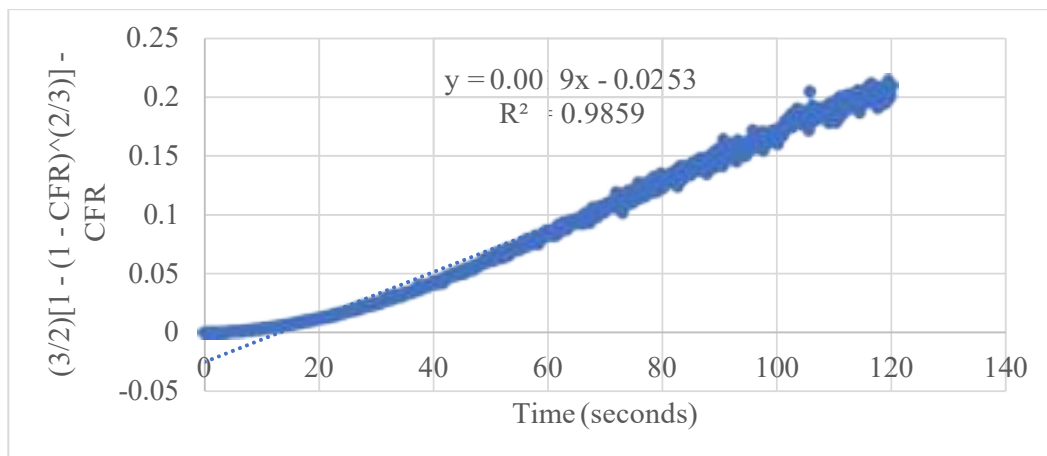
Figure 181: Baker-Lonsdale plot for RGD liposomes, batch #2, at 17.31 $\left(\dfrac{-}{c^2}\right)$
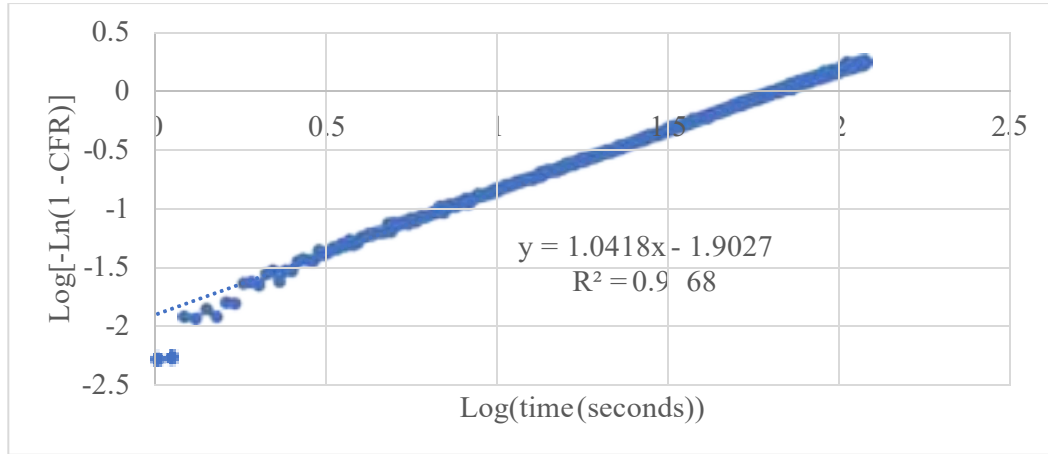
Figure 182: Weibull plot for RGD liposomes, batch #2, at 17.31 $\frac{(-)}{c^2}$

Figure 183: Hopfenberg plot for RGD liposomes, batch #2, at 17.31 $\frac{(-)}{c^2}$

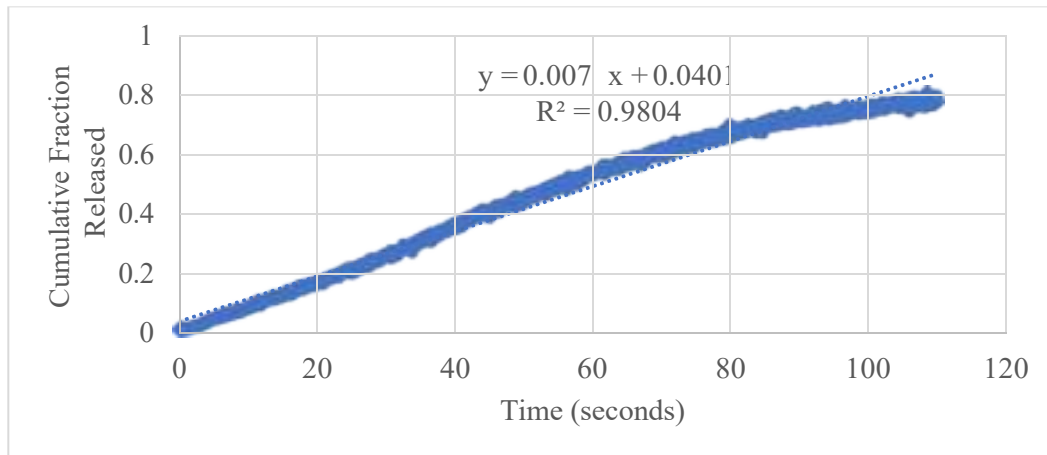**Figure 184: Gompertz plot for RGD liposomes, batch #2, at 17.31 $\frac{(-)}{c^2}$**

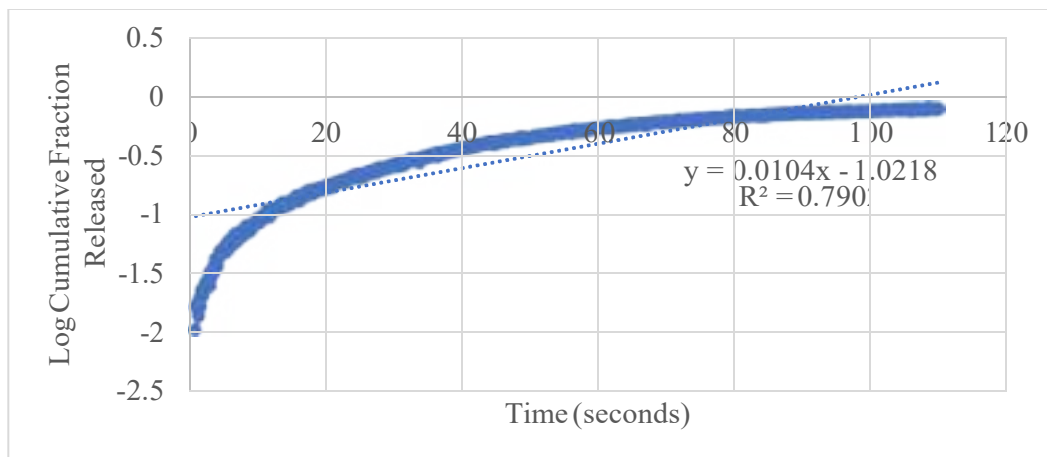**Figure 185: Zero-order plot for RGD liposomes, batch #3, at 17.31 $\left(\frac{-}{c}\right)_2$**

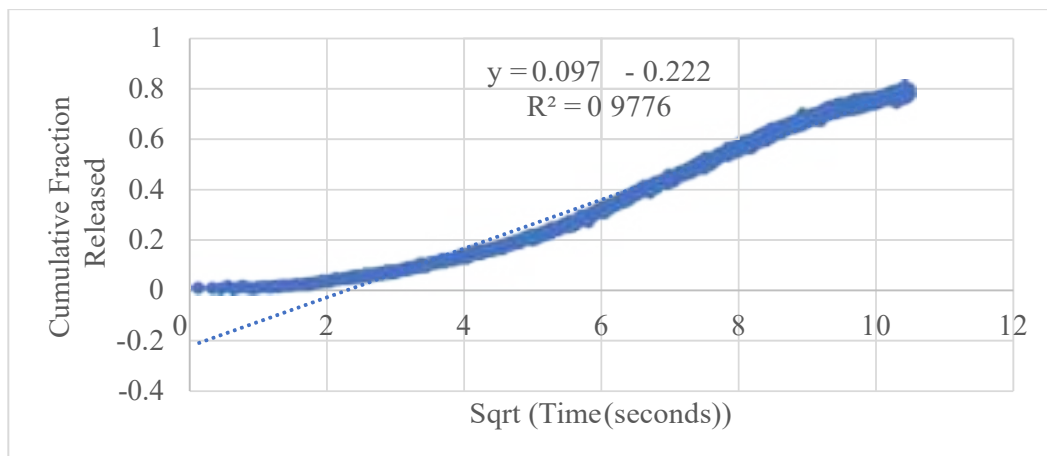**Figure 186: First-order plot for RGD liposomes, batch #3, at 17.31 $\left(\frac{-}{c}\right)_2$**

Figure 187: Higuchi plot for RGD liposomes, batch #3, at 17.31 $\left(\frac{-}{c^2}\right)$
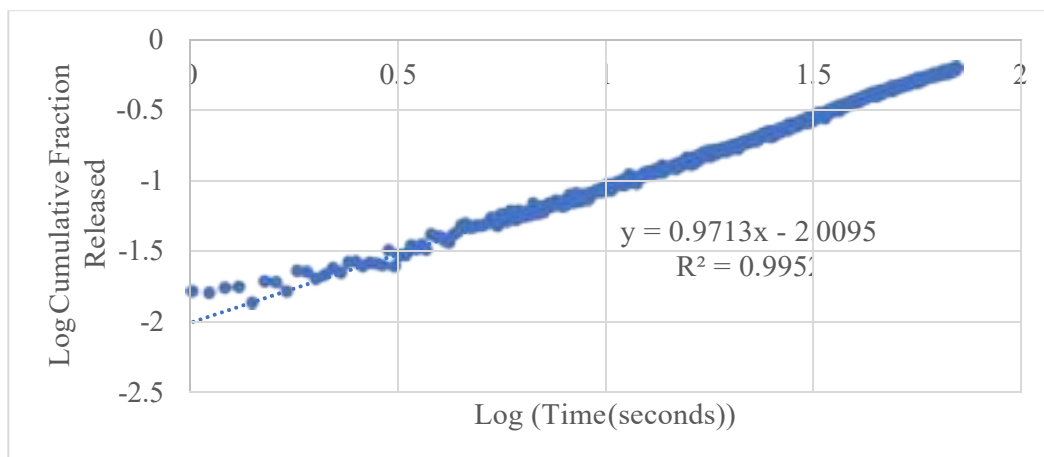
Figure 188: Korsmeyer-Peppas plot for RGD liposomes, batch #3, at 17.31 $\frac{(-)}{c^2}$
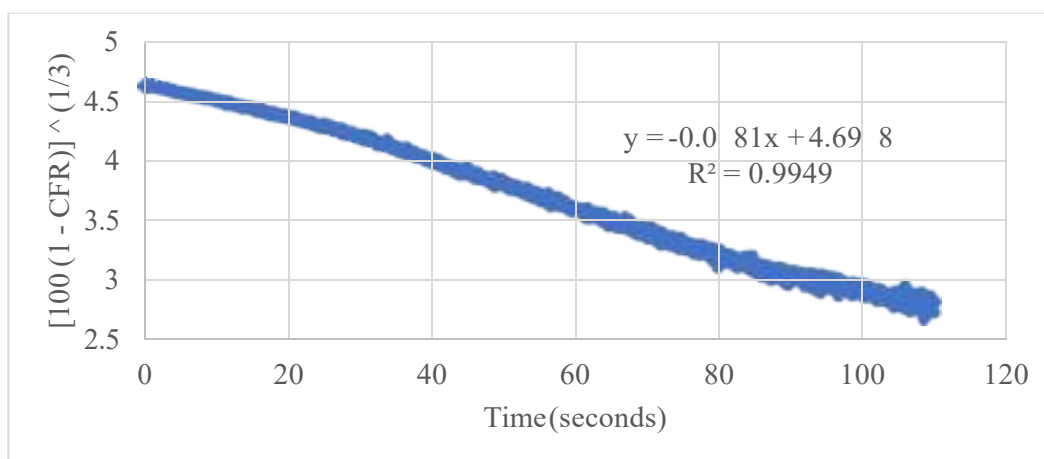

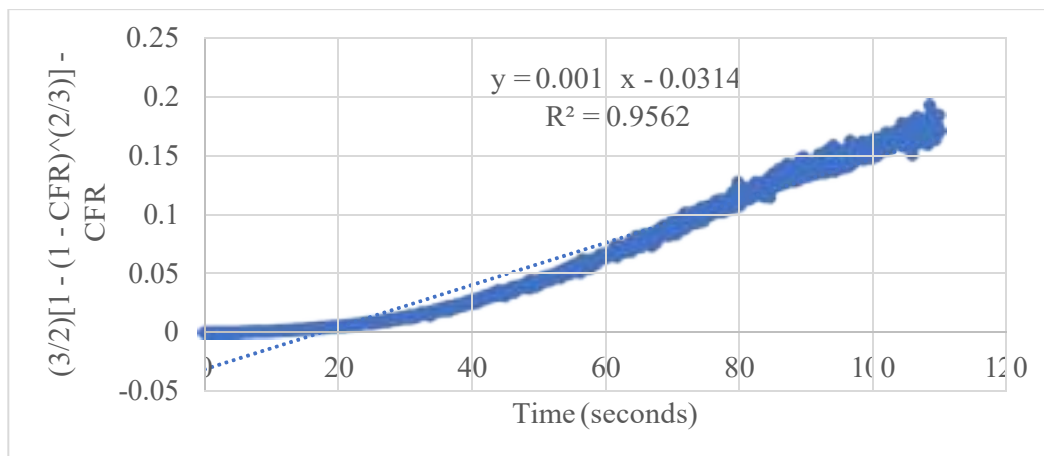**Figure 189: Hixson-Crowell plot for RGD liposomes, batch #3, at 17.31 $\frac{(-)}{c^2}$**

Figure 190: Baker-Lonsdale plot for RGD liposomes, batch #3, at 17.31 $\frac{(-)}{c^2}$
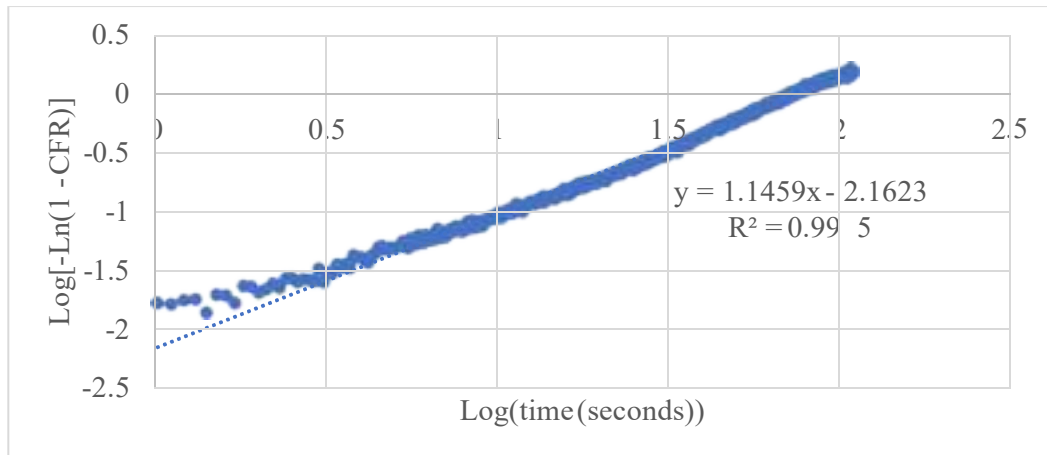
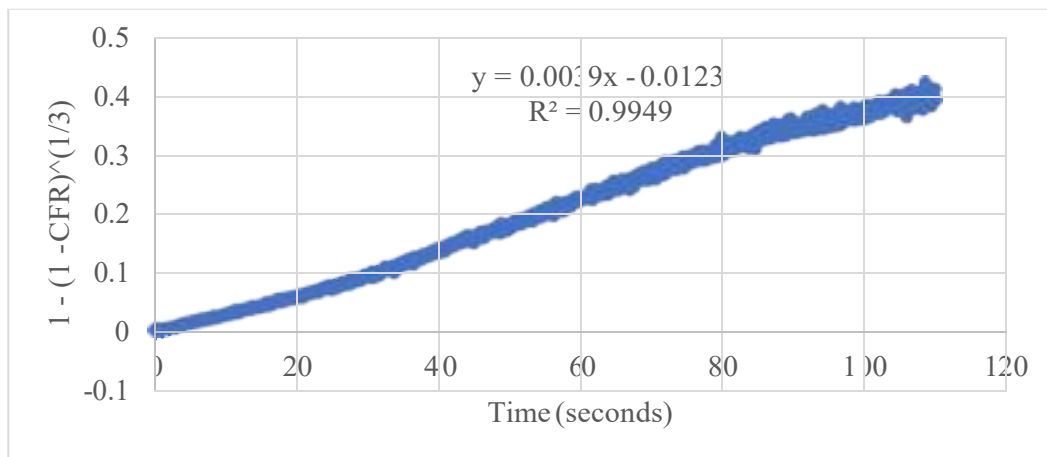**Figure 191: Weibull plot for RGD liposomes, batch #3, at 17.31 $\frac{(-)}{c^2}$**

Figure 192: Hopfenberg plot for RGD liposomes, batch #3, at 17.31 $\frac{(-)}{c^2}$
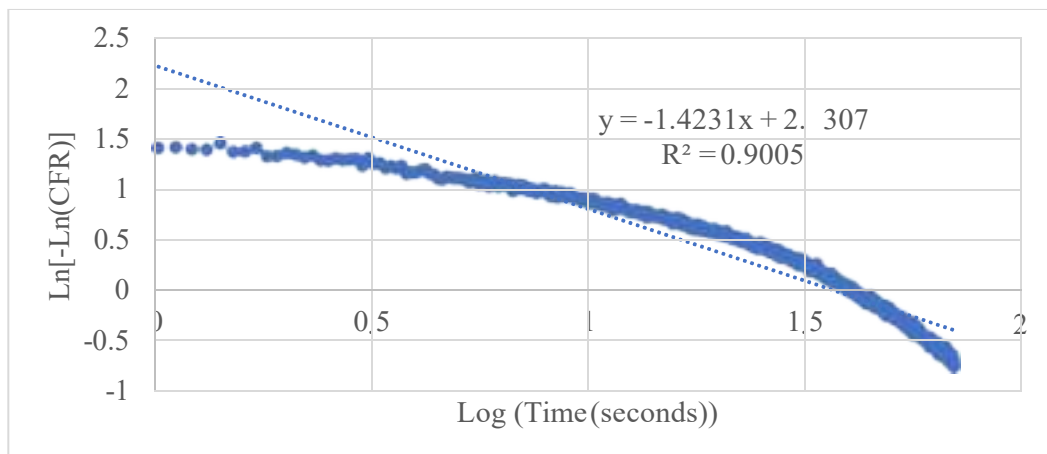

Figure 193: Gompertz plot for RGD liposomes, batch #3, at 17.31 $\frac{(-)}{c^2}$

Vita

Mohamad Mahmoud was born in 1992, in Dubai, United Arab Emirates. He received his elementary education from the Rosary Sisters School in Sharjah, United Arab Emirates. He received his secondary education from the Dubai International School in Dubai, UAE. He completed his internship at Dubai Natural Gas Company Ltd. (DUGAS) as an Engineering Intern. He received his B.Sc. degree in Chemical Engineering from the American University of Sharjah in 2013. From 2014 to 2016, he worked as a Chemical Engineer in two international companies in the United Arab Emirates. Specifically, his first position was Chemical Engineer - Technical Advising and Production Development at a specialty minerals manufacturer called OMYA, located in Sharjah, United Arab Emirates. His second position was Carelflex™ Engineer - thiochemicals division at a specialty chemicals manufacturer called Arkema France, located in Dubai, United Arab Emirates.

In January 2016, he joined the Chemical Engineering master's program at the American University of Sharjah with a part-time position as a Graduate Teaching Assistant. During his master's study, he presented the results of this thesis as a paper titled "The effect of Ultrasound on the Drug Delivery of RGD-Targeted Liposomes," in the UAE Graduate Students Research Conference 2018 (UAEGSRC-2018). His current research focuses on developing smart drug delivery nanocarriers which are active-targeting-enabled and are responsive to ultrasound to investigate their application to cancer treatments. His research interests include smart nanomaterials in advanced electrochemical energy systems and biomedical engineering, drug delivery, and kinetics modeling.